สำนักหอสมุดกลาง พระจอมเกล้าลาดกระบัง

GROWTH OF NANOCRYSTAL INDIUM TIN OXYNITRIDE AND ZINC OXYNITRIDE THIN FILMS BY REACTIVE GAS-TIMING RF MAGNETRON SPUTTERING

E058060

DON KLAITABTIM

เลขหมู่.....................................
เลขทะเบียน......58060......
วัน,เดือน,ปี......17 มี.ย. 2552......

.b...............................
.i...............................

A THESIS SUBMITTED IN FULFILLMENT

OF THE REQUIREMENT FOR THE DEGREE OF

DOCTOR OF PHILOSOPHY IN APPLIED PHYSICS

SCHOOL OF GRADUATE STUDIES

KING MONGKUT'S INSTITUTE OF TECHNOLOGY LADKRABANG

2008

KMITL-2008-SC-D-030-387

This material is reserved for educational use only, not allowed for commercial use.
Forbidden to modify the content, and cite the document when use.

COPYRIGHT 2008

SCHOOL OF GRADUATE STUDIES

KING MONGKUT'S INSTITUTE OF TECHNOLOGY LADKRABANG

This material is reserved for educational use only, not allowed for commercial use.

Forbidden to modify the content, and cite the document when use.

หัวข้อวิทยานิพนธ์	การปลูกผลึกนาโนของฟิล์มบางอินเดียมทินออกซีไนไตรด์และซิงค์ออกซีไนไตรด์โดยวิธีควบคุมเวลาก๊าซไวปฏิกิริยาอาร์เอฟแมกนีตรอนสปัตเตอริง
นักศึกษา	เรืออากาศเอก ดอน คล้ายทับทิม
รหัสประจำตัว	47063401
ปริญญา	ปรัชญาดุษฎีบัณฑิต
สาขาวิชา	ฟิสิกส์ประยุกต์
พ.ศ.	2551
อาจารย์ที่ปรึกษาวิทยานิพนธ์	รศ.ดร.จิติ หนูแก้ว
อาจารย์ที่ปรึกษาวิทยานิพนธ์ร่วม	ดร.สิรพัฒน์ ประโทนเทพ

บทคัดย่อ

วิทยานิพนธ์ฉบับนี้เป็นการศึกษาและปลูกผลึกนาโนของฟิล์มบางอินเดียมทินออกซีไนไตรด์และซิงค์ออกซีไนไตรด์ ด้วยวิธีควบคุมเวลาก๊าซไวปฏิกิริยา โดยระบบปลูกฟิล์มอาร์เอฟแมกนีตรอนสปัตเตอริง ได้วัสดุซึ่งแสดงสมบัติใหม่ทางกายภาพและทางแสงออกมา การดำเนินงานวิจัยเริ่มจากเตรียมฟิล์มบางอินเดียมทินออกไซด์และซิงค์ออกไซด์ โดยใช้ก๊าซอาร์กอนเพียงอย่างเดียวในขบวนการเตรียมฟิล์ม แล้วศึกษาถึงเงื่อนไขและผลกระทบต่างๆ ของการปลูกฟิล์มที่มีต่อสมบัติทางโครงสร้าง ทางแสงและทางไฟฟ้า โดยทำการตรวจวิเคราะห์สมบัติทางโครงสร้างด้วยเทคนิคการเลี้ยวเบนของรังสีเอกซ์ กล้องจุลทรรศน์อิเล็กตรอนแบบเลื่อนกราด เครื่องสเปกโตรสโคปีระบบโฟโตอิเล็กตรอนด้วยรังสีเอกซ์ ตรวจสอบคุณสมบัติทางแสงด้วยเครื่องสเปกโตรสโคปีระบบยูวี-วีสสิเบิล และตรวจสอบคุณสมบัติทางไฟฟ้าด้วยเครื่องวัดค่าความต้านทานเชิงแผ่นแบบสี่หัววัด จากนั้นเพิ่มก๊าซไนโตรเจนเข้าไปในระบบการปลูกฟิล์ม เพื่อให้ได้ฟิล์มบางอินเดียมทินออกซีไนไตรด์และซิงค์ออกซีไนไตรด์ หลังจากที่ได้ตรวจสอบสมบัติวัสดุแล้วมีสมบัติใหม่ ทำให้สามารถวิเคราะห์ผลกระทบของเงื่อนไขและข้อจำกัดต่างๆ ในระบบปลูกฟิล์มอาร์เอฟแมกนีตรอนสปัตเตอร์ริงที่มีต่อสมบัติเฉพาะของฟิล์มที่เตรียมได้ เช่น การควบคุมเวลาก๊าซไวปฏิกิริยา กำลังคลื่นความถี่วิทยุ อัตราการไหลของสปัตเตอริงก๊าซ และความหนาของฟิล์ม

สำหรับฟิล์มบางอินเดียมทินออกซีไนไตรด์นั้น พบว่าเมื่อเพิ่มอัตราการไหลของก๊าซไนโตรเจนเข้าทำปฏิกิริยาในขบวนการสปัตเตอริง ด้วยกำลังคลื่นวิทยุคงที่ ฟิล์มบางที่ได้มีลักษณะโครงสร้างทางพื้นผิวในระดับนาโนเมตร โดยค่าแถบพลังงานต้องห้ามทางแสงจะมีค่าลดลงจาก 3.35 ถึง 2.21 อิเล็กตรอนโวลต์ และมีค่าสภาพความต้านทานเชิงแผ่นประมาณ 15-34 $\Omega/\square$ และฟิล์มบางซิงค์ออกซีไนไตรด์ จะพบสมบัติทางโครงสร้างและทางแสงของฟิล์มมีการเปลี่ยนแปลงขึ้นกับอัตราการ

This material is reserved for educational use only, not allowed for commercial use.
Forbidden to modify the content, and cite the document when use.

ไหลของก๊าซไนโตรเจนที่เข้าทำปฏิกิริยาในขบวนการสปัตเตอริงเช่นเดียวกัน โดยเมื่อลดอัตราการไหลของก๊าซไนโตรเจนเข้าทำปฏิกิริยาหรือเพิ่มกำลังคลื่นวิทยุ จะมีผลให้ความเป็นผลึกของฟิล์มบางซิงค์ออกซีไนไตรด์ลดลงและเมื่อตรวจสอบองค์ประกอบของฟิล์มที่เตรียมได้ด้วยเงื่อนไขอัตราการไหลของก๊าซไนโตรเจนที่ 10 ลูกบาศก์เซนติเมตรมาตรฐานต่อนาที มีอัตราส่วนอะตอมของไนโตรเจนต่อซิงค์มากกว่า 0.5 ซึ่งแสดงถึงอะตอมไนโตรเจนได้เข้ารวมในฟิล์มซิงค์ออกไซด์เกิดเป็นฟิล์มบางซิงค์ออกซีไนไตรด์ที่มีค่าแถบพลังงานต้องห้ามทางแสงอยู่ในช่วง 2.98 ถึง 3.08 อิเล็กตรอนโวลต์ ขึ้นกับอัตราการไหลของก๊าซไนโตรเจนและคงมีค่าสภาพความต้านทานเชิงแผ่นใกล้เคียงกับฟิล์มบางซิงค์ออกไซด์ จากผลการทดลองข้างต้นวิธีการควบคุมเวลาก๊าซไวปฏิกิริยาเป็นเทคนิคที่สามารถปรับปรุงสมบัติวัสดุให้เหมาะสมต่อการนำไปประยุกต์ใช้งานได้ดี ควบคู่กับระบบปลูกฟิล์มอาร์เอฟแมกนีตรอนสปัตเตอริงที่มีในปัจจุบัน

This material is reserved for educational use only, not allowed for commercial use.
Forbidden to modify the content, and cite the document when use.

Thesis Title	Growth of Nanocrystal Indium Tin Oxynitride and Zinc Oxynitride Thin Films by Reactive Gas-Timing RF Magnetron Sputtering
Student	Flight Lieutenant Don Klaitabtim
Student ID.	47063401
Degree	Doctor of Philosophy
Program	Applied Physics
Year	2008
Thesis Advisor	Associate Professor Dr.Jiti Nukeaw
Thesis Co-Advisor	Dr.Sirapat Pratontep

ABSTRACT

The growth of nanocrystal indium tin oxynitride (ITON) and zinc oxynitride (ZnON) thin films using rf magnetron sputtering with reactive gas-timing method have been studied in this dissertation. The sample thin films show new physical and optical properties. Based on the study of indium tin oxide (ITO) and zinc oxide (ZnO) thin films growth using rf magnetron sputtering, argon is used as the sputtering gas. The growth conditions and effects on thin film properties are investigated. The crystal structures of sample films and, their optical, and electrical properties are investigated by X-Ray diffraction (XRD), field emission scanning electron microscopy (FE-SEM), X-Ray photoelectron spectrometer (XPS), UV-VIS spectrophotometer (UV-VIS) and the resistivity mapping system four-point probe. Then, nitrogen gas was added into the sputtering process at the optimized sputtering conditions. Both ZnON and ITON thin films at unique deposited films show newly interesting properties. It is experimentally demonstrated that the films properties are depended on the growth conditions such as reactive gas-timing, radio frequency power, sputtering gas flow rate and film thickness.

Particularly, the ITON grain sizes are in the range of nanometers. The significant change of the optical absorption edge from 3.35 to 2.21 eV with increasing nitrogen flow rate conditions at fixed sputtering rf power are also found. The electrical conductivity property of sample films is found to be around 15 to 34 ohm/square. The structure and optical property of sputtered ZnON films are also investigated. The nitrogen composition in ZnON films were actually affected on the structural and optical properties of ZnON, which depended on the nitrogen flow rate conditions. The change of the crystallinity structure with decreasing nitrogen flow rate conditions or

This material is reserved for educational use only, not allowed for commercial use.
Forbidden to modify the content, and cite the document when use.

increasing sputtering rf power conditions were also observed. At 10 sccm nitrogen flow rate condition, the most alteration of the structure property is found. The confirmation of N-incorporation into ZnO is verified by XPS analysis with high N/Zn ratios of above 0.50. The relationships of the optical band edge with decreasing nitrogen flow rate and increasing rf power conditions are shown the red shift effect, with lowest value at 2.98 eV. In addition, the resistances of ZnON films still remain the same value as ZnO films. In conclusion, the gas-timing rf magnetron sputtering deposition is a simple method of fine-tuning material properties with slight modifications to the existing sputtering technique.

This material is reserved for educational use only, not allowed for commercial use.
Forbidden to modify the content, and cite the document when use.

ACKNOWLEDGEMENTS

I would like to express my deepest gratitude to my advisor Assoc. Prof. Dr. Jiti Nukeaw for his constantly moral support, guidance, invaluable suggestion and entirely positive encouragement during my study program at KMITL.

It is a great pleasure to convey very special thanks to Dr.Sirapat Pratontep and Dr.Supanit Porntheeraphat for their constructive suggestion and their valuable comment in providing more completion of this thesis work. Gratitude is also expressed to members and ex-members of QOSLAB, Dr.Wisanu, Thutiyaporn, Benchapol, Apichart, Surachart, Sakon, Witoon, Kajpunya, Anusit, Navaphun and Annnop for their helping, assisting in many things and their cordial cooperation. I must thanks to Annop Klumcheun for collaborating and training in my first experiment of thin film deposition process.

Words of appreciation are also given to Win Bunjongpru and Nimit Somwang from TMEC for their supporting of thin film characterization. I also would like to express gratitude to my mother (Sunny) and Dr.Prathan Buranasiri for proof-reading my english writing.

I am especially indebted to Thailand Graduate Institute of Science and Technology Development Agency whose financial support made my study in KMITL possible and also brought me the chance of doing this thesis.

Finally, I wish to express my gratitude to my beloved parents and all the members of my family (Pat, Pop and Pow) for their constant love and moral support. Definitely, I can't finish my program without them, accordingly this work is also dedicated to them.

Don Klaitabtim

This material is reserved for educational use only, not allowed for commercial use.
Forbidden to modify the content, and cite the document when use.

LIST OF PUBLICATIONS

The following international journals, international proceedings and patent have resulted from the research works associated to this thesis.

International Journals:

1. **Don Klaitabtim**, Sirapat Pratontep, and Jiti Nukeaw, **"Effect of Gas-Timing Technique on Structure and Optical Properties of Sputtered Zinc Oxide Films"** Ceramics International, Volume 34, Issue 4, May 2008, Pages 1103-1107.
2. **Don Klaitabtim**, Sirapat Pratontep, and Jiti Nukeaw, **"Growth and Characterization of Zinc Oxynitride Thin Films by Reactive Gas-Timing RF Magnetron Sputtering"** Japanese Journal of Applied Physics, Volume 47, Number 1, Jan 2008, pp. 653–656.

International Proceedings:

1. **Don Klaitabtim,** Sirapat Pratontep, and Jiti Nukeaw, **"Growth and Characterization of Zinc Oxide Thin Films by Reactive Gas-Timing RF Magnetron Sputtering"** Proceeding of the first Siam Physics Congress 2006, Thai Journal of Physics series 2, 2007, pp. 78-82.
2. **D. Klaitabtim**, S. Jaroensathianchok, S. Wanitparinyakun, S. Pratontep and J. Nukeaw, **"Structural Characterization of Sputtered Zinc Oxynitride (ZnON) Thin Films",** Proceeding of International Conference on Engineering, Applied Science and Technology 2007, pp. 894-897.

Thai Patent:

1. **"วิธีการเตรียมฟิล์มบางอินเดียมทินออกซีไนไตรด์และอุปกรณ์กรองแสงนำไฟฟ้าดังกล่าว** (Preparation of Indium Tin Oxynitride Films and Applied to Conductive Optical Filter)" รศ.ดร.จิติ หนูแก้ว, นายดอน คล้ายทับทิม, น.ส.ศุภนิจ พรธีระภัทร, ดร.สิรพัฒน์ ประโทนเทพ, เลขที่คำขอ 0601006624.

This material is reserved for educational use only, not allowed for commercial use.
Forbidden to modify the content, and cite the document when use.

TABLE OF CONTENTS

PAGE

ABSTRACT (THAI)....................I
ABSTRACT (ENGLISH)....................III
ACKNOWLEDGEMENTS....................V
LIST OF PUBLICATIONS....................VI
TABLE OF CONTENTS....................VII
LIST OF TABLES....................XII
LIST OF FIGURES....................XIII
CHAPTER 1 INTRODUCTION....................1

1.1 Motivation....................1
1.2 Statement of the problems....................3
1.3 Objective....................3
1.4 Scope of this study....................3
1.5 Dissertation outline....................3
References....................4

CHAPTER 2 BACKGROUND OF INDIUM TIN OXIDE (ITO)....................7

2.1 Introduction to ITO....................7
2.2 The deposition techniques of ITO....................8
2.2.1 Thermal evaporation....................9
2.2.2 Spray pyrolysis....................10
2.2.3 Chemical vapor deposition....................11
2.2.4 Screen printing....................12
2.2.5 Pulse laser deposition....................13
2.2.6 Sputtering growth....................14
2.3 The properties of ITO....................15
2.3.1 Structural properties of ITO....................15
2.3.2 Mechanical properties of ITO....................16

This material is reserved for educational use only, not allowed for commercial use.
Forbidden to modify the content, and cite the document when use.

TABLE OF CONTENTS (cont.)

PAGE

2.3.3 Electrical properties of ITO........17

2.3.4 Optical properties of ITO........19

2.3.4.1 Optical constants........20

2.3.4.2 Band structure........20

2.4 Indium tin oxynitride (ITON)........22

2.5 Chapter summary........23

References........23

CHAPTER 3 BACKGROUND OF ZINC OXIDE (ZnO)........29

3.1 Introduction to ZnO........29

3.2 The deposition techniques of ZnO........31

3.2.1 Pulse laser deposition........32

3.2.2 Molecular beam epitaxy........33

3.2.3 Chemical vapor deposition........33

3.2.4 Radio frequency magnetron sputtering........35

3.3 The Properties of ZnO........36

3.3.1. Crystal structure of ZnO........36

3.3.2 Electronic band structure of ZnO........39

3.3.3 Mechanical properties of ZnO........40

3.3.4 Thermal properties of ZnO........42

3.3.5 Electrical properties of ZnO........45

3.3.6 Optical properties of ZnO........47

3.4 Zinc oxynitride (ZnON)........48

3.4.1 Nitrogen and other potential dopant sources........49

3.4.2 Zinc oxynitride crystal structure........50

3.5 Chapter summary........51

References........52

This material is reserved for educational use only, not allowed for commercial use.

Forbidden to modify the content, and cite the document when use.

TABLE OF CONTENTS (cont.)

PAGE

CHAPTER 4 REACTIVE GAS-TIMING RF MAGNETRON SPUTTERING................59

4.1 Introduction..59

4.2 Background of sputtering system..59

4.2.1 RF sputtering...59

4.2.2 Magnetrons...67

4.2.3 Reactive sputtering..70

4.2.4 RF bias...73

4.3 Reactive gas-timing RF magnetron sputtering................................76

4.3.1 Magnetron sputtering..76

4.3.2 Reactive RF sputtering..77

4.3.3 Gas-timing method...79

4.3.4 The Edwards Auto500 reactive RF magnetron sputtering system....80

4.3.4.1 Deposition equipments..81

4.3.4.2 Process chamber...82

4.3.4.3 Vacuum system...82

4.3.4.4 RF generator system...83

4.4 Chapter summary...83

References...84

CHAPTER 5 THIN FILM CHARACTERIZATION...85

5.1 Introduction..85

5.2 Structural characterization methods...85

5.2.1 X-ray diffraction (XRD)..85

5.2.2 X-ray photoelectron spectroscopy (XPS)..........................89

5.2.3 Field-emission scanning electron microscope (FE-SEM)..........93

5.2.4 Atomic force microscopy (AFM).....................................97

5.3 Optical characterization methods...100

This material is reserved for educational use only, not allowed for commercial use.

Forbidden to modify the content, and cite the document when use.

TABLE OF CONTENTS (cont.)

PAGE

5.3.1 UV-Vis spectroscopy (UV-VIS)..100

5.3.2 Determination of thickness and optical constants..............................102

5.4 Electrical characterization method..104

5.4.1 Resistance Measurement..104

5.5 Thickness measurement..106

5.6 Chapter summary...107

References...107

CHAPTER 6 GROWTH AND CHARACTERIZATION OF ITON THIN FILMS.........109

6.1 Introduction..109

6.2 Experimental results and discussions of ITO.................................111

6.2.1 Substrate cleaning process..111

6.2.2 ITO thin films growth without gas-timing..................................112

6.2.2.1 Sputtered ITO thin film in Ar plasma.........................112

6.2.3 ITO thin films growth with gas-timing....................................113

6.2.3.1 Effect of gas-timing on properties of ITO..........................115

6.2.3.2 Effect of film thickness on properties of ITO.....................117

6.2.3.3 Effect of RF sputtering power on properties of ITO...........117

6.2.3.4 Effect of Ar flow rate on properties of ITO.......................119

6.3 Experimental results and discussions of ITON.................................121

6.3.1 Effect of gas flow rate on properties of ITON..........................121

6.3.2 Effect of RF sputtering power on properties of ITON..................126

6.3.3 Effect of film thickness on properties of ITON.........................127

6.4 Chapter summary..128

References...129

CHAPTER 7 GROWTH AND CHARACTERIZATION OF ZnON THIN FILMS...........132

7.1 Introduction..132

This material is reserved for educational use only, not allowed for commercial use.

Forbidden to modify the content, and cite the document when use.

TABLE OF CONTENTS (cont.)

PAGE

7.2 Experimental results and discussions of ZnO....133

7.2.1 Substrate Cleaning Process....133

7.2.2 ZnO thin films growth without gas-timing....134

7.2.2.1 Sputtered ZnO thin film in Ar plasma....134

7.2.3 ZnO thin films growth with gas-timing....134

7.2.3.1 Effect of gas-timing on properties of ZnO....136

7.2.3.2 Effect of RF sputtering power on properties of ZnO....138

7.2.3.3 Effect of Ar flow rate on properties of ZnO....141

7.3 Experimental results and discussions of ZnON....142

7.3.1 Effect of gas flow rate on properties of ZnON....143

7.3.2 Effect of RF sputtering power on properties of ZnON....147

7.3.3 Effect of film thickness on properties of ZnON....150

7.4 Chapter summary....151

References....152

CHAPTER 8 CONCLUSIONS AND FUTURE PERSPECTIVES....155

8.1 Conclusions....155

8.2 Future perspectives....157

BIOGRAPHY....158

This material is reserved for educational use only, not allowed for commercial use.
Forbidden to modify the content, and cite the document when use.

LIST OF TABLES

TABLE **PAGE**

2.1 The properties of ITO thin films prepared by various growth techniques..........................8

3.1 Group I and V acceptor properties in ZnO..........................30

3.2 The properties of ZnO thin films prepared by various growth techniques..........................31

3.3 Physical properties of a ZnO single crystal..........................36

6.1 Sputtering conditions used for deposition of ITO thin films..........................114

7.1 Sputtering conditions used for deposition of ZnO thin films..........................135

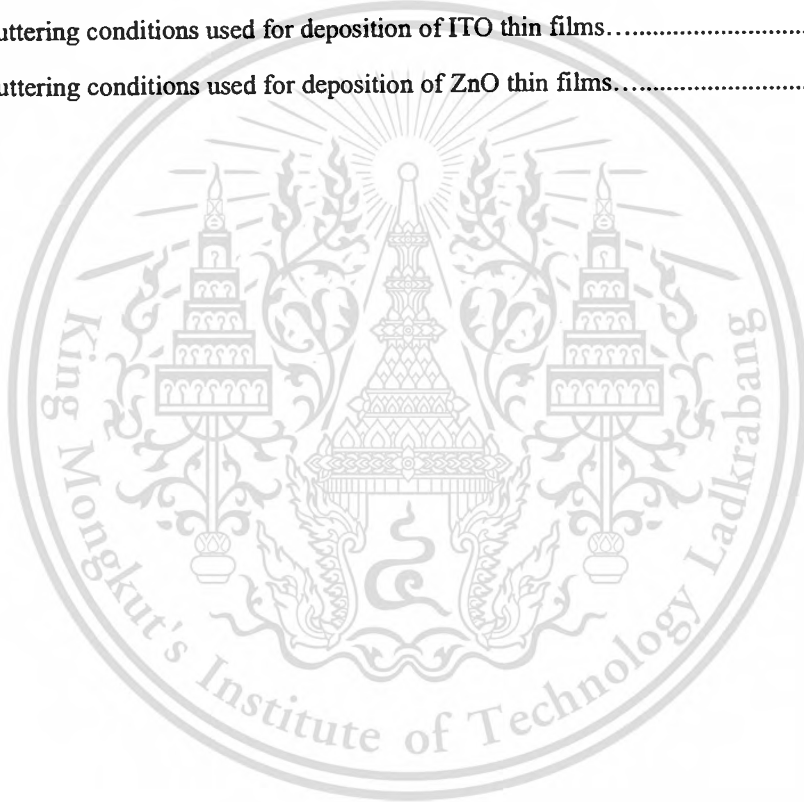

This material is reserved for educational use only, not allowed for commercial use.

Forbidden to modify the content, and cite the document when use.

LIST OF FIGURES

FIGURE **PAGE**

2.1 The crystal structure of tin (Sn) doped indium oxide....7

2.2 Evaporation from a point source and a surface source....9

2.3 (a) the spray pyrolysis equipment and (b) an aerosol transport....11

2.4 Schematic diagram of a typical CVD apparatus....12

2.5 The screen printing process....13

2.6 Schematics of PLD system are consisted of laser source, vacuum chamber, rotating target holder and target, and substrate....14

2.7 The basic configuration of rf magnetron sputtering....15

2.8 The bixbyite crystal structure of indium oxide ($In_{32}O_{48}$) showing one unit cell where the indium and oxygen atoms are represented by the black and hollow spheres....15

2.9 Two non-equivalent (a) cation sites and (b) locations of In atoms in In_2O_3 crystal....16

2.10 (a) Hardness and (b) elastic modulus of different TCO films on glass substrate as function of hydrogen partial pressure....17

2.11 Assumed parabolic band structure of undoped In_2O_3 and the effect of Sn doping....18

2.12 Transmittance and reflectance of the ITO film with thickness of 1.656 μm....19

2.13 Band gap widening of Sn doped In_2O_3, known as Moss-Burstein shift....21

3.1 Crystalline ZnO forms in wurtzite structure....29

3.2 Schematic of a pulsed laser deposition system....32

3.3 Schematic of MBE deposition system....33

3.4 Schematic of a typical CVD deposition system....34

3.5 A typical ECR sputtering apparatus....35

3.6 Stick and ball representation of ZnO crystal structures: (a) cubic rocksalt (B1), (b) cubic zinc blende (B3), and (c) hexagonal wurtzite (B4). The shaded gray and black spheres denote Zn and O atoms, respectively....36

3.7 Schematic representation of a wurtzite ZnO structure having lattice constants a in the basal plane and c in the basal direction; u parameter is expressed as the bond length or the nearest-neighbour distance b divided by c (0.375 in ideal crystal), and α and β (109.47° in ideal crystal) are the bond angles....37

This material is reserved for educational use only, not allowed for commercial use.
Forbidden to modify the content, and cite the document when use.

LIST OF FIGURES (cont.)

FIGURE **PAGE**

3.8 The wurtzite lattice of ZnO: small circles represent the zinc atoms, while large circles depict oxygen atoms....38

3.9 Band structure for ZnO for various high-symmetry lines (left). On the right hand side, the density of states (DOS) is shown. The shading between the two graphs characterizes the different band groups. The zero in the graphs is taken as the valence band upper edge...40

3.10 (a) Calculated formation energies of N_O as functions of the O chemical potential formed by atomic N (stripped off a N_2 or a N_2O molecule), NO, or NO_2 molecule. μ_O= -3.3 is the Zn-rich limit condition and μ_O = 0 is the O-rich limit condition. (b) Calculated formation energies of a $(N_2)_O$ as functions of the O chemical potential for the defects formed by N_2, N_2O, NO and NO_2 molecules....49

3.11 Crystal structure of ZnO (a) co-doped with 2N and Zn_i, and (b) doped with 2N....51

4.1 Schematic illustration of the development of a negative bias when an rf potential is coupled to a probe immersed in a plasma....61

4.2 Schematic representation of the plasma in the planar diode sputtering source....61

4.3 Schematic drawing of a planar rf diode sputtering device....62

4.4 Approximate representation of target voltage waveforms relative to the plasma potential for a balance rf system with two equal-area sputtering electrodes. V_f is the floating potential....63

4.5 Schematic circuit of single-ended rf discharge system including an equivalent circuit for the plasma discharge....64

4.6 Schematic representation of an equivalent circuit for a balanced rf system with two equal-area sputtering electrodes and center-trap ground....65

4.7 Approximate representation of voltages as functions of time, relative to the plasma potential for a single-ended rf sputtering system in which the wall area is much larger than target area. V_s is the substrate ion bombardment potential....66

4.8 Planar-magnetron structure and behavior. The electron-orbit radius is shown much larger than actual size for clarity....68

This material is reserved for educational use only, not allowed for commercial use.
Forbidden to modify the content, and cite the document when use.

LIST OF FIGURES (cont.)

FIGURE **PAGE**

4.9 Plasma flow toward the substrate along magnetic field (**B**) lines in an unbalanced magnetron....69

4.10 Sticking coefficient of N_2 measured during the continuous deposition of Ti as a function of the ratio of the getter-pumped nitrogen flux to the Ti deposition flux....71

4.11 Transitions in the steady-state operating mode of a Cr cylindrical-post magnetron sputtering source due to injection of oxygen....72

4.12 A dc self-biasing of a capacitively coupled rf waveform due to plasma-electrode asymmetry....74

4.13 A dc-bias probe with L and C size for 13 MHz operation....75

4.14 Schematic drawing of process under dc planar magnetron sputtering....77

4.15 Typical experimental curve for a reactive sputtering process exhibited in hysteresis effect. The optical emission (OES) from sputtered metal atoms represents the sputter erosion rate. Q_{tot} is expressed in standard cubic centimeters per minute (sccm)....78

4.16 The relationship between the partial pressure (P) and the flow of reactive gas (Q_{tot})....78

4.17 A schematic of vacuum and gas-timing control apparatus in the sputtering process....80

4.18 The camera image of the rf magnetron sputtering system with reactive gas-timing technique....80

4.19 The process chamber is a stainless steel cylinder with one rf magnetron sputtering head for 3 inch diameter target material....81

4.20 A high vacuum (HV) is generated by a high vacuum pump system, which is composed of a diffusion pump and a rotary pump....82

4.21 The panel schematic of rf magnetron generator (model CESAR 136)....83

5.1 Diffraction of x-rays from a crystal....87

5.2 The (222) reflected of XRD for an ITO film and the dot line represent the theoretical position of this peak....87

5.3 A photograph of D8-Bruker model-XRD diffractometer....89

This material is reserved for educational use only, not allowed for commercial use.

Forbidden to modify the content and cite the document when use.

LIST OF FIGURES (cont.)

FIGURE **PAGE**

5.4 (a) XPS process for carbon 1s core electron and the resultant spectrum and (b) the energy level diagram relating the measured kinetic energy (KE_{meas}) to the binding energy (*B.E.*) of the sample....91

5.5 A schematic of XPS system is consisted of UHV chamber, X-ray source and electron energy analyzer....92

5.6 A photograph of in-house XPS system at NSCR....93

5.7 A schematic of a SEM components and scanning process....94

5.8 Diagram illustrating the interaction of the primary electron beam with a solid surface in the production of secondary and backscattered electrons, x-rays, and other secondary radiation....94

5.9 The average distribution of secondary electrons from metals as a function of energy.....95

5.10 Schematic diagram of a scintillator tube used for the detection of secondary electrons...96

5.11 A photograph of a high resolution FE-SEM of Hitachi S4700 at TMEC....96

5.12 A simple diagram of a traditional atomic force microscope (AFM)....97

5.13 The forces between the tip and sample versus the tip-sample distance, known as intermolecular force curve....98

5.14 A photograph of an atomic force microscope, Seiko SPA-400....100

5.15 The photograph of UV-VIS spectrophotometer used in this research from Thermo electron, model Heliosγ....101

5.16 Schematic diagram of a sample transmission measurement....101

5.17 (a) The percentage of transmission spectra of ZnO thin film as a function of wavelength in nm and (b) The plot of $(\alpha h\nu)^2$ versus photon energy ($h\nu$) to achieve the energy gap from the intercept of the photon energy axis and the extrapolated line....102

5.18 Schematic of in-line (linear) four-point probe configuration....104

5.19 Photograph of the linear four-point probes instrument (OmniMap® RS35, Prometrix..106

6.1 The argon plasma is emitted purple light over the sputtering target during the sputtering process....112

This material is reserved for educational use only, not allowed for commercial use.
Forbidden to modify the content, and cite the document when use.

LIST OF FIGURES (cont.)

FIGURE **PAGE**

6.2 The different of ITO resistance at the central area and peripheral area....................113

6.3 Schematic representation of the 50:2 on-off gas-timing sequence of argon during sputtering deposition with a flow rate of 10 sccm (on) for 50 seconds and zero flow (off) for 2 seconds 114

6.4 X-ray diffraction patterns of ITO thin films grown with difference thickness of 200 nm (non gas-timing), 500 nm (non gas-timing), and 500 nm (gas-timing), from bottom to top patterns, respectively..................... 115

6.5 SEM image of 200 nm ITO thin film grown by gas-timing technique..........................116

6.6 Transmission spectra of a ITO thin film deposited by gas-timing technique with thickness of 200 nm..116

6.7 XRD results of ITO thin films grown by gas-timing rf magnetron sputtering with different thickness of 200, 300, 400 and 500 nm..117

6.8 XRD results of ITO thin films grown by gas-timing rf magnetron sputtering with different RF sputtering power of 10, 20, 30 and 40 W...118

6.9 SEM images of ITO thin films grown with different RF sputtering power at (a) 10, (b) 20, (c) 30 and (d) 40 W...119

6.10 XRD results of ITO thin films grown by gas-timing rf magnetron sputtering with different Ar flow rate conditions of 8, 9, 10 and 11 sccm.................................120

6.11 Transmission spectra of a ITO thin films deposited by gas-timing rf magnetron sputtering with different Ar flow rate conditions of (a)8, (b)9, (c)10 and (d)11 sccm................120

6.12 SEM images of (a) ITO and (b) ITON thin films grown by rf magnetron sputtering with different sputtering gas of pure Ar and N, respectively...121

6.13 The XRD patterns of ITON films deposited at various N_2 flow rate ratios in nitrogen-argon (N_2: Ar) mixed which are fed into the sputtering chamber, the maximum flow rate of argon is 10 sccm (sputtering pressure ~3.0×10^{-3} mbar); ITO(0:10), 30%(3:7), 50%(5:5), and 100%(10:0), all films have thickness of 1000 nm...........................122

6.14 The sheet resistivity of ITO and ITON films was plotted with the various N_2 flow rate ratios in nitrogen-argon (N_2:Ar) mixed gas..123

This material is reserved for educational use only, not allowed for commercial use.

Forbidden to modify the content and cite the document when use.

LIST OF FIGURES (cont.)

FIGURE **PAGE**

6.15 Transmission spectra of the films prepared at various N_2 flow rate ratios in nitrogen-argon (N_2: Ar) mixed which are fed into the sputtering chamber, the maximum flow rate of argon is 10 sccm (sputtering pressure ~$3.0x10^{-3}$ mbar); ITO(0:10), 30%(3:7), 50%(5:5), and 100%(10:0), all films have thickness of 1000 nm........................124

6.16 The relationship between optical band gap and the various N_2 flow rate ratios in nitrogen-argon (N_2: Ar) mixed gas, which are fed into the sputtering chamber, the maximum flow rate of argon is 10 sccm (sputtering pressure ~$3.0x10^{-3}$ mbar); ITO(0:10), 30%(3:7), 50%(5:5), and 100%(10:0), all films have thickness of 1000 nm........................125

6.17 Camera image of approximately 1 μm thick ITON films reflecting their high optical transparency and its color, a) ITO (0:10sccm), b) ITON (3:7 sccm), ITON (5:5 sccm) and ITON (10:0 sccm)..125

6.18 Transmission spectra of the ITO films prepared at various rf power of (a) 30, (b) 50, (c) 70, (d) 100 and (e) 150 W, all films have thickness of 1000 nm...........................126

6.19 Transmission spectra of the ITON prepared at various film thickness 200, 400, 600, and 1000 nm 127

7.1 Schematic representation of the 50:2 on-off gas-timing sequence of argon during sputtering deposition with a flow rate of 9 sccm (on) for 50 seconds and zero flow (off) for 2 seconds 135

7.2 X-ray diffraction patterns of ZnO thin films deposited at different argon gas-timing sequences (30:2, 40:2, 50:2, 60:2 sec) and fixed rf power of 30 W 136

7.3 AFM images (5x5μm^2) of ZnO thin films deposited at different argon gas-timing sequences (30:2, 40:2, 50:2, 60:2 sec) and fixed rf power of 30 W 137

7.4 Optical transmittance of ZnO thin films deposited at different argon gas-timing sequences (30:2, 40:2, 50:2, 60:2 sec) and fixed rf power of 30 W 138

7.5 X-ray diffraction patterns of ZnO thin films deposited at different RF power (30, 50, 80, 120 W) and the argon gas-timing sequence of 50:2 sec 139

7.6 AFM images (5x5μm^2) of ZnO thin films deposited at different RF power (30, 50, 80, 120 W) and the argon gas-timing sequence of 50:2 sec 140

This material is reserved for educational use only, not allowed for commercial use.
Forbidden to modify the content and cite the document when use.

LIST OF FIGURES (cont.)

FIGURE **PAGE**

7.7 Optical transmittance of ZnO thin films deposited at different RF power (30, 50, 80, 120 W) and the argon gas-timing sequence of 50:2 sec 141

7.8 ZnO thin films grown by various Ar flow rate condition of 9, 12, 14, and 16 sccm... 142

7.9 XRD patterns of ZnON films deposited on glass by rf magnetron sputtering at a fixed rf power of 80 W for nitrogen flow rates of 10, 15, and 20 sccm 144

7.10 XPS spectra (N 1s) of ZnO thin films produced by rf magnetron sputtering using only argon, and ZnON thin films produced by gas-timing sputtering at a fixed rf power of 80 W and a nitrogen flow of 10 sccm... 144

7.11 N/Zn atomic ratio as a function of nitrogen flow rate. The values for the center of the N 1s binding energy peak from XPS analysis for different nitrogen flow conditions are also given.. 145

7.12 Optical transmission spectra of ZnON films deposited on glass by rf magnetron sputtering at a fixed rf power of 80 W for nitrogen flow rates of 10, 15, and 20 sccm.. 146

7.13 Dependence of the optical band gap of ZnON thin films on the nitrogen flow rate... 147

7.14 XRD patterns of ZnON films deposited on glass by rf magnetron sputtering at a fixed nitrogen flow of 10 sccm for rf powers of 30, 50, and 80 W 148

7.15 Optical transmission spectra of ZnON films deposited on glass by rf magnetron sputtering at a fixed nitrogen flow of 10 sccm for rf powers of 30, 50, and 80 W....... 149

7.16 Dependence of the optical band gap of ZnON thin films on the rf sputtering power.... 149

7.17 XRD patterns of ZnON films deposited on glass by rf magnetron sputtering with various film thickness at a fixed nitrogen flow of 10 sccm and rf power of 80 W.............. 150

7.18 Transmission spectra of ZnON films deposited on glass by rf magnetron sputtering with various film thickness at a fixed nitrogen flow of 10 sccm and rf power of 80 W...... 151

This material is reserved for educational use only, not allowed for commercial use.
Forbidden to modify the content, and cite the document when use.

CHAPTER 1

INTRODUCTION

1.1 Motivation

The semiconductor era was dominated by silicon (Si) and germanium (Ge), which there was the first generation of semiconducting electronic materials. For next few decades, the second generation of electronic materials was investigated, as binary and ternary compound semiconductors, which is known as gallium arsenide (GaAs), indium gallium arsenide (InGaAs), gallium phosphors (GaP), indium phosphors (InP) and theirs alloys. In the last few years, the third generation of electronic materials is now come forward from the research. These materials have been designed and produced for the specific applications. The wide band gap semiconductor materials play the important role in the optical and optoelectronic devices such as gallium nitride (GaN), aluminum nitride (AlN) and zinc selenide (ZnSe).

Nowadays, a conductive transparent semiconductor is emerging from the research and development, such as tin doped indium oxide (ITO), fluoride doped tin oxide (FTO), zinc oxide (ZnO), aluminum doped zinc oxide (Al:ZnO) and indium doped zinc oxide (In:ZnO). These materials were not only conductive materials but also wide optical band gap semiconductors. The band gap of a semiconductor material is the most important parameter that determines the transport, optical properties, and other related phenomena. The large variation in the nature of the chemical bonding has brought up a wide range in energy gap covered by the metal oxide semiconductors. However, the generally wide band gap materials are a high resistivity semiconductor, thus they have been improved their electrical properties by doping method. Consequently, a few researchers have been prepared particular films with metal-doped or modified composition and/or new fabrication techniques. In the case of oxynitrides of many metals, like Ti, Zr, Hf, Zn and In [1-4] have been investigated for their properties and their potential applications in a range of devices.

Indium tin oxide (ITO) is a transparent conductive oxide material widely used in many optoelectronic devices. It is an n-type degenerate semiconductor used to contact electrode which its high conductivity is due to both important role of oxygen vacancies and tin interstitials. Moreover, it exhibits a high optical transmittance because its wide band gap, 3.5-4.06 eV [5]

This material is reserved for educational use only, not allowed for commercial use.
Forbidden to modify the content, and cite the document when use.

semiconductor. According to its properties, ITO films have found in many applications in optoelectronics such as photodetectors, organic light emitting diode (OLED), solar cells and sensors [6-10]. In a challenge to advance the properties of ITO films by doping with nitrogen to form ITON thin films, it could be apply for various future technological applications in electronics and optoelectronics.

Zinc oxide (ZnO) is the other key material in many different fields of science and technology. Their optical and structural properties make them excellent candidates for optical and optoelectronic applications, for example, as optical windows for solar cell devices [11] and transparent piezoelectric materials for surface and bulk acoustic wave devices [12]. In particular, a zinc-oxide-nitride system has been demonstrated to be an optically functional material, in which the optical band gap can be tuned within a broad energy range (2.3-3.3 eV) by controlling the nitrogen doping level [3].

A number of techniques have been used for fabrication of ITO and ZnO thin films, including chemical vapour deposition, sol–gel, spray-pyrolysis, molecular beam epitaxy, pulsed laser deposition, vacuum arc deposition, and magnetron sputtering [13–19]. Nonetheless, it remains difficult to grow ITO and ZnO films with high crystallinity, stable and sufficiently high conductivity. Plasma sputtering is one of the most promising techniques for the nitrogen incorporated ITO and ZnO films because of its capability for large-area deposition, low-temperature processing, and controllable nitrogen incorporation into the films. By making minor modifications to a conventional sputtering system, we have demonstrated a new sputtering technique, called gas timing, whereby sputtering or doping gases are controlled periodically by an on-off sequence during the sputtering deposition. The technique has been successfully applied to produce AlN and ITO thin films without substrate heating [20-21].

This research work is focused on the growth and characterization of nitrogen incorporated to ITO and ZnO, in term of designing and tailoring the optical band edge of ITON and ZnON thin films. All of nitrogen incorporated ITO and ZnO were grown by the conventional rf magnetron sputtering using the gas-timing technique. The structural, optical and electrical properties of films were investigated and studied by varying the sputtering conditions.

This material is reserved for educational use only, not allowed for commercial use.
Forbidden to modify the content, and cite the document when use.

1.2 Statement of the problems

1.2.1 In a challenge to advance the properties of ITO and ZnO films, it could be applied for various future technological applications in electronics and optoelectronics.

1.2.2 Tailoring the optical band edge of ITO and ZnO thin films by the nitrogen doping using reactive RF magnetron sputtering.

1.2.3 The newest optically functional materials as ITON and ZnON will be required for future optoelectronic devices.

1.3 Objective

As mentioned before, in order to solve the problems stated in 1.2.3, the topics of investigation include:

1.3.1 Study the possibility of doping nitrogen into ITO and ZnO.

1.3.2 Study the doping concept of the conductive transparent thin films.

1.3.3 Study the fabrication and characterization process of ITON and ZnON thin films.

1.4 Scope of this study

The study will concentrate on the growth and characterization of ITON and ZnON thin films by reactive gas-timing RF magnetron sputtering. The first scope is to study, fabricate and characterize ITO and ZnO thin films. The next task is to use the special technique known as reactive gas-timing RF magnetron sputtering grow ITON and ZnON thin films. The last task is to investigate the structural, optical and electrical properties of the prepared thin films by specific material characterization equipment.

1.5 Dissertation outline

The outline of this dissertation is as follow; chapter 1 is an overview of the research motivation, statement of the problem, objectives and scope of this research. Chapter 2, 3 and 4 provide the fundamental knowledge of ITO, ITON, ZnO, ZnON, and rf magnetron sputtering system, respectively. The reactive gas-timing is a special method used to produce thin films (described in chapter 4).

This material is reserved for educational use only, not allowed for commercial use.
Forbidden to modify the content, and cite the document when use.

Chapter 5 presents the thin film characterization methods including x-ray diffraction, x-ray photoelectron spectroscopy, scanning electron microscopy, atomic force microscopy, UV-Visible spectroscopy, and four point probe measurement used in the thesis experiments.

Chapters 6 and 7 describe the experimental growth, result and discussion of ITO, ITON, ZnO and ZnON thin films, respectively. These chapters provided the characterizations of crystalline structure, surface morphology, optical band gap energy, and other related property of ITO, ITON, ZnO, and ZnON thin films and reported experimental results and discussions.

Finally, Chapter 8 concludes the overall work and outlines the direction of the future work.

References:

[1] S. H. Mohamed, O. Kappertz, T. Niemeier, R. Drese, M. M. Wakkad, and M. Wuttig, "Effect of Heat Treatment on Structural, Optical and Mechanical Properties of Sputtered TiO_xN_y Films", **Thin Solid Films**, vol. 468, 2004, pp. 48-51.

[2] S. Venkataraj, D. Severin, S. H. Mohamed, J. Ngaruiya, O. Kappertz, and M. Wuttig, "Towards Understanding the Superior Properties of Transition Metal Oxynitrides Prepared by Reactive DC Magnetron Sputtering", **Thin Solid Films**, vol. 502, 2006, pp. 228-234.

[3] M. Futsuhara, K. Yoshioka, and O. Takai, "Optical Properties of Zinc Oxynitride Thin Films", **Thin Solid Films**, vol. 317, 1998. pp. 322-325.

[4] B. R. Natarajan, A. H. Eltoukhy, and J. E. Greene, T. L. Barr, "Mechanisms of Reactive Sputtering of Indium II: Growth of Indium Oxynitride in Mixed N_2-O_2 Discharges", **Thin Solid Films**, vol. 69, 1980, pp. 217-227.

[5] E. Aperathitis, M. Bender, V. Cimalla, G. Ecke, and M. Modreanu, "Properties of rf-Sputtered Indium-Tin-Oxynitride Thin Films", **J. Appl. Phys.**, vol. 94, 2003, pp. 1258-1266.

[6] J. Xue and S. R. Forrest, "Carrier Transport in Multilayer Organic Photodetectors: II Effects of Anode Preparation", **J. Appl. Phys.**, vol. 95, 2004, pp. 1869-1877.

[7] S. J. Martin, Alison B. Walker, A. J. Campbell, and D. D. C. Bradley, "Electrical Transport Characteristics of Single-layer Organic Devices from Theory and Experiment", **J. Appl. Phys.**, vol. 98, 2005, pp. 063709.

This material is reserved for educational use only, not allowed for commercial use.
Forbidden to modify the content, and cite the document when use.

[8] A. B. Djurišic, C. Y. Kwong, P. C. Chui, and W. K. Chan, "Indium-Tin-Oxide Surface Treatments: Influence on the Performance of CuPc/C60 Solar Cells", **J. Appl. Phys.**, vol. 93, 2003, pp. 5472-5479.

[9] Y. Mishima, N. Kondo, T. Kimura, S. Soeda, Y. Nagahiro, T. Kurahashi, and T. Akamatsu, "Resolution Improvement for Linear Image Sensors Using Indium-Tin-Oxide/Amorphous Silicon Junctions", **J. Appl. Phys.**, vol. 67, 2003, pp. 2143-2147.

[10] H. Steffes, C. Imawan, P. Fricke, H. Vohse, J. Albrecht, R. Schneider, F. Solczbacher, and E. Obermeier, "New $In_xO_yN_z$ Films for the Application in NO_2 Sensors", **Sens. Actuators B**, vol. 77, 2001, pp. 352-358.

[11] K. Ellmer, R. Cebulla, and R. Wendt, "Transparent and Conducting ZnO(:Al) Films Deposited by Simultaneous RF- and DC-excitation of a Magnetron", **Thin Solid Films**, vol. 317, 1998, pp. 413-416.

[12] J. G. E. Gardeniers, Z. M. Rittersma, and G. J. Burger, "Preferred Orientation and Piezoelectricity in Sputtered ZnO Films", **J. Appl. Phys.**, vol. 83, 1998, pp. 7844-7854.

[13] B. S. Li, Y. C. Liu, Z. S. Chu, D. Z. Shen, Y. M. Lu, J. Y. Zhang, and X. W. Fan, "High Quality ZnO Thin Films Grown by Plasma Enhanced Chemical Vapor Deposition", **J. Appl. Phys.**, vol. 91, 2002, pp. 501-505.

[14] M. J. Alam, and D. C. Cameron, "Preparation and Properties of Transparent Conductive Aluminum-doped Zinc Oxide Thin Films by Sol-gel Process", **J. Vac. Sci. Technol. A**, vol. 19, 2001, pp. 1642-1646.

[15] A. J. C. Fiddes, K. Durose, A. W. Brinkman, J. Woods, P. D. Coates, and A. J. Banister, "Preparation of ZnO Films by Spray Pyrolysis", **J. Crystal Growth**, vol. 159, 1996, pp. 210-213.

[16] T. Ohgaki, N. Ohashi, H. Kakemoto, S. Wada, Y. Adachi, H. Haneda, and T. Tsurumi, "Growth Condition Dependence of Morphology and Electric Properties of ZnO Films on Sapphire Substrates Prepared by Molecular Beam Epitaxy", **J. Appl. Phys.**, vol. 93, 2003, pp. 1961-1965.

[17] Y. R. Ryu, S. Zhu, J. D. Budai, H. R. Chandrasekhar, P. F. Miceli, and H. W. White, "Optical and Structural Properties of ZnO Films Deposited on GaAs by Pulsed Laser Deposition", **J. Appl. Phys.**, vol. 88, 2000, pp. 201-204.

This material is reserved for educational use only, not allowed for commercial use.
Forbidden to modify the content, and cite the document when use.

[18] T. Minami, S. Ida, and T. Miyata, "High Rate Deposition of Transparent Conducting Oxide Thin Films by Vacuum Arc Plasma Evaporation", **Thin Solid Films**, vol. 416, 2002, pp. 92-96.

[19] K. H. Kim, K. C. Park, and D. Y. Ma, "Structural, Electrical and Optical Properties of Aluminum doped Zinc Oxide Films Prepared by Radio Frequency Magnetron Sputtering", **J. Appl. Phys.**, vol. 81, 1997, pp. 7764-7772.

[20] N. Kietpaisalsophon, W. Bunjongpru, W. Techitdheera, and J. Nukeaw, "Photoreflectance Study of AlN Thin Films Grown by Reactive Gas-Timing RF Magnetron Sputtering", **International Journal of Modern Physics B**, vol. 16, No. 28&29, 2002, pp. 4418-4422.

[21] A. Klamchuen, N. Pornteeraphat, and J. Nukeaw, "Characterization of ITO Thin Films on PET Substrates Prepared by Gas-timing RF Magnetron Sputtering", **e-Journal of Surface Science and Nanotechnology**, vol. 3, 2005, pp. 272-275.

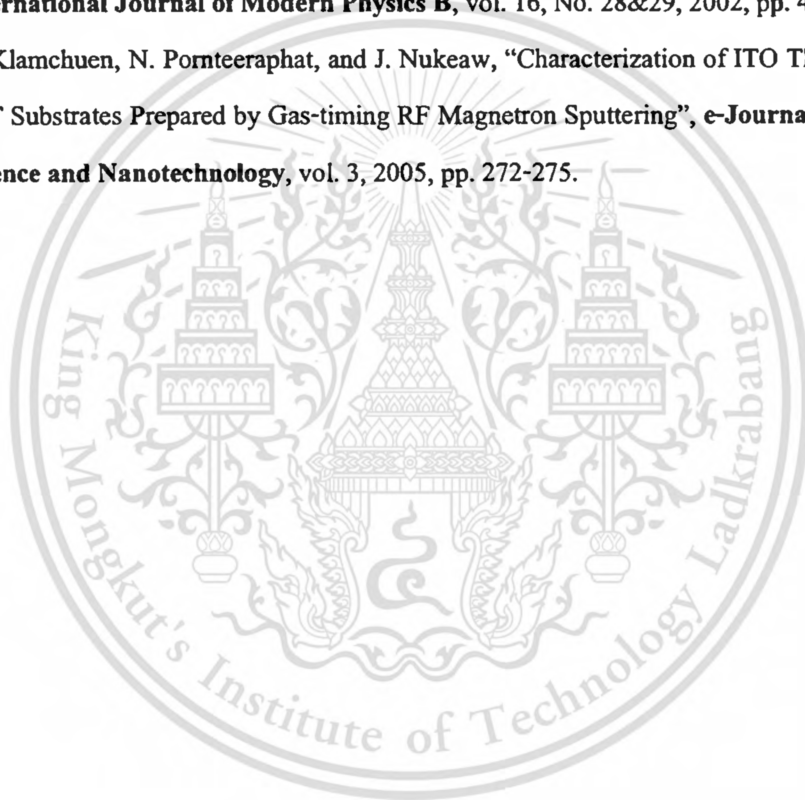

This material is reserved for educational use only, not allowed for commercial use.
Forbidden to modify the content, and cite the document when use.

CHAPTER 2

BACKGROUND OF INDIUM TIN OXIDE (ITO)

2.1 Introduction to ITO

Since the first reports of transparent and conductive cadmium oxide films appeared in 1907, interest in transparent conductors has rapidly increased [1]. Tin-doped In_2O_3, so-called indium-tin oxide (ITO), is one of the most attractive of these materials due to its high conductivity and transmission in the visible range as transparent conducting oxides (TCOs). The crystal structure of ITO is shown in Figure 2.1. The defect structures of ITO are responsible in part for their superior optical and electrical properties, which are exploited in various transparent electrode applications, such as transparent heating elements [2], antistatic coatings over electronic instrument [3,4], electro-optic devices [5,6], liquid crystal displays [7,8,9], transparent electrodes for various display devices [10,11], and transparent contact [12,13].

As an ITO films have a high transmittance in the visible range and a high conductivity simultaneously, typical high quality ITO film has the transmittance is above 90% in the range of 400-700 nm and the electrical resistivity is below 200 μΩ-cm. Thus, ITO films show an interesting and technologically important combination of properties, which they have high luminous transmittance, high infrared reflectance, good electrical conductivity, excellent substrate adherence, hardness, and chemical inertness.

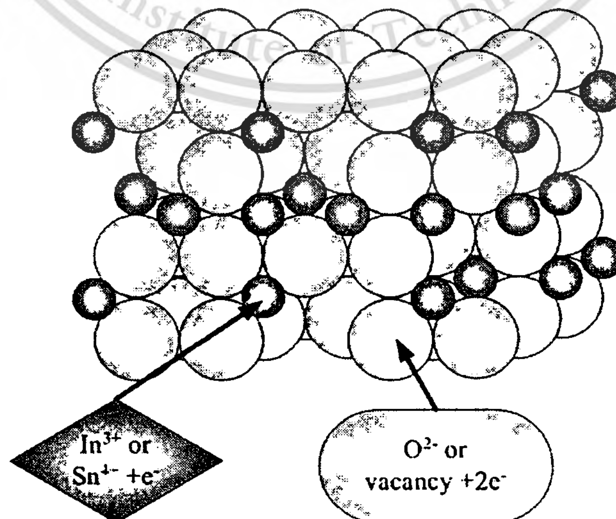

Fig. 2.1 The crystal structure of tin (Sn) doped indium oxide.

This material is reserved for educational use only, not allowed for commercial use.
Forbidden to modify the content, and cite the document when use.

The most commonly used methods for ITO deposition are sputtering, thermal evaporation, spray pyrolysis, pulsed laser deposition (PLD) and screen printing technique [14-21]. However, due to the complexity of crystal structure, tin doping level, and composition, the properties of ITO films produced by different processes vary significantly. Table 2.1 shows some of the results of previous research. From this table, we can see that the resistivity, transmittance and carrier concentrations vary significantly. This indicates that properties of ITO film strongly depend on individual processes. Electro-optic technology requires a greater understanding of the optical and electrical properties of ITO, so it is necessary to characterize an ITO film deposition process.

Table 2.1 The properties of ITO thin films prepared by various growth techniques.

Deposition techniques	**Thickness (Å)**	**Carrier concentration (cm^{-3})**	**Resistivity (Ω·cm)**	**Transmittance (%)**	**Ref.**
RF Sputtering	7500	$6.0x10^{20}$	$3.0x10^{-4}$	90	[14]
RF Sputtering	5000	$1.2x10^{21}$	$4.0x10^{-4}$	95	[15]
Pulsed laser deposition	14000	$1.0\text{-}1.2x10^{21}$	$5.0x10^{-4}$	80	[16]
Magnetron sputtering	800	$6.0x10^{20}$	$4.0x10^{-4}$	85	[17]
DC Sputtering	1000	$9.0x10^{20}$	$2.0x10^{-4}$	85	[18]
Reactive evaporation	2500	$5.0x10^{20}$	$8.0x10^{-4}$	90	[19]
Ion beam sputtering	600	$2.0x10^{20}$	$1.2x10^{-3}$	-	[20]
Spray pyrolysis	3000	$5.0x10^{20}$	$3.0x10^{-4}$	85	[21]

2.2 The deposition of ITO

Nowadays, various methods can be used to deposit ITO films including thermal evaporation [19], sputtering deposition (both diode and magnetron) with dc or rf power [14,15,17,18], pulsed laser deposition (PLD) [16], Ion beam sputtering [20], and spray pyrolysis [21]. The choice of deposition techniques is determined by various factors such as quality and reproducibility of the films, the cost and complexity of the equipments, and specific disadvantage of each technique. The techniques most widely reported in the literatures and most widely used in industry are dc magnetron sputtering, dc/rf magnetron sputtering and electron beam evaporation.

This material is reserved for educational use only, not allowed for commercial use.
Forbidden to modify the content, and cite the document when use.

However, different processing usually produces ITO films with significantly different properties. Of these, rf magnetron sputtering produces both high rates of deposition and good quality films. In the following sections, thermal evaporation, spray pyrolysis technique, pulsed laser deposition, chemical vapor deposition, screen printing techniques, pulsed laser deposition, and sputtering will be briefly introduced. In this study, ITO films were produced by rf magnetron sputtering using the reactive gas-timing technique, so this method will be introduced in more detail in chapter 5.

2.2.1 Thermal evaporation

Solid material vaporizes when heated to sufficiently high temperature. The condensation of the vapor onto a cooler substrate yields thin solid films. The high temperature can be achieved by resistively heating, or by firing an electron or ion beam at the boat containing the material to be evaporated. Under ideal circumstances, the total evaporated metal is:

$$\overline{M}_e = \int_0^t \int_{A_e} \Gamma_e dA_e dt \tag{2.1}$$

where A_e is the surface area of the source, Γ_e is the evaporation rate, M_e is the total evaporated mass and t is time.

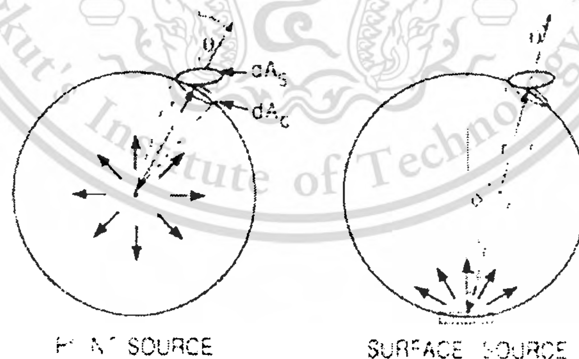

Fig. 2.2 Evaporation from a point source and a surface source [28].

In the situation illustrated in Fig. 2.2, the mass received by per area of the wafer is:

$$\frac{d\overline{M}_s}{dA_s} = \frac{\overline{M}_e \cos\theta}{4\pi r^2} \tag{2.2}$$

This material is reserved for educational use only, not allowed for commercial use.
Forbidden to modify the content, and cite the document when use.

where θ is the incident angle of the evaporated metal, r is the distance from the evaporation source to the wafer surface, A_s is the area receiving the incident evaporated species.

Thermal evaporation may be achieved directly or indirectly (via a support) by variety of physical methods [28]. This technique has several advantages: (i) it is capable of yielding films which do not contain significant amount of uncontrollable contaminations; (ii) it is relatively easy to operate; (iii) it involves a minimum of critical process parameters; and (iv) it does not cause radiation damage to the substrate [36]. The evaporation rate is a most important parameter for the film quality. When ITO is evaporated, it decomposes slightly into suboxides and free oxygen, the typical source is a 95% indium and 5% tin alloy (by weight). The oxygen release causes a non-stoichiometry in the films of a magnitude which depends critically on the details of the deposition. In order to obtain reproducible results and high-quality coatings it was necessary to carefully control the amount of oxygen. For reactive deposition in the presence of oxygen, the governing parameter is then the relative impingement rate of oxygen molecules onto the surface of the growing film, which, in its turn, is determined by the evaporation rate and the oxygen pressure. Furthermore, the reactivity of the oxygen with the surface is important, which points at the fact that substrate temperature is another crucial parameter. The temperature also mostly affects the crystallinity of the film. Reports of substrate temperatures being raised from 300°C up to 450°C during evaporation in order to enhance conductivity and transmittance are reported by Balasubramanian *et al.* [19]. However, due to the difference of the indium and tin vapor pressure, it is very hard to achieve the proper stoichiometry in the film.

2.2.2 Spray pyrolysis

Pyrolysis refers to the thermal decomposition of gaseous species at a hot surface. The major advantage of pyrolysis technique is its relatively fast deposition rate more than 1000 Å/min and it does not require a vacuum. This method has been used for the preparation of TCO films for many years because it is relatively simple and cheap. The conventional spray pyrolysis technique consists of spraying a dilute solution of appropriate chloride from an atomizer onto a heated substrate under normal atmosphere conditions or controlled atmosphere. High pressure argon, nitrogen, or air is usually used as spraying gas. A schematic diagram of such equipment and deposition mechanism as aerosol transport is shown in Fig. 2.3.

This material is reserved for educational use only, not allowed for commercial use.
Forbidden to modify the content, and cite the document when use.

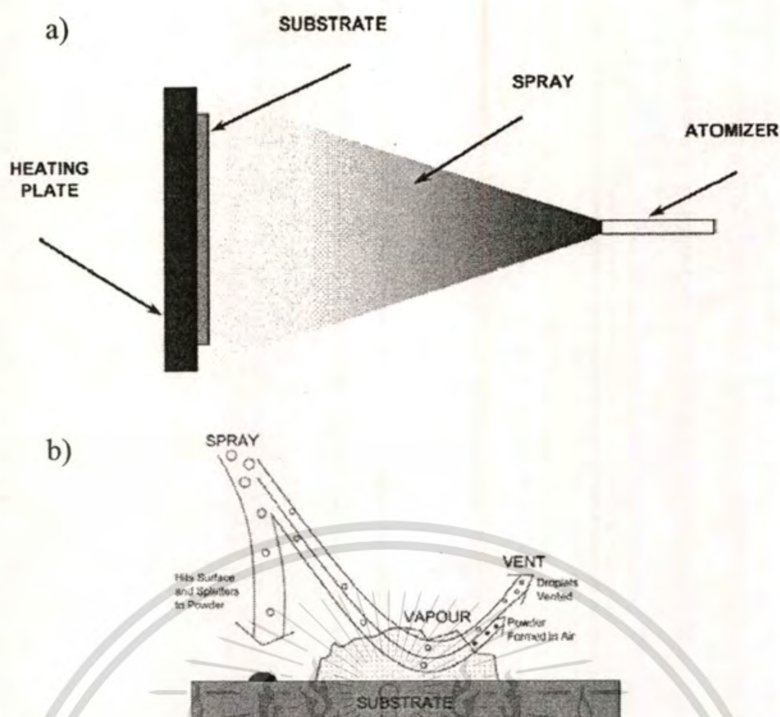

Fig. 2.3 (a) the spray pyrolysis equipment and (b) an aerosol transport.

The ITO spray is obtained from an alcoholic solution of anhydrous indium chloride ($InCl_3$) and tin chloride ($SnCl_4 \cdot 5H_2O$) with nitrogen acting as the carrier gas. The spraying is carried out in a furnace, held at 400°C. Critical parameters include positioning of the substrate and the chemical composition of the spray solution. Ashok *et. al.* [29] have reported resistivity of 1×10^{-3} Ω-cm for a 4200 Å ITO film with transmission greater than 90% at 550 nm while corresponding values obtained by Haitjema *et. al.* [21] is 3×10^{-4} Ω-cm and 85% respectively. This demonstrates an apparent trade-off between the conductivity and the transmittance of ITO films with this technique.

2.2.3 Chemical vapor deposition

Chemical vapor deposition (CVD) is a process in which a chemical reaction involving gaseous reacting species takes place on, or in the vicinity of, a heated substrate surface [31]. The schematic of a typical CVD apparatus is illustrated in Fig. 2.4. The main controlling parameters are the substrate temperature, substrate material, composition of the reaction gas mixture, gas flow, total pressure, and the geometry of the deposition system. The gas flow and the apparatus geometry determine the uniformity of the deposited films over large areas. The substrate temperature and the gas flow control the deposition rate.

This material is reserved for educational use only, not allowed for commercial use.
Forbidden to modify the content, and cite the document when use.

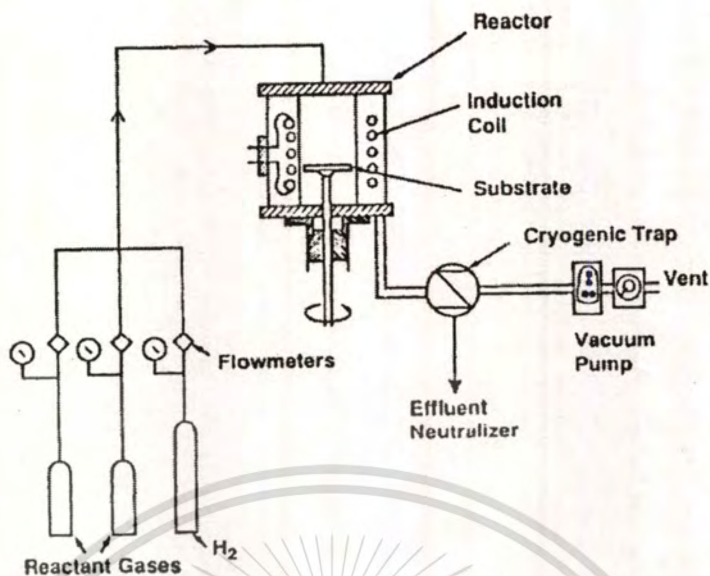

Fig. 2.4 Schematic diagram of a typical CVD apparatus.

Films with high demands for purity, stoichiometry, and structural perfection could be obtained by CVD method. This technique has also the advantage of being cost effective with respect to the apparatus. It enables the production of coatings with good properties even on substrates of complicated shapes without the use of high vacuum [32]. In particular, atmospheric pressure CVD (APCVD) is attractive in many applications in the sense that it offers high deposition rate and hence short process time. However, since CVD processes are based on interfacial chemistry, they are sensitive to contamination. The major limitations of the process are the small areas of uniform coatings and the cost of the starting reagents as in the case of indium compounds. The deposition of ITO films by the CVD method generally faces difficulties due to a lack of volatile and thermally stable source materials.

2.2.4 Screen printing technique

This technique is suitable for large scale non-device oriented applications where relatively thick layers of ITO are required such as in liquid crystal displays, black-wall contacts and anti-reflection coatings for solar cells. The principle of screen printing is shown in Fig. 2.5. A pattern is photographically defined on a stainless steel screen by means of an emulsion layer. A paste of the material such as ITO to be screen printed is pressed through the screen by means of a squeegee. Important screen printing parameters are: the viscosity of the paste, the mesh number of

This material is reserved for educational use only, not allowed for commercial use.
Forbidden to modify the content, and cite the document when use.

the screen (number of meshes per inch), the snap off distance between the screen and the substrate and the pressure and speed of the squeegee. After leveling, the printed wet film is dried (e.g. at 120 °C, 60 min). By then, the film consists of loose conglomerates of very small grains (1-2 μm). The sintering step results in a compact film, where large grains (e.g. up to 10 μm) are electronically and optically intimately connected. Sintering is a high temperature step in range of 500 to 800 °C, and is usually performed in an oven with a transport belt. Finally, the material was completely formed as a film for any application fields.

Typically, the deposited thickness of ITO film varies in the range 10 to 30 μm and the post deposition crystallization temperature can be as high as 600°C for a period exceeding an hour. The reported resistivity of ITO film is more than $4\text{x}10^{-4}$ Ω-cm can be comparable to those obtained by other deposition techniques. However, its transparency is markedly lower than 80%.

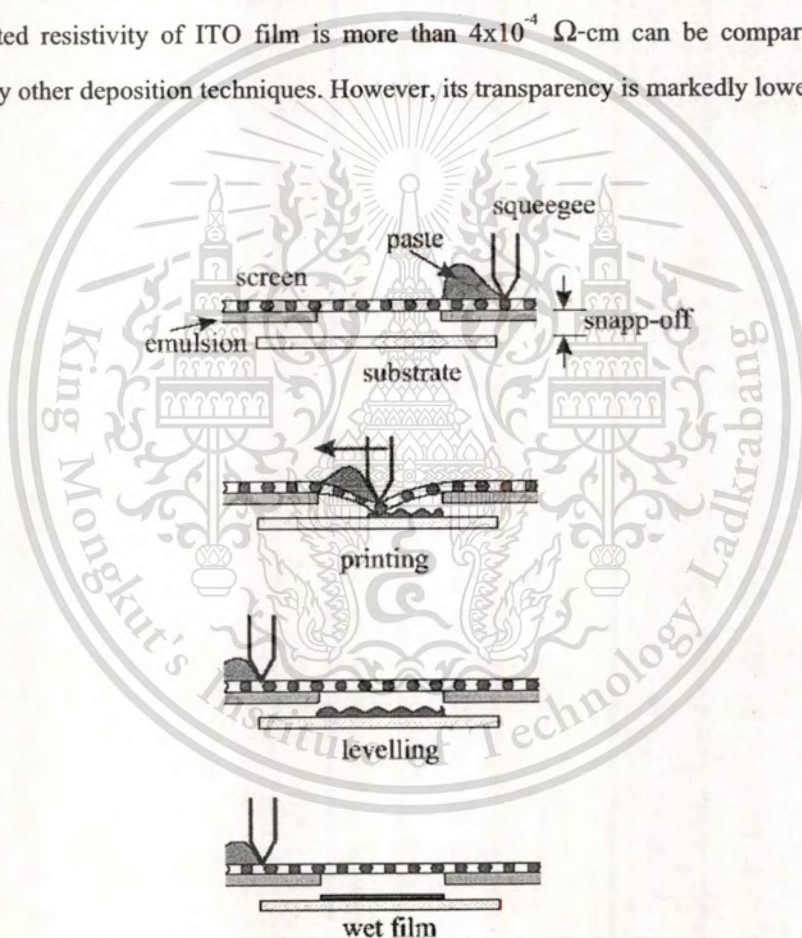

Fig. 2.5 The screen printing process.

2.2.5 Pulsed laser deposition (PLD)

Thin films can also be created by pulsed laser deposition (PLD). The principle of this technique is simple. A solid target in an ultra high vacuum chamber is evaporated by means of

This material is reserved for educational use only, not allowed for commercial use.
Forbidden to modify the content, and cite the document when use.

short and high energy laser pulses [16, 30]. In deposited ITO thin films by PLD process, a researcher places a target in a vacuum chamber, which typical target is hot-pressed pellets of 90% In_2O_3 and 10% SnO_2 by weight. A pulsed laser beam vaporizes the surface of the target, and the vapor condenses on a substrate. The main components are a laser, optics, and a vacuum system [33], as shown in Fig. 2.6. This technique is conceptually simple, cost-effective and fast, however the typical film field produced by this technique is only a few square centimeters.

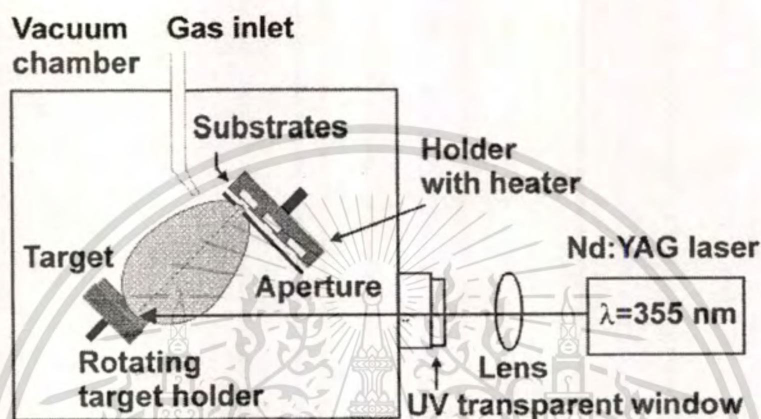

Fig. 2.6 Schematics of PLD system are consisted of laser source, vacuum chamber, rotating target holder and target, and substrate [33].

2.2.6 Sputtering growth

Since 1852, the sputtering phenomenon has been know and exploited for deposition of films. The sputtering method is one of the most extensively used techniques for the deposition of ITO films. The sputtered ITO films have been deposited by either dc or rf power using either oxide (In_2O_3-SnO_2) or metallic alloy (In-Sn) target in argon-oxygen (Ar-O_2) mixture. Sputter deposition methods used today have common simple goals: to generate and maintain desired plasma and to establish a bias or electric field for the acceleration of ions to the electrode or target being bombarded. The basic configuration of rf magnetron sputtering is shown in Figure 2.7, ions have been generated and accelerated towards a target sputtering material, which condensed at the substrate.

This study, ITO and ITON (nitrogen incorporated) thin films were grown by reactive rf magnetron sputtering with a new technique called reactive gas-timing using various growth conditions and parameters. In the process of establishing the growth conditions, other influences, such as substrate cleaning and chamber contamination, were also investigated.

This material is reserved for educational use only, not allowed for commercial use.
Forbidden to modify the content, and cite the document when use.

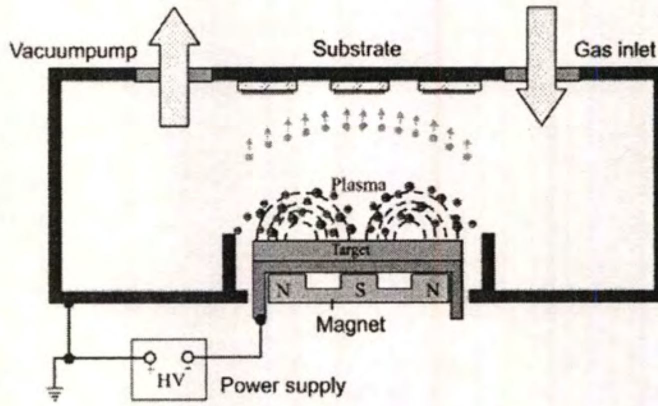

Fig. 2.7 The basic configuration of rf magnetron sputtering.

2.3 The properties of ITO

2.3.1 Structural property of ITO

The unique properties of ITO come from its structure and composition. Indium oxide has a cubic bixbyite structure which is shown in Fig. 2.8. One unit cell contains 16 units of In_2O_3. Therefore, for defect free In_2O_3 crystal, there are 80 atoms in one unit cell.

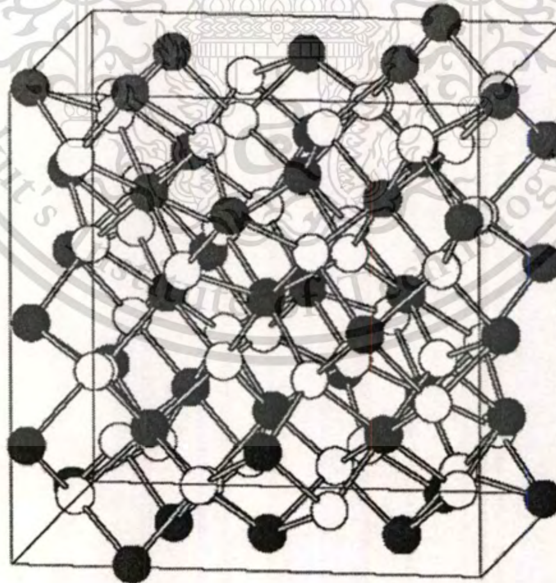

Fig. 2.8 The bixbyite crystal structure of indium oxide ($In_{32}O_{48}$) showing one unit cell where the indium and oxygen atoms are represented by the black and hollow spheres, respectively [22].

This material is reserved for educational use only, not allowed for commercial use.
Forbidden to modify the content, and cite the document when use.

The lattice constant is reported to be 10.117 Å [22]. The theoretical density is 7.12 g/cm^3. Two kinds of non-equivalent indium sites are present in In_2O_3 crystal structure which is shown in Fig. 2.9 [23]. Indium cations are located in two non-equivalent as shown in Figure 2.9(a), where 8 In^{3+} ions are located in the center of trigonally distorted oxygen octahedrons (b-site) and the remaining 24 In^{3+} ions are located in the center of the more distorted octahedrons (d-site) as shown in Figure 2.9(b) [22]. Based on the description above, both indium sites can be viewed as an incomplete body centered cubic structure with an indium atom located at the center and oxygen atoms at the corners. One fourth of the anions are missing. To vary the material properties, In_2O_3 can be extrinsically doped with tin. When tin atoms substitute for indium atoms, it forms either SnO or SnO_2. The material retains its bixbyite structure. However, if the doping level is extremely high, the tin atoms may enter interstitially and distort the lattice structure. As a polycrystalline structure, the ITO crystal grain size depends on various processing parameters such as substrate temperature and deposition rate.

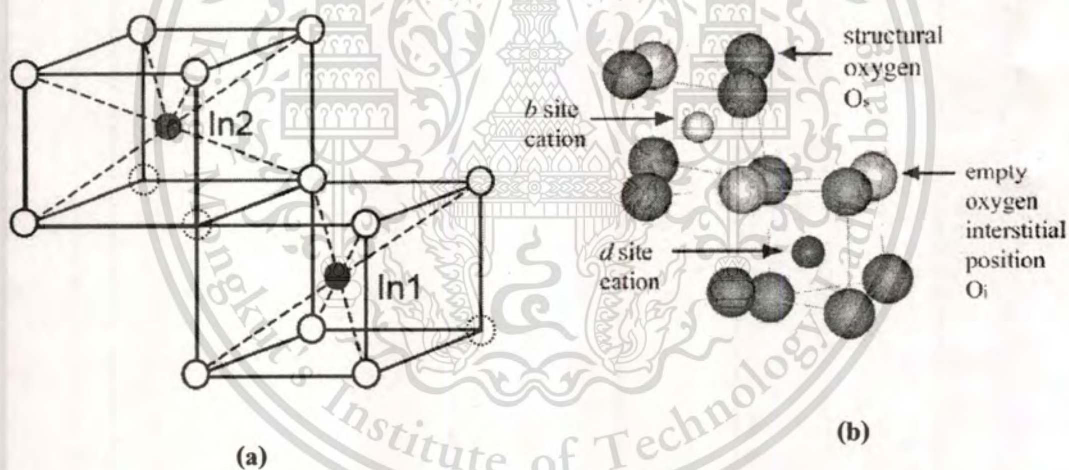

Fig. 2.9 Two non-equivalent (a) cation sites and (b) locations of In atoms in In_2O_3 crystal [22,23].

2.3.2 Mechanical properties of ITO

The mechanical properties of ITO films are important parameters for designing stress-free multi-layer thin film semitransparent and top-emitting organic light-emitting displays involving one or more layers of ITO films on both rigid and flexible substrates. The nano-indentation technique has been widely used to determine the elastic modulus and hardness of thin films. The hardness and elastic modulus of the TCO films have been measured using nano-indentation, as

This material is reserved for educational use only, not allowed for commercial use.
Forbidden to modify the content, and cite the document when use.

สำนักหอสมุดกลาง พระจอมเกล้าลาดกระบัง

shown in Fig. 2.10. The average elastic modulus and hardness of ITO films are 99.8±13.6 GPa and 6.5±1.6 GPa, respectively.

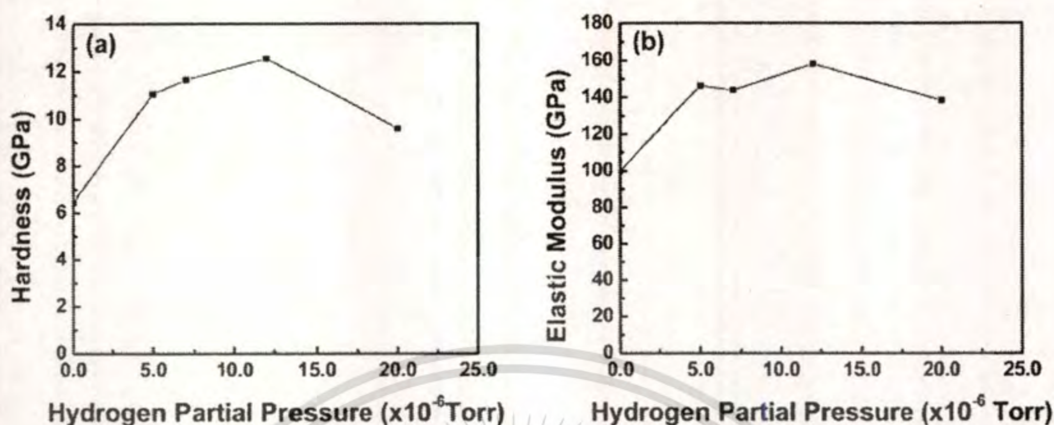

Fig. 2.10 (a) Hardness and (b) elastic modulus of different TCO films on glass substrate as function of hydrogen partial pressure [24].

2.3.3 Electrical properties of ITO

Indium oxide is a wide gap semiconductor. The band gap of In_2O_3 was reported to be 3.75 eV [25]. Generally, In_2O_3 crystal structure is not ideal since oxygen vacancies are present. The accurate formula of indium oxide is $In_2O_{3-x}(V_O)_x$, where V_O is donor-like doubly-charged oxygen vacancy, and x is the oxygen vacancy portion and depends on the oxidation state. The typical value of x is less than 0.01. Under room temperature, the excitation of electrons from valence band to conduction band is negligible. Oxygen vacancies dominate the conduction mechanism of In_2O_3 and the free charge carrier concentration has been reported to be in the range 10^{19}-10^{20}cm^{-3}. Extrinsic doping can vary the electrical properties of indium oxide significantly. If In_2O_3 is doped with Sn atom, Sn atoms will replace In atoms and form tin oxide in either SnO or SnO_2 depending on the valence. If SnO is formed, Sn acts as an acceptor since it accepts an electron. Otherwise, when SnO_2 is formed, Sn acts as donor since it gives off an electron. Usually, SnO_2 dominates, and Sn atoms act as donors. Both tin and oxygen vacancies contribute to the conductivity of ITO.

The doping level is critical for electrical properties. As the tin concentration increases, the carrier concentration increases until a saturation level is reached. An increase in the tin concentration above this saturation level causes a decrease in the free carrier concentration. This is due to an increased probability of the occupation of adjacent cation positions by two or more

This material is reserved for educational use only, not allowed for commercial use.
Forbidden to modify the document and cite the document when use.
58060

tin atoms, which can deplete the active tin concentration. The highest carrier concentration, which corresponds to the lowest resistivity, occurs when the tin doping level is about 10%. The solid solubility of tin in indium oxide is approximately 8%. Beyond this range, tin oxide phase will be formed and distort the lattice structure. This will eventually cause a decrease of free carrier concentration. In order to get resistivity lower than 10^{-3} Ω.cm and avoid the formation of tin oxide phase, the doping level is typically chosen to be 8-10%. This doping level will produce degenerative ITO [25,27].

Figure 2.11 shows the energy diagram of undoped In_2O_3 and Sn doped In_2O_3. ITO has metal like electrical properties because the carrier concentration is typically around 10^{20} to 10^{21} cm^{-3} [26]. The conduction band is curved upwards, the valence band is curved downwards and the Fermi level is located at middle of band gap for the undoped material; addition of Sn dopants results in the formation of donor states just below the conduction band. As the doping density is increased, these eventually merge with the conduction band at a critical density, n_c, which was calculated to be $2.3x10^{19}$ cm^{-3} by Gupta *et al.* [25]. Free electron properties are exhibited by the material when the density of electrons from the donor atoms exceeds this value. Hence, ITO films are degenerated semiconductor in nature. Once the material becomes degenerate, the mutual exchange and coulombic interactions shift the conduction band downwards and the valence band upwards, effectively narrowing it from Eg to Eg'.

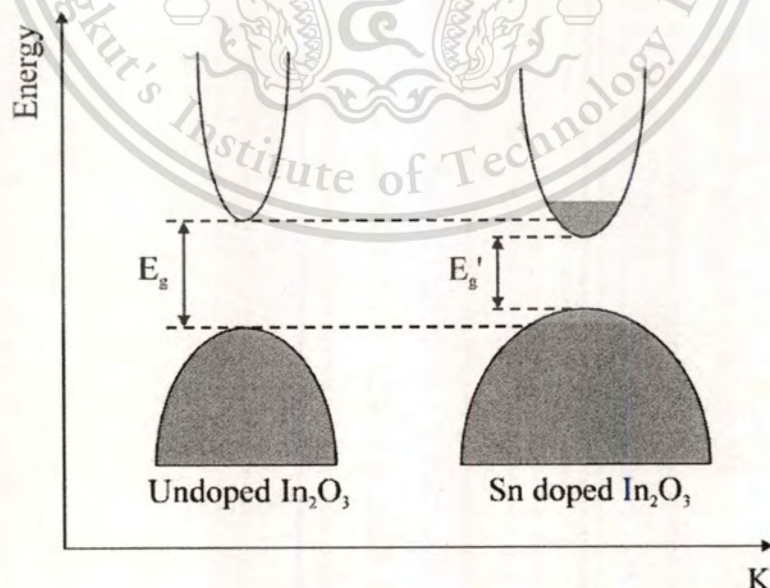

Fig. 2.11 Assumed parabolic band structure of undoped In_2O_3 and the effect of Sn doping [1].

This material is reserved for educational use only, not allowed for commercial use.
Forbidden to modify the content, and cite the document when use.

2.3.4 Optical properties of ITO

The optical transmission and reflection spectra for a typical ITO film are shown in Fig. 2.12. The optical properties of ITO in the spectral range of interest from 200 nm to 3 μm, which are controlled by three types of electronic excitation: (a) band gap transitions, (b) interband transitions from the bulk of the valence band into the bulk of the conduction band, and (c) intraband transitions of the free electrons in the conduction band. Consequently, there are three different regions can be distinguished for the transmission curve:

- In the ultraviolet region, a strong absorption edge is found. This absorption edge is called band edge which is decided by the band gap transition.
- In the visible region, the transmittance is very high and exhibits such extreme of minimum and maximum which are modified by interference effect.
- In the infrared region, the film enters a reflecting regime with metallic properties.

The strong increasing of absorption and reflection region called plasma edge, which is associated with the excitation of the free electrons in the conduction band. Consequently the transmittance window is limited towards higher wavelengths by the plasma edge and towards lower wavelengths by the band edge.

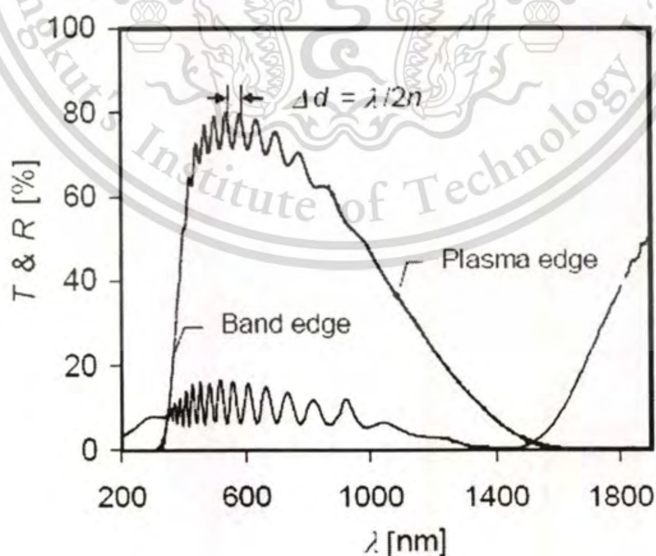

Fig. 2.12 Transmittance and reflectance of the ITO film with thickness of 1.656 μm.

This material is reserved for educational use only, not allowed for commercial use.
Forbidden to modify the content, and cite the document when use.

2.3.4.1 Optical constants

The optical properties of a material are described by the complex dielectric function ($\varepsilon = \varepsilon_1 + i\varepsilon_2$) or complex refractive index ($\tilde{n} = n + ik$). The relation between the dielectric function and the refractive index is given by:

$$\tilde{n} = \sqrt{\varepsilon}, \tag{2.3}$$

$$\varepsilon_1 = n^2 + k^2, \varepsilon_2 = 2nk, \tag{2.4}$$

where n is usually called refractive index, and k is called extinction coefficient.

The reported value for the refractive index of ITO is 1.96 [35]. The transmittance of ITO films is also influenced by a number of minor effects which include surface roughness and optical inhomogeneity in the direction normal to the film surface. Inadvertently grown dark brown (effectively translucent) metallic films of ITO have also been reported. This opaqueness has been attributed to un-oxidised Sn metal grains on the ITO surface as a result of instability due to absence of sufficient oxygen during deposition [14, 15].

2.3.4.2 Band structure

In_2O_3 is a semiconductor material with a direct band gap of about 3.75 eV [25] and an indirect band gap of about 2.6 eV [28]. The optoelectronic properties of materials are dominated by the electric structure near the band gap. According to the theoretical calculation on electronic structure of ITO by Odaka *et al.* [34], the substitution of Sn atom did not significantly destroy the shape of the density of states around the bottom of the conduction band. The only impurity band locates in the conduction band has the same s-like symmetry as that of conduction band. So the assumed parabolic shape for both valence band and conduction band around the band gap is almost retained independent of the concentration of Sn substitution.

In direct transition model, the assumed parabolic band structure of In_2O_3 and Sn doped In_2O_3 are shown in Figure 2.13. For undoped In_2O_3, the Fermi energy E_F is located in the middle of the band gap. The conduction band is empty. With the introduction of a low density of donor atoms, donor states formed just below the conduction band. And the E_F lies between the donor level and the conduction band minimum (CBM). For increased donor density, the donor states

This material is reserved for educational use only, not allowed for commercial use.
Forbidden to modify the content, and cite the document when use.

merge with the conduction band at a certain critical density n_c, which was calculated to be $2.3x10^{19}$ cm^{-3} by Gupta *et al.* [25]. When $n_e > n_c$ the material expected to exhibit free-electron properties. The intrinsic direct semiconductor band gap is 3.75 eV [36]. The direct band gap of ITO films is generally greater than 3.75 eV although a range of values from 3.5 to 4.06 eV have also been reported [37, 38]. The high optical transmittance of these films is a direct consequence of their being a wide band gap semiconductor.

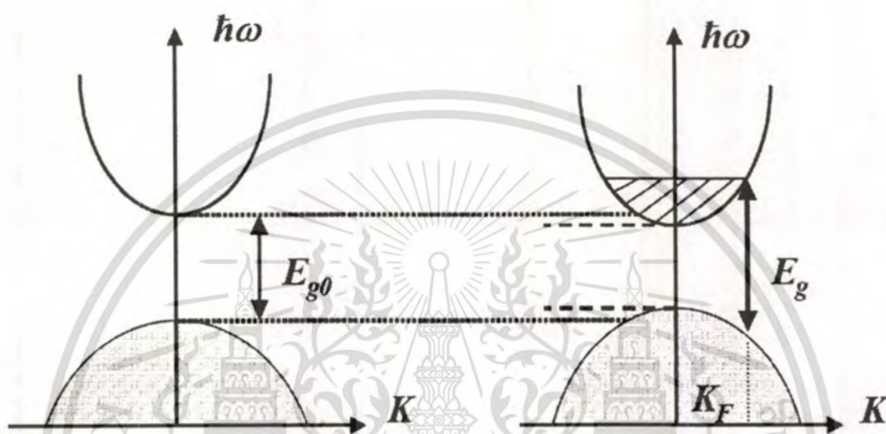

Fig. 2.13 Band gap widening of Sn doped In_2O_3, known as Moss-Burstein shift [25]

Since the Pauli's exclusion principle prevents states from being doubly occupied and the optical transitions only occur vertically, where the same of the Fermi momentum is the energy gap is given at these points. The blocking of the low energy states in the conduction band to from the widening of the band gap is known as Burstein-Moss shift (BM) [39]. For enhances parabolic band edges the Burstein-Moss shift can be given by the energy:

$$\Delta E_g^{BM} = \frac{\hbar^2 k_F^2}{2}\left(\frac{1}{m_e} + \frac{1}{m_h}\right), \tag{2.5}$$

where k_F is the Fermi wave vector, and m_e, m_h are the effective masses of the electrons and holes in the conduction band.

In ITO films, the fundamental absorption edge shifts towards high energy as the free carrier density increases. The fundamental absorption edge generally lies in the ultraviolet of the solar spectrum and shifts to shorter wavelengths with increasing carrier concentration, n. This is

This material is reserved for educational use only, not allowed for commercial use.
Forbidden to modify the content, and cite the document when use.

because the band gap exhibits an $n_e^{2/3}$ dependence due to the Burstein-Moss shift (BM). The widening band edges of ITO by BM effect can be given by:

$$\Delta E_g^{BM} = \left[\frac{\hbar^2}{2m_{vc}^*}\right](3\pi^2 n_e)^{2/3}, \tag{2.6}$$

where n_e is the density of electrons in the conduction band and m_{vc}^* is the reduced effective mass, defined by:

$$\frac{1}{m_{vc}^*} = \frac{1}{m_e} + \frac{1}{m_h}, \tag{2.7}$$

2.4 Indium tin oxynitride (ITON)

The interesting physical properties of oxynitride thin films have been the focus of extensive research due to their potential application in a wide range of electronic and optoelectronic devices. For example, monometallic and bimetallic oxynitrides have been investigated as catalysts [40], silicon-tin and lithium-phosphorus oxynitrides have been applied in thin-film lithium-ion batteries for microelectronics [41], and other oxynitrides have been investigated for either their properties as ZrON, CuON, TaON, CrON, NbON [42-45], or for specific applications like gas sensors InON [46], transparent and conductive layers in optoelectronic devices InON, ZnON [46-48], and optical or hard coatings as TiON, SiON [49, 50].

Reactive sputtering is the predominant deposition technique employed to fabricate these oxynitride thin films from either an elemental target in O_2-N_2-Ar gas mixtures or an oxide target in N_2-Ar plasma. By changing the amount of gases in plasma, the properties of the resulting thin films can be tailored between the properties of the respective oxide and those of nitride thin films. However, the reproducibility of the properties of the oxynitride films is very dependent on the sputtering processes and condition of the target and these can become very complex when plasma is formed by simultaneously using two reactive gases, like oxygen and nitrogen. Indium tin oxide (ITO) is widely used as a conductive transparent layer on many electronic and optoelectronic devices. It is an n-type degenerate semiconductor, with both substitutional oxygen vacancies and tin contributing to its high conductivity. Too many vacancies in the structure of the film will turn it into a nonstoichiometric film and the conductivity will decrease due to an increase in lattice structural disorder. The high conductivity of the films is due to the high carrier concentration

This material is reserved for educational use only, not allowed for commercial use.
Forbidden to modify the content, and cite the document when use.

rather than to the carrier's mobility. The high optical transmittance of ITO films is a direct consequence of it being a wide band gap semiconductor.

Attempts have been made to improve the electrical and/or optical properties of ITO, depending on the technological application, by changing its composition to zinc-indium-tin-oxide [51, 52] or by ion implanting H_2^+ or O^+ ions [53]. Apart from an early investigation on the properties of ITO thin films prepared from various rf sputtering plasma gases, including N_2 using gas-timing technique, there were also reported on indium tin oxide and indium tin oxynitride thin films in chapter 6.

2.5 Chapter summary

During the last decade, metal oxynitride films have received considerable attention due to their unexpected and interesting properties. The presence of nitrogen in oxide films or the presence of oxygen in nitride films enables the preparation of a range of functional materials with technological importance. The binary metal oxynitride possess superior properties of both the corresponding metallic nitride and the dielectric oxide compounds such as indium tin oxynitride.

In an ideal case, the desired film properties are focusing on the optical band gap tailoring. it can be obtained by selecting suitable process conditions and special deposition technique. More specifically, this could be the addition of nitrogen to the argon-oxygen atmosphere typically used in sputter deposition, since a substitution of oxygen atoms in the anionic lattice by nitrogen should significantly effected to their structure, electrical and optical properties.

References:

[1] S. A. Bashar "**Study of Indium Tin Oxide (ITO) for Novel Optoelectronic Devices**", Ph.D. thesis of University of London, 1997.

[2] J. Bates, C. Griffin. D. Marchant and J. Garnier, "Electrical Conductivity, Seebeck Coefficient, and Structure of In_2O_3-SnO_2", **American Ceramic Society Bulletin**, vol. 65, no.4, pp. 673-678, 1986.

[3] H. P. Lobl, M. Huppertz and D. Mergel, "ITO Films for Antireflective and Antistatic Tube Coatings Prepared by d.c. Magnetron Sputtering", **Surface and Coatings Technology**, vol. 82, 1996, pp. 90-98.

King Mongkut's Institute of Technology Ladkrabang

This material is reserved for educational use only, not allowed for commercial use.

Forbidden to modify the content, and cite the document when use.

[4] Y. Ishihara, T. Hirai, C. Sakurai, T. Koyanagi, H. Nishida and M. Komatsu, "Applications of the Particle Ordering Technique for Conductive Anti-reflection Films", **Thin Solid Films**, vol. 411, 2002, pp. 50-55.

[5] R. T. Chen and D. Robinson, "Electro-optic and All-optical Phase Modulator on An Indium Tin Oxide Single-mode Waveguide", **Appl. Phys. Lett.**, vol. 60, 1992, pp. 1541-1543.

[6] M. Kleijn, M. C. Stuart, and A. de Wit, "Electro-optic Effect in the Solid Phase of the Indium Tin Oxide/Electrolyte Solution Interface Observed by Reflectometry", **Colloids and Surfaces A: Physicochemical and Engineering Aspects**, vol. 110, 1996, pp. 213-217.

[7] K. Furuichi, J. Xu, M. Inoue, H. Furuta, N. Yoshida, A. Tounai, Y. Yanaka, A. Mochizuki, and S. Kobayashi, "Effect of Ion Trapping Films on the Electrooptic Characteristics of Polymer-stabilized Ferroelectric Liquid Crystal Display Exhibiting V-shaped Switching", **Jpn. J. Appl. Phys.**, vol. 42, no. 7A, 2003, pp. 4411-4415.

[8] S. Yoon and T. Won, "Electrode Structure for High Transmittance and Aperture Ratio in TFT-LCD", **Journal of Materials Processing Technology**, vol. 191, 2007, pp. 302-305.

[9] N. Lee, J. Park, H. Kim, and W. Lee, "Contact Resistivity between an Al Metal Line and an Indium Tin Oxide Line of Thin Film Transistor Liquid Crystal Displays", **Jpn. J. Appl. Phys.**, vol. 41, no. 2A, 2002, pp. 791-794.

[10] Y.S. Kim, J.H. Park, D.H. Choi, H.S. Jang, J.H. Lee, H.J. Park, J.I. Choi, D.H. Ju, J.Y. Lee, and D. Kim, "ITO/Au/ITO Multilayer Thin Films for Transparent Conducting Electrode Applications", **Appl. Surf. Sci.**, vol. 254, 2007, pp. 1524-1527.

[11] H. Kajii, A. Sakakibara, H. Okuya, T. Morimune, and Y. Ohmori, "Organic Transistors with Indium Tin Oxide Electrodes for Driving Organic Light Emitting Diode", **Thin Solid Films**, vol. 499, 2006, pp. 415-419.

[12] J.D. Hwang, W.T. Chang, K.H. Hseih, G.H. Yang, C.Y. Wu, and P.S. Chen, "Nonalloyed Transparent Ohmic Contact of Indium Tin Oxide to p-type $Si_{0.8}Ge_{0.2}$", **Thin Solid Films**, vol. 493, 2005, pp. 203-206.

[13] T. Nakada, Y. Hirabayashi, T. Tokado, D. Ohmori, and T. Mise, "Novel Device Structure for $Cu(In,Ga)Se_2$ Thin Film Solar Cells Using Transparent Conducting Oxide Back and Front Contacts", **Solar Energy**, vol. 77, 2004, pp. 739-747.

This material is reserved for educational use only, not allowed for commercial use.
Forbidden to modify the content, and cite the document when use.

[14] J. C. C. Fan, F. J. Bachner, and G. H. Foley, "Effect of Oxygen Partial Pressure During Deposition on Properties of r.f. Sputtered Sn-Doped In_2O_3 Films", **Appl. Phys. Lett.**, vol. 31, 1977, pp. 773-775.

[15] K. Sreenivas, T. Sundarsena Rao, A. Mansnigh, and S. Chandra, "Preparation and Characterization of r.f. Sputtered Indium Tin Oxide Films", **J. Appl. Phys.**, vol. 57, 1985, pp. 384-392.

[16] A. Khodorov, M. Piechowiak, and M.J.M. Gomes, "Structural, Electrical and Optical Properties of Indium-Tin-Oxide Thin Films Prepared by Pulsed Laser Deposition", **Thin Solid Films**, vol. 515, 2007, pp. 7829-7833.

[17] M. Buchanan, J. B. Webb, and D. F. Williams, "The Influence of Target Oxidation and Growth Related Effects on the Electrical Properties of Reactively Sputtered Films of Tin-Doped Indium Oxide", **Thin Solid Films**, vol. 80, 1981, pp. 373-382.

[18] M. Higuchi, S. Uekusa, R. Nakano, and K. Yokogawa, "Postdeposition Annealing Influence on Sputtered Indium Tin Oxide Film Characteristics", **Jpn. J. Appl. Phys.**, vol. 33, no. 1A, 1994, pp. 302-306.

[19] N. Balasubramanian and A. Subrahmanyam, "Effect of Substrate Temperature on the Electrical and Optical Properties of Reactively Evaporated Indium Tin Oxide Films", **Materials Science and Engineering B**, vol. 1, 1988, pp. 279-281.

[20] J. Bregman, Y. Shapira and H. Aharoni, "Effects of Oxygen Partial Pressure during Deposition on the Properties of Ion Beam Sputtered Indium Tin Oxide Thin Films", **J. Appl. Phys.**, vol. 67, 1990, pp. 3750-3753.

[21] H. Haitjema and J. J. Ph. Elich, "Physical Properties of Pyrolitically Sprayed Tin-Doped Indium Oxide Coatings", **Thin Solid Films**, vol. 205, 1991, pp. 93-100.

[22] S. H. Brewer and S. Franzen, "Calculation of the Electronic and Optical Properties of Indium Tin Oxide by Density Functional Theory", **Chemical Physics**, vol. 300, 2004, pp. 285-293.

[23] N. Nadaud, N. Lequeux, M. Nanot, J. Jové, and T. Roisnel, "Structural Studies of Tin-Doped Indium Oxide (ITO) and $In_4Sn_3O_{12}$", **J. Solid State Chem.**, vol. 135, 1998, pp. 140-148.

This material is reserved for educational use only, not allowed for commercial use.
Forbidden to modify the content, and cite the document when use.

[24] K. Zeng, F. Zhu , J. Hu , L. Shen , K. Zhang, and H. Gong, "Investigation of Mechanical Properties of Transparent Conducting oxide thin films", **Thin Solid Films**, 443, 2003, pp. 60-65.

[25] L. Gupta, A. Mansingh, and P. K. Srivastava, "Band Gap Narrowing and the Band Structure of Tin Doped Indium Oxide Films", **Thin Solid Films**, vol. 176, 1989, pp. 33-44.

[26] M. Bender, J. Trube, and J. Stollenwerk, "Deposition of Transparent and Conducting Indium-Tin-Oxide Films by the r.f.-superimposed DC Sputtering Technology", **Thin Solid Films**, vol. 354, 1999, pp. 100-105.

[27] S. M. Sze, **Semiconductor Devices Physics and Technology.** 2nd Ed. John Wiley & Sons, Inc, 2001.

[28] M. Ohring, **The Materials Science of Thin Films.** Academic press, 1991.

[29] S. Ashok, P. P. Sharma, S. J. Fonash, "Spray-Deposited ITO-Silicon SIS Heterojunction Solar Cells", **IEEE Transactions on Electron Devices**, vol. ED-27, no. 4, 1980, pp. 725-730.

[30] D. B. Chrisley and G. K. Hubler, **Pulsed Laser Deposition of Thin Films.** New York: Wiley, 1994.

[31] S. Wolf and R.N. Tauber, **Silicon Processing for the VLSI Era.** Volume 1 Process Technology 2nd Ed. Lattice Press, 2000.

[32] D. L. Smith, **Thin-film Deposition Principles & Practice.** New York: McGraw-Hill, 1995.

[33] B. Thestrup, J. Schou, A. Nordskov, and N. B. Larsen, "Electrical and Optical Properties of Thin Indium Tin Oxide Films Produced by Pulsed Laser Ablation in Oxygen or Rare Gas Atmospheres", **Appl. Surf. Sci.**, vol. 142, 1999, pp. 248-252.

[34] H. Odaka, Y. Shigesato, T. Murakami, and S. Iwata, "Electronic Structure Analyses of Sn-Doped In_2O_3", **Jpn. J. Appl. Phys.**, vol. 40, no. 5A, 2001, pp. 3231-3235.

[35] J. Szczyrbowski, A. Dietrich, and H. Hoffmann, "Optical and Electrical Properties of r.f. Sputtered Indium-Tin Oxide Films", **Phys. Stat. Sol. (a)**, vol. 78, 1983, pp. 243-252.

[36] I. Hamberg, C. G. Granqvist, K.-F. Berggren, B. E. Sernelius, and L. Engstrom, "Band-Gap Widening in Heavily Sn-doped In_2O_3", **Phys. Rev. B**, vol. 30, no. 6, 1984, pp. 3240-3249.

[37] J. C. C. Fan and J. B. Goodenough, "X-Ray Photoemission Spectroscopy Studies of Sn-doped Indium Oxide Films", **J. Appl. Phys.**, vol. 48, 1977, pp. 3524-3531.

This material is reserved for educational use only, not allowed for commercial use.
Forbidden to modify the content, and cite the document when use.

[38] F. Matino, L. Persano, V. Arima, D. Pisignano, R. I. R. Blyth, R. Cingolani, and R. Rinaldi, "Electronic Structure of Indium-Tin-Oxide Films Fabricated by Reactive Electron-Beam Deposition", **Phys. Rev. B**, vol. 72, 2005, pp. 085437.

[39] L. Gupta, A. Mansingh, and P. K. Srivastava, "Band-gap Narrowing in Tin-doped Indium Oxide films", **Appl. Surf. Sci.**, vol. 33-34, 1988, pp. 898-904.

[40] C. C. Yu, S. Ramanathan, and S. T. Oyama, "New Catalysts for Hydroprocessing: Bimetallic Oxynitrides M_I-M_{II}-O-N (M_I, MII= Mo, W, V, Nb, Cr, Mn, and Co)", **J. Catal.**, vol. 173, 1998, pp. 1-9.

[41] B. J. Neudecker, R. A. Zuhr, and J. B. Bates, "Lithium Silicon Tin Oxynitride (Li_ySiTON): High-performance Anode in Thin-film Lithium-ion Batteries for Microelectronics", **J. Power Sources**, vol. 81-82, 1999, pp. 27-32.

[42] M.A. Signore, A. Rizzo, L. Mirenghi, M.A. Tagliente, and A. Cappello, "Characterization of Zirconium Oxynitride Films Obtained by Radio Frequency Magnetron Reactive Sputtering", **Thin Solid Films**, vol. 515, 2007, pp. 6798-6804.

[43] A. von Richthofen, R. Domnick, R. Cremer, and D. Neuschutz, "Preparation of a New Tetragonal Copper Oxynitride Phase by Reactive Magnetron Sputtering", **Thin Solid Films**, vol. 317, 1998, pp. 282-284.

[44] S. J. Ingrey , W. D. Westwood, Y. C. Cheng, and J. Wei, "Variable Refractive Index and Birefringent Waveguides by Sputtering Tantalum in O_2-N_2 mixtures", **Appl. Opt.**, vol. 14, 1975, pp. 2194-2198.

[45] T. Savisalo, D. B. LewisT, and P.Eh. Hovsepian, "Microstructure and Properties of Novel Wear and Corrosion Resistant CrON/NbON Nano-scale Multilayer Coatings", **Serf. & Coat. Technol.**, vol. 200, 2006, pp. 2731-2737.

[46] H. Steffes, C. Imawan, P. Fricke, H. Vohse, J. Albrecht, R. Schneider, F. Solczbacher, and E. Obermeier, "New $In_xO_yN_z$ films for the application in NO_2 sensors", **Sens. Actuators B**, vol. 77, 2001, pp. 352-358.

[47] B. R. Natarajan, A. H. Eltoukhy, J. E. Greene, and T. L. Barr, "Mechanisms of Reactive Sputtering of Indium II: Growth of Indium Oxynitride in Mixed N_2-O_2 Discharges", **Thin Solid Films**, vol. 69, 1980, pp. 217-227.

[48] M. Futsuhara, K. Yoshioka, and O. Takai, "Optical Properties of Zinc Oxynitride Thin Films", **Thin Solid Films**, vol. 317, 1998, pp. 322-325.

This material is reserved for educational use only, not allowed for commercial use.
Forbidden to modify the content, and cite the document when use.

[49] N. Martin, O. Banakh, A. M. E. Santo, S. Springer, R. Sanjines, J. Takadoum, and F. Levy, "Correlation Between Processing and Properties of TiO_xN_y Thin Films sputter deposited by the Reactive gas Pulsing Technique", **Appl. Surf. Sci.**, vol. 185, 2001, pp. 123-133.

[50] L. Pinard and J. M. Mackowski, "Optical Losses of Multilayer Stacks Synthesized with Silicon Oxynitride by r.f. Magnetron Sputtering", **Thin Solid Films**, vol. 333, 1998, pp. 126-133.

[51] J. M. Phillips, R. J. Cava, G. A. Thomas, S. A. Carter, J. Kwo, T. Siegrist, J. J. Krajewski, J. H. Marshall, W. F. Peck, Jr., and D. H. Rapkine, "Zinc-Indium-Oxide: A High Conductivity Transparent Conducting Oxide", **Appl. Phys. Lett.**, vol. 67, 1995, pp. 2246-2248.

[52] T. Minami, T. Kakumu, K. Shimokawa, and S. Takata, "New Transparent Conducting ZnO-In_2O_3-SnO_2 Thin Films Prepared by Magnetron Sputtering", **Thin Solid Films**, vol. 317, 1998, pp. 318-321.

[53] Y. Shigesato, D. C. Paine, and T. E. Haynes, "Study of the Effect of Ion Implantation on the Electrical and Micro-structural Properties of Tin-doped Indium Oxide Thin Films", **J. Appl. Phys.**, vol. 73, 1993, pp. 3805-3811.

King Mongkut's Institute of Technology Ladkrabang

This material is reserved for educational use only, not allowed for commercial use.
Forbidden to modify the content, and cite the document when use.

CHAPTER 3

BACKGROUND OF ZINC OXIDE (ZnO)

3.1 Introduction to ZnO

ZnO is of particular interest due to its wide band gap and excellent optical qualities, making it a promising material for several applications such as ultraviolet optoelectronics, transparent contacts, varistors and gas sensors. It is also nearly identical in lattice spacing to GaN, meaning that integration of ZnO with GaN based systems is possible. The major difficulty in producing ZnO devices is the lack of *p*-type doping. As grown, ZnO is n-type due to structural defects from the growth process, such as oxygen vacancies, zinc interstitials and anti-sites. An anti-site occurs when a nucleus of one species occupies a lattice site that is typically occupied by another species, such as a zinc nucleus on an oxygen site in the lattice. A vacancy is an unoccupied lattice site, resulting in unsatisfied bonds within the lattice. An interstitial defect is a nucleus that does not occupy a lattice site, perturbing the periodic potential that gives rise to the ideal band structure.

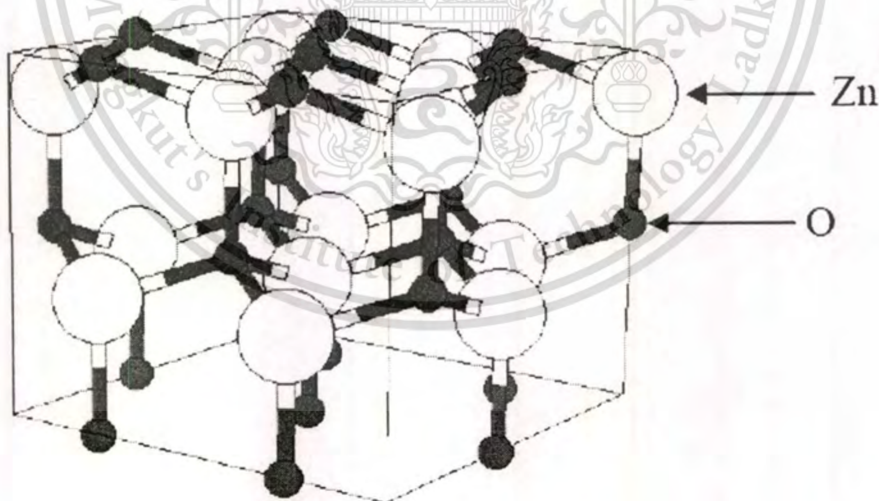

Fig. 3.1 Crystalline ZnO forms in the wurtzite structure [1].

The ideal band structure of a semiconductor is born out of the periodicity of a crystal lattice, and the periodic electric potential associated with it. Any deviation from an ideal, periodic

This material is reserved for educational use only, not allowed for commercial use.
Forbidden to modify the content, and cite the document when use.

lattice will create distinct energy levels in the band gap as deviations perturb the periodic potential. An ideal lattice is impossible to fabricate, so the objective of any film growth or deposition is to minimize the defect densities in the material, minimizing the intrinsic perturbations to the lattice. A ZnO crystal has the wurtzite structure as shown in Fig. 3.1. The large spheres represent the zinc nuclei and the smaller spheres represent the oxygen nuclei. In the wurtzite structure, a cation is bonded to four nearest neighbor anions and each anion is similarly bonded with four cations. Thus each oxygen nucleus is bound to four zinc nuclei, and each zinc nucleus is bound to four oxygen nuclei.

Production of quality p-type ZnO films has been problematic, mostly due to defects caused by dopant induced stresses in the crystal. Very low formation energies for oxygen vacancies and zinc interstitials in ZnO have been calculated and likely explain the native n-type conductivity observed in as-grown films [2]. These low energy defects may also be the cause of n-type defects, causing the self-compensation observed for acceptors. Ultimately, this makes p-type doping very difficult [3,4]. Of the possible acceptor species for ZnO, nitrogen is the favorite because the Zn-N bond (1.88 Å) is the most similar in length to the Zn-O bond it would replace (1.93 Å), as shown in table 3.1. Close matching of the bond length reduces the crystal strain and thus, reduces the likelihood of compensating defect formation. For this reason, it is preferable to develop methods of doping ZnO films with nitrogen. However, recent reports have also indicated that phosphorus, arsenic, antimony, lithium, nitrogen-aluminum and even nitrogen- tellurium can act as p-type dopants [5-10].

Table 3.1 Group I and V acceptor properties in ZnO (adapted from Park *et al.* [3]).

Dopant	Bond length (Å)	Calculated energy level (meV)	Group
Li	2.03	90	I
Na	2.10	170	I
K	2.42	320	I
N	1.88	400	V
P	2.18	930	V
As	2.23	1150	V

This material is reserved for educational use only, not allowed for commercial use.
Forbidden to modify the content, and cite the document when use.

Determining the conductivity type of ZnO is experimentally difficult for several reasons including, low mobility, difficulty in making ohmic contacts, persistent photoconductivity effects and the formation of a degenerate surface layer. However, a number of authors have reported p-type behavior and their results [11,12]. At the present stage of development of ZnO, it is likely that some of these reports may be suspect due to the measurement and material-related issues listed above. Now, we focused on nitrogen dopant, a typical method for producing ZnO by reactive sputtering is to sputter a target where the nitrogen dopant is incorporated in the desired stoichiometry depended on sputtering conditions. This technique, or variations thereof, was used to attempt growth of ZnO doped with nitrogen thin films. The new optical functionally of nitrogen incorporated ZnO thin films were expected in this research.

Table 3.2 The properties of ZnO thin films prepared by various growth techniques.

Deposition techniques	Thickness (Å)	Substrate type	Ref.
RF sputtering	5200	diamond(111)	[13]
RF sputtering	700-2000	p-type Si(001)	[14]
Chemical vapour deposition (CVD)	10000	sapphire(0112)	[15]
RF magnetron sputtering	10000	α-Al_2O_3(0001)	[16]
Molecular beam epitaxy (MBE)	2300	α-Al_2O_3(0001)	[17]
Molecular beam epitaxy (MBE)	150	sapphire(0001)	[18]
Pulsed laser deposition(PLD)	5000	epi-GaN/sapphire	[19]
Metalorganic chemical vapor deposition (MOCVD)	7600	SiO_2/Si	[20]

3.2 The growth techniques for ZnO

The early reports dealt with deposition of ZnO utilizing growth techniques such as magnetron sputtering [13,14] and chemical vapor deposition (CVD) [15] however, the films were mainly polycrystalline. Later attempts led to high-quality ZnO single crystal films prepared by rf magnetron sputtering [16] and other growth techniques allowing a fine control over the deposition procedure, such as molecular beam epitaxy (MBE) [17,18], pulsed laser deposition (PLD) [19], and metalorganic chemical vapor deposition (MOCVD) [20]. Table 3.2 compiles some of the structural and electrical properties from ZnO samples grown by different techniques. The

This material is reserved for educational use only, not allowed for commercial use.

Forbidden to modify the content, and cite the document when use.

structural, optical and electrical properties of the ZnO thin film is critically related to the specific growth technique employed and to the growth parameters used. In the following section, the briefly on ZnO deposition techniques will be presented.

3.2.1 Pulsed laser deposition (PLD)

In the pulsed laser deposition (PLD) method, high-power laser pulses are used to evaporate material from a target surface such that the stoichiometry of the material is preserved in the interaction. As a result, a supersonic jet of particles (plume) is directed normal to the target surface. The plume expands away from the target with a strong forward directed velocity distribution of different particles. The ablated species condense on the substrate placed opposite to the target. A schematic diagram of the typical PLD system is shown in Fig. 3.2. The main advantages of PLD are its ability to create high-energy source particles, permitting high-quality film growth at low substrate temperatures, typically ranging from 200°C to 800°C, its simple experimental setup, and operation in high ambient gas pressures in the 10^{-5}-10^{-1} Torr range.

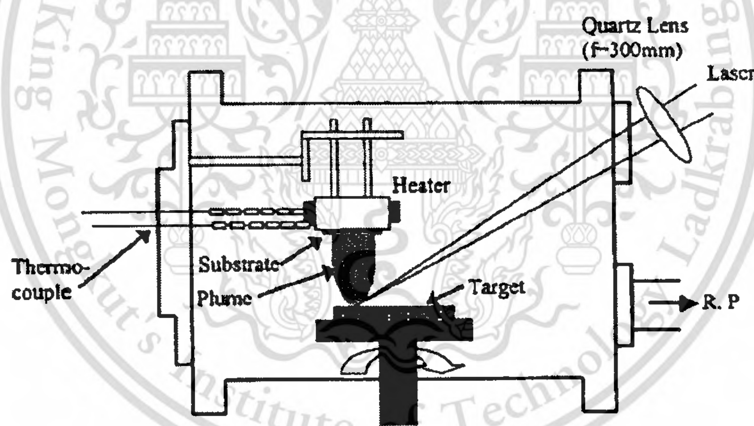

Fig. 3.2 Schematic of a pulsed laser deposition system [21].

For the growth of ZnO by PLD technique, usually UV excimer lasers (KrF: λ = 248 nm and ArF: λ = 193 nm) and Nd: yttrium aluminum garnet (YAG) pulsed lasers (λ = 355 nm) are used for ablation of the ZnO target in an oxygen environment. In some cases, Cu-vapor laser emitting at λ = 510-578 nm was also used for the same purpose [22]. Cylindrical ZnO tablets made from pressed ZnO powder are usually used as targets. Single-crystal ZnO has been used to grow high-quality ZnO thin films very recently. The properties of the grown ZnO films depend mainly on the substrate temperature, ambient oxygen pressure, and laser intensity.

This material is reserved for educational use only, not allowed for commercial use.
Forbidden to modify the content, and cite the document when use.

3.2.2 Molecular beam epitaxy (MBE)

The main advantage of molecular-beam epitaxy (MBE) is its precise control over the deposition parameters and in-situ diagnostic capabilities. With the feedback from reflection high-energy electron diffraction (RHEED), the growth mode of ZnO epilayers can be monitored in real time dynamically. For ZnO thin film deposition by MBE, Zn metal and O_2 are usually used as the source materials. High-purity Zn metal is evaporated from an effusion cell, where the cell temperature can be varied to examine the effect of the Zn flux on the growth rate and material properties. The oxygen radical beam, which can be generated by an electron cyclotron resonance (ECR) [23] or a rf plasma source [17] is directed on the film surface to obtain high-oxidation efficiency. When the O plasma is used, the chamber pressure during growth is in the 10^{-5} Torr range. Nitrogen dioxide (NO_2) was also utilized for MBE of ZnO on (0001) sapphire substrates to keep the chamber pressure low in an effort to protect sensitive filaments and heaters [24] but the resultant crystal structures and the surface morphology were not satisfactory. Successful growth of ZnO films by using hydrogen peroxide (H_2O_2) vapour as a source of active oxygen has also been reported [25]. The schematic of MBE deposition system is depicted in Fig. 3.3.

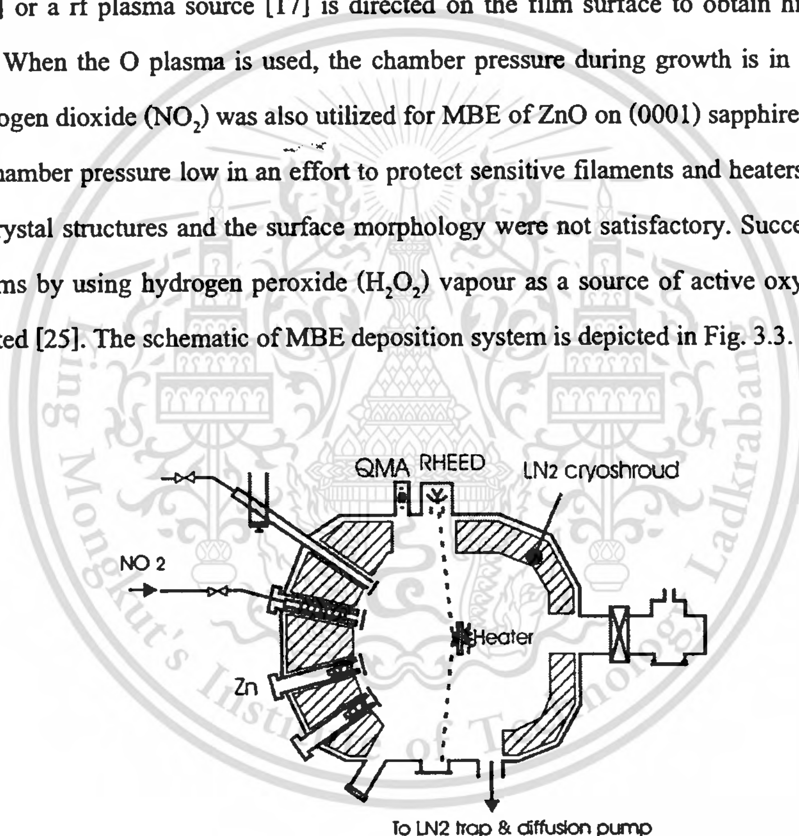

Fig. 3.3 Schematic of MBE deposition system [24].

3.2.3 Chemical-vapor deposition (CVD)

Among other growth methods, chemical-vapour deposition (CVD) technology is particularly interesting not only because it gives rise to high-quality films but also because it is applicable to large-scale production. This technique is widely used in the fabrication of epitaxial films toward various GaN-based optoelectronic devices, and similar trend might be expected for

This material is reserved for educational use only, not allowed for commercial use.
Forbidden to modify the content, and cite the document when use.

future applications of ZnO. There are several modifications of this method depending on precursors used. When metal-organic precursors are used, the technique is called metal-organic chemical-vapour deposition (MOCVD), metal-organic vapor-phase epitaxy (MOVPE), or organometallic vapor-phase epitaxy (OMVPE) [20]. The schematic of a typical CVD deposition system is shown in Fig. 3.4.

In the CVD method, ZnO deposition occurs as a result of chemical reactions of vapour phase precursors on the substrate, which are delivered into the growth zone by the carrier gas. The reactions take place in a reactor where a necessary temperature profile is created in the gas flow direction. For ZnO growth, MOCVD/MOVPE technique typically involves the use of metal alkyls, usually dimethyl zinc $[(CH_3)_2Zn]$ (DMZn) or diethyl zinc $[(C_2H_5)_2Zn]$ (DEZn) in combination with a separate source of oxygen and argon or nitrogen as a carrier gas. In earlier investigations, O_2 or H_2O were used as oxygen precursors [26-28]. However, DEZn and DMZn are highly reactive with oxygen and water vapour, so that severe premature reaction in the gas phase occurs in the cold zone of the reactor, resulting in the formation of white powder, which degrades the film quality. Nevertheless, great progress has been made in ZnO growth by MOCVD recently. The improvement of the material quality is related to improved reactor design or the use of less-reactive precursors, allowing one to minimize parasitic prereactions in the gas phase. Stable metal-organic source of zinc acetylacetonate in combination with oxygen was successfully used for the growth of high-quality ZnO films on sapphire substrates by atmospheric pressure MOCVD [29,30].

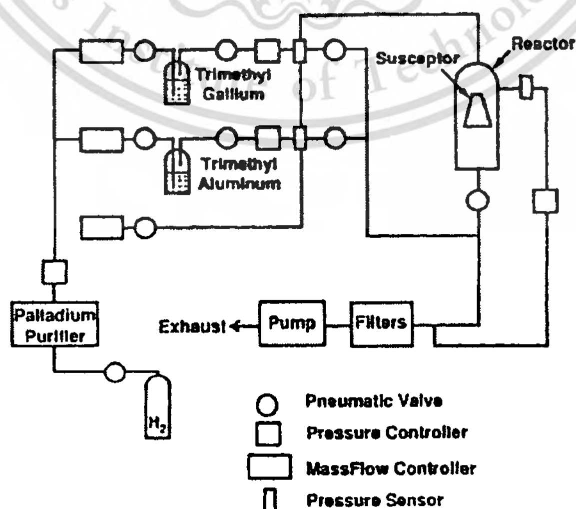

Fig. 3.4 Schematic of a typical CVD deposition system.

This material is reserved for educational use only, not allowed for commercial use.

Forbidden to modify the content, and cite the document when use.

3.2.4 Radio frequency magnetron sputtering

One of the most popular growth techniques for early ZnO investigations was sputtering such as dc sputtering, rf magnetron sputtering, and reactive sputtering. As compared to sol gel and chemical-vapour deposition, the magnetron sputtering was a preferred method because of its low cost, simplicity, and low operating temperature [31]. ZnO films grow at a certain substrate temperature by sputtering from a high-purity ZnO target using a rf magnetron sputter system. The growth is usually carried out in the growth ambient with $O_2/Ar+O_2$ ratios ranging from 0 to 1 at a pressure of 10^{-3}-10^{-2} Torr range. O_2 serves as the reactive gas and Ar acts as the sputtering enhancing gas. ZnO can also be grown by dc sputtering from a Zn target in an $Ar+O_2$ gas mixture. The rf power applied to the plasma is tuned to regulate the sputtering yield rate from the ZnO target. For these experiments, the target is pre-sputtered for 5-15 min before the actual deposition begins to remove any contamination on the target surface, make the system stable, and reach optimum condition.

Although most of the earlier sputtered materials were polycrystalline or even amorphous, some important accomplishments were reported. Upon increasing the $O_2/Ar+O_2$ ratio in the growth ambient, the visible emission was drastically suppressed without sacrificing the band-edge emission intensity in the ultraviolet region. This tendency is attributed to the reduction of the oxygen vacancies and zinc interstitials in the film induced by the improvement of the stoichiometry, indicating that the visible emission in ZnO originates possibly from oxygen vacancy or zinc-interstitial-related defects. A more advanced sputtering technique utilizes electron cyclotron resonance (ECR) source to supply the power to the plasma, as shown in Fig.3.5. The advantage of the ECR sputtering system is that it enables the production of highly ionized plasma under low gas pressures. The ZnO films deposited by ECR sputtering exhibited a high electrical resistivity and good piezoelectric and optical properties [32,33].

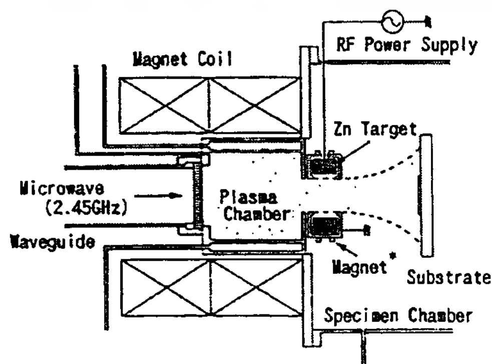

Fig. 3.5 A typical ECR sputtering apparatus [32].

This material is reserved for educational use only, not allowed for commercial use.
Forbidden to modify the content, and cite the document when use.

3.3 The properties of ZnO

Zinc (II) oxide is a chemical compound with formula ZnO, which is a binary compound semiconductor from group II-VI, its ionicity is at the boundary, is between the covalent and ionic semiconductors. Table 3.2 summarizes the most significant properties of ZnO [34-36].

Table 3.3 Physical properties of a ZnO single crystal.

Crystal system	6mm (wurtzite)
Space group	$P6_3mc$
Lattice constant	a = b = 3.253 Å, c = 5.211 Å [38]
Sublimation point	1975 ± 25 °C
Optical transparency	0.4 – 2.5 mm
Optical band gap energy	~3.2 eV (RT) [35] and ~3.44 eV (4 K) [36]
Refraction index	$n_o = 1.9985$, $n_e = 2.0147$ ($\lambda = 6328$ Å)
Thermal-expansion coefficient	$\alpha_{11} = 4.0$, $\alpha_{33} = 2.1$ (10^{-6} /°C)

3.3.1 Crystal structures

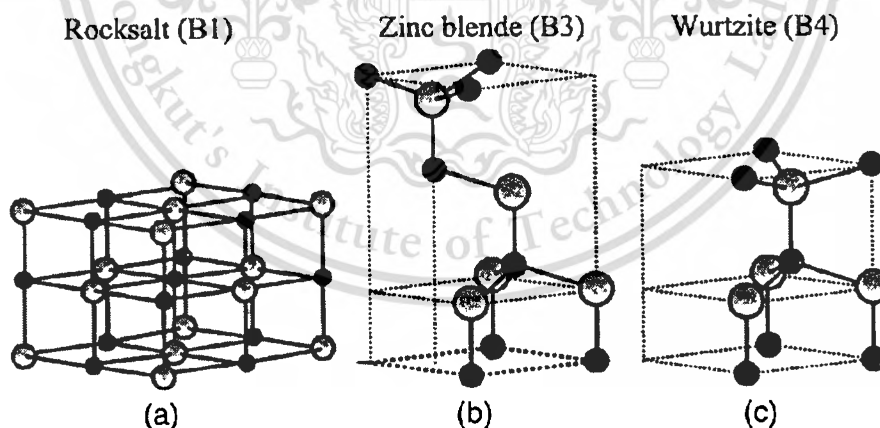

Fig. 3.6 Stick and ball representation of ZnO crystal structures: (a) cubic rocksalt (B1), (b) cubic zinc blende (B3), and (c) hexagonal wurtzite (B4). The shaded gray and black spheres denote Zn and O atoms, respectively.

Most of the group-II-VI binary compound semiconductors crystallize in either cubic zinc-blende or hexagonal wurtzite structure where each anion is surrounded by four cations at the

This material is reserved for educational use only, not allowed for commercial use.
Forbidden to modify the content, and cite the document when use.

corners of a tetrahedron, and vice versa. This tetrahedral coordination is typical of *sp*3 covalent bonding, but these materials also have a substantial ionic character. ZnO is a II-VI compound semiconductor whose ionicity resides at the borderline between covalent and ionic semiconductor. The crystal structures shared by ZnO are wurtzite (B4), zinc-blende (B3), and rocksalt (B1), as schematically shown in Fig. 3.6. At ambient conditions, the thermodynamically stable phase is wurtzite. The zinc-blende ZnO structure can be stabilized only by growth on cubic substrates, and the rocksalt (NaCl) structure may be obtained at relatively high pressures. From the crystal structure point of view, the wurtzite structure has a hexagonal unit cell with two hexagonal lattice parameters, a and c, in the ratio of $c/a = (8/3)^{1/2} = 1.633$ and belongs to the space group of $P6_3mc$. A schematic representation of the wurtzite ZnO structure is shown in Fig. 3.7.

In an ideal wurtzite structure, the structure is composed of two interpenetrating hexagonal close-packed (hcp) sublattices, each of which consists of one type of atom displaced with respect to each other along the threefold c-axis by the amount of u = 3/8 = 0.375 in fractional coordinates, which u parameter is defined as the length of the bond parallel to the c axis, in units of c. Each sublattice includes four atoms per unit cell and every atom of one kind (group II atom) is surrounded by four atoms of the other kind (group VI atom), or vice versa, which are coordinated at the edges of a tetrahedron.

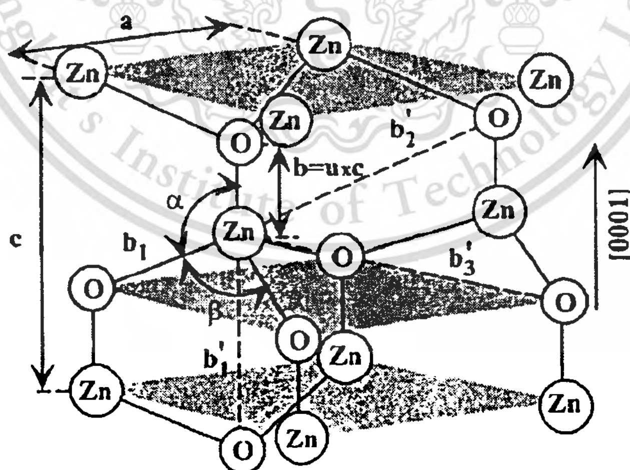

Fig. 3.7 Schematic representation of a wurtzite ZnO structure having lattice constants a in the basal plane and c in the basal direction; u parameter is expressed as the bond length or the nearest-neighbour distance b divided by c (0.375 in ideal crystal), and α and β (109.47° in ideal crystal) are the bond angles.

This material is reserved for educational use only, not allowed for commercial use.
Forbidden to modify the content, and cite the document when use.

In a real ZnO crystal, the wurtzite structure deviates from the ideal arrangement, by changing the c/a ratio or the u value. It should be pointed out that a strong correlation exists between the c/a ratio and the u parameter in that when the c/a ratio decreases, the u parameter increases in such a way that those four tetrahedral distances remain nearly constant through a distortion of tetrahedral angles due to long-range polar interactions. These two slightly different bond lengths will be equal if the following relation holds by:

$$u = \left(\frac{1}{3}\right)\left(\frac{a^2}{c^2}\right) + \frac{1}{4}, \tag{3.1}$$

Since the c/a ratio also correlates with the difference of the electronegativities (EN) of the two constituents, components with the greatest differences show the largest departure from the ideal c/a ratio [37]. The stable phase of ZnO is hexagonal wurtzite crystal structure is depicted in Fig. 3.8. The stable hexagonal wurtzite ZnO structure has lattice constants a = b = 3.253 Å, c = 5.211 Å and the ratio c/a = 1.602 [38].

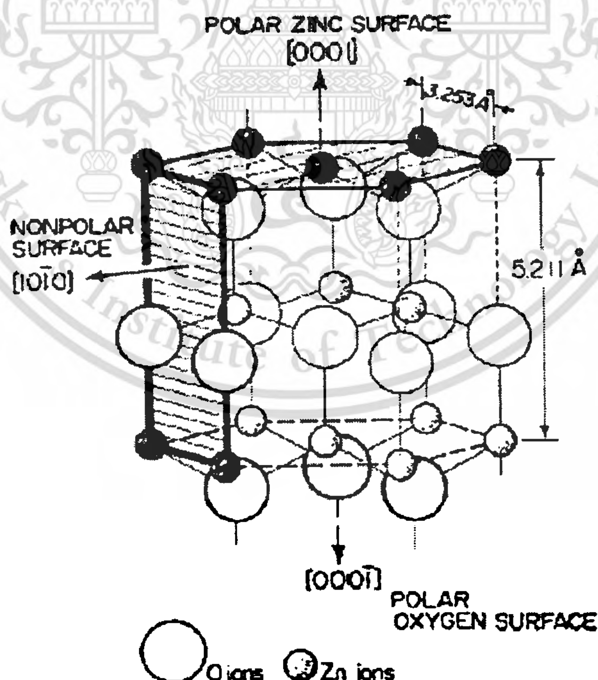

Fig. 3.8 The wurtzite lattice of ZnO: small circles represent the zinc atoms, while large circles depict oxygen atoms [38].

This material is reserved for educational use only, not allowed for commercial use.
Forbidden to modify the content, and cite the document when use.

3.3.2 Electronic band structure of ZnO

The band structure of a given semiconductor is pivotal in determining its potential utility. Consequently, an accurate knowledge of the band structure is critical if the semiconductor in question is to be incorporated in the family of materials considered for device applications. Several theoretical approaches of varying degrees of complexity have been employed to calculate the band structure of ZnO for its wurzite, zinc-blende, and rocksalt polytypes. Besides, a number of experimental data have been published regarding the band structure of the electronic states of wurtzite ZnO. X-ray or UV reflection/absorption or emission techniques have conventionally been used to measure the electronic core levels in solids. These methods basically measure the energy difference by inducing transitions between electronic levels, such as transitions from the upper valence-band states to the upper conduction-band states and from the lower valence-band states or by exciting collective modes, such as the upper core states to the lower edge of the conduction band and to excitations of plasmons. Another important method for the investigation of the energy region is based on the photoelectric effect extended to the X-ray region, namely, photoelectron spectroscopy (PES). The peaks in emission spectrum correspond to electron emission from a core level without inelastic scattering, which is usually accompanied by a far-less-intense tail region in the spectrum. More recently, angle-resolved photoelectron spectroscopy (ARPES) technique has started to be used. This technique together with synchrotron radiation excitation has been recognized as a powerful tool that enables experimental bulk and surface electronic band-structure determinations under the assumptions of k conservation and single nearly-free-electron-like final band [39]. After the theoretical work on band-structure calculation of ZnO proposed by Rössler using Green's function, namely as Korringa-Kohn-Rostoker (KKR) method [40]. In the following years, LDA and tight-binding methods were employed [41-44] by considering the Zn 3*d* states as core levels to ease calculations. A bulk band structure along the high symmetry lines in the hexagonal Brillouin zone is shown for ZnO in Fig. 3.9. The band structure was generated theoretically using an empirical tight-binding Hamiltonian [43].

From the band structure is shown on the left hand side of Fig. 3.9, the six valence bands can be seen between -6 eV and 0 eV. These six valence bands correspond to the oxygen's 2p orbital that contribute to the band structure. Below -6 eV at about -20 eV the valence band terminates with the oxygen's 2s core like state. The corresponding density of states (DOS) is shown on the right hand side of Fig. 3.9. From this figure it is clear that most of the electrons are located close

This material is reserved for educational use only, not allowed for commercial use.
Forbidden to modify the content, and cite the document when use.

to the valence band edge. According to this model, the optical band gap can be specified between the Γ_1 and $\Gamma_{1,5}$ with a value of about 3.3 eV.

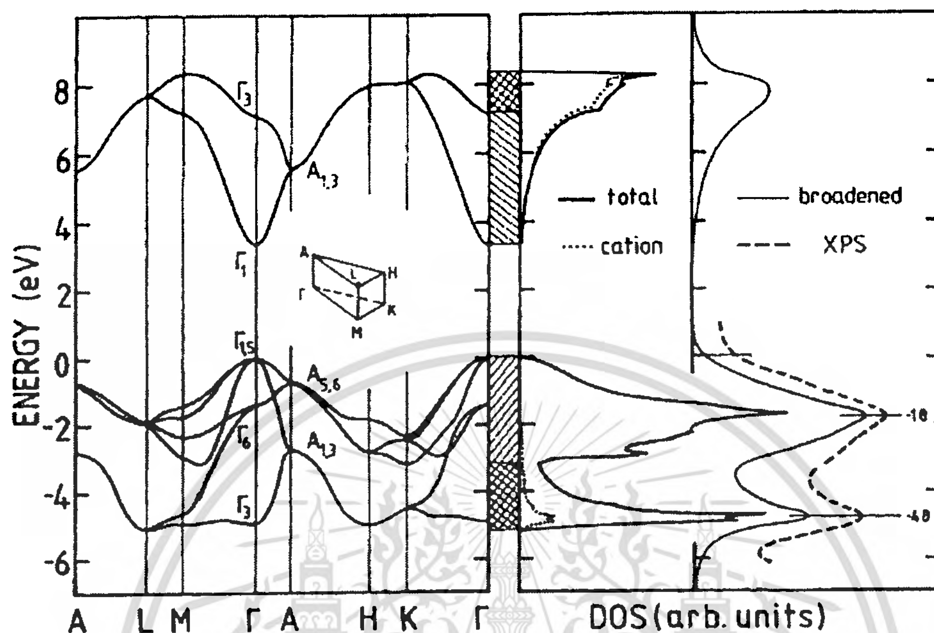

Fig. 3.9 Band structure for ZnO for various high-symmetry lines (left). On the right hand side, the density of states (DOS) is shown. The shading between the two graphs characterizes the different band groups. The zero in the graphs is taken as the valence band upper edge [43].

3.3.3 Mechanical properties of ZnO

The mechanical properties of materials involve various concepts such as hardness, stiffness, and piezoelectric constants, Young's and bulk moduli, and yield strength. In hexagonal crystals, there exist five independent elastic constants: C_{11}, C_{33}, C_{12}, C_{13}, and C_{44}. Elastic constants C_{11} and C_{33} correspond to longitudinal modes along the [1000] and [0001] directions, respectively. Elastic constants C_{44} and $C_{66} = (C_{11}-C_{12})/2$ can be determined from the sound velocity of transverse modes propagating along the [0001] and [1000] directions, respectively. The remaining constant C_{13} is present in combination with four other moduli in the velocity of modes propagating in less symmetrical directions, such as [0011]. The bulk modulus is related to the elastic constants by [45]:

$$B = \frac{(C_{11}+C_{12})C_{33}-2C_{13}^2}{C_{11}+C_{12}+2C_{33}-4C_{13}}, \quad (3.2)$$

This material is reserved for educational use only, not allowed for commercial use.
Forbidden to modify the content, and cite the document when use.

Although the wurtzite ZnO crystal is acoustically anisotropic, there is only a very small difference between the shear sound velocities v_{TA1} and v_{TA2} propagating along the [001] and [100] directions, respectively ($v_{TA2}/v_{TA1} \cong 0.98$). In the isotropic approximation, the Young modulus (E) and shear modulus (G) can also be evaluated using the relations $E = 3B(1\text{-}2\nu)$ and $G = E/2(1+\nu)$, respectively. The term ν is the Poisson ratio and is given by $\nu = C_{13}/(C_{11}+C_{12})$. It has been argued that the most precise technique used to determine the elastic moduli of compound materials is ultrasonic measurement, which requires thick single crystalline samples, about 1 cm thick, to enable precise measurement of the time required for the plane-wave acoustic pulses to propagate through the crystal. The quasi-longitudinal and quasi-shear wave velocities can be used in the following equation to calculate C_{13} [46]:

$$C_{13} = \frac{1}{\cos\alpha \sin\alpha}\sqrt{(\lambda_{22} - \rho V)(\lambda_{33} - \rho V^2)} - C_{44}, \tag{3.3}$$

where, for hexagonal symmetry,

$$\lambda_{22} = C_{11}\cos^2\alpha + C_{44}\sin^2\alpha, \tag{3.4a}$$

$$\lambda_{33} = C_{44}\cos^2\alpha + C_{33}\sin^2\alpha, \tag{3.4b}$$

Here, α is the angle between the propagation direction and the c-axis, ρ is the mass per unit volume, and V is either the quasi-longitudinal or the quasi-shear velocity.

Among the tetrahedrally bonded semiconductors, it has been stated that ZnO has the highest piezoelectric tensor or at least one comparable to that of GaN and AlN [47]. This property makes it a technologically important material for many applications, which require a large electromechanical coupling. The piezoelectric tensor has three independent components in hexagonal wurtzite phase and one (e_{14}) in the cubic zinc-blende phase, which characterize the full piezoelectric tensors of such crystals [48]. Two of these components in wurtzite phase measure the polarization induced along the c-axis, at zero electric field, by a uniform strain either along the c-axis or in the basal plane. The relevant relationship is [49]

$$P_z^{piezo} = e_{33}\varepsilon_z + e_{31}\varepsilon_\perp, \tag{3.5}$$

This material is reserved for educational use only, not allowed for commercial use.
Forbidden to modify the content, and cite the document when use.

where ε_z and $\varepsilon_\perp$ are the strain along the c-axis and in the basal plane, respectively. The e_{33} and e_{31} are the piezoelectric coefficients. The third independent component of the piezoelectric tensor, e_{15}, describes the polarization induced by a shear strain which is usually neglected for simplicity. The sign of the piezoelectric tensor is generally fixed assuming that the positive direction along the c-axis goes from the cation to the anion.

The natural structure of ZnO is wurtzite, which has a low-symmetry, resulting in the existence of spontaneous polarization along the c-direction. However, the absolute value of the spontaneous polarization in a non-ferroelectric material has never been directly measured, while one invariably measures the polarization derivatives. In semiconductors, the spontaneous polarization may be deduced by investigating the two-dimensional electron gas and the red shift of the transitions in quantum wells, indirectly. From the theoretical point of view, there have been some efforts in determining the value of the spontaneous polarization in ZnO. One conventional approach is to define the spontaneous polarization of a low-symmetry crystal (wurtzite) as the polarization difference with respect to a high-symmetry structure (zinc-blende) of the same material. The spontaneous and piezoelectric polarization in ZnO have been studied theoretically by a number of groups and compared with a few available indirect experimental results. Dal Corso *et al.* [47] demonstrated the feasibility of *ab initio* studies of piezoelectricity within an all electron scheme. A comparative analysis was performed in order to understand the microscopic origin of the particular behaviour of ZnO. They have concluded that the piezoelectric effect results from two different contributions of opposite signs, which were referred to as the clamped ion and internal strain. It has been shown that the large piezoelectric tensor of ZnO is due to the low value of its clamped ion contribution. Besides, the piezoelectric tensor is dominated by the internal relaxation of anion and cation sub-lattices induced by the macroscopic strain. Later, the piezoelectric tensor in ZnO has been calculated by using various techniques such as plane-wave analysis, ultrasoft pseudopotentials, and a generalized-gradient-approximation Hamiltonian, an all-electron basis set and HF Hamiltonian. The values of e_{31} and e_{33} were reported in the range of 0.39-0.66 and 0.92-1.30 C/m^2, respectively [47,49,50-54].

3.3.4 Thermal properties of ZnO

There are three key parameters of thermal properties of ZnO; thermal-expansion coefficients, thermal conductivity and specific heat. First one is thermal-expansion coefficients, which are defined as $\Delta a/a$ or α_a and $\Delta c/c$ or α_c, for in-plane and out-of-plane cases, respectively.

This material is reserved for educational use only, not allowed for commercial use.
Forbidden to modify the content, and cite the document when use.

They are dependent on stoichiometry, presence of extended defects, and free carrier concentration. The temperature dependence of the lattice constants a and c, and the thermal-expansion coefficients of hexagonal ZnO have been determined by the capacitive method [55]. Han *et al.* [56] studied thermal properties of ZnO films prepared by rf magnetron sputtering on Si and GaAs substrates. Thermal stresses were determined by using the bending beam technique where the specimens were thermally cycled from 250 to 400 °C. They investigated the thermal-expansion coefficient as a function of some growth parameters, such as substrate temperature and sputtering power. It has been observed that the thermal-expansion coefficient increases about 37% from 5×10^{-6} to 8×10^{-6} 1/°C within the temperature range of 250 to 400 °C. Aoumeur *et al.* [57] calculated the thermal-expansion coefficient for both the zinc-blende and rocksalt phases of ZnO using a molecular dynamics simulation based on Tersoff's potential. They found that $\alpha = 1.24\times10^{-5}$ K^{-1} for the zinc-blende and $\alpha = 0.16\times10^{-5}$ K^{-1} for rocksalt structures.

The second, thermal conductivity (κ), which is a kinetic property determined by the contributions from the vibration, rotation and electronic degrees of freedom, is an extremely important material property when high-power or high-temperature electronic and optoelectronic devices are considered. For pure crystals, phonon-phonon scattering, which is ideally proportional to T^{-1} above the Debye temperature, is the limiting process for thermal conductivity. The heat transport is predominantly determined by phonon-phonon scattering by point and extended defects, such as vacancies and impurities. As for other semiconductors, due to their imperfection, point defects play a significant role in the thermal conductivity of ZnO. The lattice contribution as phonon scattering to the thermal conductivity is obtained from the kinetic theory as [58]

$$\kappa_{lattice}(T) = \frac{1}{3} v_s C_{lattice}(T) L(T), \tag{3.6}$$

where T is the temperature, v_s is the velocity of sound, $C_{lattice}(T)$ is the lattice specific heat, and $L(T)$ is the phonon mean free path. In almost all materials, $\kappa(T)$ first increases with temperature, reaches a maximum ($\kappa_{maximum}$) at some characteristic temperature T_{ch}, and then decreases. At low temperatures L is relatively long and is dominated by extrinsic effects such as defects, crystal size and $C_{lattice}(T) \sim (T/\theta_D)^3$, where θ_D is the Debye temperature. As the temperature increases, $C_{lattice}(T)$ begins to saturate and intrinsic temperature-dependent processes become dominant, thus causing a decrease in L. For the electronic contribution to the thermal conductivity which is negligible for carrier concentrations lower than 10^{19} cm^{-3} is [59]

This material is reserved for educational use only, not allowed for commercial use.
Forbidden to modify the content, and cite the document when use.

$$\kappa_{electronic}(T) = \frac{\pi^{2} n k_B^2 T \tau_{electr}}{3m_c^*}, \tag{3.7}$$

where n is the carrier density, k_B is the Boltzman constant, τ_{electr} is the scattering time of the electrons, and m_c* is the conduction-band effective mass. The overall thermal conductivity generally decreases with increasing carrier concentration, because the decrease in the lattice component of κ due to increased phonon scattering from both the impurities and free electrons outweighs the increase in the electronic contribution to κ [60].

The last one, the specific heat of a semiconductor has contributions from lattice vibrations, free carriers, and point and extended defects. For a good quality semi-insulating crystal, the specific heat is determined mostly by the lattice vibrations. Lawless *et al.* [61] investigated the specific heat for both pure and varistor types of ZnO samples between the temperature ranges of 1.7 to 25 K, where the latter has an average grain size of 10 μm. The specific heat data for pure ZnO were further analyzed by considering two non-Debye features at different temperature regions according to $C = C_{Debye} + C_{Schottky} + C_{Einstei}$, where C_{Debye}, $C_{Schottky}$ and $C_{Einstei}$ are the Debye, Schottky, and Einstein terms of the total specific heat of ZnO, respectively. In general, the Debye expression for the temperature dependence of specific heat in a solid at a constant pressure can be expressed as

$$C_{Debye} = 18R\left(\frac{T}{\theta_D}\right)^3 \int_0^{x_D} \frac{x^4 e^x}{(e^x - 1)} dx, \tag{3.8}$$

where $x_D \equiv \theta_D/T$ and R = 8.3144 J/mol.K is the molar gas constant. The coefficient in front of the term R has been multiplied by 2 to take into account the two constituents making up the binary compound. By fitting the measured temperature-dependent heat capacity to the Debye expression, one can obtain the Debye temperature θ_D specific to the heat capacity. It is often easier to extract a Debye temperature using data either near very low temperatures or well below the Debye temperature where the specific heat has a simple cubic dependence on temperature:

$$C_{Debye} = 234R\left(\frac{T}{\theta_D}\right)^3, \tag{3.9}$$

This material is reserved for educational use only, not allowed for commercial use.
Forbidden to modify the content, and cite the document when use.

The latter, the Einstein term has an exponential dependence and is given by:

$$C_{Einstein} = 3Rr_E\left(\frac{\theta_E}{T}\right)^2 \exp\left(-\frac{\theta_E}{T}\right), \quad (3.10)$$

where r_E is the number of Einstein oscillators per formula weight and θ_E is the Einstein temperature. The Schottky term has a T^{-2} dependence and is expressed by:

$$C_{Schottky} = bT^{-2}, \quad (3.11)$$

where $b = nR(\delta/2)^2$ (n = r_E is assumed) is the Schottky coefficient.

3.3.5 Electrical properties of ZnO

Owing to direct and wide band gap material, ZnO is attracting a lot of attention for a variety of electronic and optoelectronic applications. Advantages associated with a wide band gap include higher breakdown voltages, ability to sustain large electric fields, lower noise generation, and high-temperature and high-power operation. The electron transport in semiconductors can be considered for low and high electric fields from two main reasons. Firstly, at sufficiently low electric fields, the energy gained by the electrons from the applied electric field is small compared to the thermal energy of electrons, and therefore, the energy distribution of electrons is unaffected by such a low electric field. Since the scattering rates determining the electron mobility depend on the electron distribution function, electron mobility remains independent of the applied electric field, and Ohm's law is obeyed. Secondly, when the electric field is increased to a point where the energy gained by electrons from the external field is no longer negligible compared to the thermal energy of the electron, the electron distribution function changes significantly from its equilibrium value. These electrons become hot electrons characterized by an electron temperature larger than the lattice temperature. Furthermore, as the dimensions of the device are decreased to submicron range, transient transport occurs, when there is minimal or no energy loss to the lattice during a short and critical period of time, such as during transport under the gate of a field-effect transistor or through the base of a bipolar transistor. The transient transport is characterized by the onset of ballistic or velocity overshoot phenomenon. Since the electron drift velocity is higher than its steady-state value, one can design a device operating at frequencies exceeding those expected from linear scaling of dimensions.

This material is reserved for educational use only, not allowed for commercial use.

Forbidden to modify the content, and cite the document when use.

Hall effect is the most widely used technique to measure the transport properties and assess the quality of epitaxial layers. For semiconductor materials, it yields the carrier concentration, its type, and carrier mobility. More specifically, experimental data on Hall measurements over a wide temperature range of 4.2 to 300 K provide quantitative information on impurities, imperfections, uniformity, scattering mechanisms. The Hall coefficient and resistivity (ρ) for n-type conduction are experimentally determined and then related to the electrical parameters through $R_H = r_H/ne$ and $\mu_H = R_H/\rho$, where n is the free-electron concentration, e is the unit electronic charge, μ_H is the Hall mobility, and r_H is the Hall scattering factor which is dependent on the particular scattering mechanism. The drift mobility is the average velocity per unit electric field in the limit of zero electric field and is related to the Hall mobility through the Hall scattering factor by $\mu_H = r_H\mu$. The Hall scattering factor depends on the details of the scattering mechanism, which limits the drift velocity. As the carriers travel through a semiconductor, they encounter various scattering mechanisms that govern the carrier mobility in the electronic system. The major scattering mechanisms that generally govern the electron transport in III-V semiconductors are also valid for ZnO. They are briefly listed as follows.

(1) Ionized impurity scattering is due to deflection of free carriers by the long-range Coulomb potential of the charged centers caused by defects or intentionally doped impurities. This can be thought as a local perturbation of the band edge, which affects the electron motion.

(2) Polar LO-phonon scattering is caused by the interaction of a moving charge with an electric field induced by electric polarization associated with lattice vibration due to the ionic nature of the bonds in a polar semiconductor.

(3) Acoustic-phonon scattering through deformation potential arises from the energy change of the band edges induced by strain associated with acoustic phonons, where the scattering rate increases with the wave vectors of the phonons.

(4) Piezoelectric scattering arises from the electric fields that are produced by the strain associated with phonons in a crystal without inversion symmetry.

(5) If the density of dislocations and native defects are high in a semiconductor, dislocation scattering and scattering through defects are also considered as possible scattering mechanisms. Dislocation scattering is due to the fact that acceptor centers are introduced along the dislocation line, which capture electrons from the conduction band in an n-type semiconductor. The dislocation lines become

This material is reserved for educational use only, not allowed for commercial use.
Forbidden to modify the content, and cite the document when use.

negatively charged and a space charge region is formed around it, which scatters electrons traveling across the dislocations, thus reducing the mobility.

The experimental investigation of the temperature-dependent carrier mobility and concentration can be used to determine the fundamental material parameters and understand the carrier scattering mechanisms along with an accurate comparison with theory.

3.3.6 Optical properties of ZnO

The optical properties of II-VI binary semiconductors such as ZnO are connected with both intrinsic and extrinsic effects. Intrinsic optical transitions take place between the electrons in the conduction band and holes in the valence band, including electronics excitation effects due to the Coulomb interaction. Excitons are classified into free and bound excitons. In high-quality samples with low impurity concentrations, the free excitons can also exhibit excited states, in addition to their ground-state transitions. Extrinsic properties are related to dopants or defects, which usually create discrete electronic states in the band gap, and therefore influence both optical absorption and optical emission processes. Optical transitions in ZnO have been studied by a variety of experimental techniques such as optical absorption, transmission, reflection, photoreflection, spectroscopic ellipsometry, photoluminescence, cathodoluminescence and calorimetric spectroscopy.

Recently, the optical band gap energy of pure ZnO has been reported as its minimum energy gap is ~3.2 eV at room temperature and ~3.44 eV at 4 K [35,36]. From the materials point of view, ZnO could be apply for optoelectronics device such as light emitting diodes and laser diodes if n-and reproducible p-type materials are developed. On the other important properties of ZnO are dielectric constant and refractive index dispersion. The wurtzite ZnO lacks cubic symmetry and therefore has anisotropic optical properties. The anisotropy results in uniaxial birefringence show two different refractive indices for polarization parallel (n_o, ordinary) and perpendicular (n_e, extraordinary) to the c-axis. Hu *et al.* [62] used optical transmission to measure the optical functions of ZnO thin films prepared by PLD on SiO_2 substrates. The ordinary refractive indices deduced from transmittance oscillations were 0.02-0.03 lower than the bulk ZnO crystal data [63]. The existence of grain boundaries in the films was assumed to be the source for this difference. Additionally, the measurement technique introduced a considerably large error resulting in large variations in the data. The best fits for the ordinary index using the three-term Cauchy equation

This material is reserved for educational use only, not allowed for commercial use.
Forbidden to modify the content, and cite the document when use.

$$n(\lambda) = A + \frac{B}{\lambda^2} + \frac{C}{\lambda^4}, \tag{3.12}$$

produced parameters of A = 1.9281, B = -1.1157x10^{-5} μm^2 and C = 5.9696x10^{-3} μm^4, whereas the bulk ZnO crystal [17] was best characterized by A = 1.9436, B =-1.9714x10^{-5} μm^2, and C = 7.0918x10^{-3} μm^4.

3.4 Zinc oxynitride (ZnON)

Zinc oxide (ZnO) films are key materials in many different fields of science and technology. Their optical and structural properties make them excellent candidates for optical and optoelectronic applications. In term of new functional materials research, various zinc compounds are actively investigated because of their significant properties. For example, impurity doped ZnO is a promising material for transparent, conductive films because of its high transparency in the visible range and high electron conductivity. Recently, zinc ternary oxides such as Zn-In-O and Zn-In-Sn-O systems have drawn much attention as new materials for transparent and conductive films [64,65]. However, the Zn-O-N system has been scarcely studied. Zn_3N_2 has been determined to be an n-type semiconductor with direct gap of 1.23 eV [66]. On the other hand, the optical band gap (E_{opt}) of ZnO is determined to be around 3.2 eV at RT. We can, therefore, expect to alter the optical band gap from 1.23 to 3.2 eV by varying the composition of N into ZnO films. Nitrogen not only found to incorporate into ZnO for varying the optical band gap energy but also exhibited a good candidate for p-type dopant in ZnO as well.

In particular, ZnON has been demonstrated to be an optically functional material, in which the optical band gap can be tuned within a broad energy range by controlling the nitrogen doping level [67]. ZnO is well known as a photocatalyst with high activity. It is, however, necessary to irradiate the ultra-violet rays that have higher energy than E_{opt} of ZnO to make ZnO chemically active. Hence, a material that can act in the visible range is required to use the sunlight more efficiently. Zn O N films are promising for this purpose. ZnON thin films may be fabricated by various techniques such as ultrasonic spray pyrolysis, metal-organic chemical vapour deposition (MOCVD), plasma immersion ion implantation (PIII), and reactive rf magnetron sputtering [68-71]. Plasma sputtering is one of the most promising techniques for the Zn-O-N films because of its capability for large-area deposition, low-temperature processing, and controllable nitrogen incorporation into the films.

This material is reserved for educational use only, not allowed for commercial use.
Forbidden to modify the content, and cite the document when use.

3.4.1 Nitrogen and other potential dopant sources

By success with ZnSe, nitrogen has been explored for p-type doping of II-VI semiconductors [72,73]. A number of groups have expended a good deal of effort in an attempt to realize p-type ZnO using nitrogen as a possible shallow acceptor dopant. Various types of nitrogen sources including N_2, NO, N_2O, NH_3 and Zn_3N_2 have been used depending on the growth technique.

Based on the first principles Yan *et al.* [74] proposed that the nitric oxide (NO) gas without an ECR plasma source is more efficient as a N source than N_2O or N_2. The model indicated that the defect formation energy of N on oxygen site (N_O) from NO should be lower than that from N_2O. As shown in Figure 3.10, the formation energy of N_O is negative under Zn-rich conditions, implying that no additional energy is required for N_O formation, while the formation energy of N_O from N_2 is positive, suggesting that additional energy is needed, such as plasma or high temperature. Even though the formation energy of N_O from N_2O is negative, the energy is much larger than that from NO. Therefore, it was suggested that NO molecules can be incorporated spontaneously to form N_O defects in ZnO.

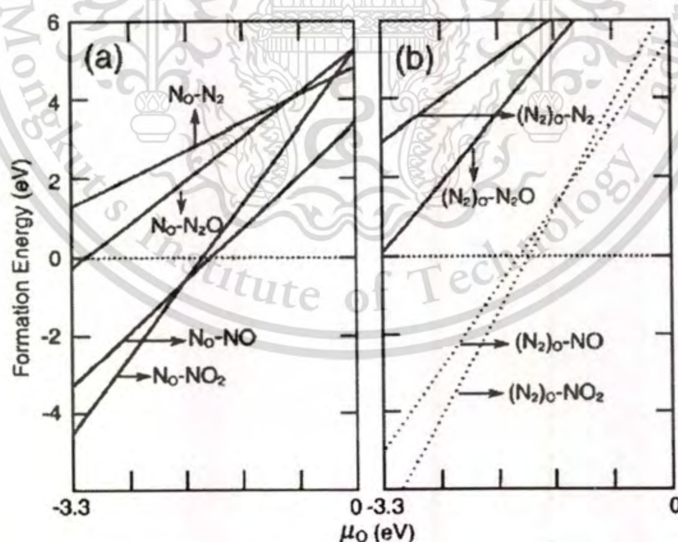

Fig. 3.10 (a) Calculated formation energies of N_O as functions of the O chemical potential formed by atomic N (stripped off a N_2 or a N_2O molecule), NO, or NO_2 molecule. μ_O= -3.3 is the Zn-rich limit condition and μ_O = 0 is the O-rich limit condition. (b) Calculated formation energies of a $(N_2)_O$ as functions of the O chemical potential for the defects formed by N_2, N_2O, NO and NO_2 molecules [74].

This material is reserved for educational use only, not allowed for commercial use.
Forbidden to modify the content, and cite the document when use.

As the result above, the solubility of nitrogen in ZnO is low and N from NO is more efficiently incorporated into ZnO than that from N_2. However, a different approach for growing nitrogen doped ZnO films was reported by Ma *et al.* [75]. ZnO in p-type was obtained after thermal annealing of zinc oxynitride (ZnON) alloy films deposited by rf reactive magnetron sputtering. The samples were grown at a relatively low substrate temperature of 200 °C compared to others [76,77] and were subjected to post-growth thermal annealing, resulting in the transformation from ZnON alloy to ZnO. In this case, annealing at a temperature of 600 °C led to p-type behavior of the films. Further increase of the annealing temperature to 1000 °C in oxygen ambient eliminated all the N dopants and replaced them by O even though the crystalline quality was improved. Results indicated that there is a tradeoff between N-doping efficiency and crystalline quality.

3.4.2 Zinc oxynitride crystal structure

Recently, Yamamoto and Katayama-Yoshida [78,79] proposed the co-doping method to solve the unipolarity in ZnO based on ab initio electronic band structure calculations. It was reported that the effects of Zn_i on the incorporation of N and a change in the Madelung energy in ZnO. It can be assume that the excess Zn incorporated would form interstitial Zn (Zn_i) in ZnO crystals. The reduction of the metal ions, Zn, leaves extra electrons in ZnO. In other words, the Zn locates as lower-valent ions in interstitial positions, which ZnO:Zn_i behaves n-type. From this viewpoint, the crystal structure of ZnO codoped with 2N and Zn_i (ZnO:2N, Zn_i) and ZnO doped 2N (ZnO:2N) which were determined using ab initio electronic band structure calculations under the condition of the minimization of the total energy. The crystal structure of ZnO:2N, Zn_i shown in Fig. 3.11(a) and ZnO:2N shown in Fig. 3.11(b). For Zn_i-free ZnO in Fig. 3.11(b), it found strong repulsive interactions between the two N acceptors, as a result, the N to N distant is the longest in the supercell model structure. On the other hand, Fig. 3.11(a) for ZnO:2N, Zn_i shows that the formation of the complex including N-Zn_i-N, which occupy nearest-neighbour sites, is energetically favourable. It indicates that the growth technique using excess Zn enhances the incorporation of N species into ZnO crystals. Considering that the above complex behaves not acceptor but neutral, it must control a partial pressure of N gas in such a way that the complex including N-Zn-N-N- or a chain-like complex, such as N-Zn-N. . .N, which occupy more distant sites from the rest of the complex will be formed. In such a case, codoping using N and excess Zn as reactive donor codopant may cause a problem of reproducibility. The reason is that the

This material is reserved for educational use only, not allowed for commercial use.

Forbidden to modify the content, and cite the document when use.

calculations show a 13.33 eV increase in the Madelung energy for intrinsic ZnO with the complex, N-Zn_i-N, compared with that for undoped ZnO with stoichiometry.

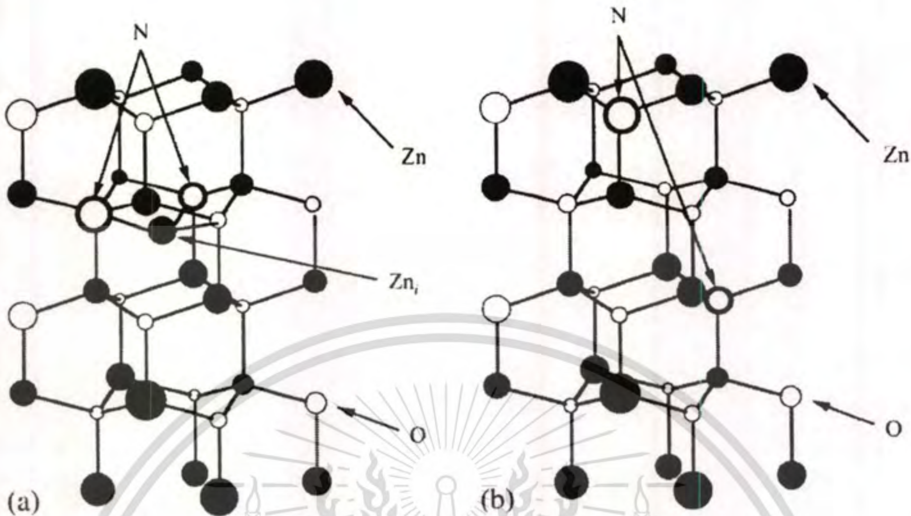

Fig. 3.11 Crystal structure of ZnO (a) codoped with 2N and Zn_i, and (b) doped with 2N [78].

3.5 Chapter summary

Large band gap II-VI semiconductor as ZnO have attracted much attention recently due to its properties for the use in optoelectronic devices. Owing to its direct wide band gap (E_g ~3.3 eV at 300K). Oxynitrides are another group of materials of intrinsic and technological importance. Metal oxynitride films have received considerable attention due to their unexpected and interesting properties. The presence of nitrogen in oxide films or the presence of oxygen in nitride films enables the preparation of a range of functional materials with technological importance.

Zinc oxynitride (ZnON) is a relatively new ceramic material which has distinct advantages over zinc oxide. ZnON can be fabricated to a thin film, fully dense isotropic and transparent polycrystalline material with an optically transparency in UV to near IR upon N-incorporations. Further important properties are piezoelectric effect, high mechanical stability, and high temperature stability. The ZnON thin films were produced by rf magnetron sputtering with reactive gas-timing of nitrogen and argon atmosphere. In expectation, the desired film properties are focusing on the optical band gap tailoring by nitrogen incorporated into films. Due to nitrogen incorporation, the structural, electrical and optical properties of ZnON were investigated.

This material is reserved for educational use only, not allowed for commercial use.
Forbidden to modify the content, and cite the document when use.

References:

[1] "**The Wurtzite (B4) Structure**", vol. 2005, pp.1, 10/21. [Online]. Available: http://cstwww. nrl.navy.mil/lattice/struk.picts/b4.s.png. 2001.

[2] F. Oba, S. R. Nishitani, H. Adachi, I. Tanaka, I. Tanaka, M. Kohyama, and S. Tanaka, "*Ab initio* Study of Symmetric Tilt Boundaries in ZnO", **Phys. Rev. B**, vol. 63, 2001, pp. 045410

[3] C. H. Park, S. B. Zhang and S. H. Wei, "Origin of P-type Doping Difficulty in ZnO: The Impurity Perspective", **Phys. Rev. B**, vol. 66, 2002, pp. 073202.

[4] S. J. Pearton, D. P. Norton, K. Ip, Y.W. Heo and T. Steiner, "Recent Progress in Processing and Properties of ZnO", **Prog. Mater. Sci.**, vol. 50, 2005, pp. 293-340.

[5] V. Vaithianathan, B. T. Lee and S. S. Kim, "Pulsed Laser Deposited P-type ZnO Films with Phosphorus Doping", **J. Appl. Phys.**, vol. 98, 2005, pp. 043519.

[6] G. Braunstein, A. Muraviev, H. Saxena, N. Dhere, V. Richter and R. Kalish, "P-type Doping of Zinc Oxide by Arsenic Ion Implantation", **Appl. Phys. Lett**., vol. 87, 2005, pp. 192103.

[7] F. X. Xiu, Z. Yang, L. J. Mandalapu, D. T. Zhao, J. L. Liu and W. P. Beyermann, "Highmobility Sb-doped P-type ZnO by Molecular-beam Epitaxy", **Appl. Phys. Lett**., vol. 87, 2005, pp. 152101.

[8] Y. J. Zeng, Z. Z. Ye, W. Z. Xu, L. L. Chen, D. Y. Li, L. P. Zhu, B. H. Zhao and Y. L. Hu, "Realization of P-type ZnO Films Via Monodoping of Li Acceptor", **J. Cryst. Growth**, vol. 283, 2005, pp. 180-184.

[9] J. G. Lu, L. P. Zhu, Z. Z. Ye, F. Zhuge, B. H. Zhao, J. Y. Huang, L. Wang and J. Yuan, "P-type ZnO Films by Codoping of Nitrogen and Aluminum and ZnO based p-n Homojunctions", **J. Cryst. Growth**, vol. 283, 2005, pp. 413-417.

[10] H. L. Porter, A. L. Cai, J. F. Muth and J. Narayan, "Enhanced Photoconductivity of ZnO Films Codoped with Nitrogen and Tellurium", **Appl. Phys. Lett**. vol. 86, 2005, pp. 211918.

[11] J. R. Duclere, M. Novotny, R. O'Haire, A. Meaney, E. McGlynn, M. O. Henry, and J. P. Mosnier, "Properties of Li-, P- and N-doped ZnO Thin Films Prepared by Pulsed Laser Deposition", **Superlattices and Microstructures**, vol. 38, 2005, pp. 397-405.

This material is reserved for educational use only, not allowed for commercial use.
Forbidden to modify the content, and cite the document when use.

[12] Y. R. Ryu, S. Zhu, D. C. Look, J. M. Wrobel, H. M. Jeong, and H. W. White, "Synthesis of P-type ZnO Films", **J. Cryst. Growth**, vol. 216, 2000, pp. 330-334.

[13] A. Hachigo, H. Nakahata, K. Higaki, S. Fujii, and S. Shikata, "Heteroepitaxial Growth of ZnO Films on Diamond (111) Plane by Magnetron Sputtering", **Appl. Phys. Lett.**, vol. 65, 1994, pp. 2556-2558.

[14] J. G. E. Gardeniers, Z. M. Rittersma, and G. J. Burger, "Preferred Orientation and Piezoelectricity in Sputtered ZnO Films", **J. Appl. Phys.**, vol. 83, 1998, pp. 7844-7854.

[15] G. Galli and J. E. Coker, "Epitaxial ZnO on Sapphire", **Appl. Phys. Lett.**, vol. 16, 1970, pp. 439-441.

[16] K.-K. Kim, J.-H. Song, H.-J. Jung, W.-K. Choi, S.-J. Park and J.-H. Song, "The Grain Size Effects on the Photoluminescence of ZnO/α-Al_2O_3 Grown by Radio-frequency Magnetron Sputtering", **J. Appl. Phys.**, vol. 87, 2000, pp. 3573-3575.

[17] P. Fons, K. Iwata, S. Niki, A. Yamada, and K. Matsubara, "Growth of High-quality Epitaxial ZnO Films on α-Al_2O_3", **J. Cryst. Growth**, vol. 201-202, 1999, pp. 627-632.

[18] Y. Chen, D. M. Bagnall, H.-J. Koh, K.-T. Park, K. Hiraga, Z.-Q. Zhu, and T. Yao, "Plasma Assisted Molecular Beam Epitaxy of ZnO on c-plane sapphire: Growth and Characterization", **J. Appl. Phys.**, vol. 84, 1998, pp. 3912-3918.

[19] R. D. Vispute et al., "Heteroepitaxy of ZnO on GaN and Its Implications for Fabrication of Hybrid Optoelectronic Devices", **Appl. Phys. Lett.**, vol. 73, 1998, pp. 348-350.

[20] S. Muthukumar, C.R. Gorla, N.W. Emanetoglu, S. Liang, and Y. Lu, "Control of Morphology and Orientation of ZnO Thin Films Grown on SiO_2/Si substrates", **J. Cryst. Growth**, vol. 225, 2001, pp. 197-201.

[21] A. V. Singh, R. M. Mehra, N. Buthrath, A. Wakahara, and A. Yoshida, "Highly Conductive and Transparent Aluminum-doped Zinc Oxide Thin Films Prepared by Pulsed Laser Deposition in Oxygen Ambient", **J. Appl. Phys.** vol. 90, 2001, pp. 5661-5665.

[22] L. N. Dinh, M. A. Schildbach, M. Balooch, and W. McLean II, "Pulsed Laser Deposition of ZnO Nanocluster Films by Cu-vapor Laser", **J. Appl. Phys.**, vol. 86, 1999, pp. 1149-1152.

[23] H. B. Kang, K. Nakamura, S.-H. Lim, and D. Shindo, "Epitaxial Growth of ZnO Films on (0001) Sapphire at Low Temperatures by Electron Cyclotron Resonance-assisted

This material is reserved for educational use only, not allowed for commercial use.
Forbidden to modify the content, and cite the document when use.

Molecular Beam Epitaxy and Their Microstructure Characterizations", **Jpn. J. Appl. Phys.**, vol. 37, no. 3A, 1998, pp. 781-785.

[24] K. Sakurai, D. Iwata, S. Fujita, and S. Fujita, "Growth of ZnO by Molecular Beam Epitaxy Using NO_2 as Oxygen Source", **Jpn. J. Appl. Phys.**, vol. 38, no. 4B, 1999, pp. 2606-2608.

[25] N. Izyumskaya, V. Avrutin, W. Schoch, W. A. El-Shaer, F. Reuss, T. Gruber, and A. Waag, "Molecular Beam Epitaxy of High-quality ZnO Using Hydrogen Peroxide as an Oxidant", **J. Cryst. Growth**, vol. 269, 2004, pp. 356-361.

[26] Y. Ma, G. T. Du, S. R. Yang, Z. T. Li, B. J. Zhao, X. T. Yang, T. P. Yang, Y. T. Zhang, and D. L. Liu, "Control of Conductivity Type in Undoped ZnO Thin Films Grown by Metalorganic Vapor Phase Epitaxy", **J. Appl. Phys.**, vol. 95, 2004, pp. 6268-6272.

[27] M. Pan et al., "Metal-organic Chemical Vapor Deposition of ZnO", **J. Cryst. Growth**, vol. 287, 2006, pp. 688-693.

[28] F. T. J. Smith, "Metalorganic Chemical Vapor Deposition of Oriented ZnO Films Over Large Areas", **Appl. Phys. Lett.**, vol. 43, 1983, pp. 1108-1110.

[29] L. Wang, Y. Pu, W. Fang, J. Dai, Y. Chen, C. Mo, and F. Jiang, "High-quality ZnO Films Grown by Atmospheric Pressure Metal-organic Chemical Vapor Deposition", **J. Cryst. Growth**, vol. 283, 2005, pp. 87-92.

[30] J. Dai, H. Liu, W. Fang, L. Wang, Y. Pu, Y. Chen, and F. Jiang, "Atmospheric Pressure MOCVD Growth of High-quality ZnO Films on GaN/Al_2O_3 Templates", **J. Cryst. Growth**, vol. 283, 2005, pp. 93-99.

[31] N. Mehan, V. Gupta, K. Sreenivas, and A. Mansingh, "Effect of Annealing on Refractive Indices of Radio-frequency Magnetron Sputtered Waveguiding Zinc Oxide Films on Glass", **J. Appl. Phys.**, vol. 96, 2004, pp. 3134-3139.

[32] M. Kadota and M. Minakata, "Piezoelectric Properties of ZnO Films on Sapphire Substrate Deposited by an RF-Magnetron-Mode ECR Sputtering System", **Jpn. J. Appl. Phys.**, vol. 37, no. 5B, 1998, pp. 2923-2926.

[33] M. Kadota, T. Miura, and M. Minakata, "Piezoelectric and Optical Properties of ZnO Films Deposited by an Electron-cyclotron-resonance Sputtering System", **J. Cryst. Growth,** vol. 237-239, 2002, pp. 523-527.

[34] K. Wasa and S. Hayekawa, **Handbook of Sputter Deposition Technology, Principles, Technology and Application**. Noyes Publication, 1992.

This material is reserved for educational use only, not allowed for commercial use.
Forbidden to modify the content, and cite the document when use.

[35] L. I. Berger, **Semiconductor Materials.** Boca Raton: CRC Press, 1997.

[36] X. Sun and H. Kwok, "Optical Properties of Epitaxially Grown Zinc Oxide Films on Sapphire by Pulsed Laser Deposition", **J. Appl. Phys.**, vol. 86, 1999, pp. 408-411.

[37] S.Zh. Karazhanov, P. Ravindran, A. Kjekhus, H. Fjellvag, U. Grossner, and B.G. Svensson, "Electronic Structure and Band Parameters for ZnX (X = O, S, Se, Te)", **J. Cryst. Growth**, vol. 287, 2006, 162-168.

[38] W. Göpel, J. Pollmann, I. Ivanov, and B. Reihl, "Angle-resolved Photoemission From Polar and Nonpolar Zinc Oxide Surfaces", **Phys. Rev B**, vol. 26, 1982, pp. 3144-3150.

[39] T.-C. Chiang, R. Ludeke, M. Aono, G. Landgren, F. J. Himpsel and D. E. Eastman, "Angle-resolved Photoemission Studies of GaAs(100) Surfaces Grown by Molecular-beam epitaxy", **Phys. Rev B**, vol. 26, 1982, pp. 3144-3150.

[40] U. Rössler, "Energy Bands of Hexagonal II-VI Semiconductors", **Phys. Rev.**, vol. 184, 1969, pp. 733-738.

[41] M. Goano, F. Bertazzi, M. Penna and E. Bellotti, "Electronic Structure of Wurtzite ZnO: Nonlocal Pseudopotential and *ab initio* calculations", **J. Appl. Phys.**, vol. 102, 2007, pp. 083709.

[42] J. R. Chelikowsky, "An Oxygen Pseudopotential: Application to the Electronic Structure of ZnO", **Solid State Commun.**, vol. 22, 1977, pp. 351-354.

[43] I. Ivanov and J. Pollmann, "Electronics Structure of Ideal and Relaxed Surfaces of ZnO: A Prototype Ionic Wurtzite Semiconductor and Its Surface Properties", **Phys. Rev. B**, vol. 24, 1981, pp. 7275-7296.

[44] D. H. Lee and J. D. Joannopoulos, "Renormalization Scheme for the Transfer-matrix Method and the Surfaces of Wurtzite ZnO", **Phys. Rev. B**, vol. 24, 1981, pp. 6899-6907.

[45] A. Polian, M. Grimsditch, and I. Grzegory, "Elastic Constants of Gallium Nitride", **J. Appl. Phys.**, vol. 79, 1996, pp. 3343-3346.

[46] T. B. Bateman, "Elastic Moduli of Single-Crystal Zinc Oxide", **J. Appl. Phys.**, vol. 33, 1962, pp. 3309-3342.

[47] A. Dal Corso, M. Posternak, R. Resta, and A. Baldereschi, "*Ab initio* Study of Piezoelectricity and Spontaneous Polarization in ZnO", **Phys. Rev. B**, vol. 50, 1994, pp. 10715-10721.

[48] J. F. Nye, **Physical Properties of Crystals**, Clarendon: Oxford, 1975.

This material is reserved for educational use only, not allowed for commercial use.
Forbidden to modify the content, and cite the document when use.

[49] F. Bernardini, V. Fiorentini, and D. Vanderbilt, "Spontaneous Polarization and Piezoelectric Constants of III-V Nitrides", **Phys. Rev. B**, vol. 56, 1997, pp. R10024-R10027.

[50] N. A. Hill and U. Waghmare, "First-principles Study of Strain-electronic Interplay in ZnO: Stress and Temperature Dependence of the Piezoelectric Constants", **Phys. Rev. B**, vol. 62, 2000, pp. 8802-8810.

[51] M. Catti, Y. Noel, and R. Dovesi, "Full Piezoelectric Tensors of Wurtzite and Zinc Blende ZnO and ZnS by First-principles Calculations", **J. Phys. Chem. Solids.**, vol. 64, 2003, pp. 2183-2190.

[52] Y. Noel, C. M. Zicovich-Wilson, B. Civalleri, Ph. D'Arco, and R. Dovesi, "Polarization Properties of ZnO and BeO: An *ab initio* Study Through the Berry Phase and Wannier Functions Approaches", **Phys. Rev. B**, vol. 65, 2001, pp. 014111.

[53] G. Carlotti, G. Socino, A. Petri, and E. Verona, "Acoustic Investigation of the Elastic Properties of ZnO Films", **Appl. Phys. Lett.**, vol. 51, 1987, pp. 1889-1891.

[54] I. B. Kobiakov, "Elastic, Piezoelectric and Dielectric Properties of ZnO and CdS Single Crystals in a Wide Range of Temperatures", **Solid State Commun.**, vol. 35, 1980, pp. 305-310.

[55] B. Yates, R. F. Cooper, and M. M. Kreitman, "Low-Temperature Thermal Expansion of Zinc Oxide. Vibrations in Zinc Oxide and Sphalerite Zinc Sulfide", **Phys. Rev. B**, **vol. 4,** 1971, pp. 1314-1323.

[56] M.-Y. Han and J.-H. Jou, "Determination of the Mechanical Properties of R.f.-magnetron-puttered Zinc Oxide Thin Films on Substrates", **Thin Solid Films**, vol. 260, 1995, pp. 58-64.

[57] F. Z. Aoumeur, Kh. Benkabou, and B. Belgoumène, "Structural and Dynamical Properties of ZnO in Zinc-blende and Rocksalt Phases", **Physica B**, vol. 337, 2003, pp. 292-297.

[58] C. M. Bhandari and D. M. Rowe, **Thermal Conduction in Semiconductors**., New York: Wiley, 1988.

[59] C. Kittel, **Introduction to Solid State Physics**. 6th ed., New York: Wiley, 1986.

[60] D. I. Florescu, V. M. Asnin, F. H. Pollak, R. J. Molnar, and C. E. C. Wood, "High Spatial Resolution Thermal Conductivity and Raman Spectroscopy Investigation of Hydride

This material is reserved for educational use only, not allowed for commercial use.
Forbidden to modify the content, and cite the document when use.

Vapor Phase Epitaxy Grown *n*-GaN/Sapphire (0001): Doping Dependence", **J. Appl. Phys.**, vol. 88, 2000, pp. 3295-3298.

[61] W. N. Lawless and T. K. Gupta, "Thermal Properties of Pure and Varistor ZnO at Low Temperatures", **J. Appl. Phys.**, vol. 60, 1986, pp. 607-610.

[62] W. S. Hu, Z. G. Liu, J. Sun, S. N. Zhu, Q. Q. Xu, D. Feng, and Z. M. Ji, "Optical Properties of Pulsed Laser Deposited ZnO Thin Films" **J. Phys. Chem. Solids**, vol. 58, 1997, pp. 853-857.

[63] W. L. Bond, "Measurement of the Refractive Indices of Several Crystals", **J. Appl. Phys.**, vol. 36, 1965, pp. 1674-1677.

[64] J. M. Phillips, R. J. Cava, G. A. Thomas, S. A. Carter, J. Kwo, T. Siegrist, J. J. Krajewski, J. H. Marshall, W. F. Peck, Jr., and D. H. Rapkine, "Zinc-Indium-Oxide: A High Conductivity Transparent Conducting Oxide", **Appl. Phys. Lett.**, vol. 67, 1995, pp. 2246-2248.

[65] T. Minami, T. Kakumu, K. Shimokawa, and S. Takata, "New Transparent Conducting ZnO-In_2O_3-SnO_2 Thin Films Prepared by Magnetron Sputtering", **Thin Solid Films**, vol. 317, 1998, pp. 318-321.

[66] M. Futsuhara, K. Yoshioka, and O. Takai, "Structural, Electrical and Optical Properties of Zinc Nitride Thin Films Prepared by Reactive RF Magnetron Sputtering", **Thin Solid Films**, vol. 322, 1998, pp. 274-281.

[67] M. Futsuhara, K. Yoshioka, and O. Takai, "Optical Properties of Zinc Oxynitride Thin Films", Thin **Solid Films**, vol. 317, 1998, pp. 322-325.

[68] J. M. Bian, X. M. Li, X. D. Gao, W. D. Yu, and L. D. Chen, "Deposition and Electrical Properties of N–In Codoped *p*-type ZnO Films by Ultrasonic Spray Pyrolysis", **Appl. Phys. Lett.**, vol. 84, 2004, pp. 541-543.

[69] C. L. Perkins, S.-H. Lee, X. Li, S. E. Asher, and T. J. Coutts, "Identification of Nitrogen Chemical States in N-doped ZnO via X-ray Photoelectron Spectroscopy", **J. Appl. Phys.**, vol. 97, 2005, pp. 034907.

[70] Y. F. Mei, R. Fu, G. G. Siu, K. W. Wong, P. K. Chu, R. S. Wang, and H. C. Ong, "Nitrogen Binding Behavior in ZnO Films with Time-resolved Cathodoluminescence", **Appl. Surf. Sci.**, vol. 252, 2006, pp. 8131-8134.

This material is reserved for educational use only, not allowed for commercial use.
Forbidden to modify the content, and cite the document when use.

[71] M.-L. Tu, Y.-K. Su, and C.-Y. Ma, "Nitrogen-doped *p*-type ZnO Films Prepared from Nitrogen Gas Radio-frequency Magnetron Sputtering", **J. Appl. Phys.**, vol. 100, 2006, pp. 053705.

[72] R. M. Park, M. B. Troffer, C. M. Rouleau, J. M. DePuydt, and M. A. Hasse, "*p*-type ZnSe by Nitrogen Atom Beam Doping during Molecular Beam Epitaxial Growth", **Appl. Phys. Lett.**, vol. 57, 1990, pp. 2127-2129.

[73] L. Svob, C. Thiandoume, A. Lusson, M. Bouanani, Y. Marfaing, and O. Gorochov, "p-type Doping with N and Li Acceptors of ZnS Grown by Metalorganic Vapor Phase Epitaxy", **Appl. Phys. Lett.**, vol. 76, 2000, pp. 1695-1697.

[74] Y. Yan, S. B. Zhang, and S. T. Pantelides, "Control of Doping by Impurity Chemical Potentials: Predictions for p-Type ZnO", **Phys. Rev. Lett.**, vol. 86, 2001, pp. 5723-5726.

[75] J. G. Ma, Y. C. Liu, R. Mu, J. Y. Zhang, Y. M. Lu, D. Z. Shen, and X. W. Fan, "Method of Control of Nitrogen Content in ZnO Films: Structural and Photoluminescence Properties", **J. Vac. Sci. Technol. B**, vol. 22, 2004, pp. 94-98.

[76] Z.-Z. Ye, J.-G. Lu, H.-H. Chen, Y.-Z. Zhang, L. Wang, B.-H. Zhao and J.-Y. Huang, "Preparation and Characteristics of *p*-type ZnO Films by DC Reactive Magnetron Sputtering", **J. Cryst. Growth**, vol. 253, 2003, pp. 258-264.

[77] J. Lu, Y. Zhang, Z. Ye, L. Wang, B. Zhao, and J. Huang, "*p*-type ZnO Films Deposited by DC Reactive Magnetron Sputtering at Different Ammonia Concentrations", **Mater. Lett.**, vol. 57, 2003, pp. 3311-3314.

[78] T. Yamamoto and H. Katayama-Yoshida, "Physics and Control of Valence States in ZnO by Codoping Method", **Physica B**, vol. 302-303, 2001, pp. 155-162.

[79] T. Yamamoto, "Codoping for the fabrication of *p*-type ZnO", **Thin Solid Films**, vol. 420-421, 2002, pp. 100-106.

This material is reserved for educational use only, not allowed for commercial use.
Forbidden to modify the content, and cite the document when use.

CHAPTER 4

REACTIVE GAS-TIMING RF MAGNETRON SPUTTERING

4.1 Introduction

The process of sputtering may be defined as the ejection of particles from a condensed-matter target due to the impingement of energetic projectile particles. The sputter deposition process involves a target and plasma of a neutral working such as argon. The target material transferred to the vapor phase by positive ion bombardment from the plasma via momentum transfer from the ions to the target atoms. The most important parameters controlling the growth and the properties of the films by sputter deposition processes are target voltage and current, reactant partial pressure and flow rate, and substrate temperature and substrate bias. For example, in conventional diode sputtering using either dc or rf, the deposition rate is dependent on target voltage and current as well as on pressure. However, these same parameters also determine the average energy of the secondary electrons, which in turn influences the floating potential and hence the bombardment of the growing film.

4.2 Background of sputtering system

4.2.1 RF sputtering

In the early, the Dc diode sputtering was used with the conducting targets. Unfortunately, Dc sputtering methods cannot be used to sputter nonconducting targets because of charge accumulation at the target surface. This difficulty can be overcome by using radio frequency (rf) sputtering. A single rf sputtering apparatus can be used to deposit electrically conducting, semiconducting, and insulating. Consequently, rf sputtering has found wide application in the electronics industry. Nonconducting and semiconducting materials which have been deposited by rf sputtering include elemental semiconductors: Si and Ge; III-V compounds: GaAs, GaSb, GaN, and AlN; II-VI compounds: CdSe and CdS; IV-VI compounds: PbTe; refractory semiconductors: SiC; ferroelectric compounds: $Bi_4Ti_3O_{12}$; Metals Oxides: In_2O_3, SiO_2, Al_2O_3, Ta_2O_5, Y_2O_3, TiO_2, ZrO_2, SnO_2, PtO, Bi_2O_3, ZnO and CdO. Often several targets are placed within a common vacuum enclosure so that multiplier coating can be deposited without breaking vacuum [1].

This material is reserved for educational use only, not allowed for commercial use.
Forbidden to modify the content, and cite the document when use.

The usefulness of rf methods for sputtering nonconducting materials is based upon the fact that a self-bias voltage, negative with respect to the plasma floating potential, develops on any surface that is coupled to a glow discharge. The basis for this potential, which forms as a consequence of the difference in mobility between electrons and ions, illustrated schematically in Fig. 4.1. The current-voltage characteristic for an electrode immersed in plasma is given in Fig. 4.1a. The floating potential is negative relative to the plasma potential by an amount that depends upon the gas species and plasma electron energy distribution function, but is typically -20 to -50 V and therefore too low to produce significant sputtering of most materials. When an alternating voltage is applied to such an electrode, more electron current flows when the electrode is positive relative to the floating potential than ion current flows, and when the electrode is negative relative to the floating potential as shown in Fig. 4.1b.

Capacitive coupling requires that there be no dc current flow, so the net current to the electrode in each rf cycle must be zero. Accordingly, a negative bias must form such that the electron current on the positive side of the cycle becomes equal to the ion current on the negative side. The negative bias is approximately equal to half the peak-to-peak voltage of the rf signal and therefore can be made large enough to produce sputtering.

The behavior illustrated in Fig. 4.1 applies strictly to the case where the electrode is passive, which is not responsible for sustaining the plasma discharge. The planar diode shown schematically in Fig 4.2 is the most commonly used apparatus for rf sputtering. The electrodes sustain the discharge and therefore have slightly different current-voltage characteristics than the one shown in Fig. 4.1, particularly at negative voltages. However, the overall effect when an rf potential is superimposed on the I-V characteristic is essentially identical.

Figure 4.3 shows a schematic drawing of a typical rf planar-diode sputtering configuration in which a nonconducting target is placed over one electrode and substrate are placed on the other one. The electrodes reverse cathode-anode roles on each half cycle. The discharge is operated at a frequency that is sufficiently high that significant ion charge accumulation does not occur during the cycle time when an electrode is serving as a cathode. Frequency in the low MHz range is required. Most systems are operated at a frequency of 13.56 MHz, since this has been allocated by the Faderal Communications Commission (FCC) for industrial-scientific-medical purposes.

This material is reserved for educational use only, not allowed for commercial use.
Forbidden to modify the content, and cite the document when use.

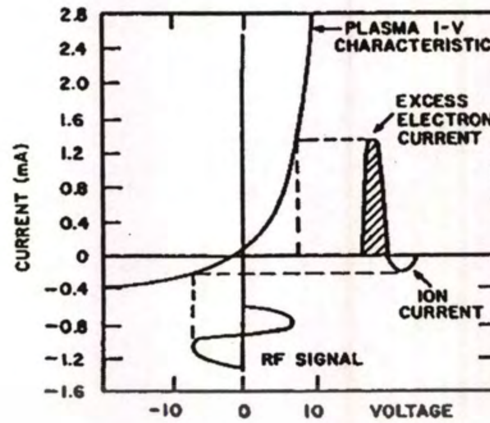

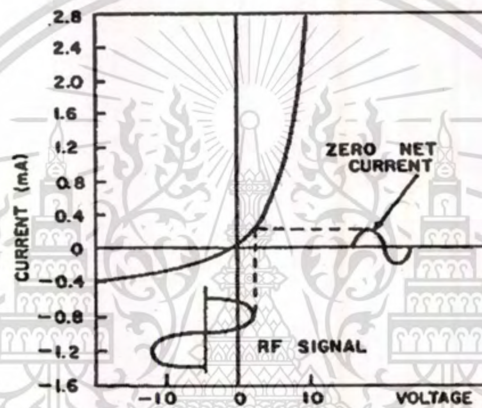

Fig. 4.1 Schematic illustration of the development of a negative bias when an rf potential is coupled to a probe immersed in a plasma [2].

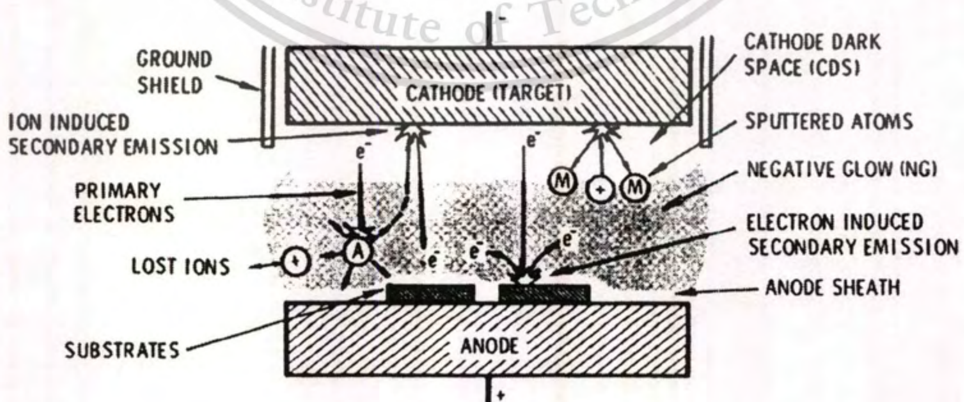

Fig. 4.2 Schematic representation of the plasma in the planar diode sputtering source [2].

This material is reserved for educational use only, not allowed for commercial use.
Forbidden to modify the content, and cite the document when use.

At MHz operating frequencies, massive ions can not follow the temporal variations in the applied potential. However, the electron can. Thus the cloud electrons in the negative glow plasma can be pictured as moving back and forth at the applied frequency in a sea of relatively stationary ions. As electron cloud approaches one electrode, it uncovers ions at the other electrode to form a positive ion sheath. This sheath takes up nearly the entire applied voltage, the same as in the dc case.

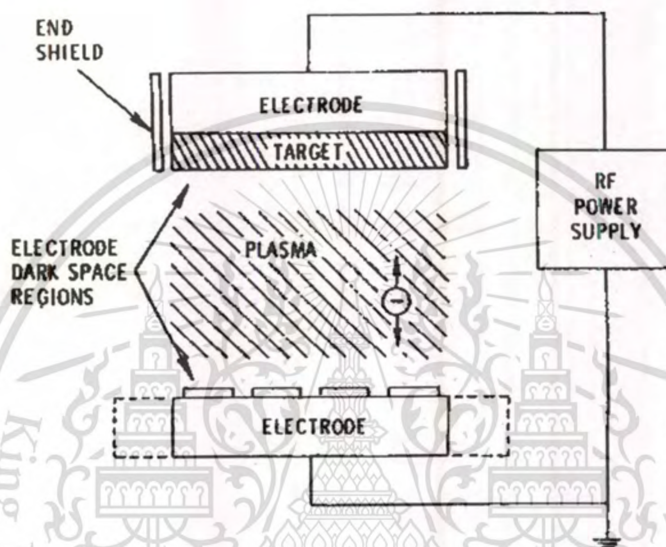

Fig. 4.3 Schematic drawing of a planar rf diode sputtering device [2].

A nonconducting target constitutes a capacitor in the electrical circuit between the electrodes. Thus there can be no dc component to the current flow. The total ion and electron charge flow to a given electrode during an rf cycle must balance to zero. However, a large electron current flows to a given electrode as the electron cloud makes a contact. Thus the electron cloud need approach a given electrode for only a small fraction of a half cycle for purposes of supplying sufficient electrons to fulfill the anode requirement such as it is used to balance the entire ion flux to the cycle. Accordingly, in the steady state both electrodes develop a negative dc bias relative to the plasma potential, such that the electrodes approach or exceed the plasma potential (and become anodes) for only very short portions of their rf cycle as indicated in Fig. 4.4.

This material is reserved for educational use only, not allowed for commercial use.
Forbidden to modify the content, and cite the document when use.

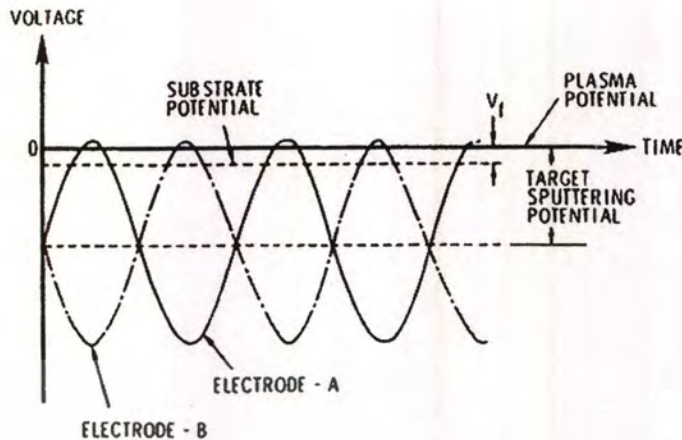

Fig. 4.4 Approximate representation of target voltage waveforms relative to the plasma potential for a balance rf system with two equal-area sputtering electrodes. V_f is the floating potential [2].

The motion of the ions, because of their inertia, can be thought of as responding to the dc potential and passing to both electrodes throughout the cycle. The electron cloud spends most of its time near the center position between the electrodes. Visually, the discharge appears a dc discharge with a cathode dark space over each electrode. Functionally, sputtering occurs continually at both electrodes.

The rf discharges in planar diode systems can be operated at considerably lower pressures than dc discharges. Typical operating pressures are 5 to 15 mTorr (1 Torr is equal to 1.33 mbar). There are two reasons: a reduction in the loss of primary electrons, and at high frequencies, an increase in the volume ionization efficiency. A fraction of lower-energy primary electrons are repelled from the electrode toward which they are accelerated and thus remain in the discharge longer to make additional ionizing collisions. In addition, electron can gain energy from the rf field by making in-phase collisions with gas atoms. That is, if an electron, accelerated in one direction during the given half-cycle, makes an elastic collision in which its direction is reversed near the end of the half-cycle, it maintains most of its velocity (due to the large mass mismatch between electron and ions) and will again be accelerated during the next half-cycle and thus have gained by energy during the complete cycle. The versatility of rf sputtering is not achieved without drawbacks. Implementation of the process is complicated. A typical circuit of single-ended rf discharge system is shown schematically in Fig. 4.5. It consists of an rf power supply, an inductive coupling to the load, and a matching network.

This material is reserved for educational use only, not allowed for commercial use.
Forbidden to modify the content, and cite the document when use.

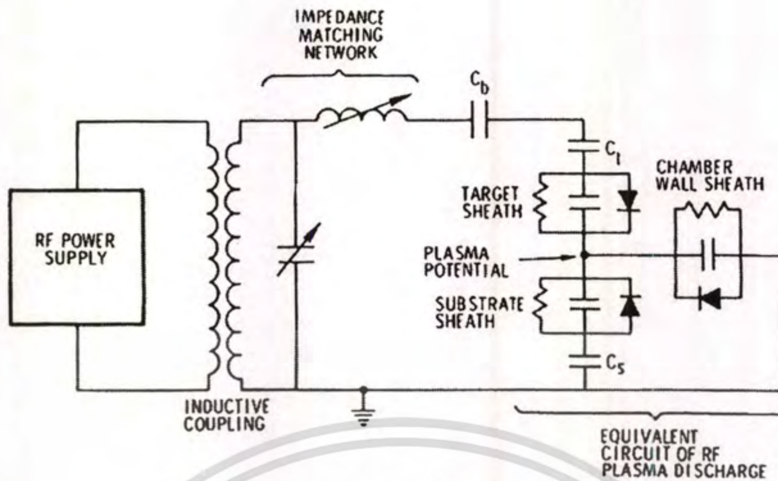

Fig. 4.5 Schematic circuit of single-ended rf discharge system including an equivalent circuit for the plasma discharge [2].

An equivalent circuit for an rf glow discharge is also shown in Fig. 4.5. The equivalent circuit assumes that both electrodes and chamber walls are in contact with the plasma, and that the impedance is dominated by the plasma sheaths. The sheath capacitances result from the charge separation across the dark space. These capacitors are shunted to the electrode surface by resistor to account for the ion current, and by diode to account for the high electron current that can flow from the plasma to an electrode that is biased positive relative to the plasma potential. The capacitor C_t accounts for capacitance of the target. C_b is a blocking capacitor that is added to make the system independent of variations in the target capacitance.

The rf current through the plasma is principally an electron current caused by the relative motion of the electron cloud. To the extent that there is no volume power transfer from the oscillating electrons to the gas, this current is out of phase with the applied voltage. The primary power transfer occurs via the relatively small ion and electron current component that are in phase with the voltage. Thus, in the equivalent circuit approximation, the power transfer to produce sputtering occurs as the ion currents pass through the sheath resistances. Efficient power transfer requires that the rf power supply operate into a resistive load. Therefore, a matching network is used to introduce inductance, and often capacitance, into the circuit in such a way that, in combination with the load, they form a resonant circuit. However, the power supply sees only the resistive component of the load, and the current passing from the power supply to the current circuit is in phase with the load and represents the power passing to the load. Many commercial

This material is reserved for educational use only, not allowed for commercial use.
Forbidden to modify the content, and cite the document when use.

sputtering sources monitor the reflected power from the load as an index of how effectively the matching network is adjusted. The reflected power should be minimized at the optimum state.

The ion current, and thus the sputtering rate at a given electrode, is determined by the average difference in potential between the electrode and the plasma. Thus it is useful to consider the plasma potential as a zero-point reference voltage in examining the performance of rf sputtering systems. The electrical character of rf sputtering systems can be classified in general as being either balanced or single-ended. In a balanced system, both electrodes are configured as identical sputtering targets and their potentials are 180° out of phase. The average sputtering voltage is about equal the peak-to-peak applied rf potential. The link center trap is placed at ground potential to stabilize the system and the chamber walls and substrates are connected to the center trap ground, as shown in Fig.4.6. Since this point is at zero potential relative to the rf voltage, no rf current will flow to these elements. Furthermore, because of the capacitance in series with each of electrodes, there is no dc current path from the plasma to the chamber wall and substrates and then back through the electrodes into the plasma. Thus a charge will develop on the capacitors such that the substrates float at a potential slightly negative with respect to the plasma, just like a floating electrode in dc plasma.

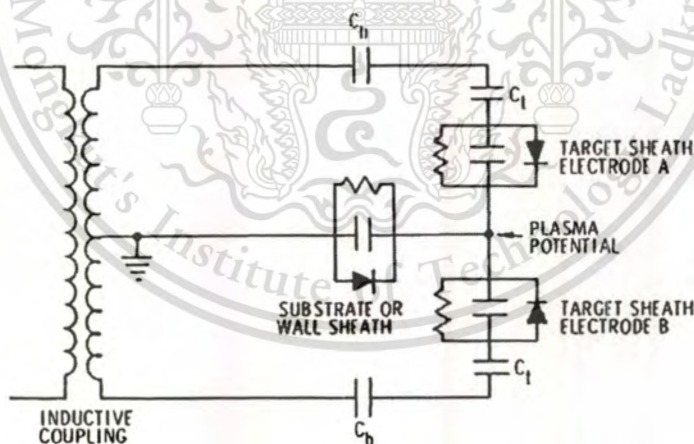

Fig. 4.6 Schematic representation of an equivalent circuit for a balanced rf system with two equal-area sputtering electrodes and center-trap ground.

In an unbalanced rf system, the electrode on which the substrates are placed is made considerably larger than the target electrode. This makes the sheath capacitance large, and the rf voltage drop across the substrate electrode small, as shown schematically in Fig. 4.7. The chamber and one side of the link are generally grounded as shown in Fig. 4.5. Again, the

This material is reserved for educational use only, not allowed for commercial use.
Forbidden to modify the content, and cite the document when use.

capacitance in both electrode circuits prevents a dc current flow to the chamber, and a negative bias develops relative to the plasma potential. A potential relative the plasma potential will exist on the substrates and chamber wall unless the substrate electrode area is large enough to reduce this potential to essentially zero and to move the rf balance point to the grounded end of the link. It is important that these voltage drops be small so that sputtering from uncontrolled surfaces does not introduce contamination into the coatings. Impedance may be added to the substrate electrode circuit so that the potential of this electrode relative to the plasma can be controlled for purposes of bias sputtering.

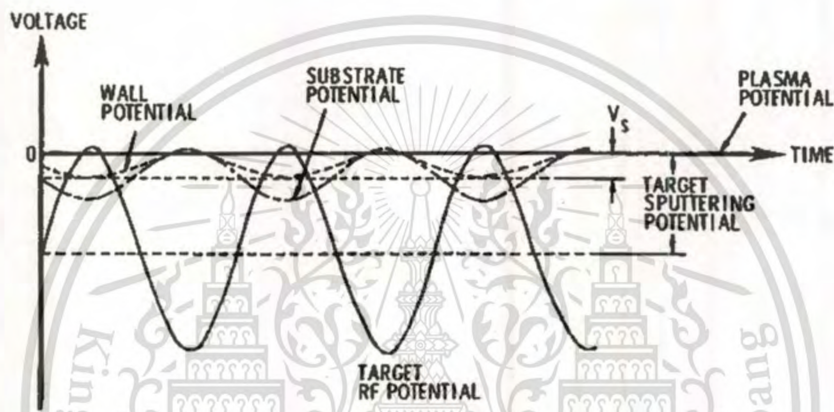

Fig. 4.7 Approximate representation of voltages as functions of time, relative to the plasma potential for a single-ended rf sputtering system in which the wall area is much larger than target area. V_s is the substrate ion bombardment potential [2].

The above discussion has been presented in the context of planar diode sputtering systems. Magnetron sputtering source can also be used for rf sputtering. Cylindrical-post, planar, and gun-type magnetrons have all been successfully operated with rf power. However, some problems are encountered. Magnetron sputtering technology is basically a dc concept. The cathodes are shaped such that, in concert with the magnetic field, they form electron traps with specific symmetry. Anodes are placed to collect electrons which diffuse out of the trap.

Effective double-ended rf magnetrons can be provided for some geometries. These configurations provide independent traps for both electrodes but allow magnetic coupling between them so that the electrons leaving one trap can diffuse freely to the vicinity of the others. However, most magnetron configurations must be operated with single-ended arrangements. The magnetic confinement produces gradients in the plasma density, so that special care is required to minimize the voltage and therefore the sputtering rate at the counter electrode. Furthermore, in the

This material is reserved for educational use only, not allowed for commercial use.
Forbidden to modify the content, and cite the document when use.

planar magnetron case, the current-density concentration under the plasma ring requires that the power level be limited to avoid cracking when using targets with low thermal conductivities. When magnetron sources are driven single-ended, they generally operate in hybrid modes with current voltage characteristics with are not representative of true magnetron behavior. Nevertheless, they provide deposition rates that are typically a factor of three greater than those achieved with rf planar diodes. Reduced electron bombardment and substrate heating are other advantages of magnetrons, as opposed to planar diodes, for rf sputtering.

4.2.2 Magnetrons

The lower limit of operating pressure in the planar-diode sputtering plasma as shown in Fig. 4.2 was imposed by the need for the beam electrons ejected from the cathode to undergo enough ionizing collisions with the gas to sustain the plasma before they reach the anode and are removed there. The magnetron has been a major advance in sputtering technology, and greatly improves upon this situation. Basically, it incorporates a crosswise magnetic field over the cathode, which traps the beam electrons in orbits in that location and thus greatly increases their path length before they finally escape to the anode by collisional scattering. Because the electron's travel path is now much longer than the electrode gap, the minimum pressure to sustain the plasma is much lower for the magnetron than for the planar-diode. The sputtered particles retain most of their kinetic energy upon reaching the substrate, so one obtains the beneficial effects of this energy on film structure. Also, the deposition rate is increased because of reduced scattering and redeposition of sputtered particles on the cathode. Finally, the increased efficiency of electron usage means that lower applied voltage (typically 500 V) is needed to sustain plasma of a given density, n_e, and that the voltage increases even less steeply with power than it does in the planar diode. Unfortunately, the magnetic field can not be made strong enough to deflect the problematic cathode-sheath voltage of a magnetron target is highly nonuniform across the surface. This pattern becomes imprinted on films deposited on stationary substrates when negative ions are affecting the film, because of the beam nature of these ions. Deposition-rate nonuniformity is less sharply imprinted, because the sputtered particles are neural and are emitted in more or less the broad cosine distribution. Both magnetrons and planar diodes can be operated using rf excitation when one needs to couple power through insulating targets.

Many configurations of magnetic field and cathode shape have been developed for various applications, but here shows magnetron operating principles with reference to the planar, circular

This material is reserved for educational use only, not allowed for commercial use.
Forbidden to modify the content, and cite the document when use.

configuration of Fig. 4.8. The target material to be sputtered in a disc 3 to 10 mm thick which is bonded for good thermal contact to a water-cooled Cu backing plate. Bonding is best done by soldering, although epoxy bonding or clamping onto a coating of thermally conductive vacuum grease can be employed instead at moderate plasma power densities. The cooling water is best deionized to prevent electrolytic corrosion between the electrically biased backing plate and the grounded water supply. The entire cathode assembly is floated off ground by a ceramic insulating ring which can also form part of vacuum wall by employing O-ring seals. The adjoining grounded metal vacuum wall then acts as the anode, although grounded shields are often added to confine the sputtered material. The anode is spaced closely enough to the edge of the cathode so that plasma cannot ignite between them. The crosswise magnetic field is established by a ring of bar magnets plus one central one, and these are connected on the back by an Fe field-return plate to complete the magnetic circuit and to confine the field. Using the strongest (Nd-Fe-B) magnets, the field over the target can approach 1 kilogauss or 0.1 Tesla.

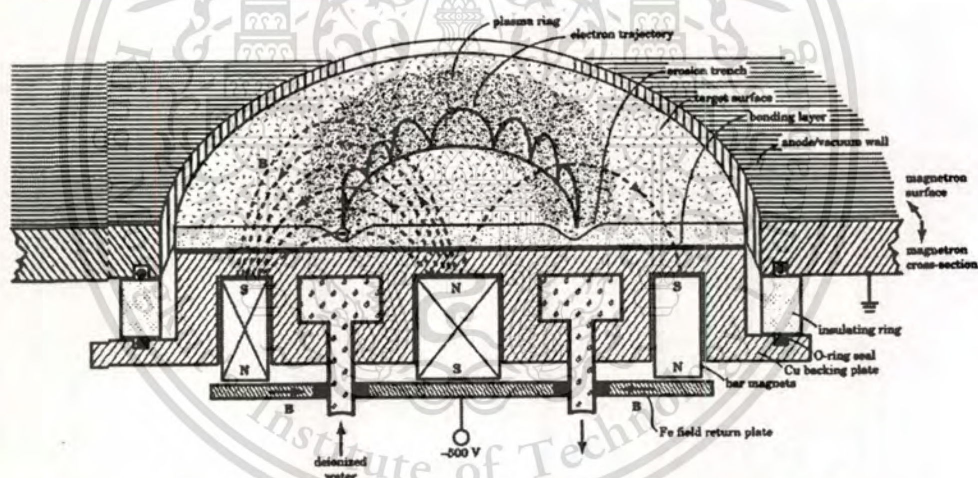

Fig. 4.8 Planar-magnetron structure and behavior. The electron-orbit radius is shown much larger than actual size for clarity [3].

Upon igniting the plasma, beam electrons emitted from the cathode become accelerated into the plasma by the cathode-sheath electric field (**E**) just as in the case of the planar-diode of Fig. 4.2. However, the presence of the magnetic fields (**B**) causes them to also curve into orbits as shown in Fig. 4.8 as the results of the Lorentz force. The orbit radius depends on **B** and electron velocity component perpendicular to **B**. At low pressure, the magnetron behaves as follows, with reference to Fig. 4.8. Electrons emitted from the target surface or created by ionization in the

This material is reserved for educational use only, not allowed for commercial use.
Forbidden to modify the content, and cite the document when use.

sheath field are accelerated vertically by **B**, so they eventually reverse direction and return toward the target, decelerating in **E** as they proceed until their direction is again reversed and the cycle repeats. The net motion is a clockwise drift around the circle of the target, known as **ExB** direction. Actually, the path is more complicated because of the collisions and because **E** decreases with distance from the target.

Localization of the plasma over the target by magnetron's transverse magnetic field results in a much lower plasma density over the substrate than in the case of the planar diode. This is desirable when the neutral sputtered particles alone carry sufficient kinetic energy to optimize film structure or when one wants to minimize the substrate heating that result from ion bombardment. In other cases, however, one may want to further increase film bombardment while retaining the low operating pressure of the magnetron. One way to do this is by unbalancing the magnets, as shown in Fig. 4.9. The central bar magnet has been replaced by a smaller one that cannot pull in all the field lines emanating from the magnets in the ring. Some of these lines then curve away toward the substrate. Since electrons traveling parallel to **B** are not acted on by **B**, they can escape along these field lines and toward the substrate, pulling positive ions along with them by ambipolar diffusion and thus increasing ion flux to the substrate. The bombardment energy may then be increased if necessary by negatively biasing the substrate.

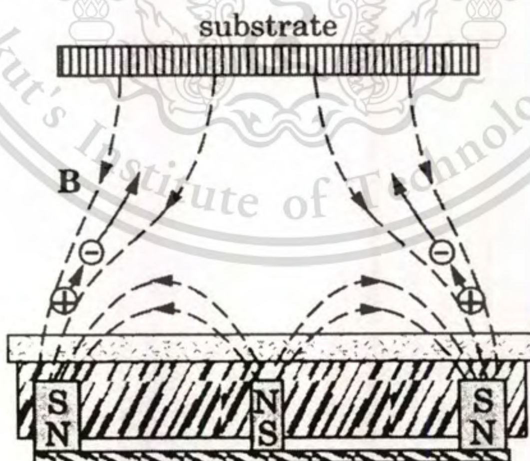

Fig. 4.9 Plasma flow toward the substrate along magnetic field (**B**) lines in an unbalanced magnetron [3].

This material is reserved for educational use only, not allowed for commercial use.
Forbidden to modify the content, and cite the document when use.

4.2.3 Reactive sputtering

Reactive Sputtering is a process in which a fraction of at least one of the coating species enters the deposition system in the gas phase [2]. The target is typically either a pure metal (or metal alloy) or a compound containing volatile species such as N in TiN, S in CdS, or O in VO_2, is provided entirely in the gas phase of N_2, H_2S, and O_2, respectively. There are three advantages of reactive sputtering: (i) compound can be formed using relatively easy-to-fabricate by metallic targets, (ii) insulating compounds can be deposited using dc power supplies, and (iii) films with graded compositions can be formed.

Although reactive sputtering is conceptually simple, it is in fact a complex and nonlinear process which involves many interdependent parameters. The presence of the reactive-gas at both the cathode surface and the substrate results in strong interactions of the reactive gas not only with the condensing material but also with the cathode surface, the so-called target poisoning. Reactions in the gas phase are ruled out for the same reasons that ions cannot be neutralized in the gas phase (there is no mechanism which can dissipate the heat of neutralization to conserve both momentum and energy in a two-body system, therefore it can only happen at a surface). These cathode reactions are seen to increase suddenly at some rate of reactive gas flow. If flow control of reactive gas is used, such reactions are marked by a change in the impedance of the operating plasma, an abrupt increase in the system pressure (or more precisely, in the reactive gas pressure), a drastic drop in the deposition rate and a change in the film from metal-rich to gas-rich (a change in the stoichiometry).

In the sputtering process with a reactive-gas/Ar mixture, the relationship between film properties and the reactive gas injection rate is generally very nonlinear. The condensing films can be considered as an additional pump for the reactive gas. The nonlinearity occurs because the sticking probability or getter-pump speed of the condensing coating depends in a complex way on its growth rate, composition, film structure, and temperature. The composition dependence is shown in Fig. 4.10 for N_2 incident on a growing Ti film [2]. Note that as the number of N_2 molecules adsorbed per Ti atom deposited approaches 0.5 (a stoichiometric TiN film), the sticking probability (α) drops by more than two orders of magnitude. The decrease in α occurs as the number of unoccupied surface adsorption sites decreases. For the simple case, when sputtering in an N_2/Ar mixture at low reactive-gas injection rates, virtually all of the injected gas can react with the film. Consequently, the nitrogen is largely removed from the working gas, and

This material is reserved for educational use only, not allowed for commercial use.
Forbidden to modify the content, and cite the document when use.

the cathode process becomes primarily one of simple Ar sputtering of a metal. The coatings deposited under such conditions are generally metallic in nature.

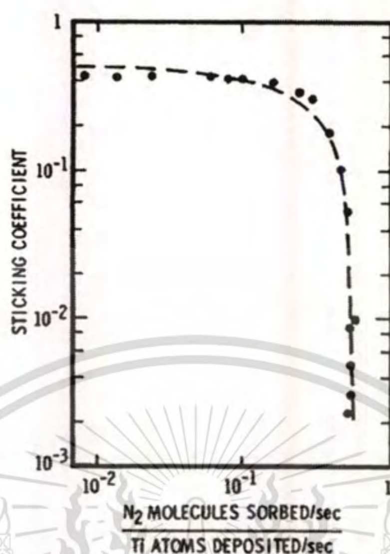

Fig. 4.10 Sticking coefficient of N_2 measured during the continuous deposition of Ti as a function of the ratio of the getter-pumped nitrogen flux to the Ti deposition flux [2].

As the reactive-gas injection rate approaches the requirement to produce a stoichiometric coating, there is an increase in the reactive-gas partial pressure in the sputtering system because of the reduced getter-pumping rate of the depositing coating. This change in the composition of the sputtering gas greatly changes the processes which occur at the cathode surface. The result is that, for most metal/reactive-gas combinations, the sputtering discharge undergoes a transition into a mode in which the metal sputtering rate, and therefore the reactive-compound deposition rate, is reduced. The cathode surface reactions in this mode produce an energetic flux of highly reactive gas atoms and molecular fractions which accompany the sputtered metal atoms to the substrate. This large flux of reactive species makes the reactive sputtering process so effective for producing a wide range of compounds. The variation in discharge voltage and relative deposition rate during a typical transition in the steady-state operating mode of a Cr cylindrical-post magnetron sputtering source due to injection of oxygen is shown in Fig. 4.11. The voltage decrease at high oxygen injection rates is the metal-to-compound transition. The voltage increase at low injection rates is the compound-to-metal transition.

This material is reserved for educational use only, not allowed for commercial use.
Forbidden to modify the content, and cite the document when use.

The reduction in sputtering rate results primarily from compound formation on the cathode surface and the reduced sputtering yield of the reactive-gas molecules, as shown in Fig. 4.11. The compounds often have higher electron secondary emission coefficients which give rise to a reduction in both the discharge voltage and the ion component in the cathode current for discharges driven at constant currents. The hysteresis effect, which is shown for discharge voltage but also applies to the deposition rate, occurs since the target compound layer, once formed, will remain until the sputtering gas is made sufficiently lean in the reactive species that a net sputter removal of the layer can occur. A cathode on which such a layer has formed is often referred to as being poisoned. The effect of cathode poisoning on the reactive sputtering process depends on the metal/reactive-gas combination and the properties of the cathode surface layer. Thus the very pronounced poisoning effect shown in Fig. 4.11 occurs for the oxygen reactive sputtering of materials such as Al, Cr, Ti, and Ta that form strong oxides. The decrease in deposition rate is generally less for other reactive gases such as N_2.

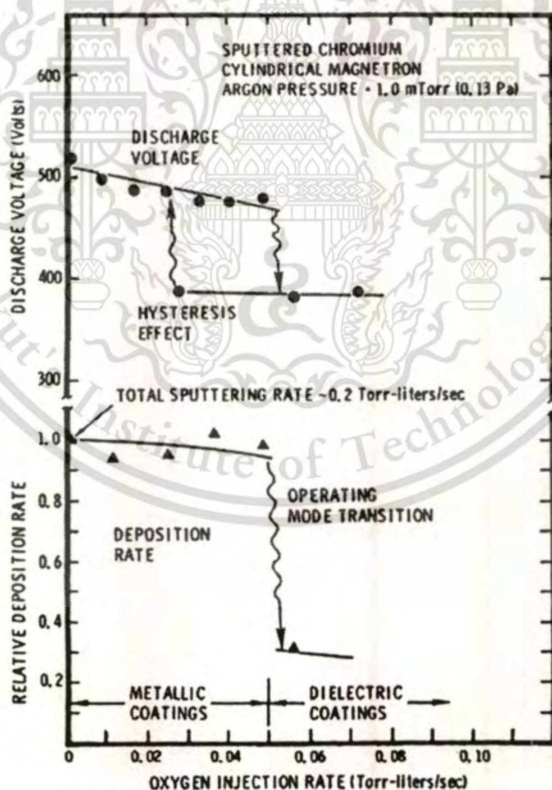

Fig. 4.11 Transitions in the steady-state operating mode of a Cr cylindrical-post magnetron sputtering source due to injection of oxygen [2].

This material is reserved for educational use only, not allowed for commercial use.
Forbidden to modify the content, and cite the document when use.

The poisoning effect introduces two practical problems. One is the loss in deposition rate. The second is that during the transition, the material being deposited often passes abruptly from a metal to a nearly stoichiometric compound. Intermediate materials such as suboxides therefore become difficult to deposit. Consequently, considerable work has been directed toward trying to operate sputtering sources at, or very near, the transition point. Transition behavior has been observed in planar diodes, planar magnetrons, and cylindrical magnetrons. The transition mechanism is important to realize that the reactive sputtering process is dependent on the total system, its geometry, and the accumulation of coating on walls and fixtures and the positions of gas injection. All these parameters must be carefully controlled in order for reactive sputtering to effectively use on a production basis. Several techniques have been developed to increase the deposition rate during reactive planar magnetron sputtering which take advantage of the nonuniform cathode current densities in these devices. For reactive sputtering in N_2, where the hysteretic behavior is more gradual than in O_2, J. M. Schneider and W. D. Sproul [4] has developed feedback control techniques which allow film deposition rates of transition-metal nitrides such as TiN, ZrN, and HfN at value very nearly equal to those of the pure metals. The feedback controls maintain constant target power, total pressure, and N_2 partial pressure.

4.2.4 RF bias

The low impedance of capacitors in the high-frequency regime allows rf power to be coupled to the driven electrode through a series capacitor as shown in Fig. 4.12. This is an importance and widely used technique, which greatly improves plasma control. Consider the typical asymmetric plasma geometry of Fig. 4.12, in which the area of grounded electrode is much larger than that of the driven electrode because it includes not only the substrate and its platform but also the entire vacuum-wall surface that is reached by the plasma. Now, recall that the ion flux or current density (j_+) injected into the sheath and arriving at the surface is determined only by plasma density (n_e) and electron temperature (T_e). If these two quantities are reasonable uniform throughout the plasma, then the electrode of smaller area (A) will receive less ion current ($I_+ = j_+A$) than will the larger electrode. Conversely, the electron current to a surface is determined by the plasma potential (V_p) relative to that surface. When the driven electrode tries to become more positive than V_p on its positive swing, the plasma instantly floats above it by discharging electrons into that electrode. Similarly, when the driven electrode tries to pull V_p below ground on its negative swing, the plasma remains above ground by discharging electron into the substrate

This material is reserved for educational use only, not allowed for commercial use.
Forbidden to modify the content, and cite the document when use.

and the wall. Thus electron current is not governed by electrode area, whereas ion current is. This means that the driven electrode in the asymmetric reactor receives less ion current than electron current, averaged over time. Because the coupling parameter blocks this net dc current, the electrode and capacitor proceed to charge up negatively. Without the capacitor (dc coupling), this dc current would flow around the circuit, and the plasma would behave as a dc plasma in parallel with an rf one.

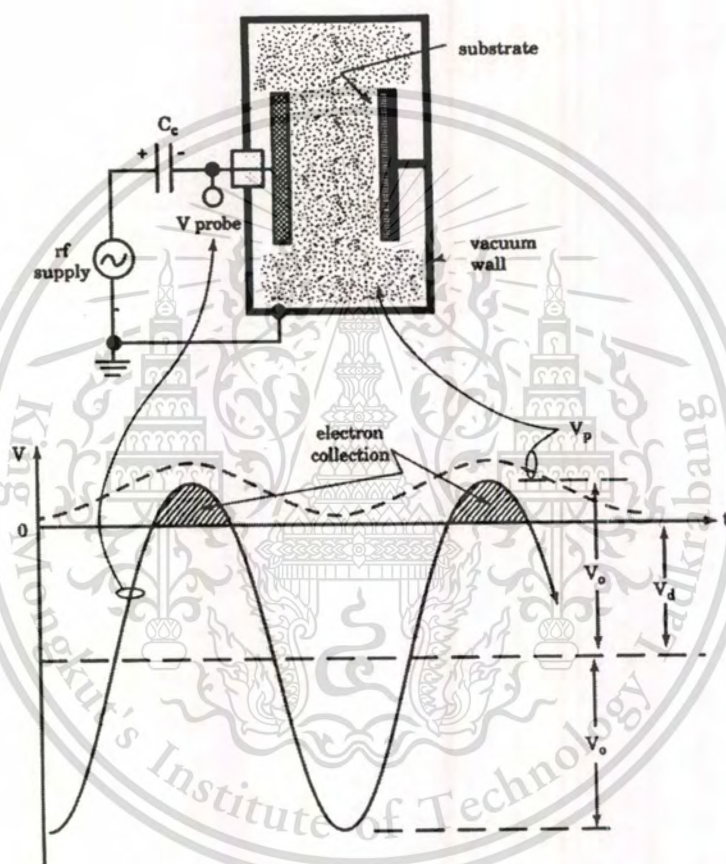

Fig. 4.12 A dc self-biasing of a capacitively coupled rf waveform due to plasma-electrode asymmetry [3].

As the coupling capacitor of the asymmetric rf plasma continues to charge negatively, the rf waveform at the electrode shifts downward as shown in Fig. 4.12, it develops a negative dc self-bias voltage (V_d). This bias reduces both the potential across which electrons are being collected from the plasma and the length of the time intervals during which this collection takes place, as represented by the shaded portion of the biased waveform. Within a few cycles, a steady state is reach, at which the time-average electron current to the driven electrode just balances the

This material is reserved for educational use only, not allowed for commercial use.
Forbidden to modify the content, and cite the document when use.

ion current. At steady state, the bias voltage often reaches its maximum possible value, V_d is closed to V_0, where the waveform is essentially all below ground potential. Meanwhile, V_p remains above ground, following a sinusoid as shown in Fig. 4.12. Currently, the maximum ion-bombardment energy in the high frequency regime is given by ion charge times the time-average of the sheath voltage drop (V_b). At the driven electrode, this energy is the time-average difference between the two sinusoid of Fig. 4.12, which is $V_0/2$ for an applied waveform symmetrical about ground and V_0 for the fully biased case.

Rf bias may also be applied to insulating substrates using the same circuitry. This is useful for ion-bombardment cleaning of the substrate prior to film deposition, or for increasing the energy of film ion bombardment during deposition to produce structural modification. When the substrate is being transported past the target or other vapor source to obtain good deposition uniformity, the rf must be coupled to it through a metal backing plate which must carry the very high rf displacement current. Sliding or rolling electrical contact is usually insufficient, but the current can be capacitively couple from an rf-driven plate spaced closely behind the moving backing plate.

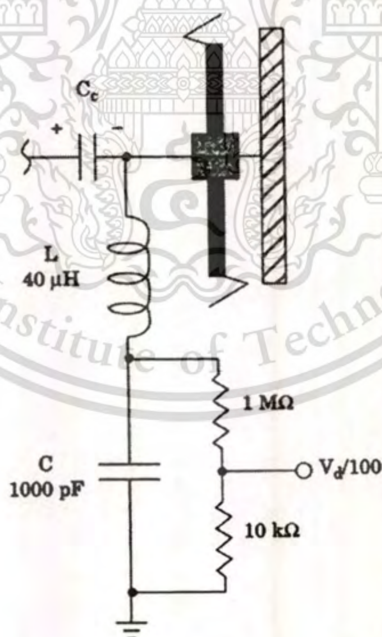

Fig. 4.13 A dc-bias probe with L and C size for 13.56 MHz operation [3].

In rf magnetron sputtering, the magnetic field applied perpendicular to the electrodes also reduces effective area by inhibiting the radial diffusion of electrons across the field lines. In the low-frequency regime, plasma spreading is further reduced because the perpendicularly directed

This material is reserved for educational use only, not allowed for commercial use.

Forbidden to modify the content, and cite the document when use.

beam electrons dominate plasma excitation. Rf bias may be hard to predict, but it is easy to measure using a high-impedance, high-voltage rf oscilloscope probe on the cathode vacuum feedthrough as shown in Fig. 4.12. It is useful to measure both V_0 and V_d in this way so that the fraction bias may be determined. Alternatively, V_d alone can be measured with the circuit of Fig. 4.13. The resistive divider reduces V_d to a conveniently measured level. At the conventional rf frequency of 13.56 MHz, the impedance of L and C shown are 3.4 kΩ and 12 Ω, respectively, so that only 0.4 percent of the rf voltage appears across the capacitor and resistive divider.

For maximum bias where V_d is closed to V_0, an upper limit on ion current (I_+) to the biased electrode can be estimated by assuming that all of the applied power (P) goes into ion acceleration across the cathode-sheath voltage drop (V_b) that is $P = I_+V_b = I_+V_d = I_+V_0$. This assumption is most reasonable for monatomic gases at low pressure and high power, where the fraction of power dissipated in other ways is smallest.

4.3 Reactive gas-timing rf magnetron sputtering

4.3.1 RF magnetron sputtering

The sputtering is a complicated process with several operation parameters being correlated. In a simple dc sputtering system the target serves as source material to be deposited. Argon is the most commonly used sputtering gas which serves as the medium where a glow discharge is initiated and sustained. Microscopically, argon ions in the discharge strike the target plate and eject neutral target atoms through energetic collisions. These atoms enter and pass through the discharge region and they eventually deposit on the substrate as growing film. The magnetic field concentrates and intensifies the plasma in the space close to the target, as a result of trapping of electrons near the target surface. This leads to larger discharge current, increased sputter deposition rates, and reduced electron bombardment of substrates. Magnetron sputtering is presently the most widely, commercially practiced sputtering method. The chief reason for its success is the high deposition rates achieved [6]. Figure 4.14 shows a schematic drawing of the process in dc planar magnetron sputtering.

This material is reserved for educational use only, not allowed for commercial use.
Forbidden to modify the content, and cite the document when use.

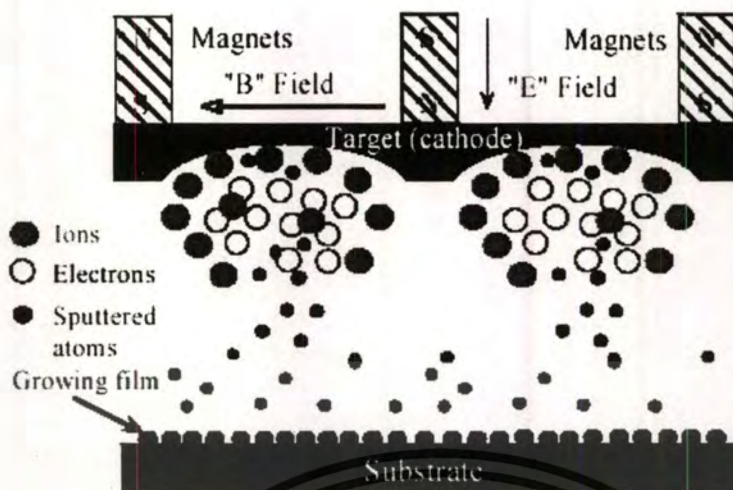

Fig. 4.14 Schematic drawing of process under dc planar magnetron sputtering.

4.3.2 Reactive rf sputtering

Reactive sputtering is a method to deposit films which have a chemical composition different from that of the target, by adding a gas to react with the target material. It is possible to form a wide variety of useful compound thin film coatings. However, the reaction mechanisms between the sputtered material and the reactive-gas may cause some processing stability problems. Combining a high deposition rate and true compound stoichiometry of the deposited film turn out to appear as contradicting desires. An important phenomenon in reactive sputtering is the hysteresis behavior. A general hysteresis process is illustrated by the change of system pressure with varying flow rate of the reactive gas. Normally, the sputtering yield of the compound material is substantial lower than the sputtering yield of the elemental target material. This causes the deposition rate to decrease as the supply of the reactive gas increases. The relationship between the film composition and supply of reactive gas is very nonlinear. This is also the case for the deposition rate versus the supply of the reactive gas. Therefore, reactive sputtering processes controlled by the supply of the reactive gas exhibit quite complex processing behavior [4]. S. Berg and T. Nyberg [5] illustrate a typical experimental processing curve for the sputter erosion rate versus the supply of the reactive gas for a reactive sputtering process (carried out with constant target current during processing) as shown in Fig. 4.15. The characteristic feature of this curve is that it exhibits a hysteresis effect. The deposition rate does not decrease and increase at the same value with the supply of the reactive gas. The separation width between the decrease and increase denotes the width of the hysteresis region. A corresponding hysteresis

This material is reserved for educational use only, not allowed for commercial use.
Forbidden to modify the content, and cite the document when use.

effect is observed for the relationship between the partial pressure and the supply rate of reactive gas as shown in Fig. 4.16. This figure clearly illustrates a difference in increasing and decreasing the supply of the reactive gas. During the increase sequence of the reactive gas supply, the partial pressure of the reactive gas remains at a very low level until reaching the upper limiting value of the hysteresis width. During a decrease of the supply of the reactive gas, the partial pressure remains significantly higher in the hysteresis region than during the increase of the gas. This points out that more gas is consumed for compound formation during the increase sequence. This may be understood by comparing the sputter erosion rate curve for the corresponding sequences. A higher sputter erosion rate needs more reactive gas to form compound coatings. As the results show the critical flow rate of reactive gas is more affected to the coated thin films properties depends on the sputtering conditions.

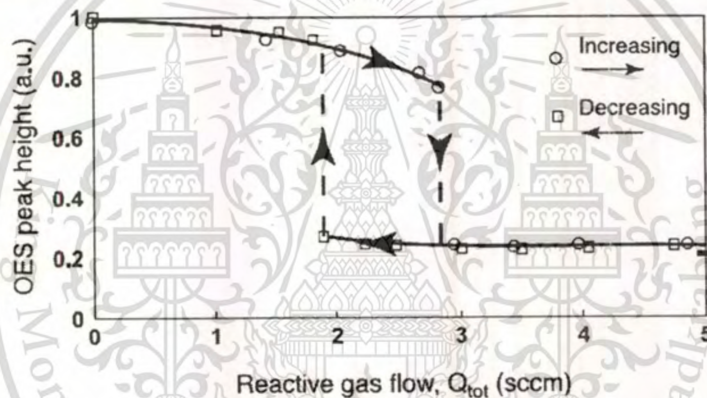

Fig. 4.15 Typical experimental curve for a reactive sputtering process exhibited in hysteresis effect. The optical emission (OES) from sputtered metal atoms represents the sputter erosion rate. Q_{tot} is expressed in standard cubic centimeters per minute (sccm).

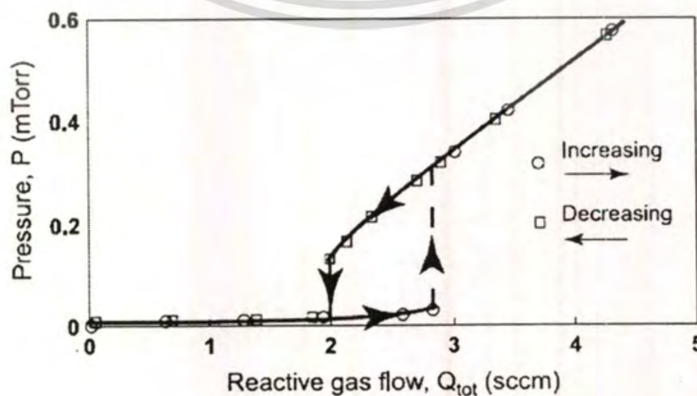

Fig. 4.16 The relationship between the partial pressure (P) and the flow rate of reactive gas (Q_{tot}).

This material is reserved for educational use only, not allowed for commercial use.
Forbidden to modify the content, and cite the document when use.

4.3.3 Gas-timing method

The gas-timing method was used to successful grown of binary and ternary oxynitride materials without substrate heating during and/or post deposition. Particularly, this method is effectively to deposit various oxides and nitrides thin films on many types of substrates. However, reactive rf magnetron sputtering continues to emerge as one of the most economical methods for depositing compound thin films. With properly configured power delivery and process control measures, high rate, arc free deposition of many oxides and nitrides is now possible. As reactive sputtering methods have matured, interest in extending the technique beyond simple binary compounds has been growing. As material complexity increases however, so do the challenges of process control as proposed in this method. This method comprising loading a substrate into a vacuum chamber having the target, introducing the process gas controlled with gas-timing technique comprising argon, nitrogen and oxygen alternately and/or intermittently into the chamber and forming plasma of the process gas in the chamber to deposit nitride film on the substrate. The gas-timing method is also desirable to obtain a stable, easy to control plasma during the sputtering process with high deposition rate.

The control of three sputtering gases in the sputtering process adds significant complexity and presents the issue of competing reactions. Since three sputtering gases can affect the state of the target surface and the plasma conditions. The timing control of sputtering gas flow rate (on-off by timing sequence) was used to control the deposition of oxide, nitride and oxynitride thin films. It is also desirable to obtain a stable and easy to control plasma during the sputtering process. The method of gas-sequence control is basically used in epitaxy growth systems such as MOCVD and MOVPE for deposition of thin films. The gas-timing is effectively method for depositing films on various substrates such as glass, plastic or other flexible substrates without substrate heating by using conventional reactive rf magnetron sputtering system. This technique has been successfully applied to produce AlN and ITO thin films without substrate heating [7,8].

The schematic of this system as shown in Fig. 4.17 comprises a sputtering cylindrical chamber, high vacuum system consists of rotary pump and oil diffusion pump, the rotated substrate holder, the material targets, thickness holder, three mass flow controllers controlled flow rate of argon, nitrogen and oxygen gases alternately and intermittently into the sputtering chamber, radio frequency generator with 13.56 MHz which irradiated in the sputtering chamber to decompose sputtering gases. The external personal computer is connected to the main system for manage the gas-timing and amount of gas flow rate control.

This material is reserved for educational use only, not allowed for commercial use.
Forbidden to modify the content, and cite the document when use.

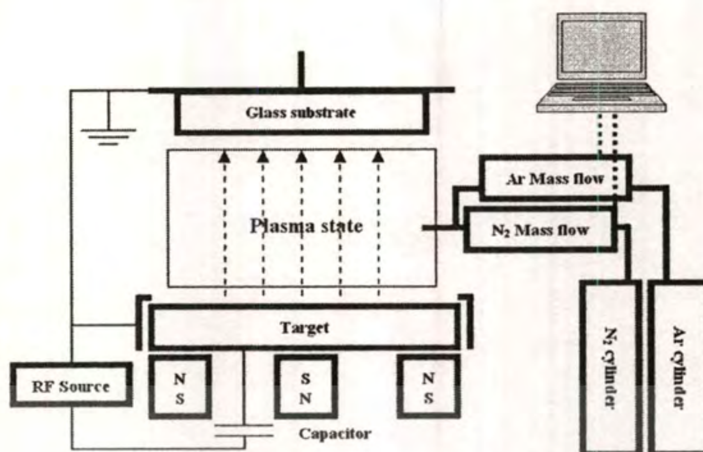

Fig. 4.17 A schematic of vacuum and gas-timing control apparatus in the sputtering process.

Fig. 4.18 The camera image of the rf magnetron sputtering system with reactive gas-timing technique.

4.3.4 The Edwards Auto 500 Reactive RF Magnetron Sputtering System

In this work, the ITO, ITON, ZnO, and ZnON films were deposited with the Edwards Auto500, made from BOC Edwards. By making minor modifications to a conventional sputtering system, we have demonstrated a new sputtering technique, called gas timing, whereby sputtering or doping gases are controlled periodically by an on-off sequence during the sputtering deposition. The camera image of the reactive gas-timing rf magnetron sputtering system was displayed in Fig. 4.18.

This material is reserved for educational use only, not allowed for commercial use.
Forbidden to modify the content, and cite the document when use.

4.3.4.1 Deposition equipment

The deposition equipments are composed of a stainless steel cylindrical chamber, high vacuum system, rf generator system, power supply, switch cabinet, etc. A computer interface is used to control the on-off gas-timing sequence of mass flow controller. The gas flow rate has been controlled a gas volume of flow in sccm. For this system, the rf is 13.56 MHz and the maximum rf power is 600 watts. It has primary two mass flow controllers and one optional working in range of 0-20 sccm. The quartz microbalance is used to monitor the growth film thickness in range of nanometer per second.

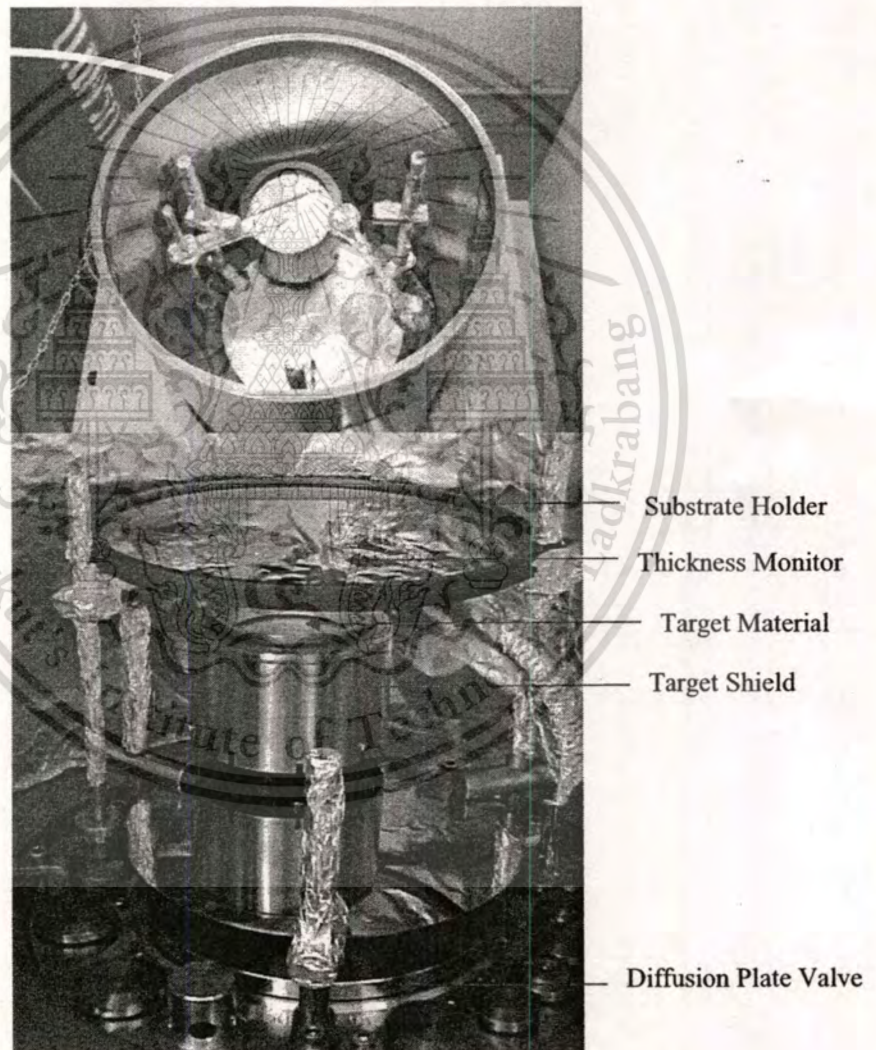

Fig. 4.19 The process chamber is a stainless steel cylinder with one rf magnetron sputtering head for 3 inch diameter target material.

This material is reserved for educational use only, not allowed for commercial use.
Forbidden to modify the content, and cite the document when use.

4.3.4.2 Process chamber

The process chamber is a stainless steel cylinder and can be evacuated to 10^{-7} mbar. It is a vertical mounted inside, where the sputter-up-mode is available, as shown in Figure 4.19. It consists of one rf magnetron sputtering head for 3 inch diameter target material, target shield, thickness monitor, and substrate holder which can rotate above the target off-axis.

4.3.4.3 Vacuum System

A high vacuum (HV) is generated by a high vacuum pump system, which is composed of a diffusion pump (E04K), a mechanical rotary pump (Edward RV12) and a two kind of pressure gauge as pirani gauge (PRM10K) and penning gauge (CP25K). The rotary and diffusion pumps are used to achieve high vacuum as the primary pumping and secondary pumping, respectively. For the primary pumping is evacuated from atmosphere pressure down to 10^{-3} mbar using the rotary pump and verified by pirani gauge, after that the secondary pumping is pumped from 10^{-3} to 10^{-8} mbar using the diffusion pump and verified by penning gauge, as shown in Fig 4.20.

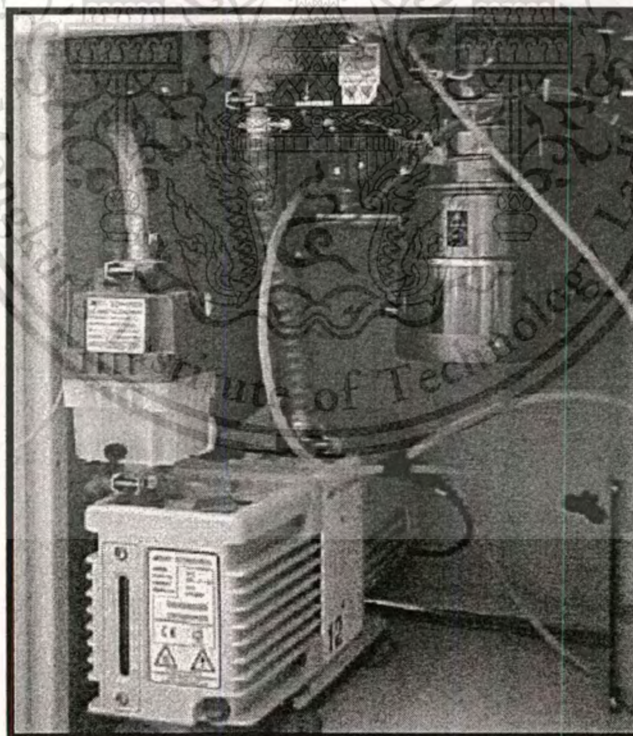

Fig. 4.20 A high vacuum (HV) is generated by a high vacuum pump system, which is composed of a diffusion pump and a rotary pump.

This material is reserved for educational use only, not allowed for commercial use.
Forbidden to modify the content, and cite the document when use.

4.3.4.4 RF sputtering system

The electrical system of rf magnetron sputtering for thin films deposition involves a rf magnetron generator (CESAR 136) operated at 13.56 MHz as shown in Fig. 4.21, a rf switching control, a rf selector switch and matchboxes. The output of the rf generator is up to 600 W. Since a plasma process is a variable complex load, whereas the rf generator is designed for 50 Ω loads, a matchbox directly connected to the application is used to transform the complex load of the plasma process to a stable 50 Ω resistive load. As the result, only rf load can be supplied with rf power at any one time. The plasma is started with this time and it went to stable state in tiny time.

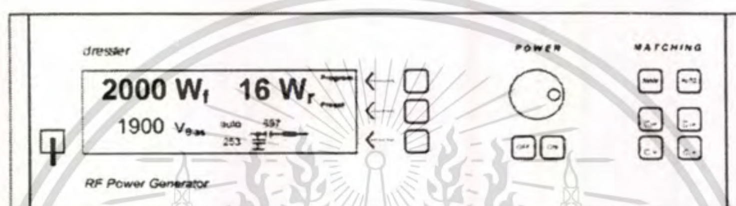

Fig. 4.21 The panel schematic of rf magnetron generator (model CESAR 136).

4.4 Chapter summary

The sputter process has almost no restrictions in the target materials, ranging from pure metals where a dc power supply can be used to semiconductors and isolators which require a rf power supply or pulsed dc. Deposition can be carried out in either non reactive (inert gas only) or reactive (mixed of inert and reactive gas) discharges with metal or compound targets. During the sputter process a magnetic field can be used to trap secondary electrons close to the target. The electrons follow helical paths around the magnetic field lines undergoing more ionizing collisions with neutral gaseous near the target than would otherwise occur. This enhances the ionization of the plasma near the target leading to a higher sputter rate. It also means that the plasma can be sustained at a lower pressure. The sputtered atoms are neutrally charged and so are unaffected by the magnetic trap.

In this research, the special technique, called gas-timing will be used to grow ITO, ITON, ZnO and ZnON thin films by rf magnetron sputtering at ambient temperature. Gas-timing technique is a process to control timing sequence of feeding gases (pure Ar, pure N_2 and/or mixed gas) into the sputtering process. The period of time sequence condition depends on thin film thickness and thin film properties requirement.

This material is reserved for educational use only, not allowed for commercial use.
Forbidden to modify the content, and cite the document when use.

References

[1] R. V. Stuart, **Vacuum Technology, Thin Films, and Sputtering: An Introduction**, New York: Academic Press, 1983.

[2] R. F. Bunshah, editor, **Deposition Technologies for Films and Coatings**, Park Ridge, New Jersey: Noyes Publications, 1982.

[3] D. L. Smith, **Thin Film Deposition: Principles and Practices**, New York: McGraw-Hill, 1995.

[4] D. A. Glocker, S. I. Shah, editors, **Handbook of Thin Film Process Technology**, Bristol: Institute of Physics Publishing, 1998.

[5] S. Berg and T. Nyberg, "Fundamental Understanding and Modeling of Reactive Sputtering Processes", **Thin Solid Films**, vol. 476, 2005, pp. 215-230.

[6] J. Musil and J. Vlcek, "A Perspective of Magnetron Sputtering in Surface Engineering", **Surf. & Coat. Technol.**, vol. 112, 1999, pp. 162-169.

[7] N. Kietpaisalsophon, W. Bunjongpru, W. Techitdheera, and J. Nukeaw, "Photoreflectance Study of AlN Thin Films Grown by Reactive Gas-Timing RF Magnetron Sputtering", **International Journal of Modern Physics B**, vol. 16, no. 28&29, 2002, pp. 4418-4422.

[8] A. Klamchuen, N. Pornteeraphat, and J. Nukeaw, "Characterization of ITO thin films on PET substrates prepared by gas-timing RF magnetron sputtering", **e-Journal of Surface Science and Nanotechnology**, vol. 3, 2005, pp. 272-275.

King Mongkut's Institute of Technology Ladkrabang

This material is reserved for educational use only, not allowed for commercial use.

Forbidden to modify the content, and cite the document when use.

CHAPTER 5

THIN FILM CHARACTERIZATION

5.1 Introduction

In this study, we aim to characterize the structural, optical and electrical properties of reactively sputtered ITO, ITON, ZnO and ZnON. This chapter was described the theoretical principles of the methods used in analyzing the films. To determine the film crystallinity and composition, we extensively used the interaction x-ray with matter and for which we provide the relevant theory and how these film properties are distinguished. To determine the film surface morphology, two techniques were used and whose principles are discussed. There are the scanning electron microscopy and atomic force microscopy. To determine the electrical property, we present the four-point probe in measuring the film sheet resistance. Lastly, the film thickness was measured by the stylus profilometer, and then confirmed by the calculated film thick from the transmission data.

5.2 Structural characterization methods

5.2.1 X-ray diffraction (XRD)

X-ray diffraction was discovered by Max von Laue in 1912. It has provided a wealth of important information to science and industry [1,2] for example, much that is known about the arrangement and the spacing of atoms in crystalline materials has been directly deduced from diffraction studies. In addition, such studies have led a much clearer understanding of the physical properties metals, polymeric materials, and other solids. XRD also provides a convenient and practical means for the qualitative identification of crystalline compounds. XRD is a very important experimental technique in revealing the crystal structure of bulk solid microstructure of thin films. The XRD methods are generally applied to films thicker than several angstroms on account of the strong penetrating power of the x-ray. Many information related to the crystal structure of the films, including lattice constants, grain size, preferred orientation of polycrystals, defects, stress, etc. can be determined from the x-ray diffraction measurement.

X-rays are electromagnetic waves, which radiate with typical photon energies in the range of 100 eV-100 keV. For diffraction applications, only short wavelength x-rays (hard X-rays) in

This material is reserved for educational use only, not allowed for commercial use.
Forbidden to modify the content, and cite the document when use.

the range of a few angstroms to 0.1 angstrom (1 keV-120 keV) are used. X-rays are produced generally by either x-ray tubes or synchrotron radiation. In an x-ray tube, which is the primary x-ray source used in laboratory x-ray instruments, x-rays are generated when a focused electron beam accelerated across a high voltage field bombards a stationary or rotating solid target. As electrons collide with atoms in the target and slow down, a continuous spectrum of x-rays are emitted, which are termed Bremsstrahlung radiation. The high energy electrons also eject inner shell electrons in atoms through the ionization process. When a free electron fills the shell, an x-ray photon with energy characteristic of the target material is emitted. Common targets used in x-ray tubes include Cu and Mo, which emits 8 keV and 14 keV x-rays with corresponding wavelengths of 1.54 Å and 0.8 Å, respectively. Because the wavelength of x-rays is comparable to the size of atoms, they are ideally suited for probing the structural arrangement of atoms and molecules in a wide range of materials. The energetic x-rays can penetrate deep into the materials and provide information about the bulk structure.

The phenomenon of the x-ray diffraction by crystals results from a scattering process in which x-rays are scattered by the electrons of the atoms without change in wavelength. X-rays primarily interact with electrons in atoms. When x-ray photons collide with electrons, some photons from the incident beam will be deflected away from the direction where they original travel, much like billiard balls bouncing off one anther. If the wavelength of these scattered x-rays did not change, the process is called elastic scattering (Thompson scattering) in that only momentum has been transferred in the scattering process. These are the x-rays that we measure in diffraction experiments, as the scattered x-rays carry information about the electron distribution in materials. On the other hand, the inelastic scattering process (Compton scattering), x-rays transfer some of their energy to the electrons and the scattered x-rays will have different wavelength than the incident x-rays. The diffracted waves from different atoms can interfere with each other and the resultant intensity distribution is strongly modulated by this interaction. If the atoms are arranged in a periodic fashion, as in crystals, the diffracted waves will consist of sharp interference maxima in term of peak intensity with the same symmetry as in the distribution of atoms. A diffracted beam is produced by such scattering only when certain geometrical conditions are satisfied, which may be expressed in either of two forms, the Bragg law or the Laue equations [3]. The peaks in a x-ray diffraction pattern are directly related to the atomic distances. The incident x-ray beam was interacting with the atoms arranged in a periodic manner as shown in

This material is reserved for educational use only, not allowed for commercial use.
Forbidden to modify the content, and cite the document when use.

Fig. 5.1. The atoms, represented as periodically solid spheres, can be viewed as forming different sets of planes in the crystal.

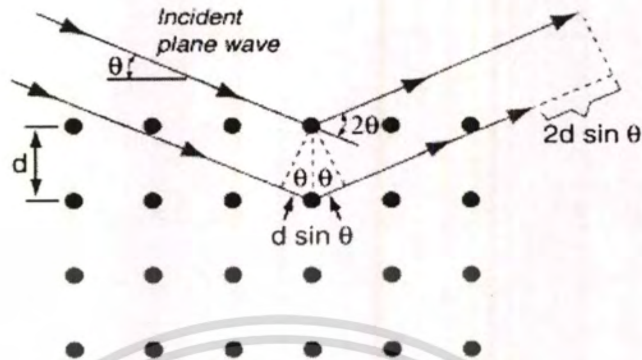

Fig. 5.1 Diffraction of x-rays from a crystal.

The crystal information obtained from the characteristic of x-ray diffraction peak. The resulting diffraction pattern of a crystal, comprising both the positions and intensities of the diffraction effects, is a fundamental physical property of the material. Analysis of the positions of the diffraction effect leads immediately to a knowledge of the size, shape and orientation of the unit cell. Figure 5.2 shows a typical x-ray diffraction pattern together with the line spectrum of ITO ($In_2Sn_2O_{7-x}$) powders recorded in the JCPDS (Joint Committee on Powder Diffraction Standard) No. 39-1058.

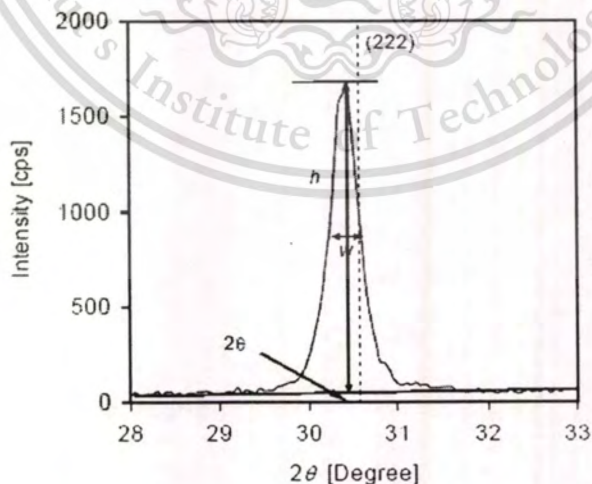

Fig. 5.2 The (222) reflected of XRD for an ITO film and the dot line represent the theoretical position of this peak.

This material is reserved for educational use only, not allowed for commercial use.
Forbidden to modify the content, and cite the document when use.

In order to characterize the microstructure of the materials, three important parameters should be obtained from the diffraction pattern as the position of the peaks 2θ, the height of the peaks h and the full width at the half maximum (FWHM) height of the peaks w. The distance between the two adjacent lattice planes is derived from the experimental peak position by means of Bragg formula:

$$N\lambda = 2d_{\exp}\sin\theta, \tag{5.1}$$

where N is an integer representing the order of diffraction peak, λ is the wavelength of measured x-ray, d_{exp} is the distance between parallel consecutive atomic planes from the experimental peak position and θ is the angle between these planes and the incident beam. Different elements or compounds are then identified by analysis of the d_{exp} values that are characteristic for the crystalline phase. Whereas, its theoretical value d_{hkl} can be calculated from the lattice constant (a_0 = 1.0118 nm of ITO) by:

$$d_{hkl} = \frac{a}{\sqrt{h^2 + k^2 + l^2}}, \tag{5.2}$$

where h, k and l are Miller indices of the corresponding lattice planes.

The coherence length D of the scattering material is determined from the half width w of the reflexes by means of the Scherrer's formula:

$$D = \frac{K\lambda}{w\cos\theta}, \tag{5.3}$$

where D is the effective grain size, K is a shape factor and assumes a value of 0.9 for spherical particles, w is the measured broadening of the diffraction line peak at an angle of 2θ, at half its maximum intensity (full width at half maximum, FWHM) in radian and θ is the half diffraction angle of crystal orientation peak.

The equipment used in this work is a D8-Bruker model-XRD diffractometer with CuKα radiation with wavelength 1.540598 Å, as shown in Fig. 5.3. The XRD spectra were collected in the 20-80° of 2-theta range with a measurement step of 0.02°, the scan time/step is 2 second. Measurements were taken under beam acceleration condition of 40 kV/40 mA. Crystallite size

This material is reserved for educational use only, not allowed for commercial use.
Forbidden to modify the content, and cite the document when use.

and lattice parameters were determined by Scherrer's formula and Bragg equation from the main diffraction peaks respectively.

Fig. 5.3 A photograph of D8-Bruker model-XRD diffractometer.

5.2.2 X-ray photoelectron spectroscopy (XPS)

In recent years the photoelectron spectroscopy (PES) technique has been developed to the degree that such experiments in many cases now give the most precise and accurate information on the electronics structure of gases, liquids and solids. Both core and valence electrons are being studied with high accuracy. The technique is expanding vary rapidly not only in physics but also in many other areas of scientific and technological importance.

The principle in photoelectron spectroscopy experiments is to study the properties of electrons photo-emitted from a sample by mono-energetic photons. There are basically three measurable properties of the photoelectron: (i) the kinetic-energy distribution and its variation with photon energy, (ii) the angular distribution of photoelectron intensity, and (iii) the spin distribution of the emitted photoelectrons. Most of the experiments performed to date have been concerned only with measurements of the kinetic-energy distribution. The fundamental for the photoelectric process is based on the energy-conservation principle [4]:

This material is reserved for educational use only, not allowed for commercial use.
Forbidden to modify the content, and cite the document when use.

$$h\nu = E^f(k) - E^i + E_{kin}, \tag{5.4}$$

where $h\nu$ is the energy of the incident photon, $E^f(k)$ is the total energy of the final state with a hole in the kth subshell, E^i is the total energy of the initial state, and E_{kin} is the kinetic energy of the electron expelled from the kth subshell. The photon energy thus determines the depth to which photoelectron spectroscopy can probe the electron energy levels. Due to the lack of readily available mono-energetic photon sources in the range of UV to soft x-ray region, photoelectron electron spectroscopy has developed in two distinct areas characterized by the energy of excitation are ultraviolet photoelectron spectroscopy (UPS) and x-ray photoelectron spectroscopy (XPS). In UPS, valence electrons (E < 40 eV) are emitted by using UV-light (from a noble gas discharge lamp, usually a He-discharge lamp), while in XPS core level electrons (E > 40 eV) are excited using soft x-ray radiation. Frequently, for XPS a dual anode x-ray gun (Al $K\alpha$, Mg $K\alpha$) is used in a common laboratory setup. The x-ray photoelectron spectroscopy technique often referred to as ESCA (Electron Spectroscopy for Chemical Analysis), thereby emphasizing its important chemical applications.

Referring to the energy-conservation principle, the energy of the final state $E^f(k)$ will be reflected in the photoelectron spectrum. In the case of the final being simply a hole left in the kth electron energy level, $E^f(k)$- E^i is equal to the electron binding energy of the kth electron referred to the vacuum level of the sample:

$$(B.E.)_{vacuum} = E^f(k) - E^i, \tag{5.5}$$

For thin film samples, the Fermi level is usually a more convenient reference level, and the work function of the sample becomes involved in the energy equation. If the definition of E_{kin} is changed slightly to mean the kinetic energy as measured (KE_{meas}) in the electron spectrometer, then we must account for the fact that photoelectron will have adjusted to the work function of the spectrometer material ϕ_{spec}. The energy equation therefore becomes:

$$h\nu = (B.E.)_{Fermi} + \phi_{spec} + KE_{meas}, \tag{5.6}$$

This material is reserved for educational use only, not allowed for commercial use.
Forbidden to modify the content, and cite the document when use.

A binding energy is defined as the required energy to remove an electron from the band state to infinity. However, the binding energy of a core electron has a single, uniquely defined value only for a closed-shell element in the form of a monatomic gas. Most binding energy has been performed on solids. In the case of conducting sample as metal it is convenient to use the Fermi level in the sample as a reference level for binding energy. This procedure avoids the inclusion of the work function is critically dependent on the physical condition of the sample surface, whereas the spectrometer work function should be relatively constant with the time. Therefore, the conducting samples were placed in electrical contact with the spectrometer, usually by simply grounding the sample and the spectrometer. Under this condition, the Fermi level of the sample and the spectrometer are at the same reference level.

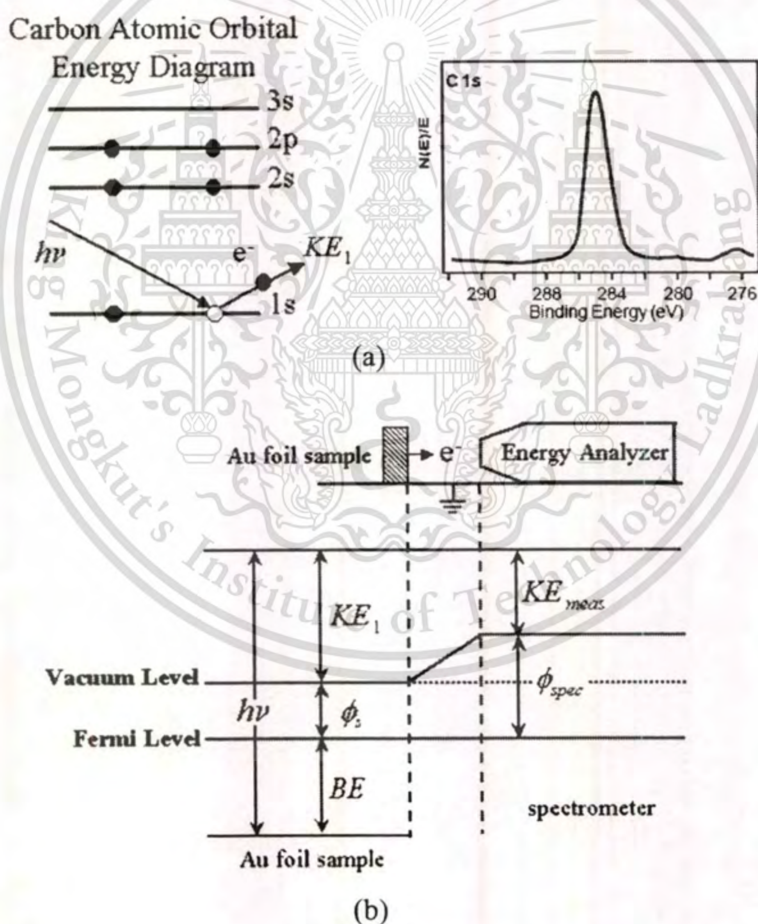

Fig. 5.4 (a) XPS process for carbon 1s core electron and the resultant spectrum and (b) the energy level diagram relating the measured kinetic energy (KE_{meas}) to the binding energy ($B.E.$) of the sample.

This material is reserved for educational use only, not allowed for commercial use.
Forbidden to modify the content, and cite the document when use.

Accordingly, the energy-conservation equation was defined as illustrated in Fig. 5.4, where the simple case of a carbon 1s is used for illustration. A simplified depiction of the XPS process is shown in Fig. 5.4(a). An x-ray of energy (*hv*) ejects a carbon 1s electron. The emitted electron has a kinetic energy (KE_l) that can be measured by an electron energy analyzer (typically referred to as a spectrometer). XPS spectra are given as a plot of intensity versus binding energy (*B.E.*). The binding energy of the photoelectron is characteristic of the atomic orbital from which the electron originated. Therefore, the *B.E.* will provide the identity of the atoms present in the analysis volume. Furthermore, since the *B.E.* is sensitive to the local electron density, shifts in *B.E.* for a given atom provides an indication of the oxidation state of the atom. In Koopman's approximation [4], the *B.E.* of the photoelectron is related to the measured kinetic energy (KE_{meas}) as equation 5.6. As indicated in Fig. 5.4(b), the kinetic energy that is measured by the spectrometer is not necessarily equivalent to the kinetic energy of the electron emitted from the sample volume. Often times, the sample and spectrometer work functions are different and unknown. The spectrometer work function can be estimated by using an internal *B.E.* standard within the sample volume. In this thesis, a *B.E.* of 84.0 eV for the Au $4f_{7/2}$ peak is used as the internal standard. The laboratory XPS setup is typically consisted of ultra-high vacuum chamber (UHV), x-ray source and electron energy analyzer. For the spectrometer, an electron energy analyzer preferred option for photo-emission experiments is a concentric hemispherical analyzer which uses an electric field between two hemispherical surfaces to disperse the electrons according to their kinetic energy. A typical XPS experimental setup is depicted in Fig. 5.5.

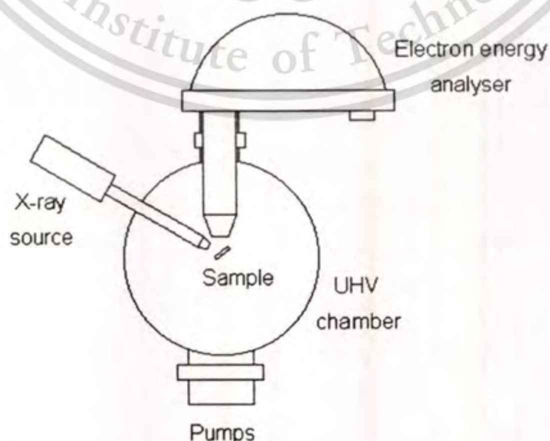

Fig. 5.5 A schematic of XPS system is consisted of UHV chamber, x-ray source and electron energy analyzer.

This material is reserved for educational use only, not allowed for commercial use.
Forbidden to modify the content, and cite the document when use.

The different peaks in a photoelectron spectrum reflect the electronic structure of the sample. Every element has a unique set of binding energies and, therefore, an XPS spectrum gives information about the chemical composition of the sample. Moreover, it is also possible to determine the valence states of the different elements present at the surface (chemical shift). Hence XPS can provide chemical bonding information as well.

In this research, XPS was used to confirm nitrogen incorporation into the ITO and ZnO films. The equipment used in this work is an in-house XPS system at NSRC as shown in Fig. 5.6. Pressure in an analytical chamber was kept lower than ~6.0×10^{-9} mbar. A monochromatic Mg $K\alpha$ was used for an x-ray source (1253.6 eV).

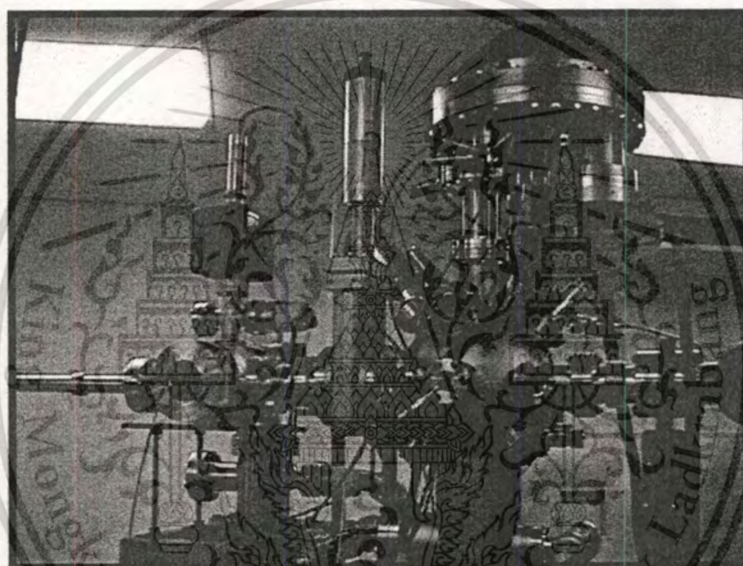

Fig. 5.6 A photograph of in-house XPS system at NSCR.

5.2.3 Field-emission scanning electron microscope (FE-SEM)

The scanning electron microscope (SEM) uses electrons rather than light to form an image. In a scanning electron microscope, a beam of electrons is produced at the top of the microscope by field-emission electron source (Tungsten), as shown in Fig. 5.7. The electron beam follows a vertical path through the column of the microscope. It makes its way through electromagnetic lenses which focus and direct the beam down towards the sample. Once it hits the sample, other electrons (backscattered or secondary) are ejected from the sample. Detectors collect the secondary or backscattered electrons, and convert them to a signal that is sent to a monitor producing an image.

This material is reserved for educational use only, not allowed for commercial use.
Forbidden to modify the content, and cite the document when use.

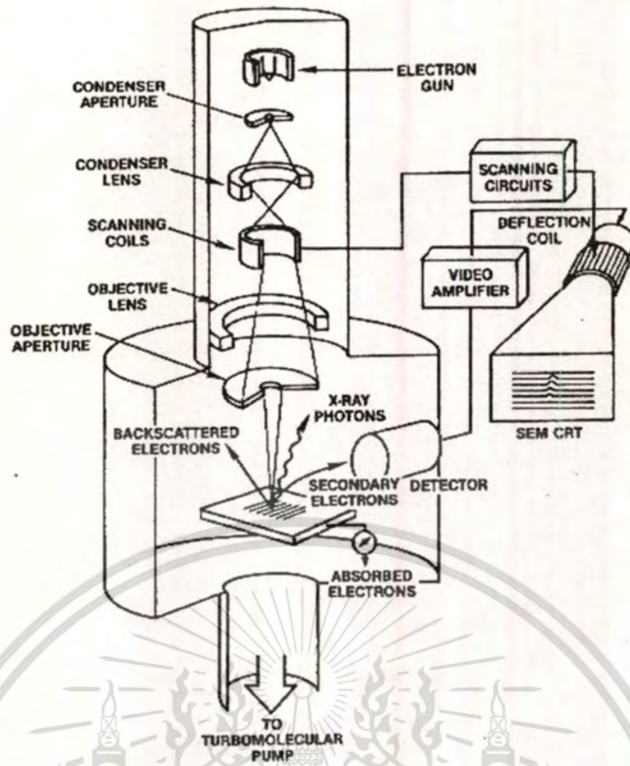

Fig. 5.7 A schematic of a SEM components and scanning process.

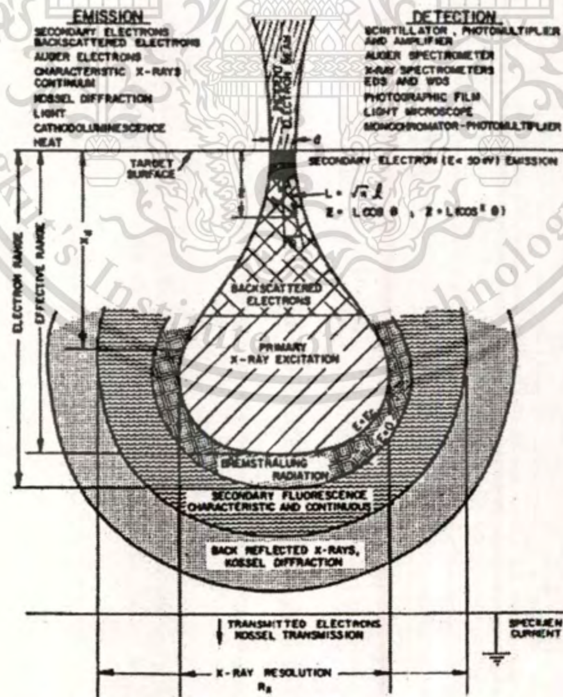

Fig. 5.8 Diagram illustrating the interaction of the primary electron beam with a solid surface in the production of secondary and backscattered electrons, x-rays, and other secondary radiation.

This material is reserved for educational use only, not allowed for commercial use.
Forbidden to modify the content, and cite the document when use.

SEM is surface imaging of solid using electron-beam generated secondary electrons [2]. Fig. 5.8 illustrates the electron beam interaction with a solid. The primary beam may be focused to a spot size lower than 50 Å in diameter. Upon interaction with the solid, secondary electrons are generated which are utilized to image the surface. As the high energy primary electrons penetrate the solid, they undergo scattering which increases the interaction volume. Some of the primary electrons will be backscattered toward the surface with little or no loss in energy. Energetic primary electrons ionize atoms in the solid producing x-ray which are characteristic of the elements that are present. With suitable detectors, the x-rays may be detected to provide elements that are present. With suitable detectors, the x-ray may be detected to provide elemental analysis, known as Energy Disperse X-Ray Spectroscopy (EDX).

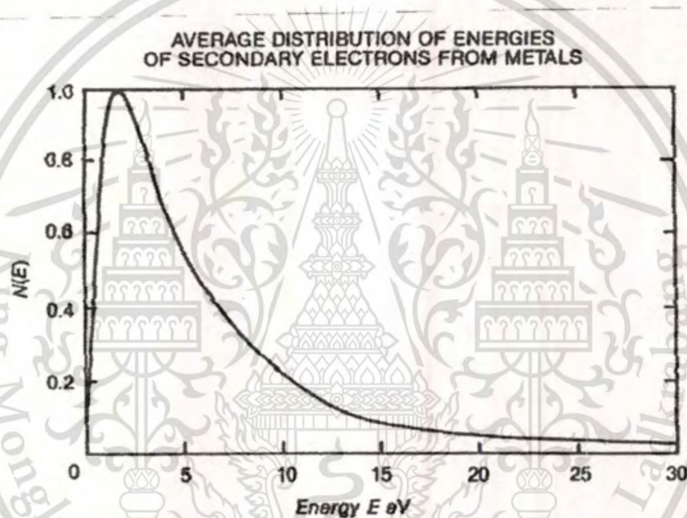

Fig. 5.9 The average distribution of secondary electrons from metals as a function of energy.

The peak in the electron energy distribution is below 5 eV. In order to efficiently collect the secondary electrons, a high potential bias is applied to a scintillator tube which is positioned in proximity to the sample. The signal was converted to light and fed out through a light pipe to a photomultiplier tube as shown in Fig. 5.9. SEM images at less than 20 Å resolutions have been obtained higher magnification with greater depth resolution than optical microscopes. SEM images may become distorted by the surface potential that builds up on insulators or edge effects at sharp contours. Insulators may be coated with a thin (~100 Å) conductive layer to dissipate the surface charge.

This material is reserved for educational use only, not allowed for commercial use.
Forbidden to modify the content, and cite the document when use.

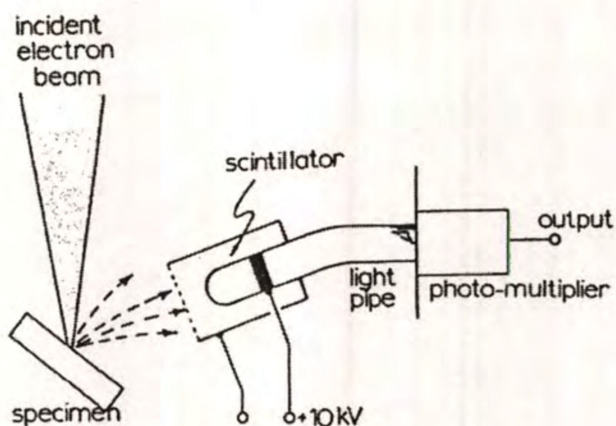

Fig. 5.10 Schematic diagram of a scintillator tube used for the detection of secondary electrons.

Secondary electrons are low energy even though the primary electron beam is several keV or higher. Fig. 5.10 shows the average energy distribution of secondary electrons from metals. A high resolution FE-SEM is S4700 from Hitachi was used to study a morphology grain size and surface of ITO, ITON, ZnO and ZnON thin films as shown in Fig. 5.11.

Fig. 5.11 A photograph of a high resolution FE-SEM of Hitachi S4700 at TMEC.

This material is reserved for educational use only, not allowed for commercial use.
Forbidden to modify the content, and cite the document when use.

5.2.4 Atomic force microscopy (AFM)

Atomic force microscopy is commonly used to characterize surface topography of given samples. Technologies affecting the electronics, biological, chemical and automotive industries use the AFM to solve processing and materials problems. The materials being investigated include thin and thick film coatings, semiconductors, ceramics, metals and micromechanical properties of biological samples. The AFM is a powerful addition to microscopy, surpassing light and electron microscopy through its ability to generate high-resolution 3-dimensional images at nanometer resolution with no sample pre-treatment and working in air or liquid environments. Both conducting and dielectric materials can be detected by AFM.

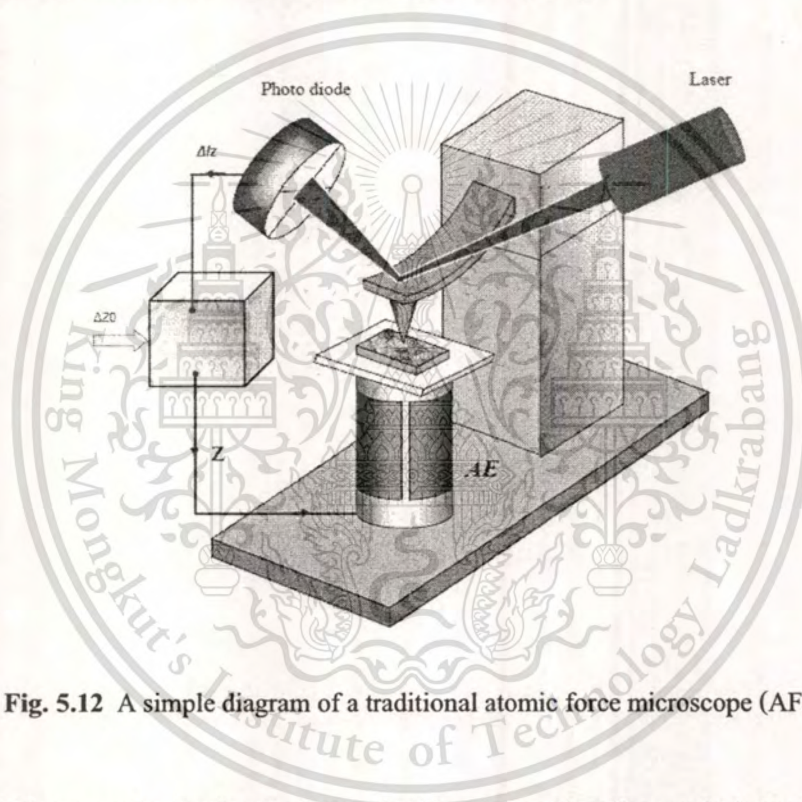

Fig. 5.12 A simple diagram of a traditional atomic force microscope (AFM).

AFM is a recently developed advanced microscopy and surface analysis instrument, which was invented in 1986 on the basis of scanning tunneling microscopy (STM) by Binning *et al.* [5]. Today, most AFMs use a laser beam detection system which is shown schematically in Fig. 5.12. In the optical AFM, a laser beam is reflected from the back surface of a cantilever beam onto a position-sensitive photodiode. The photodiode is divided into four quadrants. When the cantilever is not interacting with the sample, the laser is positioned at the center of the photodiode as a reference point. When the sharp tip of the cantilever beam was came in close contact with the sample surface, the cantilever beam bends in response to the forces between the tip and the sample which causes the laser beam to shift its position on the photodiode. As a result, one

This material is reserved for educational use only, not allowed for commercial use.
Forbidden to modify the content, and cite the document when use.

quadrant of the photodiode will be illuminated more than another. By measuring the difference in light intensities between the upper and lower portions of the photodiode, a differential signal is created and converted to a voltage signal. This signal is used in a control feedback loop to help maintain a constant force between the tip and the sample as the beam is raster scanned across the sample surface.

The sample typically sits on a positioning device made from piezoelectric ceramics. This positioning device, usually a tube scanner, is capable of sub-angstrom resolution in the x-, y-, and z-directions. Motion in the x- and y-directions typically performs the raster movement. Surface mapping is usually accomplished by maintaining a constant force between the tip and sample by moving the sample up and down with the help of a computer controlled feedback system. When the tip passes over a bump in the surface, the tip-sample separation becomes smaller which causes the cantilever to feel a force thereby bending the cantilever upward. The photodiode detects the deflection, converts the deflection to a voltage signal and adjusts the tip-sample separation by sending the signal to the z-piezo via the feedback system until the cantilever no longer experiences a deflecting force. The voltages used to maintain constant tip-sample forces are converted to distances and used to obtain the 3-dimensional image.

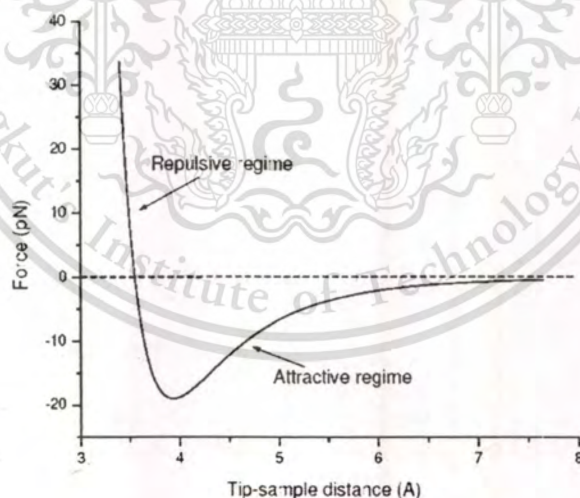

Fig. 5.13 The forces between the tip and sample versus the tip-sample distance, known as intermolecular force curve.

In the measurement with AFM, there are three primary modes of AFM: contact mode, non-contact mode, and tapping mode. In contact mode operation (usually called atomic force microscope, AFM), as the name implies, the tip is in close contact with the sample surface as it is

This material is reserved for educational use only, not allowed for commercial use.
Forbidden to modify the content, and cite the document when use.

scanned over the sample. The force on the tip is in the repulsive regime of the intermolecular force curve, as shown in Fig. 5.13. By operating in the repulsive regime, high resolution images are obtained because the forces in this region are greater than in the attractive region. The main drawback to the contact mode of operation is that large lateral forces exist on the sample as the tip is dragged across the surface. Damage to the tip as well as the sample is possible.

In non-contact mode operation (referred to dynamic force microscope, DFM), the tip of the cantilever flies 50-150 Å above the sample surface. Attractive forces are the dominant forces between the tip and the sample. Forces in the attractive region are significantly weaker than forces in the repulsive region and, therefore, small oscillations are given to the tip of the cantilever via a dither piezoelectric crystal located within the cantilever holder. The forces between the tip and the sample are detected by measuring changes in amplitude, phase or frequency of the oscillating cantilever.

In tapping mode operation, the tip of the cantilever is oscillated at or near the cantilever's resonant frequency and taps the surface of the sample. The tip of the cantilever comes into contact with the sample surface for very brief periods of time. By operating in the repulsive regime, high resolution is obtained, yet, the short duration of time that the cantilever is in contact with the sample limits the amount of damage associated with contact mode. The cantilever is driven at or near its resonant frequency by a dither piezoelectric crystal located within the cantilever holder. During scanning, the tip of the cantilever typically oscillates at a frequency of 50-500 kHz. As the tip comes in intermittent contact with the sample, the amplitude of oscillation is reduced due to energy loss. The reduction in oscillation amplitude is used to identify and measure surface features.

In section analysis, a cross-sectional line can be drawn across any part of an image, and the line profile is displayed. Therefore, depth, height, or width measurements of surface features can be easily made using section analysis. The root mean square roughness (R_{rms}), which presents the standard deviation of the z values within a given area, can be determined using the software on the basis of the equation:

$$R_{rms} = \sqrt{\left(\frac{1}{N}\sum_{1}^{N}(h_i - \bar{h})^2\right)}, \tag{5.7}$$

where N is the number of data points, h_i are the data points that describe the relative vertical height of the surface, and $\bar{h}$ is the mean height of the surface. R_{rms} only provides the average

This material is reserved for educational use only, not allowed for commercial use.
Forbidden to modify the content, and cite the document when use.

surface roughness. The equipment used in this work is SPA-400 Atomic Force Microscope from Seiko, as shown in Fig. 5.14. The R_{rms} and the surface morphology of films were measured.

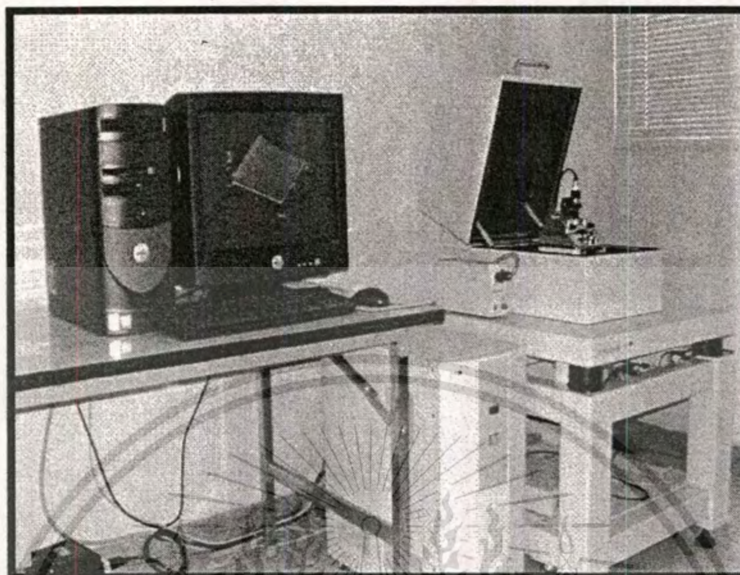

Fig. 5.14 A photograph of an atomic force microscope, Seiko SPA-400.

5.3 Optical characterization method

5.3.1 UV-Vis Spectroscopy

Transmission measurements or absorption spectroscopy can be used to determine the optical quality of thin films. Absorption spectroscopy responds to processes that have large density of states, such as the absorption edge, and provides a measure of the bulk properties of the crystal. This technique is quick and non-destructive and is therefore a good complementary tool to the photoluminescence measurements. Two different types of light sources are used in the instrument in order to cover the whole spectral range. A deuterium, tungsten and halogen lamps can provide UV, visible and near IR light source, respectively. A photomultiplier (PMT) tube is used to detect signals in the UV and visible range (200-800 nm). A lead sulfide detector is used to detect infrared light. The UV-VIS spectrophotometer used for transmittance measurement in this research is shown in Fig. 5.15.

This material is reserved for educational use only, not allowed for commercial use.
Forbidden to modify the content, and cite the document when use.

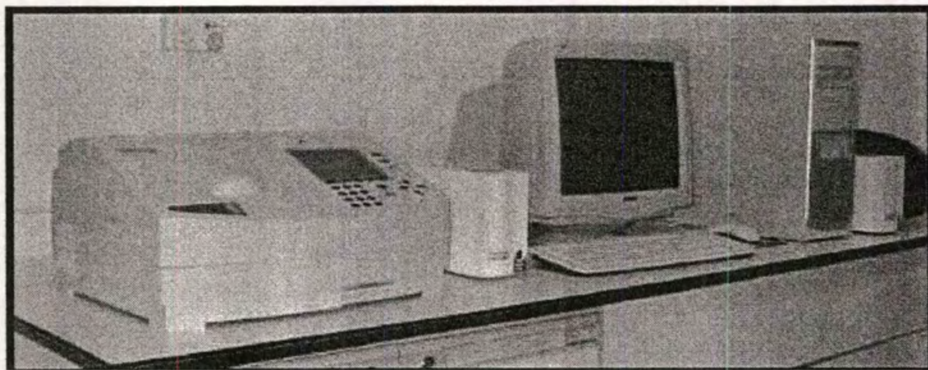

Fig. 5.15 The photograph of UV-VIS spectrophotometer used in this research from Thermo electron, model Heliosγ.

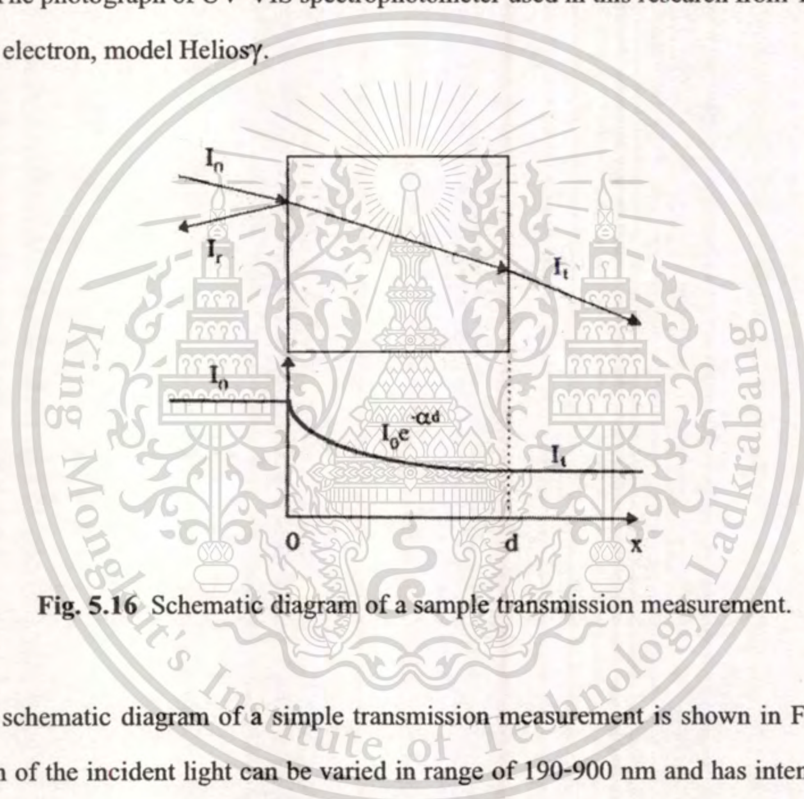

Fig. 5.16 Schematic diagram of a sample transmission measurement.

The schematic diagram of a simple transmission measurement is shown in Fig. 5.16. The wavelength of the incident light can be varied in range of 190-900 nm and has intensity (I_0). The light passes through the sample of thickness (d) and the intensity of the transmitted light is measured by the detector. The detected intensity (I) is defined as

$$I = I_0 e^{-\alpha d}, \tag{5.8}$$

where α is an absorption coefficient. Finally, transmission (T) is obtained from

$$T = \frac{I}{I_0} = e^{-\alpha d}, \tag{5.9}$$

This material is reserved for educational use only, not allowed for commercial use.
Forbidden to modify the content, and cite the document when use.

and then,

$$\alpha = \frac{1}{d}(-\ln T) = \frac{1}{d}\ln\left(\frac{I_0}{I}\right), \tag{5.10}$$

From the transmission spectra, one also can obtain the band gap of the materials. As interband transition of a direct band gap semiconductor,

$$\alpha(h\nu) \cong 4\times10^6\left(\frac{m_r^*}{m_0}\right)^{\frac{3}{2}}\frac{\left(h\nu - E_g\right)^{\frac{1}{2}}}{h\nu}, \tag{5.11}$$

where m_r^* is a reduced electron-hole mass. $h\nu$ is a photon energy of the light source. Thus, $(\alpha h\nu)^2$ is proportional to $(h\nu\text{-}E_g)$. By plotting $(\alpha h\nu)^2$ as a function of photon energy ($h\nu$), the energy gap can be achieved from the intercept of the photon energy axis and the extrapolated line, know as Tauc's plot. For example, the transmission spectra and $(\alpha h\nu)^2$ versus $h\nu$ plot of ZnO thin film, which show the calculated optical band gap of 3.289 eV as shown in Fig.5.17.

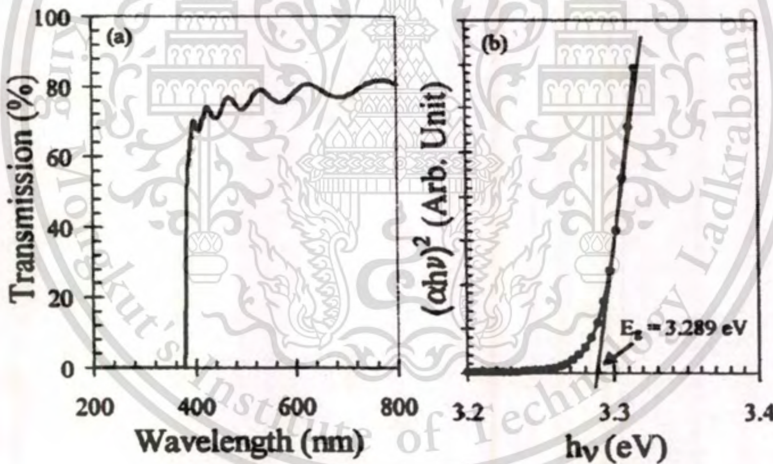

Fig. 5.17 (a) The percentage of transmission spectra of ZnO thin film as a function of wavelength in nm and (b) The plot of $(\alpha h\nu)^2$ versus photon energy ($h\nu$) to achieve the energy gap from the intercept of the photon energy axis and the extrapolated line.

5.3.2 Determination of thickness and optical constants

In recent applications of thin dielectric or semiconductor films, the optical properties of interest cover a photon energy range around the fundamental absorption edge of the material. Optical transmittance provides accurate and rapid information on the spectral range where the material goes from complete opacity to some degree of transparency. As a consequence, the

This material is reserved for educational use only, not allowed for commercial use.
Forbidden to modify the content, and cite the document when use.

problem of retrieving the optical constants ($\tilde{n}(\lambda) = n(\lambda) + ik(\lambda)$) and the thickness (d) of thin films, from transmission data only, is of particular importance. Some useful approximate solutions have been found in cases where the transmittance displays an interference pattern in a highly transparent spectral region. Recently, a pointwise constrained optimization approach was originated by Chambouleyron *et al.*, which allows to solve the general case [6-8]. The method defines a nonlinear programming problem, the unknowns of which are the coefficients to be estimated, with linear constraints that represent prior knowledge about the physical solution. The retrieval of the correct thickness and optical constants of the films does not rely on the existence of interference fringes. This method was successful in retrieving d and $\tilde{n}(\lambda)$ from very different transmission spectra of computer simulation and real deposited films [9-11]. Therefore, the optical parameter extraction was produced by a transmittance data fitting method, name as a pointwise unconstrained minimization approach (PUMA).

Having measurements of the transmission at (many) different wavelengths, the unknowns were estimated. At a first glance, this problem is highly undetermined since, for each wavelength, the single equation

$$\text{Theoretical transmission} = \text{Measured transmission} \quad (5.12)$$

It has three unknowns d, $n(\lambda)$, $k(\lambda)$ and only d is repeated for all values of λ. The driving idea in was to incorporate prior knowledge on the functions $n(\lambda)$ and $k(\lambda)$ in order to decrease the degrees of freedom of equation 5.12 up to a point that only physically meaningful estimated parameters are admitted.

In [7,8], instead of imposing a functional form to $n(\lambda)$ and $k(\lambda)$, the phenomenological constraints that restrict the variability of these functions were stated explicitly so that the estimation problem took the form:

$$Minimize \sum_{\lambda} [Theoretical : tranmission(\lambda) - Measured : transmission(\lambda)]^2 \quad (5.13)$$

In this way, well behaved functions $n(\lambda)$ and $k(\lambda)$ can be obtained without severe restrictions that may damage the quality of the curve fitting as equation 5.12.

This material is reserved for educational use only, not allowed for commercial use.
Forbidden to modify the content, and cite the document when use.

5.4 Electrical characterization method

5.4.1 Resistance measurement

The four-point probe is a very versatile device used widely for the investigation of electrical phenomena. When an electric field (E) is applied to a sample, an electric current will flow. This current density is given by:

$$J = \sigma E, \tag{5.14}$$

where the electrical conductivity of the layer is given by σ. When a rectangular-shaped sample with dimensions l x w x d, were l, w, d are the length, the width and the thickness of this rectangle, respectively, is considered. The resistance is given by:

$$R = \rho\left(\frac{l}{wd}\right), \tag{5.15}$$

If $l = w$ then equation 4.6 becomes:

$$R = \frac{\rho}{d} = R_s, \tag{5.16}$$

The quantity R_s is known as the sheet resistance of one square of the film that is independent of the size of the square. The most common method of measuring this sheet resistance is with the four-point probe method. The effect of the contact resistance could be eliminated with the use of such configuration in Fig. 5.18.

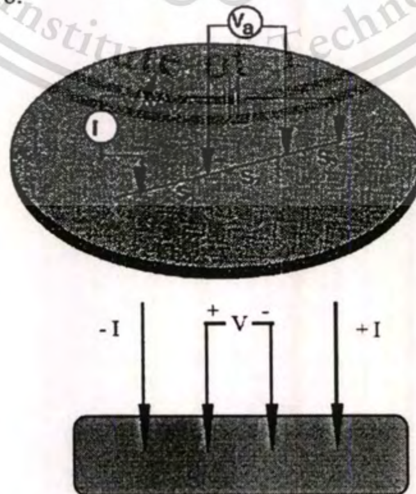

Fig. 5.18 Schematic of in-line (linear) four-point probe configuration.

This material is reserved for educational use only, not allowed for commercial use.
Forbidden to modify the content, and cite the document when use.

In the measurement, the four metal tips have been attached to the test sample. A high impendence current source (I) has been used to supply current through the outer two probes; a voltmeter measured the voltage (V) across the inner two probes. The probe spacing was normally 1 mm or depended on the instrument. The resistivity is given as:

$$\rho = 2\pi x\left(\frac{V}{I}\right), \tag{5.17}$$

were x is the probe spacing. If the material is in the form of an infinitely thin film resting on an insulating support then equation 5.15 can be written as:

$$\rho = \frac{\pi d}{\ln 2}\left(\frac{V}{I}\right), \tag{5.18}$$

Consequently, the sheet resistance (R_s) of the film is derived from the formula:

$$R_s = \frac{\rho}{d} = \frac{\pi}{\ln 2}\left(\frac{V}{I}\right) = 4.532\left(\frac{V}{I}\right), \tag{5.19}$$

where the factor of $\pi/\ln 2$ is on account of the effect of the current extending. If the film thickness is known, the resistivity is readily obtained from

$$\rho = R_s d, \tag{5.20}$$

where d is the film thickness. The mean value of three measurements has been taken in order to reduce the measuring error. The linear four-point probes instrument (OmniMap® RS35, Prometrix) is used in this research, as shown in Fig. 5.19.

King Mongkut's Institute of Technology Ladkrabang

This material is reserved for educational use only, not allowed for commercial use.
Forbidden to modify the content, and cite the document when use.

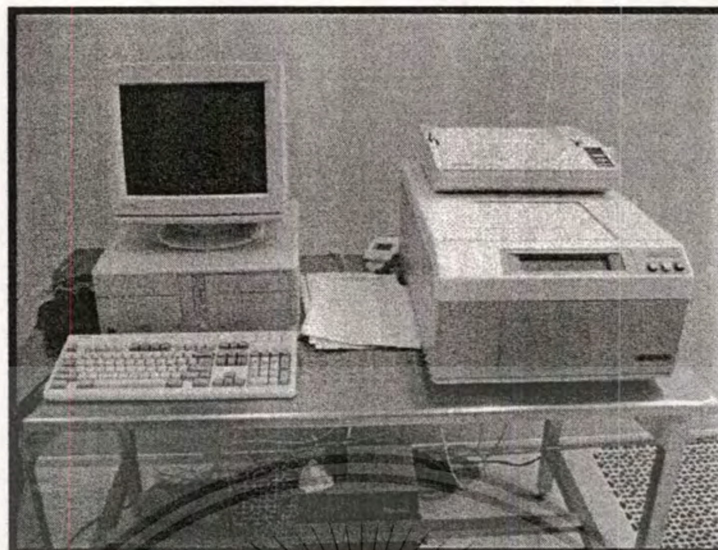

Fig. 5.19 Photograph of the linear four-point probes instrument (OmniMap® RS35, Prometrix).

5.5 Thickness measurement

Film thickness is one of the very important attributes of the films to be determined. Although, during sputtering process, the growth film thickness is monitored by thickness monitor system. The thickness of sputtered thin film was verified again after deposition process. The reason is that many properties of the films are dependent on the film thickness and other parameters such as mass density can be derived from thickness. There are various methods to measure the film thickness, which can be classified into optical method and mechanical method. The geometrical thickness was determined at a film edge by a TENCOR P.10 profilometer. The TENCOR P.10 is a computerized, highly sensitive surface profiler that measures roughness, step height, and other surface characteristics in a variety of applications. During measuring, a diamond-tipped stylus directly contacts the surface and follows height variations as the sample is moved. The height variations are converted into electrical signals, producing a profile. The resulting trace represents a cross-section view with high vertical and spatial resolution. The measurement range spans distance from 200 Å to 65 μm, and the vertical resolution is ~10 Å. Several factors limiting the accuracy of stylus measurements are; (a) Stylus penetration and scratching of films, (b) substrate roughness and (c) vibration of the equipment.

In order to produce a step on the films, a line was marked on the substrate with an aluminum tape before coating and removed later together with the material deposited on the top of it. Film thickness is thus directly read out as the height of the resulting step-contour trace. The

This material is reserved for educational use only, not allowed for commercial use.
Forbidden to modify the content, and cite the document when use.

mark line is made to about 5 mm long, located at the edge of the substrate along its diameter. The measurements are always carried out on the inner side of the mark. In order to reduce the measuring error, a mean value of four measurements at different positions was taken. Consequently, the effective film thickness is derived.

5.6 Chapter summary

The ITO, ITON, ZnO and ZnON thin films grown by reactive gas-timing rf magnetron sputtering in this research were determined by the characterizations methods. The crystallized orientation and surface morphology of thin films were obtained by XRD, XPS FE-SEM and AFM, respectively. The optical band gap energy of thin films was successfully investigated by UV-Visible spectrophotometer. The optical parameter extraction was produced by a transmittance data fitting method, name as a pointwise unconstrained minimization approach (PUMA). The sheet resistance of ITO films was measured by four-point probes instrument. In additional, the thickness of all films was monitored and measured by a quartz crystal microbalance in thickness monitor system and stylus profilometer, respectively. All measurement gave us to understand and reproduced our grown films, which can apply for devices applications.

References

[1] D. L. Smith, **Thin Film Deposition: Principles and Practices**, New York: McGraw-Hill, 1995.

[2] D. A. Glocker, I. Shah, editors, **Handbook of Thin Film Process Technology**, Bristol: Institute of Physics Publishing, 1995.

[3] B. D. Cullity, **Elements of X-Ray Diffraction** 2nd edition, Reading, MA: Addison-Wesley 1978.

[4] L. V. Azaroff, editor, **X-Ray Spectroscopy**, New York: McGraw-Hill, 1974.

[5] G. Binning, C.F. Quate, and Ch. Gerber, "Atomic Force Microscope", **Phys. Rev. Lett.**, vol. 56, 1986, pp. 930-933.

[6] I. Chambouleyron, S. Ventura, E. G. Birgin, and J. M. Martinez, "Optical Constants and Thickness Determination of Very Thin Amorphous Semiconductor Films", **J. Appl. Phys.**, vol. 92, 2002, pp. 3093-3102.

This material is reserved for educational use only, not allowed for commercial use.
Forbidden to modify the content, and cite the document when use.

[7] I. Chambouleyron, J. M. Martinez, A. C. Moretti, and M.Mulato, "Retrieval of Optical Constants and Thickness of Thin Films From Transmission Spectra", **Applied Optics**, vol. 36, 1997, pp. 8238-8247.

[8] I. Chambouleyron, J. M. Martinez, A. C. Moretti, and M. Mulato, "Optical constants of thin films by means of a pointwise constrained optimization approach", **Thin Solid Films**, vol. 317, 1998, pp. 133-136.

[9] E. G. Birgin, I. Chambouleyron, J. M. Martinez, and S. D. Ventura, "Estimation of Optical Parameters of Very Thin Films", **Applied Numerical Mathematics**, vol. 47, 2003, pp. 109-119.

[10] E. G. Birgin, I. Chambouleyron, and J. M. Martinez, "Estimation of the Optical Constants and the Thickness of Thin Films Using Unconstrained Optimization", **J. Comp. Phys.**, vol. 151, 1999, pp. 862-880.

[11] E. G. Birgin, I. Chambouleyron, and J. M. Martinez, "Optimization Problems in the Estimation of Parameters of Thin Films and the Elimination of the Influence of the substrate", **Journal of Computational and Applied Mathematics**, vol. 152, 2003, pp. 35-50.

King Mongkut's Institute of Technology Ladkrabang

This material is reserved for educational use only, not allowed for commercial use.
Forbidden to modify the content, and cite the document when use.

CHAPTER 6

GROWTH AND CHARACTERIZATION OF ITON THIN FILMS

6.1 Introduction

Transparent conducting oxides (TCOs) have been known for more than century. Since the first report of transparent conducting cadmium oxide (CdO) films in 1907 [1], there have been remarkable developments in optoelectronics technology, with progress in ceramic materials paralleling electronics developments. Because of the increasing interest in the interactions of light with electricity and electronically active materials, transparent electrically conducting films are particularly attractive. Many new materials and manufacturing techniques have been developed to satisfy stringent technological requirements. The required quality of the films increases with increasing sophistication of the applications. These materials find applications in wide areas such as liquid crystal displays, transparent electrodes of solar cells, and photodetectors. The simultaneous occurrence of high optical transparency (~90%) in the visible region together with electronic conductivity require the creation of electron degeneracy in wide gap oxides, normally more than 3 eV by suitably introducing nonstoichiometry and appropriate dopants. These conditions can be fulfilled in various oxides of cadmium, tin, zinc, indium, and their corresponding alloys in film form. In view of their practical importance, great deals of basic research and development have been carried out on the electrical and optical properties of indium oxide based ceramics. Including indium-tin oxide ternary system was produced for famous TCOs thin films on glass [2]. Since then, various manufacturing techniques have been attempted to meet both economic and technological demands. Dc and rf sputtering, spray pyrolysis, chemical vapour deposition, and vacuum evaporation are some of the preparation methods currently used. In recent years, solution processes including the sol-gel reaction have arisen as promising techniques for the preparation of materials of technological interest.

In particular, considerable attention has been devoted to the study of tin doped indium oxide (ITO) films with the intention of their utilization in technology. There is also fundamental interest in the electrical conduction and optical transmission mechanism. The association of physical properties with details of the microstructure has been the objective of many solid state

This material is reserved for educational use only, not allowed for commercial use.
Forbidden to modify the content, and cite the document when use.

science studies carried out on these films. Such a quantitative correlation requires knowledge of the crystallite size and orientation, as well as of the density of planar, linear, and point defects. Achievement of the lowest possible resistivity is of practical significance in the respect that it provides some flexibility in selecting the film thickness in order to achieve high optical transmission while still retaining low sheet resistance. However, transparency in the visible region is strongly affected by the electrical properties of the film as well. The mechanisms of electrical conduction and optical transmission are very much interdependent [3]. Good electrical properties can be achieved but often at the expense of transmission. The properties of ITO films are strongly dependent on the preparation method. There is a wide diversity in the reported band gap values as well as the optimized dopant concentration among other properties and parameters. Attempts aimed at understanding the limiting physical phenomena in oxide semiconductors are obstructed by the variety of preparation methods. Many research groups [3-7] have reviewed the methods of preparation and the properties of transparent conductors and their importance in thin film technology. Hamberg and Grangvist [8] summarized the basic optical properties of oxide semiconductors and discussed their applicability to coatings for obtaining the energy efficiency of windows.

In an effort to improve the properties of ITO films, for various technological applications, researchers have been prepared films with modified composition, like Zn-In-Sn-O [9] or ITO:H [10]. Even though the oxynitride of many metals, like Ti, Ta, In, Li-Si-Sn [11-14] have been investigated for their properties and their potential applications in a range of devices, the properties of indium-tin-oxynitride have not been investigated in more details [15].

In this thesis, we were experimented that by introducing nitrogen (N) into the argon (Ar) plasma during the deposition of the ITO by rf sputtering, the properties of the deposited indium tin oxynitride (ITON) thin films were very much dependent on the sputtering conditions. The issue of this section concerns the study of thin films of ITO and ITON fabricated by rf magnetron sputtering with reactive gas-timing technique. Using gas-timing control in the sputtering process, the argon and nitrogen ions have effectively to yield ITON film. This deposition technique is shown to be an extremely useful tool in the growth of ITON polycrystalline structure. It was expected that there was a significant improvement of the optical properties of oxynitride films deposited in pure N plasma when compared to the respective properties of both the ITON film fabricated in a mixture of Ar-N gases and the ITO film deposited in pure Ar plasma. We were observed the optical band gap energy of ITON obtained from UV to green wavelength regions by

This material is reserved for educational use only, not allowed for commercial use.
Forbidden to modify the content, and cite the document when use.

various nitrogen flow rate and rf power conditions. With this approach, the ITO and ITON thin films can be performed in nano-sizes polycrystalline structures. The crystalline structure, morphology, nitrogen incorporated state, sheet resistance and optical band gap energy of the samples were characterized by XRD, XPS, FE-SEM, four-point probe and UV-VIS spectroscopy, respectively.

6.2 Experimental results and discussions of ITO

6.2.1 Substrate cleaning process

In order to obtain high quality film, it is necessary to clean the substrate thoroughly. Since the condition of substrate surface would influent the quality and adhesion of deposited thin films. The glass slides (Menzel-Glaser German model: Superfrost) were used as the substrates for all thin film growth in this study. The glass substrate cleaning process is as below,

1) Wash the glass surface with detergent solution for 15 minutes in ultrasonic bath cleaner.
2) Rinse with water.
3) Etch the oxide and contamination on the surface with standard piranha solution (3:1 mixture of H_2SO_4 (95%) and H_2O_2 (30%) by volume) for 30 minutes.
4) Rinse in deionized (DI) water for 20 minutes.
5) Deep rinse in deionized (DI) water for 30 minutes in ultrasonic bath cleaner.
6) Dry out the surface with nitrogen gas.
7) Bake the substrates in oven at 120 °C for 30 minutes.

Prior to set up the glass substrate on the substrate holder in sputtering chamber, the cleaned glass substrates were purge by blowed nitrogen gas again. Two thickness-verification purpose samples were marked with a strip of an aluminum tape on the surface, which placed one at the central and other one at the peripheral of the substrate holder. After sputtering process, removal of aluminum tape was obtained thickness measurable mark on the sample. The thin film thickness were determined by physical stylus profilometer, and then, compared to the film thickness value from the sputtering thickness monitor.

This material is reserved for educational use only, not allowed for commercial use.
Forbidden to modify the content, and cite the document when use.

6.2.2 ITO thin films growth without gas-timing

6.2.2.1 Sputtered ITO thin film in Ar plasma

The design of experiment is required with first two-point as no rf reflected and achieved the lowest resistance, which pure Ar was used as a plasma gas. A compound ceramics indium oxide and tin oxide (90% In_2O_3 + 10% SnO_2) from Kurt J. Lesker was used as a target material with a diameter of 3 inch. The substrate distance to the target is 50 mm. The base pressure of the chamber was $6x10^{-7}$ mbar. The Ar purity of 99.999% was used to bombard the target with rf power 30 W. Figure 6.1 shows photograph through the chamber window during Ar plasma process in the vacuum chamber, the plasma of Ar gas shows purple emission.

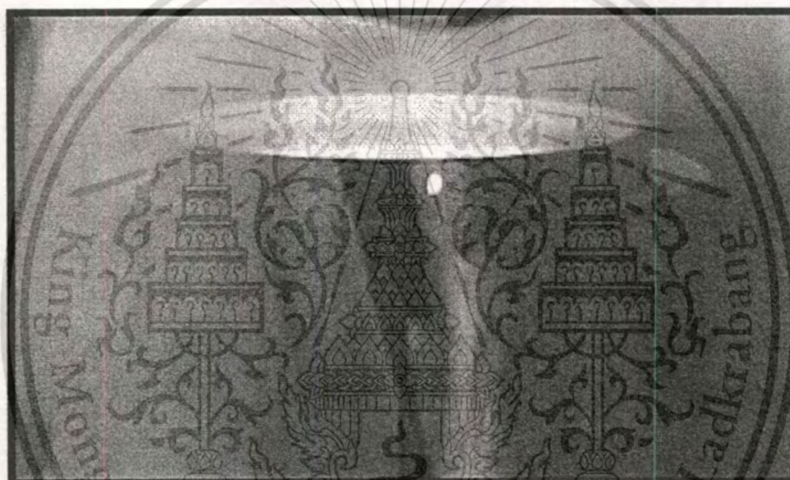

Fig. 6.1 The argon plasma is emitted purple light over the sputtering target during the sputtering process.

King Mongkut's Institute of Technology Ladkrabang

The flow rate of Ar was varied of 8, 9, 10, 11 sccm and the film growth rates were recorded. The excess ions in the chamber may collies each other affected to the decreasing of sputtering yield so the thin film growth rate was decreased when the flow rate of Ar increased. From this experiment, the Ar flow rate of 10 sccm was selected because the plasma is stable with no rf reflection effect during the process and the film resistance of 70-100 ohm at the central area and 20-40 ohm at the peripheral area was achieved, as shown in Fig 6.2.

This material is reserved for educational use only, not allowed for commercial use.
Forbidden to modify the content, and cite the document when use.

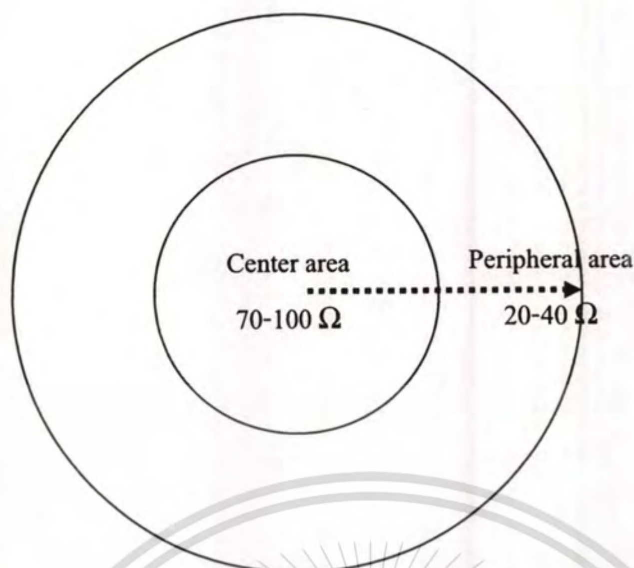

Fig. 6.2 The different of ITO resistance at the central area and peripheral area.

6.2.3 ITO thin films growth with gas-timing

From the previous report on successfully growth of ITO by Klamchune *et al.* [16], the special technique was used to sputter ITO thin film on plastic substrate at RT with a commercial rf sputtering system, namely gas-timing technique. The ITO sputtering deposition was conducted with an Edwards AUTO 500 plant equipped with a RF magnetron sputtering set. The sputtering target was a compound ceramics indium oxide and tin oxide (90% In_2O_3 + 10% SnO_2) from Kurt J. Lesker. The glass substrates were not intentionally heated during the sputtering process. The main adjustable process parameters were the rf power and the sputtering gas flow rate. A quartz crystal microbalance was employed to monitor film thickness during deposition. The chamber was evacuated to 1.0×10^{-6} mbar. The target-substrate distance was 50 mm.

An on-off gas-timing sequence was used to control the flow of argon into the sputtering chamber. This was realized by a mass flow controller with an external control program. The flow rate of argon during the 'on' sequence was fixed at 10 sccm. Figure 6.3 depicts the gas-timing sequence of argon gas that flows for 50 seconds then stops for 2 seconds. The RF plasma sputtering conditions are listed in Table 6.1. The thickness of the deposited ITO thin films was all normally set at 200 nm.

This material is reserved for educational use only, not allowed for commercial use.
Forbidden to modify the content, and cite the document when use.

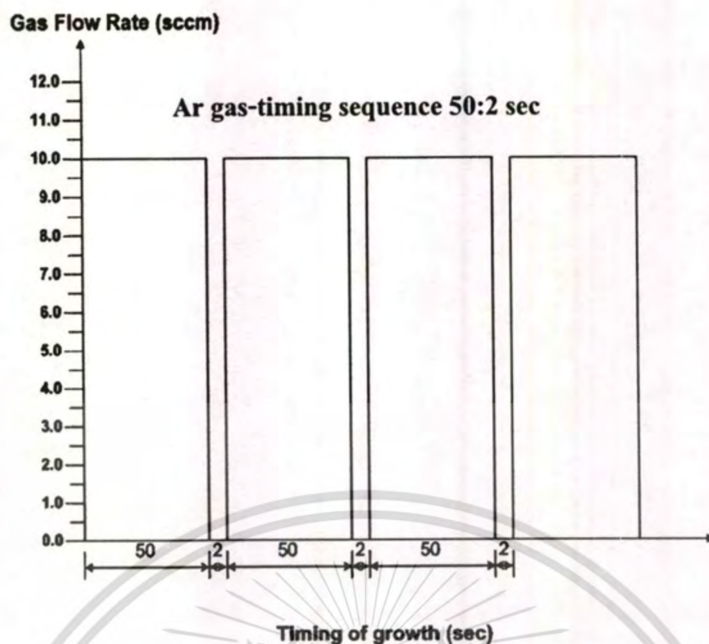

Fig. 6.3 Schematic representation of the 50:2 on-off gas-timing sequence of argon during sputtering deposition with a flow rate of 10 sccm (on) for 50 seconds and zero flow (off) for 2 seconds.

After the sputtering process, the film thickness was measured by a profilometer (TENCOR, Alphastep 500). The crystallinity of the films was investigated by X-ray diffractometer (Bruker, D8) using CuKα with the radiation wavelength (λ) of 0.154056 nm. The surface morphology of selected film was scanned by the field emission scanning electron spectroscopy (Hitachi, S4700). The optical transmittance spectroscopy was performed with a single beam UV-VIS spectrophotometer (Thermo electron, Heliosγ).

Table 6.1 Sputtering conditions used for deposition of ITO thin films

Deposition parameters	Conditions
Base pressure	1.0×10^{-6} mbar
RF power	10, 20, 30, 40 Watt
Substrate-target distance	50 mm
Substrate temperature	Unheated and uncontrolled
Sputtering pressure	2.8×10^{-3} mbar, argon gas activated
Ar flow rate	8, 9, 10, 11 sccm
Ar gas-timing (on:off)	50:2 seconds

This material is reserved for educational use only, not allowed for commercial use.
Forbidden to modify the content, and cite the document when use.

6.2.3.1 Effect of reactive gas-timing on the properties of ITO

Crystal orientation of the samples is studied via X-ray diffraction technique. We observed that these films deposited with gas-timing and without gas-timing timing at ambient temperature, which were showed significant difference in crystalline property. For ITO films, without gas-timing technique have a strong (400) diffraction peak when increasing film thickness from 200 to 500 nm which indicates a preferred orientation along [100] direction, whereas the ITO film, with gas-timing technique has a strong in (222) diffraction peak which indicates a preferred orientation along [111] direction as shown in Fig. 6.4. The numbers above the XRD peaks of ITO corresponded to the values of crystal faces indices (hkl) are fairly in agreement with the data of $In_2Sn_2O_{7-x}$ powders recorded in the JCPDS No. 39-1058. This variation of the orientation from (400) to (222) as the special deposition technique is gas-timing rf magnetron sputtering, which this result also found with increasing the substrate temperature in rage of 200 to 400 °C by Meng et al. [16]. From this effect, the gas-timing technique is may be produced the average energy of the partial sputtered from the cathode is considerably higher than that of conventional sputtering. Therefore, we can fabricated high (222) preferred orientation crystal of ITO thin films at ambient temperature as well. The SEM images show surface morphologies of ITO thin film in nanocrystal size in Fig. 6.5.

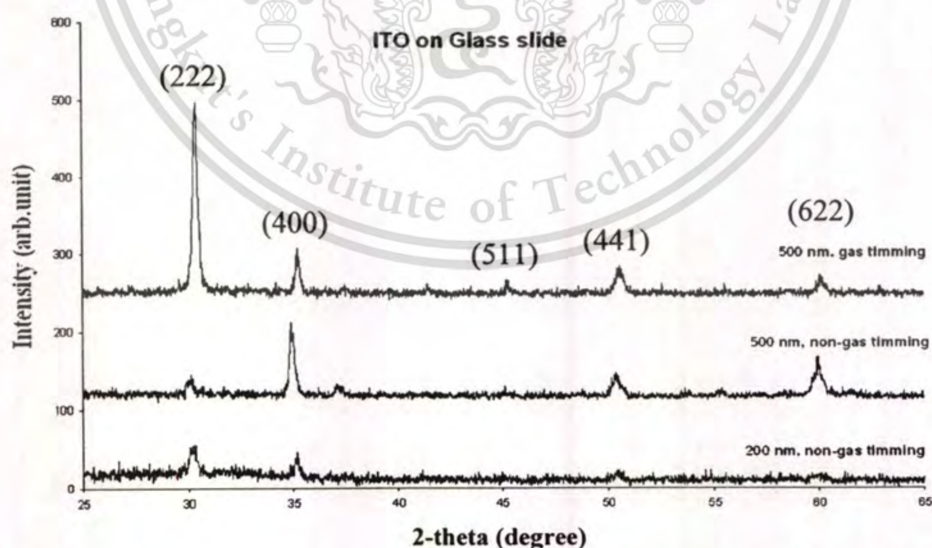

Fig. 6.4 X-ray diffraction patterns of ITO thin films grown with difference thickness of 200 nm (non gas-timing), 500 nm (non gas-timing), and 500 nm (gas-timing), from bottom to top patterns, respectively.

This material is reserved for educational use only, not allowed for commercial use.
Forbidden to modify the content, and cite the document when use.

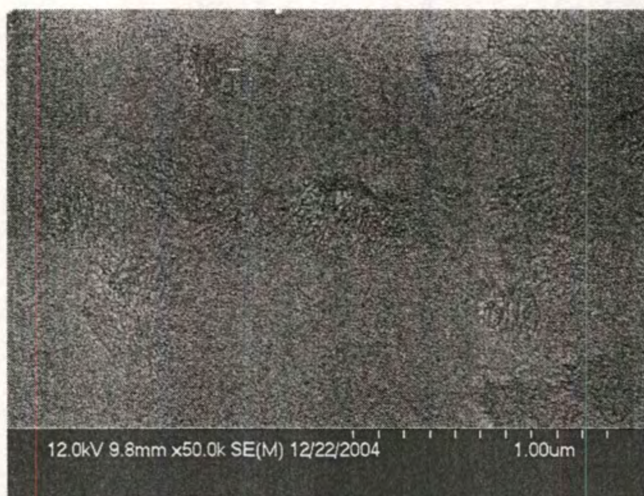

Fig. 6.5 SEM image of 200 nm ITO thin film grown by gas-timing technique.

The gas-timing technique was not only affected to ITO crystal structure but also the film resistance was reduced. The 200 nm ITO film was deposited by gas-timing technique, whish is a low resistance of 50 ohm at the central area and 10 ohm at the peripheral area was achieved. Actually, the sheet resistance of the film was verified at ~15 ohm/square by the linear four-point probe system. The optical transmittance of the films was measured with a single beam spectrophotometer; scanned in the UV-Visible region (300~1000 nm). The optical transmission spectra of ITO thin film show that the films are highly transparent in visible region, as shown in Fig. 6.6. The average transmission was found higher than 85% in visible light region.

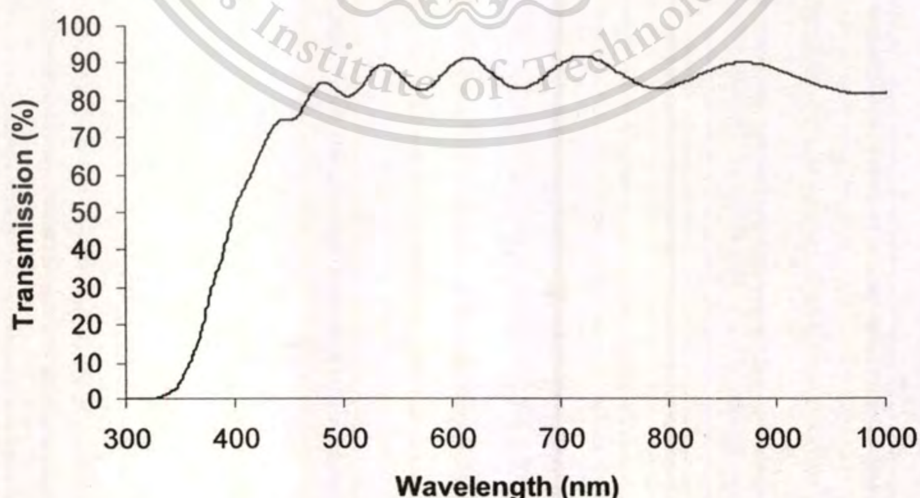

Fig. 6.6 Transmission spectra of a ITO thin film deposited by gas-timing technique with thickness of 200 nm.

This material is reserved for educational use only, not allowed for commercial use.
Forbidden to modify the content, and cite the document when use.

6.2.3.2 Effect of film thickness on the properties of ITO

The XRD pattern of ITO thin film was deposited on glass substrate with thickness of 200 nm as shown in Fig. 6.7. The result has XRD peaks at 2θ = 30.273°, 35.165°, 50.978° and 59.940° which correspond to (222), (400), (441) and (622) planes, respectively, indicated as a polycrystalline cubic bixbyite structure. The SEM micrograph of ITO thin film in Fig. 6.5 has the grain size smaller than 100 nm.

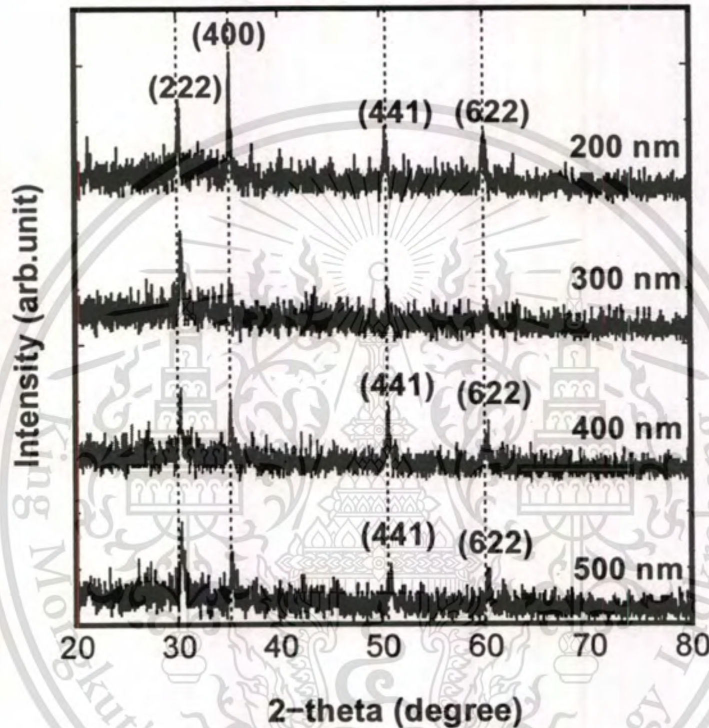

Fig. 6.7 XRD results of ITO thin films grown by gas-timing rf magnetron sputtering with different thickness of 200, 300, 400 and 500 nm.

From, the film thickness was increased from 200 nm to 500 nm, which effected to the (400) diffraction peak was decreased, where as the (222) was increased. As the results, the higher film thickness has a higher density than the other one, then the (222) preferred orientation is exhibited.

6.2.3.3 Effect of rf sputtering power on the properties of ITO

The 200 nm thick ITO thin films were grown on plain glass substrates by gas-timing technique. The base pressure of chamber was $1.0\text{x}10^{-6}$ mbar. The flow rate of Ar was fixed at 10 sccm and gas-timing at 50:2 sec. In this section experiment, the rf power of sputtering was varied at 10, 20, 30 and 40 W, respectively. The crystalline structure and surface morphology of all

This material is reserved for educational use only, not allowed for commercial use.
Forbidden to modify the content, and cite the document when use.

samples were investigated by XRD and SEM. The sheet resistance and transmittance of films were also investigated. Figure 6.8 shows XRD results from ITO thin films grown with rf sputtering power of 10, 20, 30 and 40 W, respectively. The XRD peaks at 30.273° and 35.165° of samples correspond to the crystallinity in plane of (222) and (400), respectively. The surface morphology of all samples was shown in Fig. 6.9. In other hand, the preferred properties of ITO is actually required on low resistivity and high transparent. At proper sputtering rf power is 30 W, due this condition was produced the lower sheet resistance and remained high transparent.

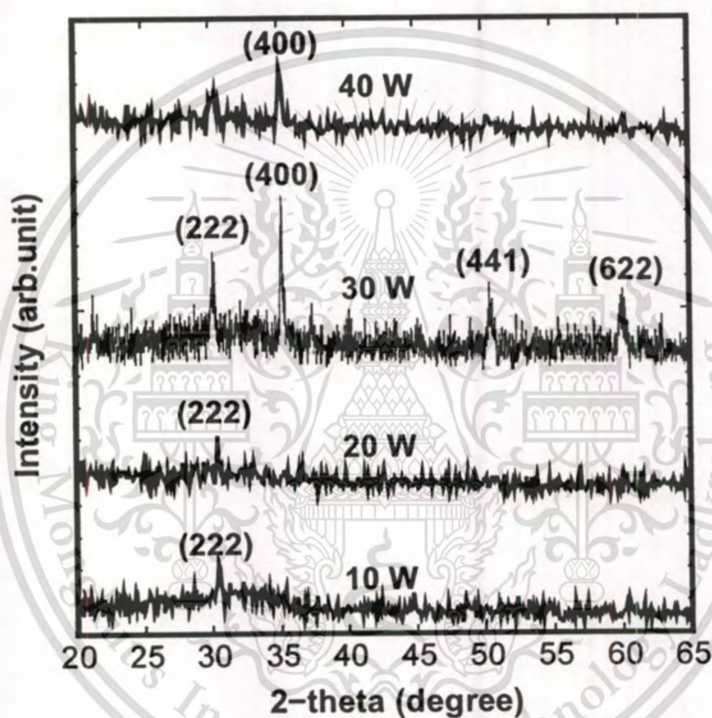

Fig. 6.8 XRD results of ITO thin films grown by gas-timing rf magnetron sputtering with different RF sputtering power of 10, 20, 30 and 40 W.

This material is reserved for educational use only, not allowed for commercial use.
Forbidden to modify the content, and cite the document when use.

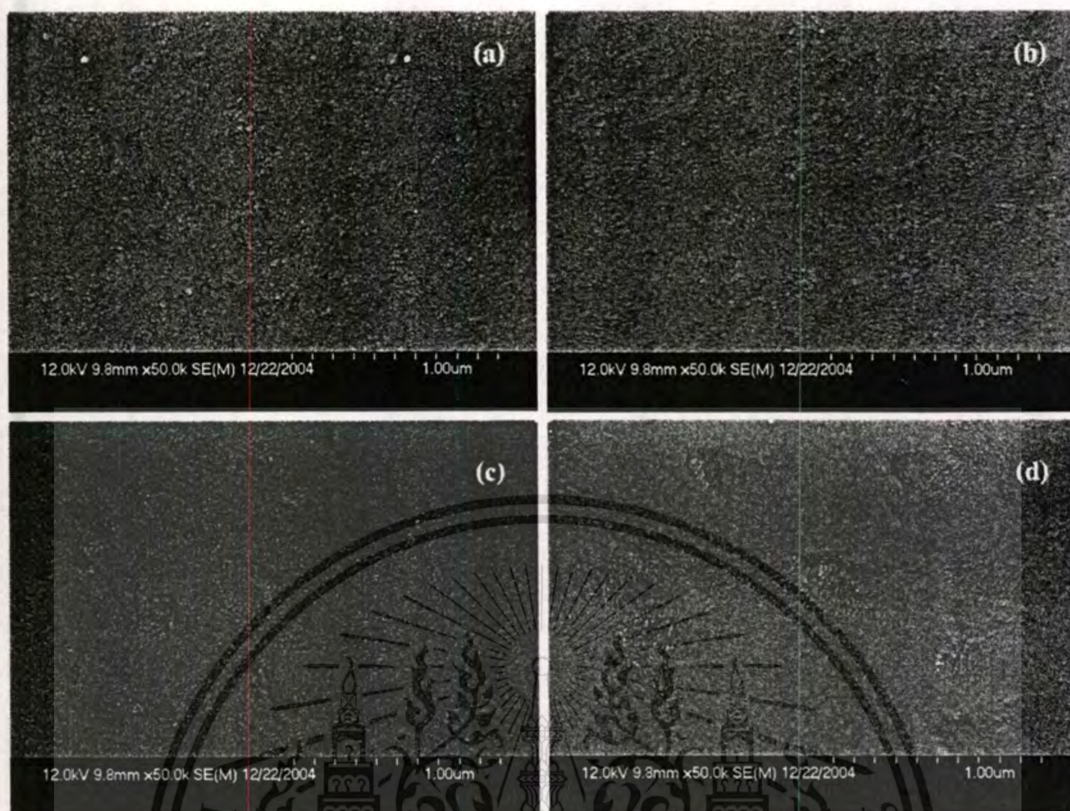

Fig. 6.9 SEM images of ITO thin films grown with different RF sputtering power at (a) 10, (b) 20, (c) 30 and (d) 40 W.

6.2.3.4 Effect of Ar flow rate on the properties of ITO

The 200 nm thick of ITO thin films were grown on plain glass substrates by gas-timing technique. The various Ar flow rate conditions were used to deposited ITO thin films by rf power of 30 W and gas-timing at 50:2. In this experiment, the flow rate of Ar was varied in range of 8, 9, 10 and 11 sccm. The base pressure of the chamber was 1.0×10^{-6} mbar and the sputtering pressure was in range of 3.0×10^{-3}-4.0×10^{-3} mbar. The crystalline structure of all samples was investigated by XRD as shown in Fig. 6.10. The result has XRD peaks at $2\theta = 30.273°$, 35.165°, 50.978° and 59.940° which correspond to (222), (400), (441) and (622) planes, respectively, indicated as a polycrystalline cubic bixbyite structure. At the lowest Ar flow rate, it unobserved any peak because the film was not completely grown-up due to low sputtering yield. However, the intensity of (400) peak also seem to decrease with an increase in Ar flow rate. But the intensity of (222) peaks were increased. The sheet resistance of all thin films as most the same value in range of 8-10 ohm/□ and transmittance of films were also investigated as shown in Fig. 6.11. The highest optical transmittance of ITO thin film occurs at the Ar flow rate of 10 sccm.

This material is reserved for educational use only, not allowed for commercial use.
Forbidden to modify the content, and cite the document when use.

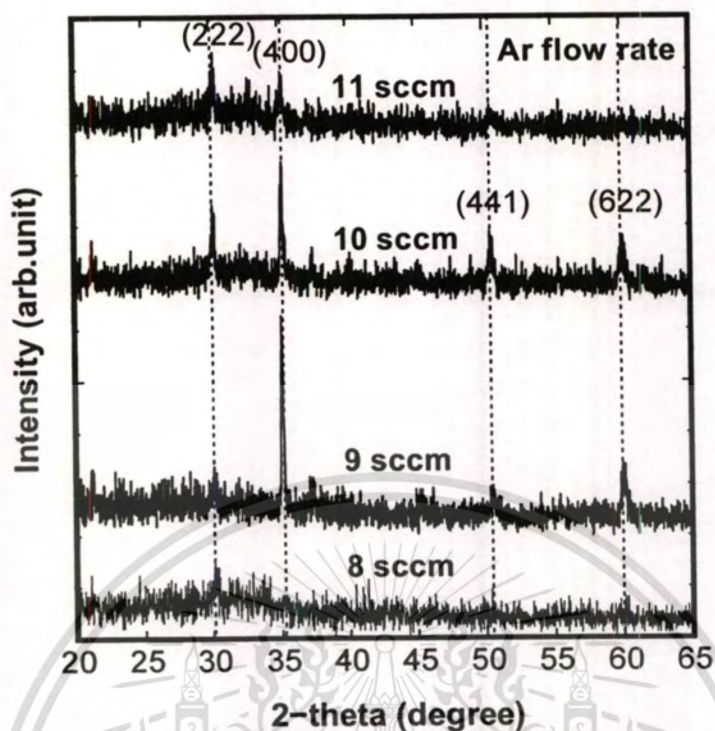

Fig. 6.10 XRD results of ITO thin films grown by gas-timing rf magnetron sputtering with different Ar flow rate conditions of 8, 9, 10 and 11 sccm.

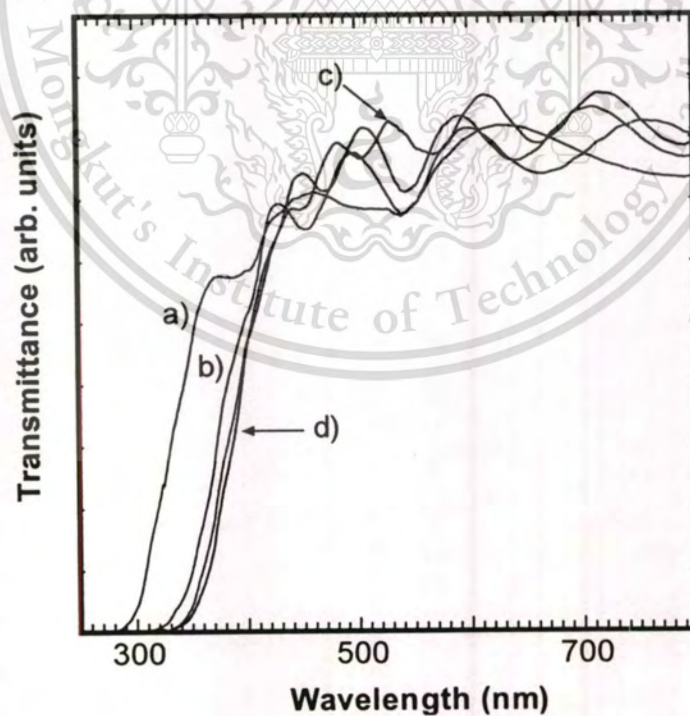

Fig. 6.11 Transmission spectra of a ITO thin films deposited by gas-timing rf magnetron sputtering with different Ar flow rate conditions of (a) 8, (b) 9, (c) 10 and (d) 11 sccm.

This material is reserved for educational use only, not allowed for commercial use.
Forbidden to modify the content, and cite the document when use.

6.3 Experimental results and discussions of ITON

As the deposited ITO thin films in the previous section, we were provided ITO thin films by gas-timing technique. On the other hand, this experiment was produced ITON thin films by reactive nitrogen technique. Moreover, the focused properties comparison between ITO and ITON was discussed. The firstly comparing of surface morphology of ITO and ITON is shown Fig. 6.12. The SEM image of ITON thin film was clearly alternated from ITO thin film. From the required properties of ITO are low resistivity and high transmission in visible light region. Therefore, this section, we report on remarkable structural, optical and electrical properties of ITO and ITON.

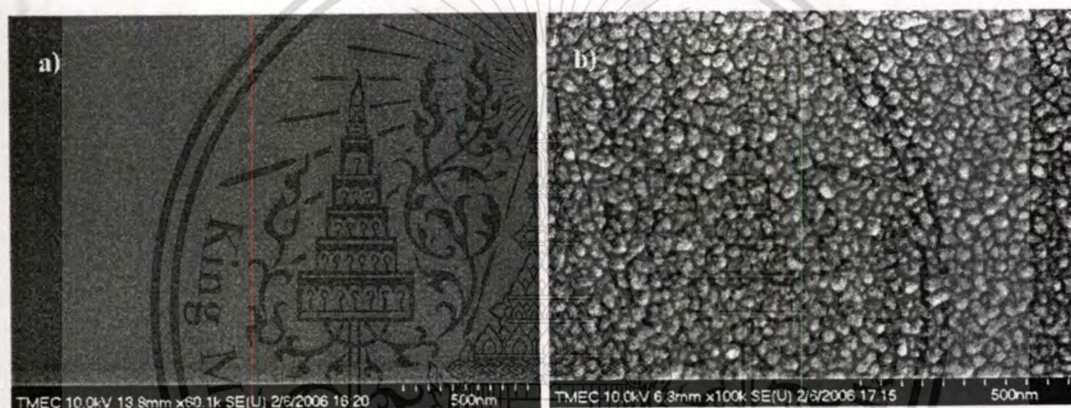

Fig. 6.12 SEM images of (a) ITO and (b) ITON thin films grown by rf magnetron sputtering with different sputtering gas of pure Ar and N, respectively.

6.3.1 Effect of gas flow rate on the properties of ITON

This investigation was discovering the new optically functional of ITON by nitrogen-incorporated into ITO. Therefore, this section, we study on structural, optical and electrical properties of ITO and ITON, which focused on the redshift of the optical band edge energy by various nitrogen flow rate conditions.

In sputtering process, the rf power was set at 30 watt. The deposition rate of the ITO and ITON films deposited by pure argon flow rate of 10 sccm was 15 nm/min, which it was reduced to 6 nm/min by pure nitrogen flow rate of 10 sccm. In additional, increasing the gas flow rate to 20 sccm hence reduced the deposition rate for both of ITO and ITON. The deposition rate of the ITO and ITON films deposited by pure argon flow rate of 20 sccm was 12 nm/min, as the same

This material is reserved for educational use only, not allowed for commercial use.
Forbidden to modify the content, and cite the document when use.

results it was reduced to 4 nm/min by pure nitrogen flow rate of 20 sccm. The deposition rate of the ITON films were found to be lower than that of the ITO films, which is in accordance with the lower sputtering yield of nitrogen than that of Ar [17]. The plasma species are known to be less energetic as the difference argon and nitrogen plasma. Thus, the decrease in deposition rate with nitrogen in the plasma, as the results are attributed to the lower nitrogen sputtering yield compared to that of argon [18, 19].

Crystal orientation of the samples is studied via x-ray diffraction technique. We observed that these films remain in a poly-phase (either amorphous or crystalline) from pure argon (ITO) deposition up to a certain pure nitrogen flow (ITON), at which the films became less crystalline property. For ITO films, with the pure argon has (211) and (400) crystal orientations, whereas the oxynitride films were amorphous shown in Fig. 6.13. The numbers above the XRD peaks of ITO correspond to the values of crystal faces indices (hkl) are fairly in agreement with the data of $In_2Sn_2O_{7-x}$ powders recorded in the JCPDS No. 06-0416. In the other hand, the XRD peaks of ITON thin films were not found, with increasing of nitrogen flow rate in nitrogen-argon mixed sputtering process.

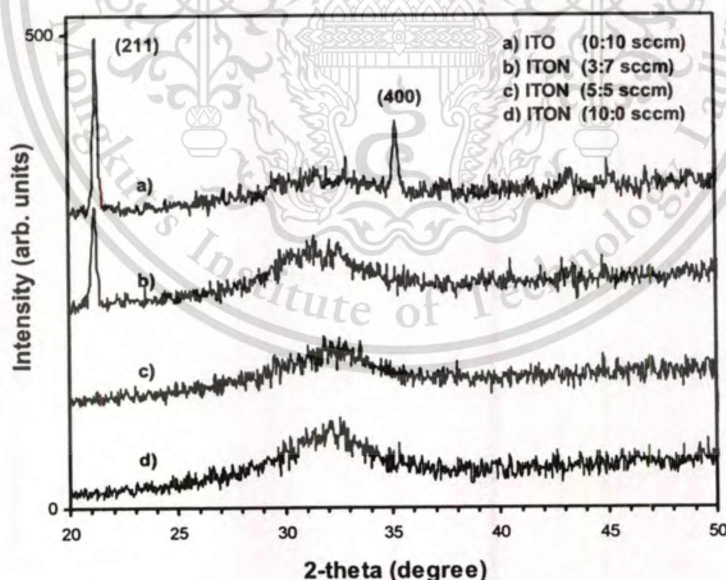

Fig. 6.13 The XRD patterns of ITON films deposited at various N_2 flow rate ratios in nitrogen-argon (N_2: Ar) mixed which are fed into the sputtering chamber, the maximum flow rate of argon is 10 sccm (sputtering pressure ~$3.0x10^{-3}$ mbar); ITO(0:10), 30%(3:7), 50%(5:5), and 100%(10:0), all films have thickness of 1000 nm.

This material is reserved for educational use only, not allowed for commercial use.
Forbidden to modify the content, and cite the document when use.

The ITON film, this structure is changed, while for nitrogen flow, the systems favour to form their corresponding tin-substitute indium site in indium oxide structure with the thermodynamically stable phase [20]. The increasing of nitrogen flow, the films maintain the metal-oxide structure as long as sufficient oxygen is present until the films form metal-oxide-nitride structure by mean of deficiency of oxygen in the mixed-gas glow discharge process. This can be explained by the lower reactivity of nitrogen which the formation of metal-nitrogen bonds less than metal-oxygen bonds [21]. Therefore, it can be understood that the increase of nitrogen and decrease of argon in the reactive nitrogen-argon mixture until the pure nitrogen flow, the probability to from indium-tin-oxide-nitride compounds such as indium nitride.

The sheet resistances of the ITO and ITON films were measured by the resistivity mapping system four point probes. The sheet resistivity of films was plotted with the nitrogen flow rate as shown in Fig 6.14. The sheet resistance of thin films also rises from ~15 to ~34 ohm/□ when the N_2 flow rate increases. In fact, the electrical property of ITO is well known to be related to the oxygen vacancies in the thin films, one vacancy generates two electrons on the conduction band to satisfy the charge neutrality. Consequently, it is expected that the increasing of nitrogen flow rare has an effect on increasing of ITON films sheet resistance. From these results we suggested that, the increase of sheet resistance with higher nitrogen flow rate is attributed to the diffusion of nitrogen into films caused the decrease the oxygen vacancies in the structure of the films [22].

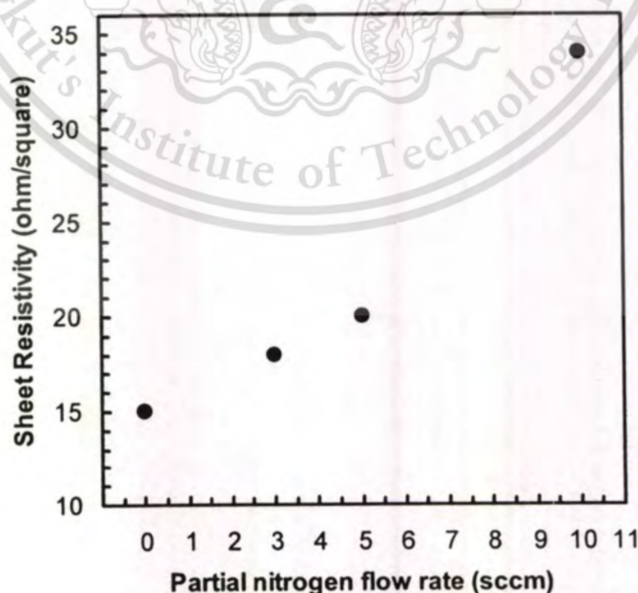

Fig. 6.14 The sheet resistivity of ITO and ITON films was plotted with the various N_2 flow rate ratios in nitrogen-argon (N_2: Ar) mixed gas.

This material is reserved for educational use only, not allowed for commercial use.
Forbidden to modify the content, and cite the document when use.

The film transmittances in the UV-Visible range (300-1100 nm) were measured in different nitrogen-argon mixed flow rate and film thickness. The transmittance for the ITON films deposited at the different nitrogen-argon mixed plasma in the sputtering process was shown in Fig. 6.15, along with the transmittance of the glass substrate as the baseline. The most important results in the transmission spectra of ITON films, the fundamental absorption edge shifts toward longer wavelength side with increasing nitrogen flow rate into the sputtering process. The absorption coefficients were calculated from the transmission spectra results using unconstrained minimization algorithm [23]. To determine the absorption edge energy or optical band gap energy (E_{opt}) of the films, the famous method where the absorption edge energy of ITO is evaluated in standard manner from a plot of α^2 as function the energy of the incident radiation and extrapolated the linear part of the curve to intercept the energy axis.

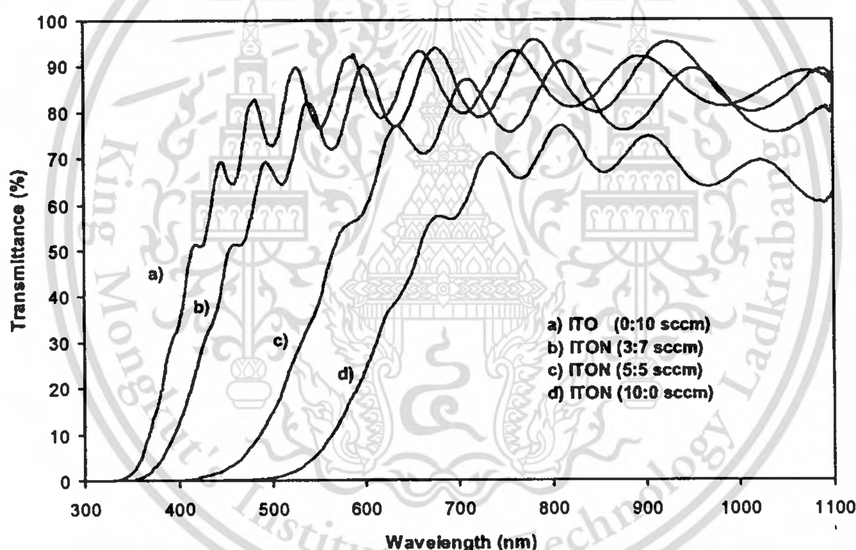

Fig. 6.15 Transmission spectra of the films prepared at various N_2 flow rate ratios in nitrogen-argon (N_2: Ar) mixed which are fed into the sputtering chamber, the maximum flow rate of argon is 10 sccm (sputtering pressure ~3.0×10^{-3} mbar); ITO(0:10), 30%(3:7), 50%(5:5), and 100%(10:0), all films have thickness of 1000 nm.

The relationship between E_{opt} and the nitrogen flow rate in sputtering process is showed in Fig. 6.16, indicate the E_{opt} decreased from 3.35 to 2.21 eV with increasing nitrogen flow rate from 2 to 10 sccm. The observed red shift in transmittance, and consequently the decrease of the optical band gap (E_{opt}) of ITON, could be explained by the difference in ionicity between In-Sn-O and In-Sn-N bonds. According to the Pauling theory [24], ionicity in an ionic bond increases with

This material is reserved for educational use only, not allowed for commercial use.

Forbidden to modify the content, and cite the document when use.

the difference in values of electron negativity between two elements formed the single bond. The electron negativity of O (3.5) is larger than that of N (3.0), which indicates that the In-Sn-O bond has larger ionicity than the In-Sn-N bond. The decrease in E_{opt} is probably attributed to the decrease in ionicity due to the formation of In-Sn-N bonds. Thus, the shift of optical band gap observed for the ITON films is possibly related to basic structural changes, which take place with the introduction of nitrogen into the film.

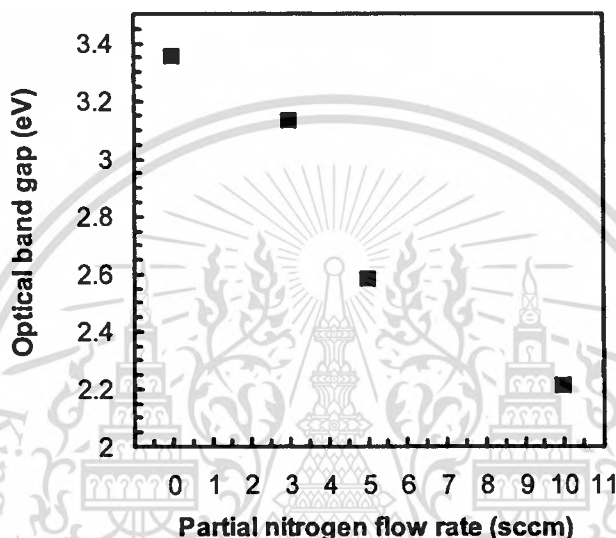

Fig. 6.16 The relationship between optical band gap and the various N_2 flow rate ratios in nitrogen-argon (N_2: Ar) mixed gas, which are fed into the sputtering chamber, the maximum flow rate of argon is 10 sccm (sputtering pressure ~3.0×10^{-3} mbar); ITO(0:10), 30%(3:7), 50%(5:5), and 100%(10:0), all films have thickness of 1000 nm.

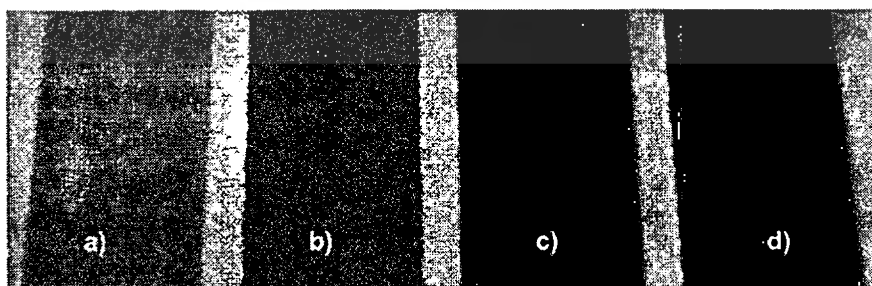

Fig. 6.17 Camera image of approximately 1 μm thick ITON films reflecting their high optical transparency and its color, a) ITO (0:10sccm), b) ITON (3:7 sccm), ITON (5:5 sccm) and ITON (10:0 sccm).

This material is reserved for educational use only, not allowed for commercial use.
Forbidden to modify the content, and cite the document when use.

As the results, the films colours were changing from clear to brown depend on the nitrogen flow rate conditions as shown in Fig. 6.17. Furthermore, it became also apparent that the properties of the ITON films depend not only on the amount of nitrogen in plasma but also on the amount of nitrogen in the structure and consequently on the rf power used in sputtering process.

6.3.2 Effect of rf sputtering power on the properties of ITON

Due to the previous experimental on effect of gas flow rate, the nitrogen incorporated ITO thin films were deposited by various of gas flow rate conditions at fixed rf power of 30 W. As the results indicated that the optical band gap shift was depended on the amount of nitrogen incorporated into ITO thin films. Hence, the rf power is another one significant parameter in the sputtering process. Then we were studied focus on the effect of rf power on the optical properties of ITON by different sputtering rf power condition of 30, 50, 70, 100 and 150 W. The transmission spectra of all films are shown in Fig. 6.18. The transmittance in the UV-Visible range (300-1000 nm) for the ITON films deposited at the five different rf power conditions, along with the transmittance of the glass substrate. The films after deposition showed different transmittance. When increasing the rf power from 30 W to 100 W, the transmittance of the ITON films were decreasing, and the most important change by increasing rf sputtering power was the shift of the onset of transmittance to higher wavelength. But the high rf sputtering power at 150 W, the transmittance curve was shifted to lower wavelength.

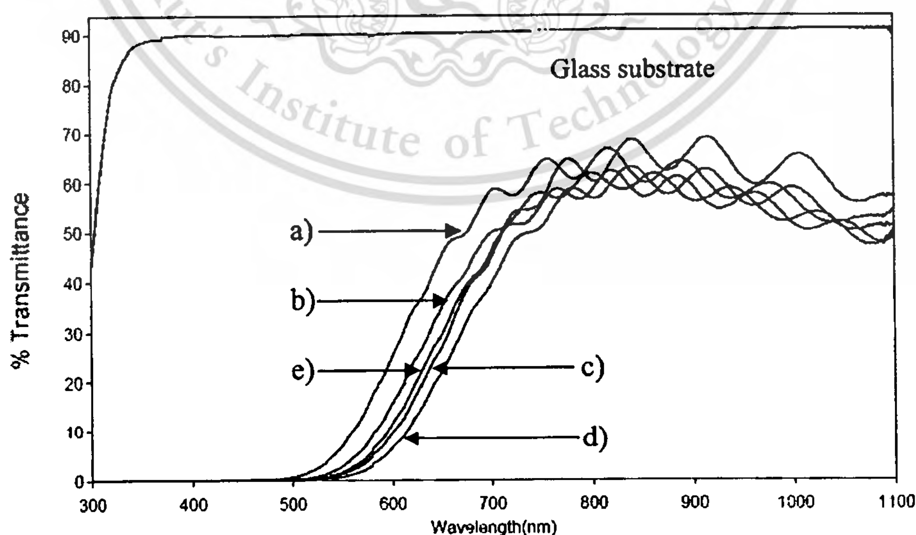

Fig. 6.18 Transmission spectra of the ITO films prepared at various rf power of (a) 30, (b) 50, (c)70, (d) 100 and (e) 150 W, all films have thickness of 1000 nm.

This material is reserved for educational use only, not allowed for commercial use.
Forbidden to modify the content, and cite the document when use.

The observed red shift in transmittance, and consequently the decrease of the optical band gap of ITON films, can be explained by the effect of more nitrogen incorporated in the structure of the ITON films by increased rf sputtering power. The critical value of rf sputtering power is 100 W for maximum red shift phenomenon, and then it will be changed to higher wavelength when increasing the rf sputtering power of 150 W. Thus, the lower band gap observed for the ITON films (30, 50, 70 and 100 W) were possibly related to basic structural changes, which take place with the introduction of nitrogen into the films. However the excess rf sputtering power is affected to amount of nitrogen incorporated in ITON films. The sputtered ITON film by rf sputtering power of 150 W was showed the blue shift in transmittance. Furthermore, it became also apparent that the properties of the ITON films depend not only on the amount of nitrogen in plasma (nitrogen flow rate) but also on the amount of nitrogen in the structure and consequently on the rf power used.

6.3.3 Effect of film thickness on the properties of ITON

The film thickness of ITON was directly effect to the optical properties by the absorption phenomenon. In other hand, the increase of film thickness was also increasing the resistivity, due to the increasing of nitrogen incorporated into ITO. The transmittance spectra of ITON thin films with different thickness of 200, 400, 600, and 1000 nm are shown in Fig. 6.19. The calculated optical band gap was shifted to lower photon energy with thickness increasing. This result is good agreement to the absorption model [25].

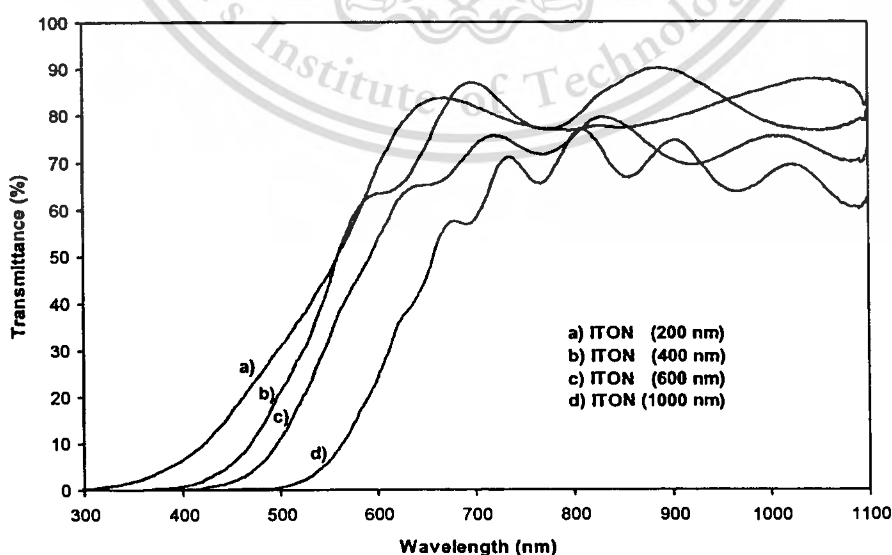

Fig. 6.19 Transmission spectra of the ITON prepared at various film thickness of 200, 400, 600, and 1000 nm.

This material is reserved for educational use only, not allowed for commercial use.
Forbidden to modify the content, and cite the document when use.

6.4 Chapter summary

In this chapter, we first studied with in doped indium oxide (ITO) thin film deposition. ITO is one material, which used to TCOs in many devices application. The two requirement properties of ITO are low resistance and high transmittance. Achievement of the lowest possible resistivity is of practical significance in the respect that it provides some flexibility in selecting the film thickness in order to achieve high optical transmission while still retaining low sheet resistance. However, transparency in the visible region is strongly affected by the electrical properties of the film as well. For that reason, we deposited ITO thin films on cleaned glass substrate by the special technique with a conventional rf magnetron sputtering system, namely gas-timing technique. The focus properties of all the samples thin films were investigated. The enhanced optical property of ITO was consequently approached, which introduced nitrogen to ITO to from ITON thin films. The crystalline structure, morphology, nitrogen incorporated state, sheet resistance and optical band gap energy of the samples were characterized by XRD, XPS, FE-SEM, four-point probe and UV-Visible spectroscopy, respectively.

Now we successfully fabricated high quality ITO thin films on unintended-heat glass substrate by gas-timing rf magnetron sputtering. As the experimental results, the ITO films grown at very low rf power but still obtained theirs important properties. Therefore, we also fabricated ITO thin film on other substrate such as plastic and some organic material. For indium tin oxynitride (ITON) thin films, we had shown that by introducing nitrogen (N) into the argon (Ar) plasma during the deposition of the ITO by rf sputtering, the properties of the deposited (ITON) thin film were very much dependent on the amount of nitrogen in the plasma during deposition. It was found that there was a significant improvement of the optical properties of oxynitride films deposited in pure N plasma when compared to the respective properties of both the ITON film fabricated in a mixture of Ar-N gases and the ITO film deposited in pure Ar plasma.

We concluded that there was a significantly variation of the optical properties of ITON films deposited on glass in mixed N_2-Ar plasma (identify by nitrogen fraction) when compared to the respective properties of the ITO film deposited in pure Ar plasma. The absorption coefficients are calculated from the transmission spectra to determine the optical band gap energy. The absorption edge of the ITON films deposited in pure N_2 plasma was shifted towards lower energies to 2.21 eV from 3.35 eV (ITO deposited in pure Ar plasma). The sheet resistance of films also rises from ~15 to ~34 ohm/square when the N_2 concentration increases. It is believed that the incorporation of more nitrogen into the film could tailor the optical and keep electrical

This material is reserved for educational use only, not allowed for commercial use.
Forbidden to modify the content, and cite the document when use.

properties of the ITON films. As the final point, ITON is a promising conductive optically functional material that can use as a novel optical filter in near UV to visible region.

References:

[1] B. J. Ingram, G. B. Gonzalez, D. R. Kammler, M. I. Bertoni, and T. O. Mason, "Chemical and Structural Factors Governing Transparent Conductivity in Oxides", **Journal of Electroceramics**, vol. 13, 2004, pp. 167-175.

[2] M. J. Zunick, **"Conductive Coating on Glass"**, U.S. patent no. 25161663, 1947.

[3] J. L. Vossen and E. S. Poliniak, "The Properties of Very Thin R.F. Sputtered Transparent Conducting Films of SnO_2:Sb and In_2O_3:Sn", **Thin Solid Films**, vol. 13, 1972, pp. 281-284.

[4] T. J. Coutts, D. L.Young, and X. Li, "Characterization of Transparent Conducting Oxides", **MRS Bulletin**, 2000, pp. 58-65.

[5] J. C. Manifacier, "Thin Metallic Oxides as Transparent Conductors", **Thin Solid Films**, vol. 90, 1982, pp. 297-308.

[6] A. L. Dawar and J. C. Joshi, "Semiconducting Transparent Thin Films: Their Properties and Applications", **J. Mater. Sci.**, vol. 19, 1984, pp. 1-23.

[7] K. L. Chopra, S. Major, and D. K. Pandya, "Transparent Conductors-A Status Review", **Thin Solid Films**, vol. 102, 1983, pp. 1-46.

[8] I. Hamberg and C. G. Grangvist, "Evaporated Sn-doped In2O3 Films: Basic Optical Properties and Applications to Energy-efficient Windows", **J. Appl. Phys.**, vol. 60, 1986, pp. R123-R159.

[9] T. Minami, T. Kakumu, K. Shimokawa, and S. Takata, "New Transparent Conducting ZnO-In_2O_3-SnO_2 Thin Films Prepared by Magnetron Sputtering", **Thin Solid Films**, vol. 317, 1998, pp. 318-321.

[10] M. Ando, E. Nishimura, K.-I. Onisawa, and T. Minemura, "Effect of Microstructures on Nanocrystallite Nucleation and Growth in Hydrogenated Amorphous Indium-Tin-Oxide Films", **J. Appl. Phys.**, vol. 93, 2003, pp. 1032-1038.

[11] N. Martin, O. Banakh, A.M.E. Santo, S. Springer, R. Sanjines, J. Takadoum, and F. Levy, "Correlation between Processing and Properties of TiO_xN_y Thin Films Sputter Deposited by the Reactive Gas Pulsing Technique", **Appl. Surf. Sci.**, vol. 185, 2001, pp. 123-133.

This material is reserved for educational use only, not allowed for commercial use.
Forbidden to modify the content, and cite the document when use.

[12] L. Pinard and J.M. Mackowski, "Optical Losses of Multilayer Stacks Synthesized with Silicon Oxynitride by R.f. Magnetron Sputtering", **Thin Solid Films,** vol. 333, 1998, pp. 126-133.

[13] H. Steffes, C. Imawan, P. Fricke, H. Vohse, J. Albrecht, R. Schneider, F. Solczbacher, and E. Obermeier, "New $In_xO_yN_z$ films for the application in NO_2 sensors", **Sens. Actuators B,** vol. 77, 2001, pp. 352-358.

[14] B.J. Neudecker, R.A. Zuhr, and J.B. Bates, "Lithium Silicon Tin Oxynitride (Li_ySiTON): High-performance Anode in Thin-film Lithium-ion Batteries for Microelectronics", **J. Power Sources,** vol. 81-82, 1999, pp. 27-32.

[15] M. A. Morales-Paliza, M. B. Huang, and L. C. Feldman, "Nitrogen as Background Gas in Pulsed-Laser Deposition Growth of Indium Tin Oxide Films at Room Temperature", **Thin Solid Films,** vol. 429, 2003, pp. 220-224

[16] A. Klamchuen, N. Pornteeraphat, and J. Nukeaw, "Characterization of ITO Thin Films on PET Substrates Prepared by Gas-timing RF Magnetron Sputtering", **e-Journal of Surface Science and Nanotechnology**, vol. 3, 2005, pp. 272-275.

[17] E. Aperathitis, M. Modrean, M. Bender, V. Cimalla, G. Ecke, M. Androulidaki, and N. Pelekanos, "Optical Characterization of Indium-Tin-Oxynitride Fabricated by RF-puttering", **Thin Solid Films**, vol. 450, 2004, pp. 101-104.

[18] W.-H. Lee, J.-C. Lin, and C. Lee, "Characterization of Tantalum Nitride Films Deposited by Reactive Sputtering of Ta in N_2/Ar Gas Mixtures", **Mater. Chem. Phys.**, vol. 68, 2001, pp. 266-271.

[19] K. B. Sundaram and J. Alizadeh, "Deposition and Optical Studies of Silicon Carbide Nitride Thin Films", **Thin Solid Films,** vol. 370, 2000, pp. 151-154.

[20] S.H. Mohamed, O. Kappertz, T. Niemeier, R. Drese, M.M. Wakkad, and M. Wuttig, "Effect of Heat Treatment on Structural, Optical and Mechanical Properties of Sputtered TiO_xN_y films", **Thin Solid Films**, vol. 468, 2004, pp. 48-56.

[21] S. Venkataraj, D. Severin, S.H. Mohamed, J. Ngaruiya, O. Kappertz, and M. Wuttig, "Towards Understanding the Superior Properties of Transition Metal Oxynitrides Prepared by Reactive DC Magnetron Sputtering", **Thin Solid Films**, vol. 502, 2006, pp. 228-234.

[22] R. B. H. Tahar, T. Ban, Y. Ohya, and Y. Takahashi, "Tin Doped Indium Oxide Thin Films: Electrical Properties", **J. Appl. Phys.**, vol. 83, 1998, pp. 2631-2645.

This material is reserved for educational use only, not allowed for commercial use.
Forbidden to modify the content, and cite the document when use.

[23] M. Mulato, I. Chambouleyron, E. G. Birgin, and J. M. Martinez, "Determination of Thickness and Optical Constants of Amorphous Silicon Films From Transmittance Data", **Appl. Phys. Lett.**, vol. 77, 2000, pp. 2133-2135.

[24] L. Pauling, **The Nature of the Chemical Bond.** Ithaca, New York: Cornell University, 1960.

[25] H. A. Macleod, **Thin-Film Optical Filters.** 3rd edition, Philadelphia, USA: Institute of Physics Publishing, 2001.

This material is reserved for educational use only, not allowed for commercial use.
Forbidden to modify the content, and cite the document when use.

CHAPTER 7

GROWTH AND CHARACTERIZATIONS OF ZnON THIN FILMS

7.1 Introduction

Zinc oxide (ZnO), one of the most important binary II-VI compounds, is a direct wide band gap semiconductor of wurtzite structure. Its minimum energy gap is ~3.2 eV at room temperature and ~3.44 eV at 4K [1,2]. The remarkable properties of ZnO are large bond strength, good optical quality, extreme stability of excitons, and excellent piezoelectric properties. Consequently, ZnO has been actively studying in various fields, with potential applications in many technological domains, such as transparent conducting electrodes in display devices and solar energy cells, surface and bulk acoustic wave devices (SAW), optical-wave guide and acoustic-optical devices, and light-emitting diodes (LEDs) and laser diodes (LDs) [3-8]. Another advantage of zinc oxide relative to other materials is its low price, placing it as a strong candidate for industrial applications. A number of techniques have been employing for fabricating ZnO thin films, including chemical vapor deposition, sol-gel, spray-pyrolysis, molecular beam epitaxy, pulsed laser deposition, vacuum arc deposition, and magnetron sputtering [9-15]. Nonetheless, there remain difficulties in growing stable and high quality ZnO films. One of the most important deposition techniques for ZnO thin films is the rf plasma sputtering, which permits deposition at low temperature, and gives better adhesion, larger coverage and higher film density than other methods. However, the quality of the films regard to the crystal structure depends strongly on the sputtering conditions, such as rf power, sputtering pressure and target-to-substrate distance. By making minor modifications to a conventional sputtering system, we have demonstrated a new sputtering technique, called gas timing, whereby sputtering or doping gases are controlled periodically by an on-off sequence during the sputtering deposition. This technique obtained high quality crystalline thin films at low rf power and at ambient temperature.

In the current state of ZnO, Ozgur *et al.* [16] distinguish the numerous researches in five challenge ways. The first one is studying on the defects of ZnO in order that it effected to the optical transition in ZnO. The second one is focusing on the I-group or V-group element doped ZnO to from a high stability p-type ZnO. The third one is dealing with the ZnO-based dilute

This material is reserved for educational use only, not allowed for commercial use.
Forbidden to modify the content, and cite the document when use.

magnetic semiconductor such as (Zn,Mn)O, (Zn,Co)O and (Zn,V)O. The fourth one is studying on the band-gap engineering based ZnO alloys such as $Mg_xZn_{1-x}O$ and $Cd_xZn_{1-x}O$. The newest research is growing and investigating on nanostructures of ZnO such as nanowires, nonorods, combs and tubes structure and nanopropeller.

In particular, a zinc-oxide-nitride system was demonstrated to be an optically functional material, in which the optical band gap can be tuned within a broad energy range (2.3-3.3 eV) by controlling the nitrogen doping level [17]. Zinc oxynitride (ZnON) thin film can be fabricated by various techniques. Plasma sputtering is one of the most promising techniques for the ZnON films because of its capability for large-area deposition, low-temperature processing, and controllable nitrogen incorporation into the films.

Here we report on the fabrication of ZnO and ZnON thin films on glass substrate by pure argon and nitrogen reactive gas-timing rf magnetron sputtering of a ceramic ZnO target. The substrates remained at room temperature during the deposition. The structural properties, the nitrogen doping levels, and the optical band gaps of the ZnON thin films were investigated with regard to the sputtering parameters, i.e., the sputtering gas flow rate and rf power.

7.2 Experimental results and discussions of ZnO

7.2.1 Substrate cleaning process

In order to obtain high quality film, it is necessary to clean the substrate thoroughly. Since the condition of substrate surface would influent the quality and adhesion of deposited thin films. The glass slides (Superior W. Germany) be use to the substrate for all deposited thin films in this study. The glass substrate cleaning process is as below,

1) Wash the glass surface with detergent solution for 15 minutes in ultrasonic bath cleaner.
2) Rinse with water.
3) Etch the oxide and contamination on the surface with standard piranha solution (3:1 mixture of H_2SO_4 (95%) and H_2O_2 (30%) by volume) for 30 minutes.
4) Rinse in deionized (DI) water for 20 minutes.
5) Deep rinse in deionized (DI) water for 30 minutes in ultrasonic bath cleaner.
6) Dry out the surface with nitrogen gas.
7) Bake the substrates in oven at 120 °C for 30 minutes.

This material is reserved for educational use only, not allowed for commercial use.
Forbidden to modify the content, and cite the document when use.

Prior to set up the glass substrate on the substrate holder in sputtering chamber, the cleaned glass substrates were purge with nitrogen gas again. Two thickness-verification purpose samples were marked with a strip of an aluminum tape on the surface, which placed one at the central and other one at the peripheral of the substrate holder. After sputtering process, the removal of aluminum tap was performed the measurable mark on the sample. The thickness of thin films had determined by physical stylus profilometer, and compared to the film thickness value from the sputtering thickness monitor.

7.2.2 ZnO thin films growth without gas-timing

7.2.2.1 Sputtered ZnO thin film in Ar plasma

The ZnO sputtering deposition was conducted with an Edwards AUTO 500 plant equipped with a rf magnetron sputtering set. A compound ceramic zinc oxide (99.999% impurity) from Kurt J. Lesker was used as a target material with a diameter of 3 inch. The substrate holder has an ambient temperature during the sputtering process. The main adjustable process parameters were the rf power and the sputtering gas pressure. A quartz crystal microbalance was employed to monitor film thickness during deposition. The chamber was evacuated down to 5.0×10^{-7} mbar. The target-substrate distance was 50 mm. The design of experiment is required with first two-point as no rf reflected and achieved the high crystallinity, which Ar purity of 99.999% was used as a plasma gas to bombard the target with rf power in range of 30 to 120 W. The flow rate of Ar was varied of 9 to 16 sccm and the film growth rates were recorded. The excess ions in the chamber may collies each other affected to the decreasing of sputtering yield so the thin film growth rate was decreased when the flow rate of Ar increased and inversely in case of rf power increased at fixed Ar flow rate. From this experiment, the Ar flow rate of 9 sccm was selected because the plasma is stable with no rf reflection effect during the process. The comparison of sputtered ZnO thin films by gas-timing and without gas-timing is significant on film resistance. The gas-timing sputtered ZnO film has film resistance in range of 50-100 ohm but the other one is actually insulator film.

7.2.3 ZnO thin films growth with gas-timing

An on-off gas-timing sequence was used to control the flow of argon into the sputtering chamber. This was realized by a mass flow controller with an external control program. The flow

This material is reserved for educational use only, not allowed for commercial use.
Forbidden to modify the content, and cite the document when use.

rate of argon during the 'on' sequence was fixed at 9 sccm. Figure 7.1 depicts the gas-timing sequence of argon gas that flows for 50 seconds then stops for 2 seconds.

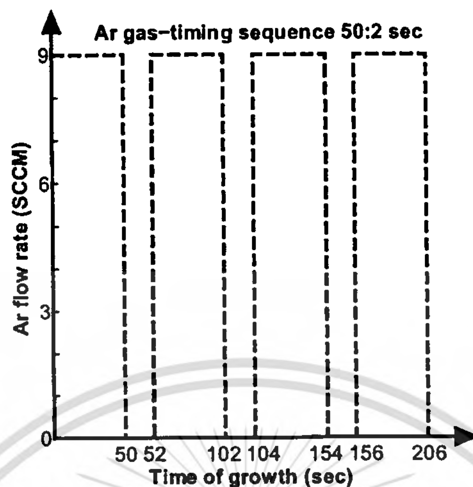

Fig. 7.1 Schematic representation of the 50:2 on-off gas-timing sequence of argon during sputtering deposition with a flow rate of 9 sccm (on) for 50 seconds and zero flow (off) for 2 seconds.

Table 7.1 Sputtering conditions used for deposition of ZnO thin films

Deposition parameters	Conditions
Base pressure	5.0×10^{-7} mbar
RF power	30, 50, 80, 120 Watt
Substrate-target distance	50 mm
Sputtering pressure	2.8×10^{-3} mbar, argon gas activated
Ar flow rate	9, 12, 14, 16 sccm
Ar Gas-timing (on:off)	30:2, 40:2, 50:2, 60:2 seconds

The summaries of rf plasma sputtering conditions are listed in Table 7.1. The thickness of the deposited ZnO thin films were all set at 200 nm. After the sputtering process, the film thickness was measured by a profilometer (TENCOR, Alphastep 500). The crystallinity of the films was investigated by x-ray diffractometer (Bruker, D8) using CuKα with the radiation wavelength (λ) of 0.154056 nm. The optical transmittance spectroscopy was performed with a single beam UV-Visible spectrophotometer (Thermo electron corporation, Heliosγ). The RMS roughness and the surface morphology of films were measured by the Atomic Force Microscope (Seiko, SPA-400).

This material is reserved for educational use only, not allowed for commercial use.
Forbidden to modify the content, and cite the document when use.

7.2.3.1 Effect of gas-timing on the properties of ZnO

For structural studies, the crystalline structure of the deposited films was investigated by the XRD technique. The XRD patterns of ZnO thin films deposited at different gas-timing sequences and rf powers indicate the difference in the crystalline quality. At the optimized argon gas-timing sequence of 50:2 seconds, the highest peak intensity for the (002) plane oriented wurtzite structure has been observed, as shown in Fig. 7.2. A possible mechanism for this enhancement in the crystallinity is balanced between a specific gas-timing sequence with the temporal characteristics of the nucleation and growth of ZnO thin films. In addition to the preferential (002) reflection, all the films exhibit a weak (100) reflection. The AFM images ($5x5\mu m^2$) of ZnO thin films prepared at different argon gas-timing sequences and a fixed RF power of 30 W are shown in Fig. 7.3. The results indicate that the films have uniform morphology of possibly the polycrystalline nature, with a relatively small root mean square (rms) surface roughness of less than 12 nm. Comparable roughness values have been found in other reports with sputtering deposition methods [19,20].

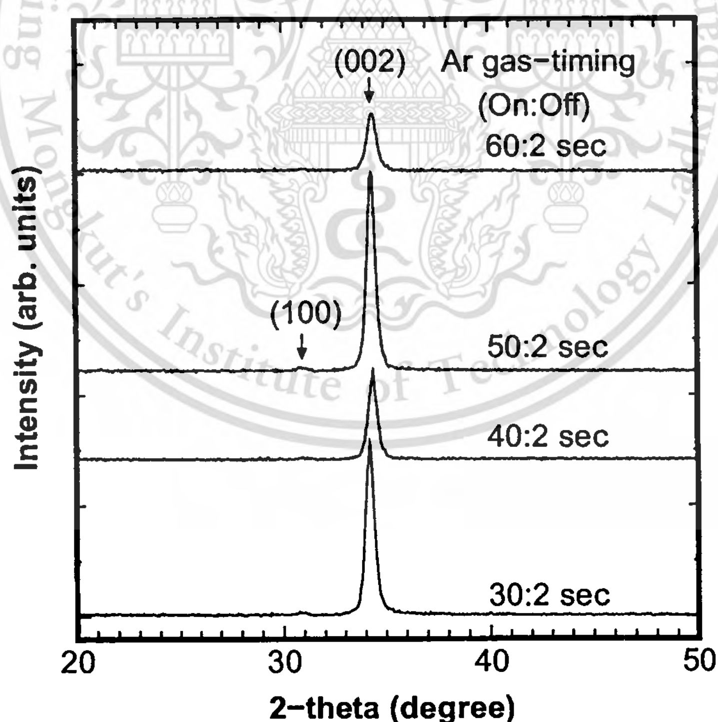

Fig. 7.2 X-ray diffraction patterns of ZnO thin films deposited at different argon gas-timing sequences (30:2, 40:2, 50:2, 60:2 sec) and fixed rf power of 30 W.

This material is reserved for educational use only, not allowed for commercial use.
Forbidden to modify the content, and cite the document when use.

Fig. 7.3 AFM images ($5x5\mu m^2$) of ZnO thin films deposited at different argon gas-timing sequences (30:2, 40:2, 50:2, 60:2 sec) and fixed rf power of 30 W.

King Mongkut's Institute of Technology Ladkrabang
This material is reserved for educational use only, not allowed for commercial use.
Forbidden to modify the content, and cite the document when use.

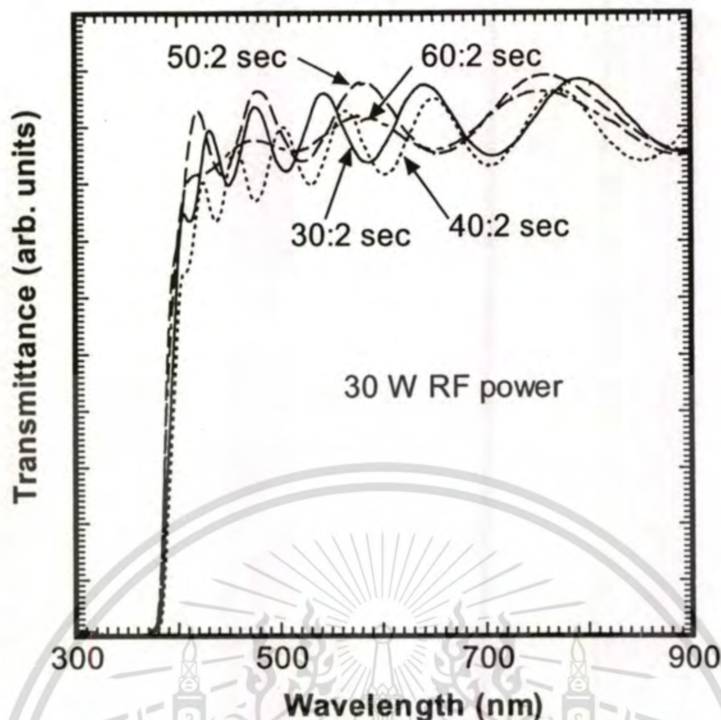

Fig. 7.4 Optical transmittance of ZnO thin films deposited at different argon gas-timing sequences (30:2, 40:2, 50:2, 60:2 sec) and fixed rf power of 30 W.

The optical transmittance of the films has been measured in the wavelength range of 300-900 nm. As shown in Fig. 7.4, the optical transmittance of the films grown at different gas-timing sequence conditions all exhibit an average transmittance in the visible range over 85%. Thus the optical transmittance of these films has not been significantly influenced by the gas-timing method.

7.2.3.2 Effect of rf sputtering power on the properties of ZnO

The XRD patterns of ZnO thin films deposited at different rf powers indicate the difference in the crystalline quality. Figure 7.5 illustrates the XRD patterns of the ZnO films grown at different RF powers of 30, 50, 80 and 120 W. The gas-timing sequence for all the samples was 50:2 seconds. Strong XRD peaks in the (002) reflection, at around 34.2 degree, can be observed for all the samples. The intensity of the (002) peak also seems to decrease with an increase in RF power. The highest (002) peak intensity occurs at the RF power of 30 W. It should be noted that the plasma sputtering power of 30 W is sufficient for the growth of hexagonal ZnO thin films.

This material is reserved for educational use only, not allowed for commercial use.
Forbidden to modify the content, and cite the document when use.

Comparing to other plasma-based film deposition methods, the gas-timing technique requires lower RF plasma power levels [18]. In general, high RF power also induces faster reaction and more damages on the surface, resulting in a poor crystallinity of thin films.

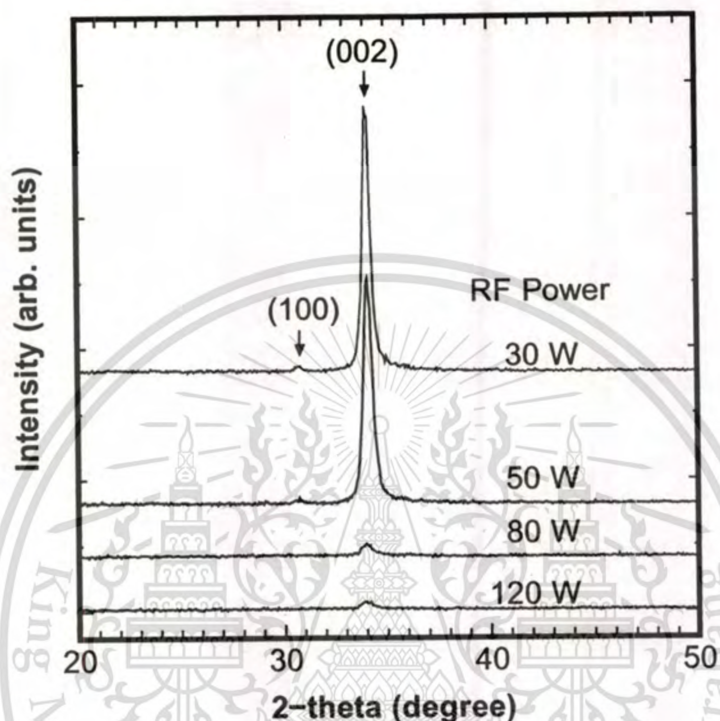

Fig. 7.5 X-ray diffraction patterns of ZnO thin films deposited at different RF power (30, 50, 80, 120 W) and the argon gas-timing sequence of 50:2 sec.

Figure 7.6 shows the AFM images ($5x5\mu m^2$) of ZnO thin films deposited at different RF powers and a fixed argon gas-timing sequence of 50:2 seconds. The surface morphology of the films for the AFM measurements implies that the grain size tends to be larger at higher RF powers [18,20]. Thus at higher RF powers, an improvement of surface density is expected. On the other hand, the more energetic sputtered particles may induce higher surface roughness [19]. In addition, despite larger grain sizes, the films grown at high RF powers have low crystallinity, as suggested by the XRD measurements. For our results, the optimized conditions for a smooth and crystalline ZnO thin film are the sputtering power of 30 W and the argon gas-timing sequences of 50:2 seconds. The rms surface roughness of the film deposited at these conditions is approximately 6.4 nm.

This material is reserved for educational use only, not allowed for commercial use.
Forbidden to modify the content, and cite the document when use.

Fig. 7.6 AFM images ($5x5\mu m^2$) of ZnO thin films deposited at different RF power (30, 50, 80, 120 W) and the argon gas-timing sequence of 50:2 sec.

This material is reserved for educational use only, not allowed for commercial use.
Forbidden to modify the content, and cite the document when use.

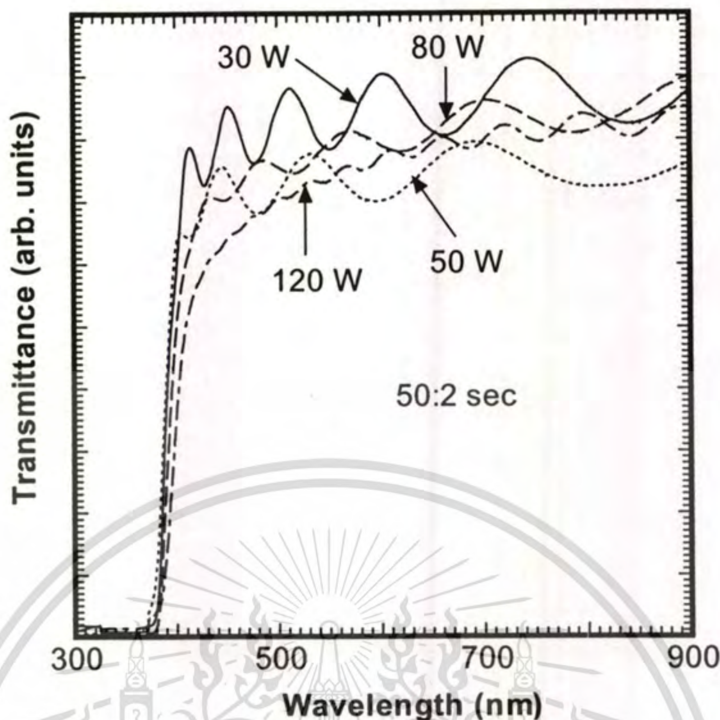

Fig. 7.7 Optical transmittance of ZnO thin films deposited at different RF power (30, 50, 80, 120 W) and the argon gas-timing sequence of 50:2 sec.

The optical transmittance of ZnO thin films deposited at different RF powers, which indicates that the transmittance gradually decreases with an increasing RF power, as illustrated in Fig. 7.7. This characteristic may be caused by increased scattering, reflection and optical absorption of the films, owing to larger surface roughness and amorphous contents of the films deposited at higher RF powers [21]. The absorption coefficients, the film thickness, and the optical band gap (E_g) can be extracted from the optical transmittance spectra by using the unconstrained minimization algorithm [22,23]. The values of E_g for the films deposited at various gas-timing sequences and RF powers are in the range ~3.17 to ~3.21 eV.

7.2.3.3 Effect of Ar flow rate on the properties of ZnO

From the survey experimental results, the ZnO thin films grown by various Ar flow rate condition of 9, 12, 14, and 16 sccm were show any different crystal structure property. Figure 7.8 was depicted the XRD patterns of different Ar flow rate conditions, all peak indicated (002) preferred orientation of ZnO. However, the increasing of Ar gas flow rate directly affected to the XRD peak intensity reduced. As the results, the crystallinity of the ZnO film was deteriorated by

This material is reserved for educational use only, not allowed for commercial use.

Forbidden to modify the content, and cite the document when use.

increasing Ar flow rate, due to increasing of sputtering pressure then the mean free path of ions were decreased, and the energy per atom was reduced. The energy formation of deposited thin film is not sufficient growing a high quality thin film.

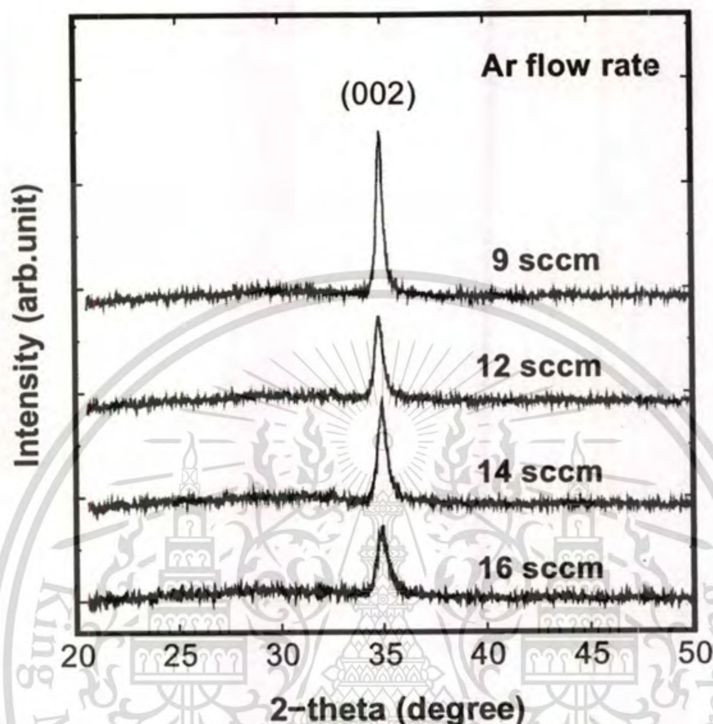

Fig. 7.8 X-ray diffraction patterns of ZnO thin films grown by various Ar flow rate condition of 9, 12, 14, and 16 sccm.

7.3 Experimental results and discussions of ZnON

Due to the experimental results of sputtered ZnO thin film in early section, the nitrogen doped zinc oxide or zinc oxynitride films thin film has been growing by the similar technique, but at on-sequence of 50 second for Ar changed to nitrogen and off-sequence of 2 second changed to on-sequence of 2 second for Ar. So on, the rf plasma had alternate species of argon and nitrogen. The ZnON thin films on glass substrates were prepared by the reactive gas-timing rf magnetron sputtering of a 99.999% purity ZnO target. The sputtering gas mixture consisted of argon mixed with nitrogen. The nitrogen partial pressure was controlled and varied periodically during the sputtering by a mass flow controller to produce an on-off sequence with 50 second of nitrogen injection and 2 second of argon injection. The purpose of applying the gas-timing technique is to enhance the sputtering rate of ZnO while the nitrogen incorporation into the film is maintained. The distance between the target and the substrate was 50 mm. The sputtering chamber was

This material is reserved for educational use only, not allowed for commercial use.

Forbidden to modify the content, and cite the document when use.

evacuated to a base-pressure of approximately 1.0×10^{-6} mbar, and then filled with Ar at 10 sccm. For each deposition run, the ZnO target was presputtered for 10 min at an rf power of 30 W. ZnON thin films were grown to a fixed thickness of 1000 nm and monitored using a quartz crystal microbalance. Different sputtering conditions were investigated: nitrogen flow rates of 10, 15, and 20 sccm (at a fixed rf power of 80 W) and rf powers of 30, 50, and 80 W (at a fixed nitrogen flow rate of 10 sccm). The sputtering pressure and bias voltage were monitored during the process at nitrogen flow rates of 10, 15, and 20 sccm. The total sputtering gas pressures were 0.3, 0.65, and 0.85 Pa, and the sputtering voltages were 192, 176, and 165 V, respectively. After sputtering, the thickness of the films was confirmed using a profilometer (TENCOR Alphastep 500). The crystalline nature of the films was investigated using an X-ray diffractometer (XRD; Bruker D8) using Cu $K\alpha_1$ radiation at a wavelength (λ) of 0.154056 nm. A UHV X-ray photoelectron spectroscopy (XPS) system with a monochromatic Mg $K\alpha$ X-ray source was employed to measure the atomic composition ratio and confirm nitrogen incorporation into the ZnO films. Optical transmittance measurements were performed using a single-beam UV-vis spectrophotometer (Thermo Electron; Helios α).

7.3.1 Effect of gas flow rate on the properties of ZnON

The thickness of all ZnON films were confirmed using the thickness profiler to be ~1 μm. Figure 7.9 shows XRD patterns of the deposited ZnON films processed under various nitrogen flow rate conditions. For all the sample films, the strongest XRD peak is observed to be the ZnO (002) reflection. The films produced at different nitrogen flow rates, the XRD patterns exhibit an additional small peak representing ZnO (103) reflection. Note that the intensities of both the ZnO (002) and the ZnO (103) peaks increase with the nitrogen flow rate. As discussed later, XPS measurements confirm that nitrogen atoms have been incorporated into the ZnO films, even though no zinc nitride peaks appear. In addition, the XPS results also show a surprising result that the nitrogen composition of the ZnON films decreases at a higher flow rate, leading to an improvement in the crystallinity of ZnO. Scherrer's formula [24] can be used to calculate the average grain size from the full width at half maximum (FWHM) of XRD peaks. The ZnON grain sizes at nitrogen flow rates of 10, 15, and 20 sccm are 18.94, 18.24, and 27.47 nm, respectively. Therefore, our results demonstrate that the ZnON films produced by the gas-timing technique are polycrystalline. The crystallinity of the films increases at a higher nitrogen flow rate, which coincides with a larger average grain size but lower nitrogen doping in the films.

This material is reserved for educational use only, not allowed for commercial use.
Forbidden to modify the content, and cite the document when use.

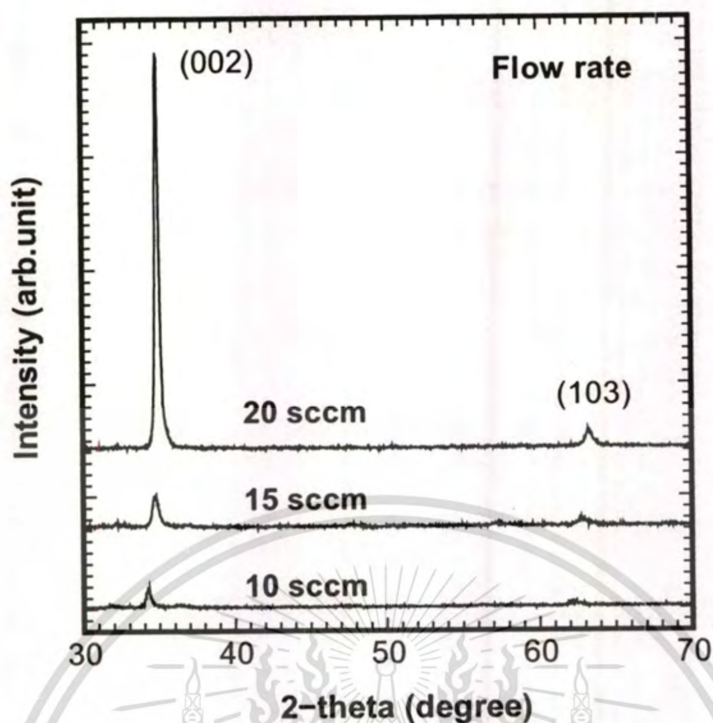

Fig. 7.9 XRD patterns of ZnON films deposited on glass by rf magnetron sputtering at a fixed rf power of 80 W for nitrogen flow rates of 10, 15, and 20 sccm.

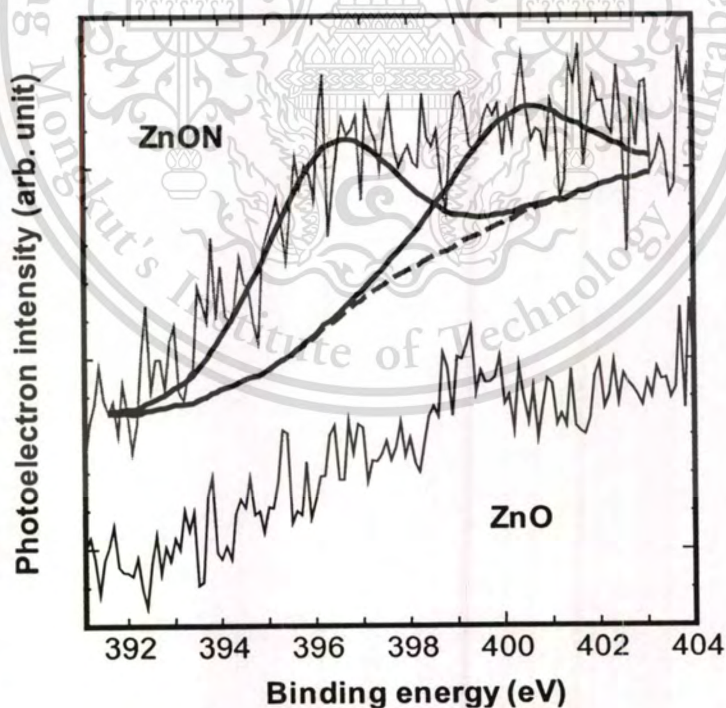

Fig. 7.10 XPS spectra (N 1s) of ZnO thin films produced by rf magnetron sputtering using only argon, and ZnON thin films produced by gas-timing sputtering at a fixed rf power of 80 W and a nitrogen flow of 10 sccm.

This material is reserved for educational use only, not allowed for commercial use.
Forbidden to modify the content, and cite the document when use.

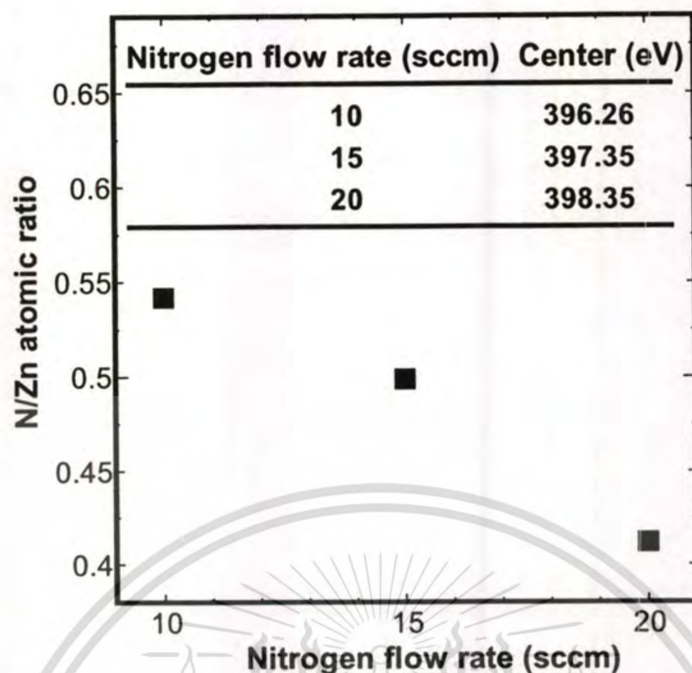

Fig. 7.11 N/Zn atomic ratio as a function of nitrogen flow rate. The values for the center of the N 1s binding energy peak from XPS analysis for different nitrogen flow conditions are also given.

XPS was conducted to verify the nitrogen composition in the ZnON films as a function of the nitrogen flow rate. As illustrated in Fig. 7.10, the XPS measurements show two N1s peaks with binding energies of 396.6 and 400.4 eV for the ZnON produced at 80 W rf power and a nitrogen flow of 10 sccm. In contrast, the sputtered films produced with only argon gas do not show N1s signals within the XPS detection limit. The lower binding energy peak corresponds to the substitution of a nitrogen atom for an oxygen sublattice atom, [25] and the higher binding energy is still unidentified but is closest to the energy for the substitution of a nitrogen molecule for an oxygen sublattice atom at 404.9 eV. Figure 7.11 shows the nitrogen-to-zinc (N/Zn) atomic ratio as a function of nitrogen flow rate at 10, 15, and 20 sccm. The results show that the N/Zn atomic ratio unexpectedly decreases when the nitrogen flow rate is increased. Thus, it appears that the amount of nitrogen atoms or ions in the sputtering gases decreases as the nitrogen flow rate increases. Tu *et al.* [26] have reported a similar decrease in the nitrogen composition ratio as the nitrogen flow rate into the sputtering chamber was increased. The mechanisms are unresolved and will need to be investigated further. Nevertheless, our experimental results clearly confirm the incorporation of nitrogen into the ZnO film. The simplest ZnON doping model suggests that

This material is reserved for educational use only, not allowed for commercial use.

Forbidden to modify the content, and cite the document when use.

nitrogen incorporation involves substituting an oxygen atom with a nitrogen atom at one of the ZnO crystal lattice sites, at which the substituted nitrogen can also function as a p-type acceptor in the ZnON film [27]. Using our technique, we have achieved ZnON films with high N/Zn ratios of above 0.50.

Optical transmittance measurements in the range 300-800 nm were conducted on the ZnON films deposited at different nitrogen flow rates as depicted in Fig. 7.12. The results exhibit a significant shift in the optical absorption edge to a longer wavelength when the rf power is increased. The absorption coefficient (α) was calculated from the transmission spectra using the unconstrained minimization algorithm [22]. To extract the absorption edge energy or the optical band gap energy (E_{opt}) of the films, we employed a standard method in which α^2 is plotted as a function of the incident radiation energy (eV) and the linear part of the curve is extrapolated to intercept the energy axis. The relationships of E_{opt} with the nitrogen flow rate and the rf power are shown in Fig. 7.13. E_{opt} for the films produced at nitrogen flow rates of 10, 15, and 20 sccm are 2.98, 3.08, and 3.07 eV, respectively. The observed redshift in the transmittance of the ZnON films as a result of the decrease in E_{opt} may be explained by the difference in the ionicity between the Zn-O and Zn-N bonds.

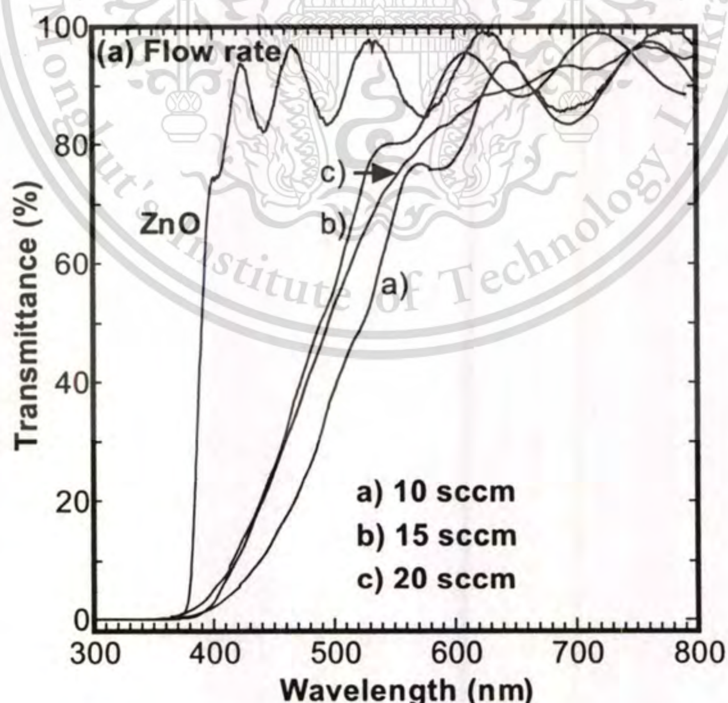

Fig. 7.12 Optical transmission spectra of ZnON films deposited on glass by rf magnetron sputtering at a fixed rf power of 80 W for nitrogen flow rates of 10, 15, and 20 sccm.

This material is reserved for educational use only, not allowed for commercial use.
Forbidden to modify the content, and cite the document when use.

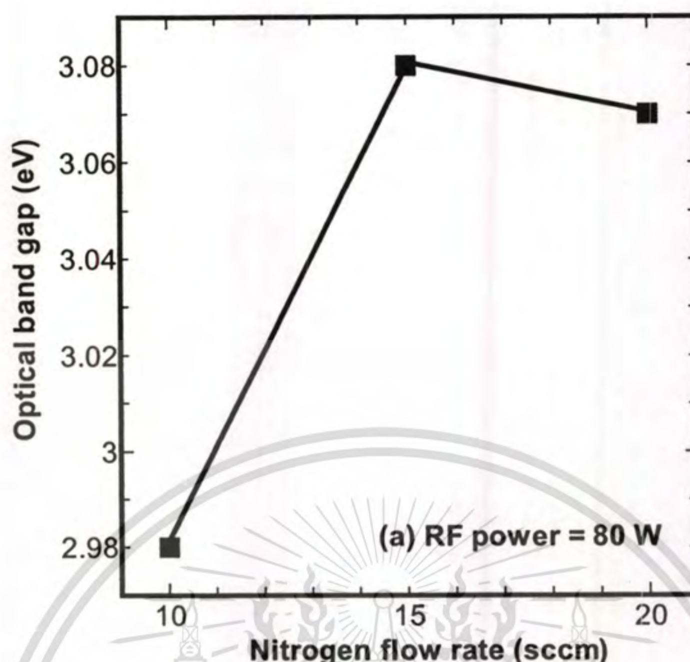

Fig. 7.13 Dependence of the optical band gap of ZnON thin films on the nitrogen flow rate.

According to Pauling's theory, [28] the ionicity in an ionic bond increases with the difference in electronegativity values between the two elements forming the bond. The electronegativity of O (3.5) is larger than that of N (3.0), which indicates that the Zn-O bond has greater ionicity than the Zn-N bond. Thus, the decrease in E_{opt} should be attributed to a reduction in the overall ionicity due to the formation of Zn-N bonds. Consequently, the color of the films changes from clear to yellowish, depending on the amount of nitrogen incorporated in the films.

7.3.2 Effect of rf sputtering power on the properties of ZnON

Figure 7.14 shows XRD patterns of the deposited ZnON films processed under various rf power conditions. For the ZnON produced at different rf powers, the XRD patterns show the same main peak representing the ZnON (002) reflection, which increases at a lower rf power. The ZnON grain sizes produced at the rf powers of 80, 50, and 30 W are 18.94, 19.58, and 26.71 nm, respectively. Therefore, varying the rf sputtering power seems to strongly affect the crystal orientation of the nitrogen-incorporated ZnO films. Strong subsidiary XRD peaks can be observed for the films produced at 50 W, which they seem to be associated with the formation of zinc nitride [26], suggesting some phase separation in the films.

This material is reserved for educational use only, not allowed for commercial use.
Forbidden to modify the content, and cite the document when use.

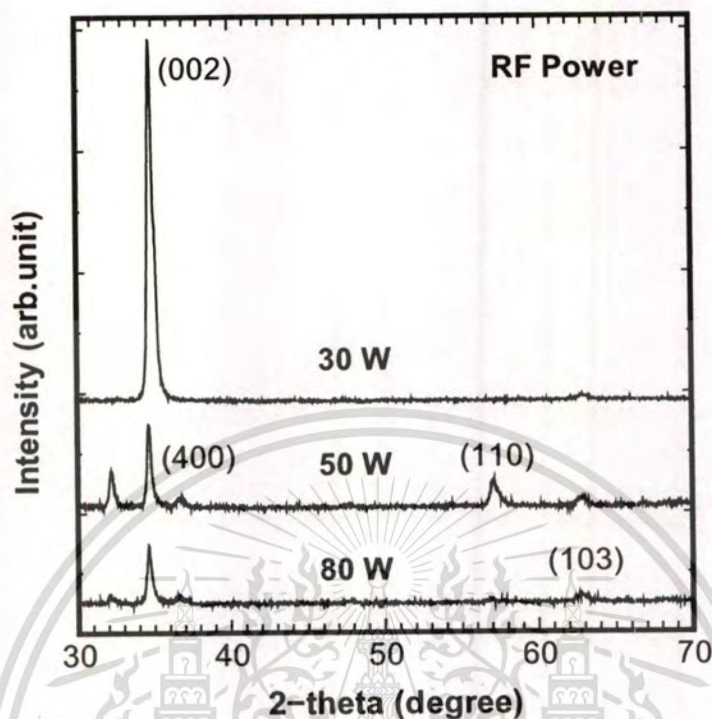

Fig. 7.14 XRD patterns of ZnON films deposited on glass by rf magnetron sputtering at a fixed nitrogen flow of 10 sccm for rf powers of 30, 50, and 80 W.

The mechanism for the effect of the rf power on the film structure is not yet resolved. The effect may arise from the complexity of plasma chemistry, which is influenced by many factors, such as the atomic and molecular ion compositions and energies of the sputtered materials.

Optical transmittance measurements in the range 300-800 nm were conducted on the ZnON films deposited at different sputtering rf powers, as depicted in Fig. 7.15. The results exhibit a significant shift in the optical absorption edge to a longer wavelength when the nitrogen flow is decreased. The absorption coefficient (α) was also calculated from the transmission spectra using the unconstrained minimization algorithm. The relationships of E_{opt} with the rf power are shown in Fig. 7.16. E_{opt} for the films produced at sputtering rf powers of 30, 50, and 80 W are 3.08, 3.0, and 2.98 eV, respectively. The observed redshift in the transmittance of the ZnON films as results of the decrease in E_{opt} as function of sputtering rf power may be explained by the increasing of nitrogen incorporated in ZnON.

This material is reserved for educational use only, not allowed for commercial use.
Forbidden to modify the content, and cite the document when use.

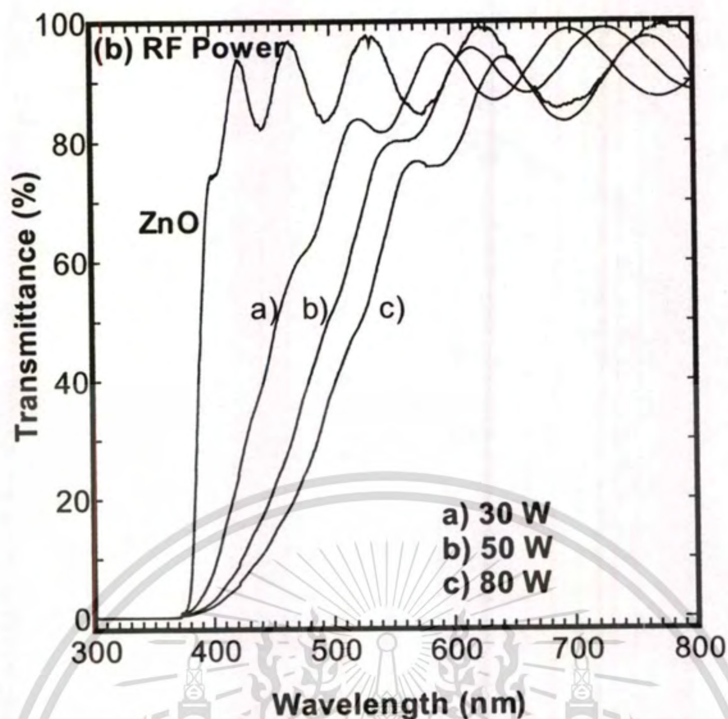

Fig. 7.15 Optical transmission spectra of ZnON films deposited on glass by rf magnetron sputtering at a fixed nitrogen flow of 10 sccm for rf powers of 30, 50, and 80 W.

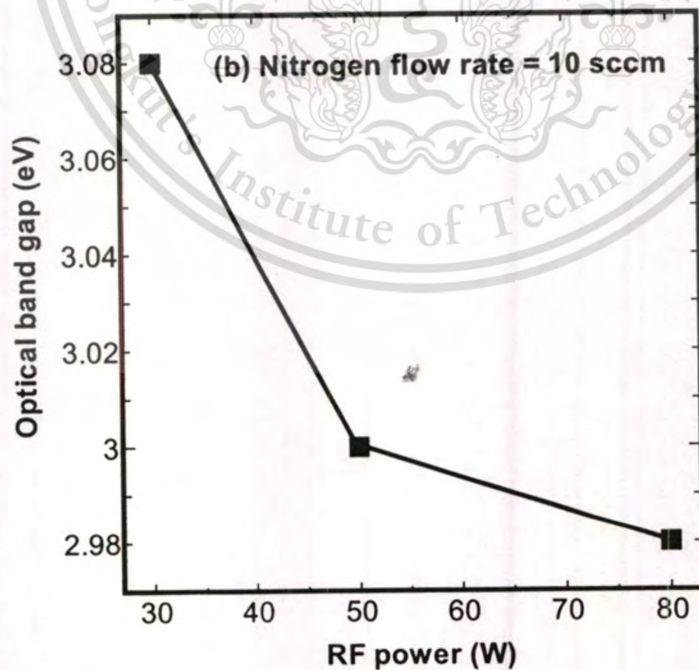

Fig. 7.16 Dependence of the optical band gap of ZnON thin films on the rf sputtering power.

This material is reserved for educational use only, not allowed for commercial use.
Forbidden to modify the content, and cite the document when use.

7.3.3 Effect of film thickness on the properties of ZnON

As the results from the previous sections, the sputtered 1000 nm ZnON thin film grown by gas-timing condition of 50:2 second for N:Ar is the most optimization for amount of nitrogen incorporation into ZnON thin film at rf power of 80 W. The effect of film thickness was observed by sputtering with various film thickness conditions of 200, 400, 800 and 1000 nm. The structural and optical properties of ZnON thin films were investigated by XRD and UV-Vis spectroscopy. The XRD results of ZnON thin films with different thickness as shown in Fig. 7.17. Note that the intensities of the ZnO (002) peaks increase with the film thickness, which is the crystallinity of films also increase. The optical transmittance spectra of ZnON thin films with different thickness as shown in Fig. 7.18. The film thickness of ZnON was directly affected to the optical property by the absorption model in red shift phenomenon [29].

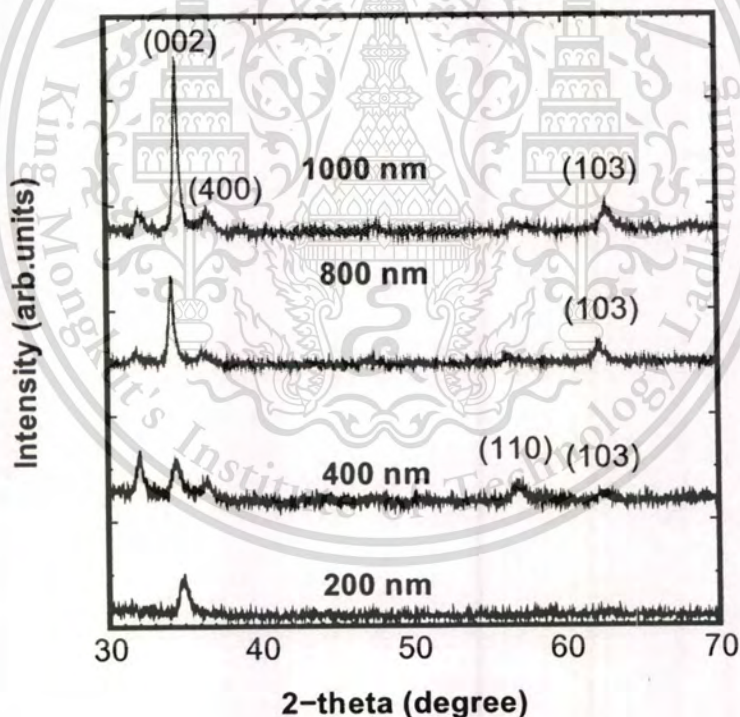

Fig. 7.17 XRD patterns of ZnON films deposited on glass by rf magnetron sputtering with various film thickness at a fixed nitrogen flow of 10 sccm and rf power of 80 W.

This material is reserved for educational use only, not allowed for commercial use.
Forbidden to modify the content, and cite the document when use.

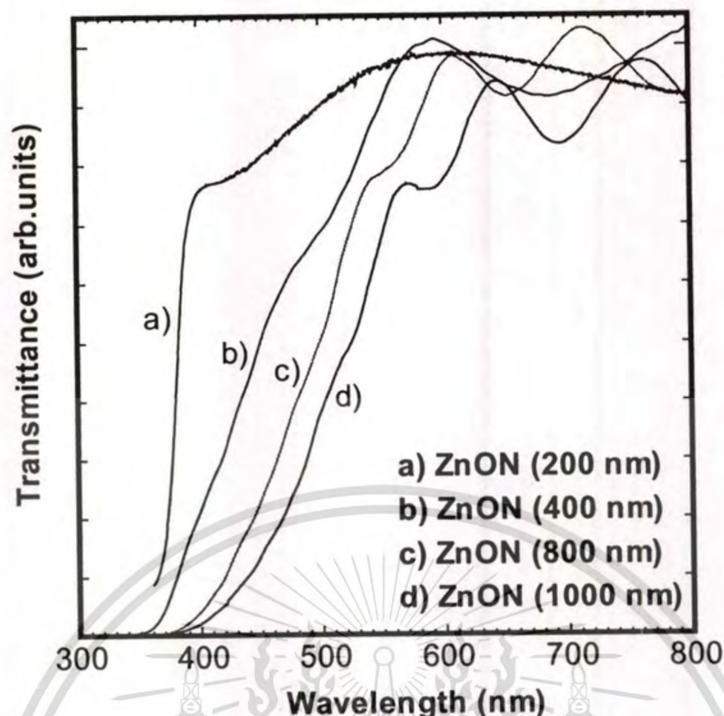

Fig. 7.18 Transmission spectra of ZnON films deposited on glass by rf magnetron sputtering with various film thickness at a fixed nitrogen flow of 10 sccm and rf power of 80 W.

7.4 Chapter summary

The experiments in this chapter deal with the growth and characterizations of ZnO and ZnON films, which explained in more details in previous section. For ZnO, this chapter demonstrates that the gas-timing RF sputtering technique successfully applied to produce high quality polycrystalline zinc oxide thin films on glass substrates at room temperature and without any thermal treatment of the films. The optimized conditions for the wurtzite ZnO films have been found to be the RF power of 30 W and the gas-timing sequence of 50:2 seconds. The films deposited at these conditions also exhibit a small surface roughness, with the rms value of less than 7 nm. Moreover, the films have high optical transmittance in the visible range of over 85%. The calculations of the optical band gap from the optical transmittance spectra give the band gap values for the films deposited at various gas-timing sequences and RF powers to be in the range ~3.17 to ~3.21 eV. With further studies, this technique may be applied to fabricate ZnO thin films at room temperature for transparent electronics such as transparent thin film transistors and flexible OLED displays.

This material is reserved for educational use only, not allowed for commercial use.
Forbidden to modify the content, and cite the document when use.

In the study of ZnON, we successfully prepared nitrogen-doped zinc oxide thin films by nitrogen reactive rf magnetron sputtering at ambient temperature by using the gas-timing technique. We investigated the effects of two important sputtering deposition parameters on the properties of the ZnON films, namely, the rf sputtering power and the nitrogen flow rate. We found that the optical and structural properties of the ZnON films depend not only on the amount of nitrogen in the plasma but also on the amount of nitrogen incorporated inside the films and the rf sputtering power. The nitrogen incorporation in the ZnON film was confirmed by XPS measurements. In addition, the optical band gap energy can be tuned by varying the processing conditions in the range from 2.98 to 3.08 eV. After further investigation, the gas-timing technique should be applicable for the fabrication of many functional optical devices that require tunable material properties and low-temperature processing.

References:

[1] L. I. Berger, **Semiconductor Materials.** Boca Raton: CRC Press, 1997.

[2] X. Sun and H. Kwok, "Optical Properties of Epitaxially Grown Zinc Oxide Films on Sapphire by Pulsed Laser Deposition", **J. Appl. Phys.**, vol. 86, 1999, pp. 408-411.

[3] F. R. Blom, F. C. M. Van de Pol, G. Bauhuis, and Th. J. A. Popma, "R.F. Planar Magnetron Sputtered ZnO Films II: Electrical Properties", **Thin Solid Films**, vol. 204, 1991, pp. 365-376.

[4] W. E. Devaney, W. S. Chen, J. M. Stewart, and R. A. Mickelsen, "Structure and Properties of High Efficiency ZnO/CdZnS/CuInGaSe_2 Solar Cells", **IEEE Trans. Electron Devices**, vol. 37, 1990, pp. 428-433.

[5] N. Fujimara, S. Azuma, N. Aoki, T. Yoshimura, and T. Ito, "Growth Mechanism of $YMnO_3$ Film as a New Candidate for Nonvolatile Memory Devices", **J. Appl. Phys.**, vol. 80, 1996, pp. 7084-7088.

[6] Y.H. Lee, M.H. Song, B.K. Ju, D.K. shin, and M.H. Oh, "Thin Film Phosphor Prepared by Physical Vapour Deposition for Field Emission Display Application", **J. Vac. Sci. Technol.**, vol. B15, 1997, pp. 512-515.

[7] F.S. Mahmood, R.D. Gould, A.K. Hassan, and M.H. Salih, "D.c. Properties of ZnO Thin Films Prepared by R.f. Magnetron Sputtering", **Thin Solid Films**, vol. 270, 1995, pp. 376-379.

This material is reserved for educational use only, not allowed for commercial use.
Forbidden to modify the content, and cite the document when use.

[8] C. R. Gorla, N. W. Emanetoglu, S. Liang, W. E. Mayo, Y. Lu, M. Wraback, and H. Shen, "Structural, Optical, and Surface Acoustic Wave Properties of Epitaxial ZnO Films Grown on (0112) Sapphire by Metalorganic Chemical Vapor Deposition", **J. Appl. Phys.**, vol. 85, 1999, pp. 2595-2602.

[9] B. S. Li, Y. C. Liu, Z. S. Chu, D. Z. Shen, Y. M. Lu, J. Y. Zhang, and X. W. Fan, "High Quality ZnO Thin Films Grown by Plasma Enhanced Chemical Vapor Deposition", **J. Appl. Phys.**, vol. 91, 2002, pp. 501-505.

[10] M.J. Alam, and D.C. Cameron, "Preparation and Properties of Transparent Conductive Aluminum-doped Zinc Oxide Thin Films by Sol-gel Process", **J. Vac. Sci. Technol.**, vol. A19, 2001, pp. 1642-1646.

[11] A.J.C. Fiddes, K. Durose, A.W. Brinkman, J. Woods, P.D. Coates, and A.J. Banister, "Preparation of ZnO Films by Spray Pyrolysis", **J. Cryst. Growth**, vol. 159, 1996, pp. 210-213.

[12] T. Ohgaki, N. Ohashi, H. Kakemoto, S. Wada, Y. Adachi, H. Haneda, and T. Tsurumi, "Growth Condition Dependence of Morphology and Electric Properties of ZnO Films on Sapphire Substrates Prepared by Molecular Beam Epitaxy", **J. Appl. Phys.**, vol. 93, 2003, pp. 1961-1965.

[13] Y. R. Ryu, S. Zhu, J. D. Budai, H. R. Chandrasekhar, P. F. Miceli, and H. W. White, "Optical and Structural Properties of ZnO Films Deposited on GaAs by Pulsed Laser Deposition", **J. Appl. Phys.**, vol. 88, 2000, pp. 201-204.

[14] T. Minami, S. Ida, and T. Miyata, "High Rate Deposition of Transparent Conducting Oxide Thin Films by Vacuum Arc Plasma Evaporation", **Thin Solid Films**, vol. 416, 2002, pp. 92-96.

[15] K. H. Kim, K. C. Park, and D. Y. Ma, "Structural, Electrical and Optical Properties of Aluminum Doped Zinc Oxide Films Prepared by Radio Frequency Magnetron Sputtering", **J. Appl. Phys.**, vol. 81, 1997, pp. 7764-7772.

[16] Ü. Özgür, Ya. I. Alivov, C. Liu, A. Teke, M. A. Reshchikov, S. Dogan, V. Avrutin, S.-J. Cho and H. Morkoç, "A Comprehensive Review of ZnO Materials and Devices", **J. Appl. Phys.**, vol. 98, 2005, pp. 041301.

[17] M. Futsuhara, K. Yoshioka, and O. Takai, "Optical Properties of Zinc Oxynitride Thin Films", **Thin Solid Films**, vol. 317, 1998, pp. 322-325.

This material is reserved for educational use only, not allowed for commercial use.
Forbidden to modify the content, and cite the document when use.

[18] I. Sayago, M. Aleixandre, A. Martinez, M.J. Fernandez, J.P. Santos, J. Gutierrez, I. Gracia, and M.C. Horrillo, "Structural Studies of Zinc Oxide Films Grown by RF Magnetron Sputtering", **Synthetic Metals**, vol. 148, 2005, pp. 37-41.

[19] H.-C. Lee and J.-Y. Lee, "Effects of Sputtering Pressure and Nitrogen Concentration on the Preferred Orientation of AlN Thin Films", **J. Mater. Sci: Mater. Electron.**, vol. 5, 1994, pp. 221-225.

[20] H. W. Kim and N. H. Kim, "Structural Studies of Room-temperature RF Magnetron Sputtered ZnO Films Under Different RF Powered Conditions", **Mater. Sci. Eng.**, vol. B103, 2003, pp.297-302.

[21] R. O.-Ndong, F. P.-Delannoy, A. Boyer, A. Giani, and A. Foucaran, "Structural Properties of Zinc Oxide Thin Films Prepared by R.f. Magnetron Sputtering", **Mater. Sci. Eng.**, vol. B97, 2003, pp. 68-73.

[22] M. Mulato, I. Chambouleyron, E. G. Birgin, and J. M. Martinez, "Determination of Thickness and Optical Constants of Amorphous Silicon Films From Transmittance Data", **Appl. Phys. Lett.**, vol. 77, 2000, pp. 2133-2135.

[23] I. Chambouleyron, S. Ventura, E. G. Birgin, and J. M. Martinez, "Optimization Techniques for the Estimation of the Thickness and the Optical Parameters of Thin Films Using Reflectance Data", **J. Appl. Phys.**, vol. 92, 2002, pp. 3093-3102.

[24] B. D. Cullity, **Elements of X-Ray Diffraction.** , Reading, MA: Addison-Wesley, 1978.

[25] B. Yao et al., "Effects of Nitrogen Doping and Illumination on Lattice Constants and Conductivity Behavior of Zinc Oxide Grown by Magnetron Sputtering", **J. Appl. Phys.**, vol. 99, 2006, pp. 123510.

[26] M.-L. Tu, Y.-K. Su, and C.-Y. Ma, "Nitrogen-doped *p*-Type ZnO Films Prepared From Nitrogen Gas Radio-frequency Magnetron Sputtering", **J. Appl. Phys.**, vol. 100, 2006, pp. 053705.

[27] Y. Yan, S. B. Zhang, and S. T. Pantelides, "Control of Doping by Impurity Chemical Potentials: Predictions for *p*-Type ZnO", **Phys. Rev. Lett.**, vol. 86, 2001, pp. 5723-5726.

[28] L. Pauling, **The Nature of the Chemical Bond.** Ithaca, New York: Cornell University, 1960.

[29] R. P. Howson, "The Reactive Sputtering of Oxides and Nitrides", **Pure & Appl. Chem.**, vol. 66, 1994, pp. 1311-1318.

This material is reserved for educational use only, not allowed for commercial use.
Forbidden to modify the content, and cite the document when use.

CHAPTER 8

CONCLUSIONS AND FUTURE PERSPECTIVES

8.1 Conclusions

This section is explaining the overall results of this dissertation. This work presents a comprehensive study of indium tin oxide (ITO), indium tin oxynitride (ITON), zinc oxide (ZnO) and zinc oxynitride (ZnON) thin films. By facilitating of gas-timing technique, nanocrystal-ITON and nanocrystal-ZnON thin films were grown on glass substrates by rf magnetron sputtering system at an ambient temperature. The literatures of ITO and ZnO are reviewed in chapters 2 and 3, respectively. Theoretical background of rf magnetron sputtering system and thin film characterization equipment are briefly described in chapters 4 and 5. The growth parameters, including gas flow rate, gas-timing, rf sputtering power, and film thickness, have been adjusted to grow the films in various conditions. After that, a detailed characterization of thin films has been carried out using x-ray diffraction, scanning electron microscope, x-ray photoelectron spectroscopy, UV-VIS spectroscopy and four point probe measurement. In the following sections the growth conditions, characterization results and significantly discussion points of sputtered ITO, ITON, ZnO and ZnON films were summarized.

In chapter 6, the ITO and ITON deposition process was successfully developed according to the gas-timing technique. The structural, electrical and optical properties of the ITO thin films were characterized. The requirement properties of ITO are low resistance and high transmittance. Achievement of the lowest possible resistivity is of practical significance in the respect that it provides some flexibility in selecting the film thickness in order to achieve high optical transmission while retaining low sheet resistance. The properties of ITO as functions of the deposition parameters were quantified and optimized. The result shows large processing window for reliable ITO films. With the argon flow rate fixed at 10 sccm, to get ITO film with transmission greater than 90%, the power can be reduced to 30 W and the gas-timing condition is on-off at 50:2 second provided the low sheet resistance of 8 ohm/square.

With the ITON thin films, we had shown that by introducing nitrogen (N) into the argon (Ar) plasma during the deposition of the ITO by rf sputtering, the optical properties of ITON thin films were very much dependent on the amount of nitrogen in the plasma during deposition. We concluded that there was a significantly variation of the optical properties of ITON films

This material is reserved for educational use only, not allowed for commercial use.

Forbidden to modify the content, and cite the document when use.

deposited on glass in mixed N_2-Ar plasma (identify by nitrogen fraction) when compared to the respective properties of the ITO film deposited in pure Ar plasma. The absorption coefficient was calculated from the transmission spectra to determine the optical band gap energy. The absorption edge of the ITON films deposited in pure N_2 plasma was shifted towards lower energies to 2.21 eV from 3.35 eV (ITO deposited in pure Ar plasma). The results found are currently not present in any publication. The sheet resistance of films also rises from ~15 to ~34 ohm/square when the N_2 concentration increases. It is believed that the incorporation of more nitrogen into the film could tailor the optical and affect the electrical properties of the ITON films.

In chapter 7, the ZnO and ZnON deposition process was accomplished by gas-timing rf magnetron sputtering. The experiments in this chapter deal with the growth and characterizations of ZnO and ZnON films, which were deeply explained about the effect of deposition parameters on the thin film properties. For ZnO, the high quality polycrystalline ZnO thin films were grown on glass substrates at ambient temperature without any thermal treatment. The optimized conditions for the wurtzite ZnO films have been found to correspond to the rf power of 30 W and the gas-timing sequence of 50:2 seconds. The films deposited at these conditions also exhibit a small surface roughness, with the rms value of less than 7 nm. Moreover, the films have high optical transmittance in the visible range of over 85%. The calculations of the optical band gap from the optical transmittance spectra give the band gap values for the films deposited at various gas-timing sequences and rf powers to be in the range ~3.17 to ~3.21 eV.

In the study of ZnON, we successfully prepared nitrogen-doped zinc oxide thin films by rf magnetron sputtering at an ambient temperature by using the nitrogen gas-timing technique. We investigated the effects of three important sputtering deposition parameters on the properties of the ZnON films including the nitrogen flow rate, rf sputtering power and gas-timing condition. It was found that the optical and structural properties of the ZnON films depend not only on the amount of nitrogen in the plasma but also on the amount of nitrogen incorporated inside the films and the rf sputtering power. The ZnON grain sizes at nitrogen flow rates of 10, 15, and 20 sccm are 18.94, 18.24, and 27.47 nm, respectively. The crystallinity of the films increases at a higher nitrogen flow rate, which coincides with a larger average grain size but lower nitrogen doping in the films. The nitrogen incorporation in the ZnON film was confirmed by XPS measurements. At the optimized sputtering condition, we have achieved ZnON films with high N/Zn ratios of above 0.50. In addition, the tuning of optical band gap energy was achieved by varying the processing conditions in the range of 2.98 to 3.08 eV, from the optical ban gap of ZnO at 3.35 eV.

This material is reserved for educational use only, not allowed for commercial use.
Forbidden to modify the content, and cite the document when use.

8.2 Future perspectives

The further research work of this dissertation is emphasizing on the coupled of electrical domain and optical domain on novel functionally ITON and ZnON films.

Although ITON films with excellent electrical and optical properties were obtained, this process can be further improved. The uniformity variation resulted from 3 inch target can be solved by larger diameter target. The film properties variation between runs still requires to be minimized. In order to further research, ITON is a promising conductive optically functional material that can use as a novel optical filter in near ultraviolet to visible region.

With further studies of ZnON, this technique may be applied to fabricate ZnON thin films at room temperature for *p*-type layer in transparent electronics devices. The deposition parameters of sputtered ZnON thin films need to be optimized.

The gas-timing technique should be applicable for the fabrication of many functional optical devices that require tunable material properties and low-temperature processing.

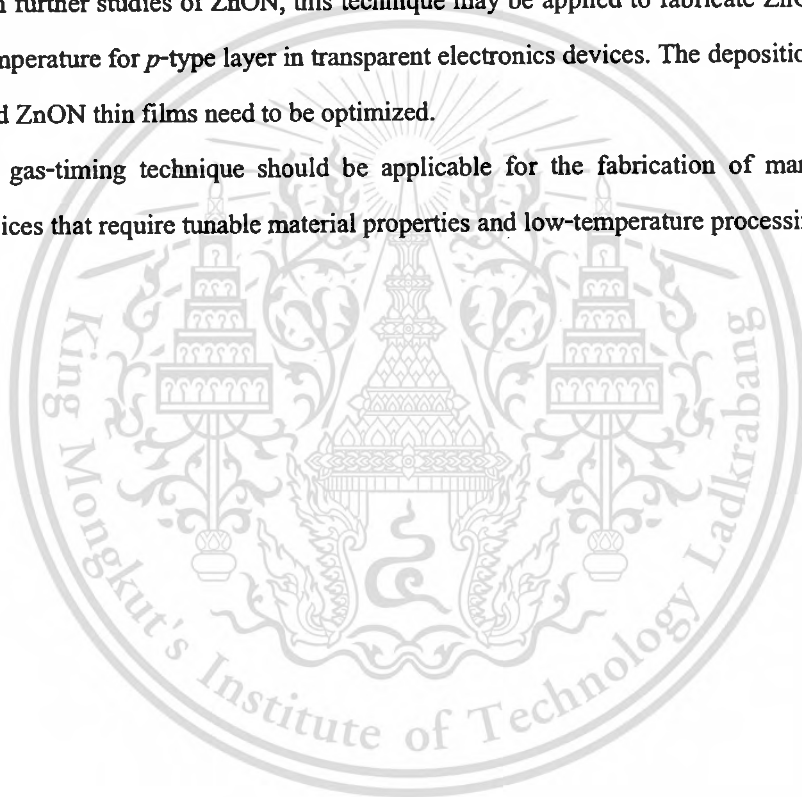

This material is reserved for educational use only, not allowed for commercial use.
Forbidden to modify the content, and cite the document when use.

AUTHOR BIOGRAPHY

Flight Lieutenant Don Klaitabtim was born in Bangkok Thailand on September 5, 1975. He received B.Eng degree in Electrical Engineering from The Royal Thai Air Force Academy (RTAFA), Thailand in 1998 and M.Eng degree in Microelectronics from Asian Institute of Technology (AIT), Thailand in 2003. He is now studying toward the Ph.D. degree in Applied Physics at King Mongkut's Institute of Technology Ladkrabang (KMITL), Thailand and working with The Royal Thai Air Force at Communications and Electronics depot level maintenance division, Directorate of Communication and Electronics, Air Support Command.

His research interests include thin film fabrication and characterization, MEMS design and simulation based on multiphysics finite element analysis and FPGA Implementation.

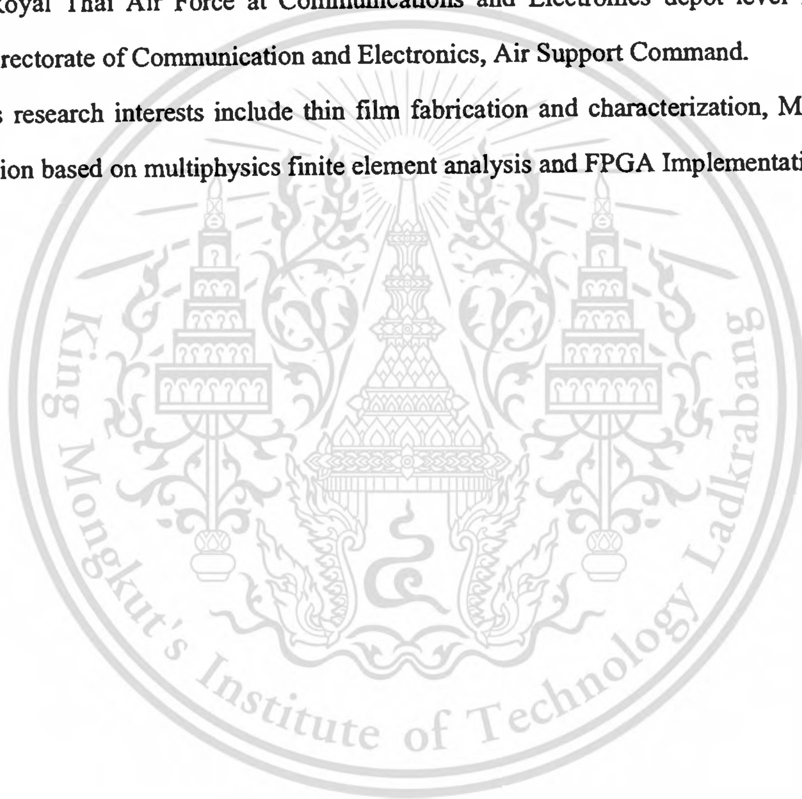

This material is reserved for educational use only, not allowed for commercial use.
Forbidden to modify the content, and cite the document when use.